

POLYTECHNIQUE MONTRÉAL

affiliée à l'Université de Montréal

**BRIDGING MACRO-SCALE EXPERIMENTAL AND DUAL-SCALE
VIRTUAL TESTING FOR PERMEABILITY OF TEXTILE
REINFORCEMENTS WITH DIGITAL MATERIAL TWINS**

BIN YANG

Département de génie mécanique

Thèse présentée en vue de l'obtention du diplôme de *Philosophiæ Doctor*

Génie mécanique

Avril 2024

POLYTECHNIQUE MONTRÉAL

affiliée à l'Université de Montréal

Cette thèse intitulée :

**BRIDGING MACRO-SCALE EXPERIMENTAL AND DUAL-SCALE
VIRTUAL TESTING FOR PERMEABILITY OF TEXTILE
REINFORCEMENTS WITH DIGITAL MATERIAL TWINS**

présentée par **Bin YANG**

en vue de l'obtention du diplôme de *Philosophiæ Doctor*
a été dûment acceptée par le jury d'examen constitué de :

Sébastien LECLAIRE, président

Cédric BÉGUIN, membre et directeur de recherche

Philippe CAUSSE, membre et codirecteur de recherche

Jihui WANG, membre et codirecteur de recherche

David VIDAL, membre

Cyprien SOULAINE, membre externe

DEDICATION

*To my supervisors,
To my family, friends, and other loved ones,
To anyone who has shown me kindness, encouragement,
and support throughout this adventure.*

ACKNOWLEDGEMENTS

This adventure began with an unexpected opportunity. Prof. François Trochu was invited to give a lecture in China, and it was a follow-up email I sent to him that opened the door to my internship and doctoral journey at Polytechnique. Together, we discussed the possibility of establishing a team that would span North America, Asia, and Europe, dedicated to the technology of liquid composite molding. We also shared moments of climbing Mont Royal and enjoying ice skating and skiing as friends. Regrettably, he left us forever before the conclusion of my study. His visionary thinking, inclusiveness, and patience have profoundly influenced me and left an indelible mark on my professional and personal growth.

I owe special thanks to my supervisors, Profs. Cédric Béguin and Philippe Causse, for guiding me through the past four years. They granted me the freedom to make my own choices in research. Yet, they were always there to offer guidance when I veered off course, steering me back to the right path. I am also deeply grateful to my co-supervisor, Prof. Jihui Wang from Wuhan University of Technology, who established for me a valuable bridge to the industry. He helped me understand that research should be based on practical requirements and real-world needs.

I would also like to thank the jury members, Profs. Sébastien Leclaire, David Vidal, and Cyprien Soulaine, for their remarks and comments, which allowed me to gain perspective on my subject and open up prospects for future development. Acknowledgments also go to Prof. Shuxin Li from Wuhuan University of Technology, Dr. Chengliang Li, Dr. Junwei Cui, and Yan Liu from Sinoma Wind Power Blade Co., Ltd., Dr. Mehdi Ghazimoradi from Linamar Corporation Inc., Xiuhua Xu from Jinling AOC Resins Co., Ltd., and Ahmed Ouezgan from Ecole Nationale Supérieure d'Electricité et de Mécanique de Casablanca for their discussions and insights on LCM, permeability, and textile modeling.

My sincere thanks also go to Anna Madra and Wei Huang, who took the initial steps in this topic and set the stage for the subsequent work. And of course, I wish to thank our team members, Yuwei Feng, Yixun Sun, Zaynab Grofti, Ariana Zelaya Matamoros, Jieyao Deng, Mohammadreza Moeini and Christian-Charles Martel. Thanks for your support in research and in life.

Finally, I would like to express gratitude to my family members for their unwavering and unconditional support. None of this would have been achievable without your presence and encouragement.

RÉSUMÉ

Au cours des dernières années, les procédés d'injection sur renforts (*Liquid Composite Molding, LCM*) ont significativement gagné en popularité dans la fabrication de composites pour différentes industries telles que l'aérospatiale, la marine, l'énergie éolienne et l'industrie automobile. Ces méthodes de fabrication sont notamment avantageuses en raison de leur coût modéré et de leur potentiel de production élevée. L'imprégnation des renforts textiles par la résine est une étape critique du procédé de mise en forme. L'utilisation de la simulation numérique est une méthode courante pour développer des stratégies d'injection optimales.

Améliorer la fiabilité des résultats numériques reste un défi. Une des difficultés réside dans la caractérisation de la perméabilité transverse, en raison notamment de la compressibilité des renforts. Une structure de support est donc nécessaire pour le test de perméabilité transverse afin d'éviter la déformation. Cependant, cela perturbe l'écoulement dans la cavité du moule. Les résultats obtenus lors d'un récent exercice de comparaison international font état de différences allant jusqu'à deux ordres de grandeur dans les mesures expérimentales. Une cause possible est que les montages expérimentaux utilisés par les 26 participants présentent des configurations variables. La perméabilité et la qualité d'imprégnation sont par ailleurs étroitement liées à la structure à double échelle des renforts textiles. Une analyse de la structure à plus petite échelle est nécessaire pour comprendre le comportement de l'écoulement. Cet aspect est négligé dans la simulation à l'échelle de la pièce, car elle repose sur des variables moyennées en volume.

Ce projet étudie les écoulements à double échelle, macroscopique et mésoscopique, dans les renforts textiles. L'étude commence par identifier les facteurs influençant les essais de perméabilité transverse réalisés à l'aide de la méthode unidirectionnelle. Les résultats indiquent que la structure de support (également connue sous le nom de plaque de distribution de l'écoulement) est un facteur important. La perméabilité transverse est sous-estimée en raison de la restriction de l'écoulement dans la section du dispositif expérimental. Cet effet a notamment été montré expérimentalement pour la première fois.

Un indicateur de performance adimensionnel, le coefficient de décharge, a été proposé pour quantifier l'efficacité de transfert de masse d'un moule de test unidirectionnel. Nos résultats ont montré que l'indicateur dépend à la fois de l'anisotropie de la perméabilité et de l'épaisseur de l'échantillon en raison de la trajectoire de l'écoulement en 3D causée par les plaques. En utilisant cet indicateur, une procédure numérique a été conçue pour cartographier les performances des dispositifs d'essai. De plus, nous avons proposé un algorithme pour

déterminer et corriger la perméabilité intrinsèque en utilisant la carte des performances. La méthodologie a été appliquée pour étudier la disparité de mesure entre deux moules différents utilisés respectivement à Polytechnique Montréal et à l’Université de Technologie de Wuhan. Les résultats ont démontré une bonne précision et reproductibilité.

L’analyse macroscopique décrite ci-dessus constitue les premier et deuxième articles de revues présentés dans la thèse. Les articles 3 et 4 présentent ensuite des méthodes innovantes pour la modélisation paramétrique de la géométrie des renforts textiles au niveau mésoscopique. Les renforts textiles ont d’abord été caractérisés par microtomographie aux rayons X. Ensuite, une représentation explicite de chaque toron de fibres est dérivée du jeu de données segmenté. Une méthode fondée sur l’estimation de densité par noyau est employée pour rééchantillonner de manière stochastique les données. Ceci permet de minimiser les incertitudes causées par le prétraitement de l’image et permet de représenter les torons de façon paramétrique. Le krigeage dual constitue la théorie fondamentale derrière cette technique. Les sections normales des torons sont alors déterminées par intersection de plans implicites avec la surface paramétrique. Cela permet l’évaluation de la variabilité spatiale dans les textiles et fournit des informations pour créer des modèles de haute fidélité connus sous le nom de Jumeaux Numériques de Matériaux (*Digital Material Twin, DMT*).

Finalement, une nouvelle librairie distribuée sous licence libre, PolyTex, est développée pour automatiser le processus d’analyse et de modélisation de la géométrie. De plus, l’interopérabilité avec d’autres environnements numériques, tels que OpenFOAM et Abaqus, est fournie. Cela permet aux utilisateurs de développer leurs propres modèles DMT et de les utiliser dans des simulations, même avec des connaissances limitées en traitement d’images et en modélisation géométrique. À des fins de démonstration, une étude de cas a été réalisée pour prédire la perméabilité avec des modèles DMT.

En résumé, ce travail fournit des directives pour la conception et l’étalonnage des montages de caractérisation de la perméabilité transverse et un algorithme de correction pour identifier la perméabilité intrinsèque. Par la suite, un outil automatique pour l’analyse et la modélisation de la géométrie textile, PolyTex, a été développé pour aider à étudier l’écoulement à double échelle, les sources d’erreurs de mesure de la perméabilité et les défauts de fabrication potentiels. Il est finalement important de remarquer que les modèles DMT ne se limitent pas aux études numériques d’écoulement à double échelle, mais pourront également être utilisés dans le futur pour prédire les propriétés mécaniques ainsi que la progression de l’endommagement.

ABSTRACT

Over the past years, Liquid Composite Molding (LCM) gained significant popularity for composite fabrication in various industries such as aerospace, marine, wind energy, and automotive sectors due to its moderate cost and high production efficiency. The impregnation of textile reinforcements with resin is a critical step in the manufacturing process. Utilizing numerical simulation is a common way for developing optimal injection strategy.

Improving the reliability of numerical results remains challenging. One of the difficulties is the characterization of the transverse permeability. This stems from the deformability of the reinforcements. Support structure is therefore required for transverse permeability test to avoid deformation. However, this disturbs the flow pattern in the mold cavity. The results of the recent international benchmark reveal a maximum discrepancy of two orders of magnitude. One potential cause is that the testing devices used by the 26 participants exhibit varying configurations. Permeability and impregnation quality are also intricately connected to the dual-scale structure of textile reinforcements. An analysis of the lower-scale structure is necessary to understand the flow behavior. This aspect is neglected in part-scale simulation, as it relies on volume-averaged variables.

This project studies both macroscopic and mesoscopic dual-scale flow in textile reinforcements. The study begins by identifying the factors that influence the unidirectional transverse permeability tests. The results indicate that the support structure (also known as the flow distribution plate) is an important factor. The transverse permeability is underestimated due to restricted flow exchange in the test section. This effect was revealed by our experiments for the first time.

A dimensionless performance indicator, the discharge coefficient, was proposed to quantify the mass transfer efficiency of an unidirectional test mold. Our results showed that the indicator depends on both the anisotropy of permeability and the thickness of the specimen due to the 3D flow trajectory caused by the plates. Using this indicator, a numerical procedure was devised to map the performance of the test devices. Moreover, we proposed an algorithm to determine and correct the intrinsic permeability using the performance map. The methodology was applied to investigate the measurement discrepancy between two different molds located respectively in Polytechnique Montréal and Wuhan University of Technology. The results demonstrated good accuracy and reproducibility.

The macroscopic analysis described above constitutes the first and second journal articles presented in the thesis. Articles 3 and 4, on the other hand, introduced innovative methods

for parametric modeling of the geometry of textile reinforcements at the mesoscopic level. The textiles were first characterized with microcomputed tomography. Then an explicit representation of each fiber tow is derived from the segmented dataset. A method based on kernel density estimation is employed to stochastically resample the data. This helps minimize the uncertainties caused by image pre-processing, and allows depicting tows by a parametric approach. Dual kriging serves as the foundational theory behind this technique. The normal cross-sections of tows are solved by intersecting planes with fiber tow surface, thanks to the parametric kriging. This enables the evaluation of material spatial variability and provides information for creating high-fidelity models known as Digital Material Twins (DMT).

Finally, an open-source code, *PolyTex*, is developed to automate the geometry analysis and modeling process. Moreover, interoperability with other numerical environments, such as OpenFOAM and Abaqus, is provided. It allows users to develop their own DMT models and utilize them in simulations, even with limited knowledge of image processing and geometry modeling. For demonstration purposes, a case study was performed to predict permeability with DMT models.

In summary, this work provides guidelines for the design and calibration of unidirectional transverse permeability test devices and a correction algorithm to identify intrinsic transverse permeability. Subsequently, an automatic tool for textile geometry analysis and modeling, *PolyTex*, was developed to assist in investigating dual-scale flow behavior, sources of permeability measurement errors, and potential manufacturing defects. Finally, it should be noted that DMT models are not restricted to numerical investigations of dual-scale flow, but can also be utilized to predict the mechanical properties and the damage progression of composites in future investigation.

TABLE OF CONTENTS

DEDICATION	iii
ACKNOWLEDGEMENTS	iv
RÉSUMÉ	v
ABSTRACT	vii
TABLE OF CONTENTS	ix
LIST OF TABLES	xiv
LIST OF FIGURES	xv
LIST OF APPENDICES	xxv
 CHAPTER 1 INTRODUCTION	1
1.1 Basic definitions and concepts	1
1.1.1 Liquid composite molding	1
1.1.2 Dual-scale structure of tow-based textile reinforcements	2
1.1.3 Permeability of fibrous reinforcements	3
1.2 Elements of the problem	4
1.2.1 Research issues	4
1.2.2 Research scope	6
1.3 Research objectives	7
1.4 Outline of the dissertation	8
 CHAPTER 2 LITERATURE REVIEW	10
2.1 Phenomena encountered in LCM	10
2.1.1 Characterization of transverse flow	10
2.1.2 Quantification of textile reinforcement structure distortions	11
2.1.3 Composite quality and dual-scale flow	11
2.2 Characterization of textile permeability	13
2.2.1 Classification of experimental measurement methods	14
2.2.2 A brief journey through the history of permeability measurements . .	22
2.2.3 Summary	27

2.3	The formation, prediction and minimization of voids	27
2.3.1	Defects present in composites in the real world	27
2.3.2	Formation mechanism of voids	28
2.3.3	Voidage prediction	29
2.3.4	Voidage minimization	33
2.3.5	Summary	34
2.4	Mesoscopic geometry modeling of textile reinforcements	34
2.4.1	Internal geometry characterization	35
2.4.2	Simplified mesostructural models	37
2.4.3	Realistic mesostructural models	38
2.4.4	Digital material twins	39
2.4.5	Summary	44
2.5	Volumetric image aided virtual testing of permeability	45
CHAPTER 3 ARTICLE 1: ON THE DESIGN OF TEST MOLDS BASED ON UNIDIRECTIONAL SATURATED FLOWS TO MEASURE TRANSVERSE PERMEABILITY IN LIQUID COMPOSITE MOLDING		48
3.1	Chapter overview	48
3.2	Abstract	48
3.3	Introduction	49
3.4	Review of literature	53
3.5	Cavity deformation for unidirectional mold with perforated plates	55
3.5.1	Compressibility of engineering fabrics	55
3.5.2	Simulation of perforated plate deformation	56
3.6	Through-thickness flow pattern	60
3.6.1	Theory	60
3.6.2	Geometrical models	61
3.6.3	Effect of perforations	63
3.6.4	Effect of sample and material properties	65
3.6.5	Flow distribution layer	67
3.6.6	Saturated flow analysis	69
3.6.7	Pressure drop in empty mold	71
3.7	Experimental verification	71
3.8	Conclusion	74

CHAPTER 4 ARTICLE 2: PERFORMANCE EVALUATION OF UNIDIRECTIONAL MOLDS USED FOR MEASURING SATURATED TRANSVERSE PERMEABILITY OF ENGINEERING TEXTILES	78
4.1 Chapter overview	78
4.2 Abstract	78
4.3 Introduction	79
4.4 Evidence for permeability underestimation of the conventional 1D method	81
4.4.1 Equipment and method	81
4.4.2 Permeability of reference porous medium	83
4.4.3 Performance of unidirectional molds	85
4.5 Numerical characterization of 1D experimental setup	86
4.5.1 Motivation	86
4.5.2 Governing equations	86
4.5.3 Geometrical model and boundary conditions	87
4.6 Correction of permeability measurements with isotropic materials	88
4.6.1 Numerical evaluation of mold performance	88
4.6.2 Permeability correction and validation	89
4.7 Correction of permeability measurements with orthotropic materials	89
4.7.1 Influence of global permeability anisotropy	90
4.7.2 Evaluation of mold performance	92
4.7.3 Iterative framework for transverse permeability identification	93
4.7.4 Validation	95
4.7.5 Sensitivity analysis	97
4.8 Effect of test device on transverse permeability characterization	99
4.8.1 Mold description and analysis of performance	99
4.8.2 Permeability and measurement consistency	101
4.9 Conclusion	104
CHAPTER 5 ARTICLE 3: TOMOGRAPHIC MODELING AND INTERNAL STRUCTURE ANALYSIS OF ENGINEERING TEXTILES: A PARAMETRIC APPROACH	107
5.1 Chapter overview	107
5.2 Abstract	107
5.3 Introduction	108
5.4 Material characterization	111
5.5 Methodology	112
5.5.1 Parametric representation of tow geometry	112

5.5.2	Point cloud clustering and resampling	113
5.5.3	Reconstruction of tow geometry	115
5.5.4	Tow trajectory and local orientation	118
5.5.5	Normal cross-sections of fiber tow	118
5.5.6	Geometry smoothing	120
5.5.7	Code implementation	120
5.6	Comparative analysis and case study	120
5.6.1	Effects of point clustering on geometry approximation	120
5.6.2	Geometry smoothing	121
5.6.3	Tow trajectory and local orientation	124
5.6.4	Normal cross-sections of fiber tow	125
5.6.5	Textile geometry modeling	128
5.7	Conclusion	130
5.8	Acknowledgements	132
CHAPTER 6 ARTICLE 4: OPEN-SOURCE TOOL FOR MICRO-CT AIDED MESO-SCALE MODELING AND MESHING OF COMPLEX TEXTILE COMPOSITE STRUCTURES		133
6.1	Chapter overview	133
6.2	Abstract	133
6.3	Introduction	134
6.4	The design of <i>PolyTex</i>	136
6.5	Data handling and structural representation	139
6.5.1	Specifications of input data	139
6.5.2	Morphological features	141
6.5.3	Data persistence	141
6.5.4	Cross-tool interoperation	142
6.6	Theory	145
6.6.1	Robust noise reduction and data resampling	145
6.6.2	Geometry representation with kriging	145
6.6.3	Normal cross-section identification	148
6.6.4	Local permeability	148
6.7	Case studies	150
6.7.1	Digital material twin	151
6.7.2	Governing equations	153
6.7.3	Boundary conditions	154

6.7.4	Result and discussion	155
6.8	Conclusion	157
6.9	Appendix	158
6.10	Mesh file specifications	158
6.11	Configurations for reference sample printing and permeability testing	159
CHAPTER 7 CONCLUSION		163
7.1	Summary of works	163
7.2	Limitations	164
7.3	Future research	165
REFERENCES		167
APPENDICES		194

LIST OF TABLES

Table 2.1	Formulas for in-plane permeability calculation	17
Table 2.2	Micro-CT image pre-processing and image segmentation methods . .	36
Table 2.3	Solvers commonly used for virtual permeability testing	47
Table 3.1	Configurations of perforated plates reported in the scientific literature.	54
Table 3.2	Deflections for similar open space ratios and different perforation patterns.	57
Table 3.3	List of simulation cases considered to study the effect of perforations.	63
Table 3.4	Influence of permeability on the fill coefficient.	67
Table 4.1	Transverse permeability of the reference porous medium.	85
Table 4.2	Transverse permeability test configurations of TG96N.	96
Table 4.3	The transverse permeability test configurations for Benchmark III. . .	101
Table 4.4	In-plane permeability of the two benchmark fabrics.	102
Table 6.1	Attributes and methods of the <code>Tow</code> and <code>Textile</code> classes	139
Table 6.2	3D mesh data structure for VTK unstructured grid, polyMesh, and Abaqus inp Formats	145
Table 6.3	Summary of drift and generalized covariance functions available in <i>PolyTex</i>	147

LIST OF FIGURES

<p>Figure 1.1 Resin flow patterns during infusion: (a) only in-plane flow is involved in Vacuum Assisted Resin Infusion (VARI); (b) Seeman Corporation Resin Infusion Molding Process (SCRIMP) introduced transverse flow to accelerate the impregnation process (adapted from [9]). The green arrows show the flow direction at the flow front.</p> <p>Figure 1.2 Dual-scale structure of fibrous reinforcements</p> <p>Figure 2.1 Coupling between different phenomena in LCM</p> <p>Figure 2.2 The complex flow front encountered during the manufacturing of sandwich composites: wind turbine blades utilize balsa wood and PolyVinyl Chloride (PVC) foamcore sandwich composites on the shear web (a) for weight reduction. The balsa wood was perforated in the thickness direction, whereas PVC foamcore was not only perforated but also grooved on the surface to distribute resin flow; (b) serrated flow front due to grooves and (c) impregnation through the thickness because of the perforations. <i>Photos were taken at Sinoma Wind Power Blade Co., Ltd., China</i></p> <p>Figure 2.3 Dual-scale flow in textile reinforcements: (a) partially saturated flow with a length of L_{sat} due to the dual-scale structure of the woven fabric [30]; (b) capillary fingering along fiber tows indicated between dashed lines [31].</p> <p>Figure 2.4 The notation used for the permeability components is usually k_x and k_y for the in-plane components, while k_z is used for the transverse permeability, as indicated by the Cartesian coordinate.</p> <p>Figure 2.5 Techniques for in-plane permeability measurement: the channel flow method (1D), the radial injection method (2D) and the three-dimensional method (3D). [37]</p> <p>Figure 2.6 Channel flow method: (a) schematic representation of testing setup [36]; (b) In-plane permeability test device at Polytechnique Montréal.</p> <p>Figure 2.7 Radial injection approach for in-plane permeability measurement: (a) schematic representation of the test approach [40]; (b) the anisotropy of fibrous preforms can be measured directly with the radial injection approach [51].</p>	<p>2</p> <p>3</p> <p>11</p> <p>12</p> <p>13</p> <p>14</p> <p>15</p> <p>16</p> <p>18</p>
--	---

Figure 2.8	Three-dimensional (3D) method for permeability measurement: (a) schematic representation of the test approach; (b) flow front tracking with X-ray radioscopy setup for permeability measurement [37].	19
Figure 2.9	Methods for transverse permeability measurement used by participants of the first international benchmark exercise launched in 2018 [13]. The number on the pie chart indicates the number of results measured by each method.	20
Figure 2.10	Actual flow pattern during saturated transverse permeability measurement	21
Figure 2.11	Progress and milestones in the standardization of measuring the permeability of textile reinforcement. The first global standard for assessing in-plane permeability, ISO 4410:2023 [73], was released in July 2023, as an outcome of the benchmark exercises.	23
Figure 2.12	In-plane permeability K_1 for (a) twill carbon fiber fabric G0986 [36] (b) measured at the first benchmark [35].	24
Figure 2.13	In-plane permeability k_1 for twill carbon fiber fabric G0986 measured at the second benchmark: (a) calculated with the SFF method [36]; (b) calculated with the LSF method [36].	25
Figure 2.14	Transverse permeability at different compaction levels for all participants of the first benchmark on transverse permeability. (a) Woven fabric; (b) NCF fabric. The presence of dashed lines on the graph signifies a range of values where the ratio between the upper and lower bounds is 4 [13].	26
Figure 2.15	Typical structure of wind turbine blades.	28
Figure 2.16	Manufacturing defects appearing on wind blades: LE stands for leading edge, TE for trailing edge, PS for pressure side of shell and SS for suction side of shell, as illustrated in Figure 2.12.	29
Figure 2.17	Void formation caused by dual-scale flow under (a) low and (b) high impregnation velocity [78].	30
Figure 2.18	Voidage (void content) as a function of flow front velocity (a) and capillary number (b) [79].	31
Figure 2.19	Time-difference based void prediction model (a) void formation inside the tow; (b) void formation in the channel between the tows; (c) void is prevented due to the uniform flow front [84].	32

Figure 2.20	Contours of the (a) maximum final void content found in the 2D slices of the Rovcloth 2454, (b) volume-averaged final void content considering each of the two-dimensional slices, (c) dimensionless excess flow time and (d) combined parameter on a Capillary number-Reynolds number plane for the Rovcloth 2454 [86].	33
Figure 2.21	Virtual testing environment for textiles or composites built on the meso-level textile processor WiseTex [133].	38
Figure 2.22	Descriptions of fiber tows in simplified models: (a) tows described by base cross sections sweeping along its path [135]; Analytical yarn cross sections modeled (b) using a power ellipse with exponents [0.5, 1, 2, 3], where the colors transition from blue to purple, and (c) with a lenticular shape with distortion distance $[-h/3, -h/6, 0, h/6, h/3]$, where the colors transition from blue to green [136].	39
Figure 2.23	(a) Micro-tomographic image; (b) Digital material twin (voxel model) [110]	40
Figure 2.24	Representation of fiber tows with parametric kriging: (a) representation of tow contour with parameters (s, t) ; (b) parametric reconstruction of fiber tow surface and (c) smoothing with nugget effect [122]. . .	41
Figure 2.25	Variations of fiber tow cross-sectional area perpendicular to the horizontal plane at three compaction levels [113]	42
Figure 2.26	Creation of a 3D mesh for a fiber tow: (a) complete tow, (b) incomplete tow, and (c) adjusting the density of the mesh for a given fiber tow [20].	43
Figure 2.27	Models with different accuracy and the corresponding tensile stress field in x direction obtained through numerical simulation. The simplified model, realistic model, and DMT are shown from left to right [151]. .	44
Figure 2.28	Categories of volumetric image aided permeability virtual testing according to the handling of fiber tows in the model: (a) solid tow [154]; (b) porous tow, flow along x -axis [155]; (c) fiber resolved [156].	46
Figure 3.1	Example of one-dimensional transverse permeability test mold: (a) tool with pressure sensors near the inlet and outlet. (b) Perforated plate..	50
Figure 3.2	The fibrous preform being held between two perforated plates, this figure shows typical non-unidirectional flow patterns created by perforations [15]. Convergent and divergent flows can be observed in zones of the specimen facing impermeable parts in the perforated plates. . .	52
Figure 3.3	Dry and wet compressibility measurement for the two benchmark fabrics (measured at Wuhan University of Technology).	56

Figure 3.4	Analysis of perforated plate deformation: (a) boundary conditions for the 3D stiffness finite element analysis of a circular sector. (b) Mean deflection as a function of the open space ratio and plate thickness for the three pressure levels considered (aluminum).	58
Figure 3.5	Geometrical models and boundary conditions used to conduct filling and saturated flow simulations: (a) boundary conditions (pressure inlet of 100 kPa in red and outlet at 0 Pa in blue) for filling flow simulations with PAM-RTM. (b) Mesh of the geometrical domain considered for the saturated steady state flow simulations including the preform, the two perforated plates, the flow distribution layers under and above the specimen and part of the inlet and outlet mold cavity. The pressure is 100 kPa in the bottom inlet surface and 0 Pa in the upper outlet surface.	62
Figure 3.6	Effect of two geometrical parameters on flow patterns for a 7 mm thick preform: (a) number of perforations for nearly the same open space ratio and reduced hole diameters. (b) Support width (for simulations based on the configuration of Table 3.1).	64
Figure 3.7	Influence of hole packing calculated for a 20 mm thick preform: (a) non-uniform distribution of perforations near the edge of the mold cavity. (b) Uniformly distributed perforations. (c) Vertical transverse velocity fields in the XZ and YZ planes in case A. (d) Vertical transverse velocity fields in the XZ and YZ planes in case B. the vertical velocity decreases near the edges of the mold cavity. The decrease spreads more in case A, which is consistent with the larger fill coefficient obtained (1.58 vs. 1.31 in case B).	65
Figure 3.8	(a) Results of numerical simulations for the existing tool to investigate the relationship between the fill coefficients and preform thickness. As expected, larger preform thicknesses give smaller fill coefficients. (b) Transverse velocity in the cross-section shown by arrows in (a). In each case considered, the velocity is divided equally into 15 color levels from the minimum to the maximum values. As thickness increases, the zones of larger transverse flow velocity become relatively smaller with respect to the whole flow domain.	66
Figure 3.9	Fill coefficient as a function of an isotropic flow distribution layers (FDL) permeability. The principal permeability of the 4-millimeter-thick isotropic preform is $3.0 \times 10^{-12} \text{ m}^2$	68

Figure 3.10	Transverse velocity distribution inside the mold cavity: (a) 3D view obtained by volume rendering for $F = 5.1$. (b) 3D view obtained by volume rendering for $F = 1.1$. (c) Transverse velocity component w along the z -axis for $F = 5.1$. (d) Transverse velocity component w along the z -axis and cross-sectional view of the flow pattern for $F = 1.1$.	70
Figure 3.11	Typical transverse permeability experimental results obtained with a 1D test device compared with measurements with flow distribution layers (FDL) after correcting for perforated plate deformation.	73
Figure 3.12	Kriging profiles for parametric surface kriging of the deflection field under a 100 kPa load.	77
Figure 4.1	Schematic diagram of a typical unidirectional transverse permeability test device.	80
Figure 4.2	Transverse permeability test mold at Polytechnique Montréal (a) and its perforated plate of 6.5 mm in thickness (b).	82
Figure 4.3	Reference porous medium (a) and two test configurations: apparent permeability test with flow distribution plates (b) and intrinsic permeability test in freestanding conditions (c).	83
Figure 4.4	Measured pressure drop across the thickness direction for the reference porous specimens with thickness (h) of 11.6 mm and 25 mm.	84
Figure 4.5	Geometrical model and boundary conditions for 3D flow simulation.	87
Figure 4.6	Discharge coefficient (scatters) and transverse permeability underestimation for isotropic materials as a function of sample thickness for the test device shown in Figure 4.2. Red stars indicate experimental measurements whereas all other markers correspond to numerical simulations.	89
Figure 4.7	Comparison of apparent, intrinsic, and identified transverse permeability based on numerically determined discharge coefficient for the reference porous medium.	90
Figure 4.8	Parametric investigation of fluid exchange through distribution plates for different preform thickness h and anisotropy α_g : the magnitude of intrinsic average velocity vector in the visualization zone of (a) is shown in (b) superimposed with streamlines (only shown on the right half of each subplot). The gray color in (b) represents the solid part of perforated plates which is impermeable.	91
Figure 4.9	Characteristic performance map for the mold presented in Figure 4.2.	93

Figure 4.10	Transverse permeability of TG96N: (a) raw data with and without secondary flow distribution layers; (b) corrected values with Huang's model and the two newly proposed iterative frameworks.	98
Figure 4.11	Comparison of numerically identified permeability for aligned and not aligned perforated plates: two extreme conditions for hexagonal packing holes as depicted by the inset.	99
Figure 4.12	Transverse permeability test mold of Wuhan University of Technology (a) and its perforated plate of 7 mm in thickness (b); Characteristic performance map of the mold (c).	100
Figure 4.13	The apparent and the identified permeability of (a) woven and (b) non-crimp fabric.	103
Figure 4.14	The apparent and identified permeability of (a) woven fabric and (b) non-crimp fabric after being corrected to nominal fiber volume fractions.	105
Figure 5.1	Woven structure of the 3D orthogonal textile TG96N from Texonic Inc.	111
Figure 5.2	Textile internal architecture characterization: (a) The Region of Interest (ROI) subjected to subsequent analysis; (b) Schematic of Micro-CT slices. These Micro-CT slices do not always align perpendicularly with the fibers within the tow.	111
Figure 5.3	Parametric representation of fiber tows: profile t along the axial direction (a) and profile s in the radial direction (b) are mapped on to a rectangular parameter domain Ω with different resolution (c). The dashed line in (c) represents the cutting path along which the tow surface is unfolded.	113
Figure 5.4	Illustration of point cloud clustering and resampling: (a) A fiber tow represented by a point cloud consisting of 11088 points in geometric space $(x, y, z) \in \mathbb{R}^3$; (b) Distribution of points and associated probability density in parameter space $(s, t) \in \Omega$; (c) Impact of bandwidth h on probability density estimation using Gaussian kernel; (d) Fiber tow profile reconstructed with the cluster centers. Kriging-based estimator is used to map the resampled point cloud back to the geometric space. Red and green horizontal lines in (b) represent the cluster centers and boundaries. Only four clusters are decomposed here for illustration purposes.	115

Figure 5.5	Normal cross-section identification: (a) envelop surface of a fiber tow segmented from Micro-CT slices; (b) trajectory of tows with its tangent identified; (c) intersection detection between an implicit plane (defined by the trajectory tangent \vec{n} and its origin) and the parametric surface of fiber tow; (d) the identified normal cross-sections that are perpendicular to the tow trajectory.	119
Figure 5.6	Effect of point cloud clustering on geometry approximation accuracy: (a) Point clustering and resampling globally considering the entire tow or locally with a moving window (indicated by different colors) sliding along the axial direction; Global clustering with (b) $m = 30$ (each tow cross-section approximated with a polygon of 30 vertices) and (c) $m = 50$; Local clustering with (d) $m = 50$ and (e) $m = 100$; The geometry approximated with the resampled points (in red) is overlaid onto the reference fiber tow structure (in gray). (f) Derivation of geometry features from ground truth for the cases shown in (b) - (e).	122
Figure 5.7	Tow surface smoothing: (a) Tow volume versus iterations (or smooth factor σ^2 for the proposed method) for various smoothing algorithms. Anisotropic smoothing along the radial direction (b) or the axial direction (c) of a fiber tow using the proposed method. No smoothing is applied to the perpendicular direction. Both the top and bottom views of the tow are shown and visualized with Gaussian curvature.	123
Figure 5.8	Suppression of spurious fluctuations in a binder tow trajectory using various techniques: (a) kriging; (b) Savitzky-Golay filter; (c) Fast Fourier Transform (FFT); (d) Median filter. The insets labeled “2x” and “4x” indicate curves enlarged by a factor of 2 and 4, respectively.	125
Figure 5.9	Fiber tow trajectories (a) and local orientations (b) in a single layer of the textile shown in Figure 5.2a.	126
Figure 5.10	Effect of smoothing strength using the proposed method on local fiber orientations. I and II correspond to the regions labeled in Figure 5.9b.	127
Figure 5.11	Illustration of mesh trimming method (a) and projection method (b) for cross-sectional profile identification and local cross-section area calculation; (c) a comparison between the normal cross-sections determined with the proposed method and the profiles obtained directly from Micro-CT image slices.	128

Figure 5.12	Comparison of local cross-sectional area determined by various methods: (a) - (d) correspond to binder tows located at the positions indicated by the insets in the upper-left corner. A portion of the curves were magnified two-fold and presented in the inset located in the upper right corner of each subplot. (e) and (f) correspond to a warp tow and a weft tow located at the positions indicated by the insets in the upper-left corner.	129
Figure 5.13	Internal geometric modeling of the 3D orthogonal textile reinforcements shown in Figure 5.2a using various methodologies: (a) the simplified and (b) the realistic geometry models created with TexGen; (c) the digital material twin model created with the proposed method. (d) - (f): Visual comparison of the cross-sections indicated by the dashed frames. The selected cross-sections are overlaid with the corresponding micro-CT image.	131
Figure 6.1	Design of the object-oriented textile modeling code, <i>PolyTex</i> (abbreviated to <i>ptx</i>): (a) hierarchical and modular architecture; (b) customized interfaces to various software. Implemented features are represented by solid line with arrows, while features to be added in the future are represented by dashed arrows.	137
Figure 6.2	Data structure of input dataset for <i>PolyTex</i> : (a) Volumetric image of a composite in the provided coordinate system, where the matrix is depicted in darker tones, and the fibers are represented in lighter shades. The weft tow 0 is highlight in blue; (b) typical fiber tow represented by point cloud; (c) the data structure used to store the input dataset of a point cloud; (d) segmented masks associated with the weft tows shown in (a), the matrix is left in black; With the coordinate system defined in (a), the fiber tow geometry obtained after segmentation can be represented either by point cloud explicitly or by image masks implicitly. <i>PolyTex</i> can handle both types of input data.	140
Figure 6.3	Morphological features of each fiber tow are calculated and stored in a Pandas DataFrame (a) with parameters defined in (b) and Eq. 6.1. . .	142
Figure 6.4	Object serialization and deserialization at different stages of analysis aid in reducing repetitive work and facilitate data sharing.	143
Figure 6.5	File structure of OpenFOAM case template prepared automatically by calling <code>tex_inst.export_as_openfoam()</code> and <code>tex_inst.case_prepare()</code>	144

Figure 6.6	Illustration of the procedure for fiber tow geometry modeling: (a) stochastic point cloud resampling and data smoothing; (b) concepts of parametric kriging for geometry modeling; (c) The behavior of tow volume vs. iterations (or smooth factor for the proposed method) for the selected algorithms.	146
Figure 6.7	(a) presents the cross-sections of a fiber tow extracted from image slices directly, which may not necessarily be perpendicular to the orientation of the wavy tow. <i>PolyTex</i> offers two algorithms that can automatically determine normal cross-sections and compute geometric information, such as area and circularity, for each cross-section. (b) Normal sections determined using the newly proposed kriging-based method. (a) and (b) are two of the visualization interfaces provided by <i>PolyTex</i> . Users can decide whether to visualize the results upon invoking relevant functions.	149
Figure 6.8	Digital Material Twin (DMT) model of a 3D orthogonal textile reconstructed from a volumetric image scanned with a resolution of $22\ \mu\text{m}$. The size of the model is $11.4 \times 13.12 \times 5.35\ \text{mm}$. (a) woven structure; (b) the DMT model discretized with hexhedral elements; (c) porosity distribution of warp, weft and binder tows; (d) fiber orientations. The elements for mesopores are hidden to clearly show the fiber tows.	151
Figure 6.9	TexGen-created models of TG96N: (a) An idealized model featuring constant tow width, height, and spacing. The "Refine" option in TexGen was utilized to automatically adjust yarn cross-sections for the desired layer thickness; (b) A realistic model created with the geometrical analysis results from <i>PolyTex</i> , capable of replicating spatial variability to a certain extent.	152
Figure 6.10	Spatial variation of fiber tow permeability rendered with ellipsoid tensor glyph. Only a portion of the DMT model shown in Figure 6.8b is presented to more clearly display the permeability distribution.	154
Figure 6.11	The boundaries of the numerical domain are referred to as right (X+), left (X-), front (Y+), back (Y-), top (Z+) and bottom (Z-) according to their positions in the Cartesian coordinate system. To predict transverse permeability, an injection pressure of 1000 Pa is specified at the top (Z+) and 0 Pa at the opposing boundary.	154
Figure 6.12	Dual-scale flow simulation with DMT models: (a) pressure contour across the thickness and (b) streamlines.	155

Figure 6.13	Comparison of transverse permeability predicted with ideal (Figure 6.9a), realistic (Figure 6.9b) and DMT (Figure 6.8) models. A reference value was obtained experimentally with a 3D printed sample of the DMT model to establish a baseline for the comparison.	156
Figure 6.14	Representation and storage of hexahedral meshes: (a) VTK unstructured grid; (b) <i>Abaqus</i> input file (.inp); (c) components of <i>polyMesh</i> for <i>OpenFOAM</i> ; (d) file structure of <i>polyMesh</i>	159
Figure 6.15	Flow channel size estimation: (a) pore size of mesopores estimated by fitting the maximum sphere that can be accommodated at the pixel location (1 pixel = 22 μm); (b) pore size distribution and flow capacity estimated with the Hagen-Poiseuille equation.	161
Figure 6.16	Reference sample for permeability validation: (a) . (b) the printed sample.	162
Figure C.1	Radial lines of a fiber tow	198
Figure C.2	Axial lines of a fiber tow	199
Figure C.3	Normal cross sections identified by proposed method based on parametric Kriging.	200
Figure C.4	Visualization of voxel mesh in PolyTex.	201

LIST OF APPENDICES

Appendix A	Installation of PolyTex package	194
Appendix B	Sample scripts for the use of PolyTex package	195
Appendix C	Screenshots of PolyTex visualization tools	198
Appendix D	Conference presentations, papers, and posters	202

Acronyms

LCM	Liquid Composite Molding
RTM	Resin Transfer Molding
VARTM	Vacuum Assisted Resin Transfer Molding
VARI	Vacuum Assisted Resin Infusion
SCRIMP	Seeman Corporation Resin Infusion Molding Process
FI	Flexible Injection
C-RTM	Compression Resin Transfer Molding
Micro-CT	X-ray Micro-computed tomography
DRP	Digital Rock Physics
DMT	Digital Material Twin
API	Application Programming Interfaces
PVC	PolyVinyl Chloride
RVE	Representative Volume Elements
MLTP	Meso-Level Textile Processor
CAD	Computer-Aided Design
GLC	Grey Level Co-occurrence

CHAPTER 1 INTRODUCTION

High-performance composites with continuous fibers and a polymer matrix can be used as an effective substitute for traditional materials such as metal alloys, resulting in lighter and larger components. These features lead to reduced assembly costs and energy savings. Consequently, the use of composite materials has experienced substantial growth in various industrial applications. Among advanced polymer composite manufacturing techniques, Liquid Composite Molding (LCM) is becoming increasingly popular due to the ability to produce high-performance composite parts in high-volume production [1] and its economic advantage compared to autoclave. Wind power [2], automotive [3], and marine industries [4] have all seen successful use of the LCM process. In recent years, the aerospace industry has also increasingly adopted this technology, such as the resin-infused aircraft wing on the Airbus A220 (formerly Bombardier C series) [5], the fan blades on the CFM LEAP and GEnx engines TM [6] and the thermal protection systems for solid rocket motors [7].

1.1 Basic definitions and concepts

1.1.1 Liquid composite molding

Liquid Composite Molding (LCM) is a group of advanced composite fabrication techniques in which a liquid resin is injected into a mold to saturate a dry fibrous preform. Several common steps can be identified in different variants of LCM, including mold preparation, fibrous reinforcement preforming, resin injection and cure, and demolding. Resin Transfer Molding (RTM), Vacuum Assisted Resin Transfer Molding (VARTM) and Vacuum Assisted Resin Infusion (VARI) are among the first LCM variants created and are used most frequently. In these processes, the resin flows along the in-plane directions of the dry fibrous preform until it is completely saturated, as shown in Figure 1.1a. The impregnation process can take hours due to the low permeability of the preform. To address this issue, TPI Technology, Inc. introduced and patented the SCRIMP [8]. This technique involves placing a highly permeable flow distribution medium at the top of the preform to facilitate horizontal spread of the resin and subsequent saturation through the thickness (see Figure 1.1b). The SCRIMP method significantly improves impregnation efficiency, particularly for composite parts with a thickness much smaller than the in-plane size.

Several new LCM variants have been developed over the years to further accelerate the filling process, such as Flexible Injection (FI) [10] and Compression Resin Transfer Mold-

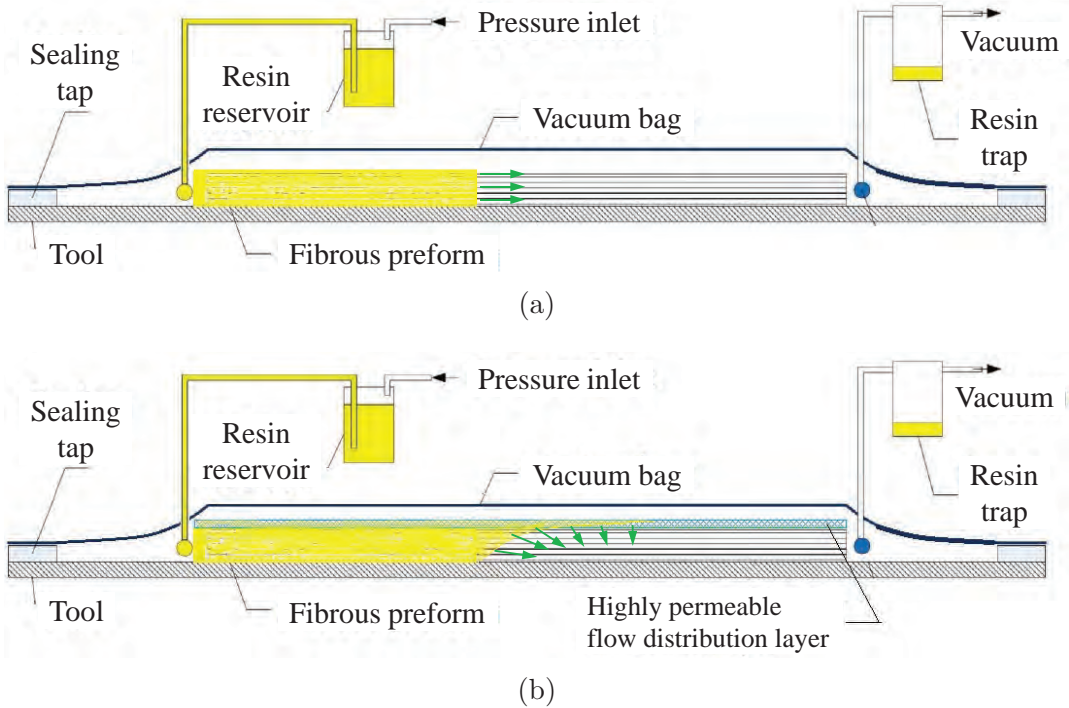


Figure 1.1 Resin flow patterns during infusion: (a) only in-plane flow is involved in VARI; (b) SCRIMP introduced transverse flow to accelerate the impregnation process (adapted from [9]). The green arrows show the flow direction at the flow front.

ing (C-RTM) [11]. The former was developed at the Chaire sur les composites à haute performance (CCHP) at Polytechnique Montréal and was successfully employed in the processing of fan blades for the CFM LEAP engine. The latter has been extensively utilized in the mass production of automotive components. In these processes, an empty open space above the preform is maintained, serving as a distribution layer for subsequent impregnation. The resin is injected into the open space and spreads rapidly, after which the fibrous reinforcement is impregnated by a nearly unidirectional through-thickness flow. These LCM variants expand the limitations of injection into rigid molds, such as the RTM process, and allow the automated manufacturing of advanced composite parts for mass production.

1.1.2 Dual-scale structure of tow-based textile reinforcements

The architecture of a tow-based textile reinforcement has two distinct length scales, as illustrated in Figure 1.2. Mesopores with millimeter-scale dimensions appear between fiber tows, while micropores with dimensions at the micrometer scale are present in fiber tows. The volume of micropores is approximately two orders of magnitude smaller than that of

mesopores. The dual-scale pore network evolves in two manners as the compaction level increases due to preforming, mold closing, or pressure changing: rearrangements of fiber tows, which leads to the decrease in the volume of the mesopores and filament rearrangement in the fiber tows, which decreases the volume of micropores. The specific area, tortuosity, and fiber volume content on the mesoscale and microscale are altered. Understanding this dual-scale structure is essential because it profoundly influences both the manufacturing process and the properties of finished composite parts.

1.1.3 Permeability of fibrous reinforcements

The successful implementation of LCM processes is reliant on an intricate understanding and control of various process parameters. Permeability plays a pivotal role among these parameters, as it dictates resin impregnation through dry fibrous reinforcements. It is a symmetrical second-order tensor \mathbf{K} that relates fluid velocity and pressure:

$$\mathbf{v} = \begin{bmatrix} v_x \\ v_y \\ v_z \end{bmatrix} = -\frac{1}{\mu} \mathbf{K} \begin{bmatrix} \frac{\partial p}{\partial x} \\ \frac{\partial p}{\partial y} \\ \frac{\partial p}{\partial z} \end{bmatrix}, \quad \mathbf{K} = \begin{bmatrix} k_{xx} & k_{xy} & k_{xz} \\ k_{xy} & k_{yy} & k_{yz} \\ k_{xz} & k_{yz} & k_{zz} \end{bmatrix} \quad (1.1)$$

Equation (1.1) is known as Darcy's law, which was named after Henry Darcy [12]. \mathbf{v} is Darcy velocity vector representing the directional volume flow rate of the liquid per unit area. p and μ are the pressure (Pa) and the dynamic viscosity (Pa·s or kg/(m·s)) of the liquid. When the principal axes of a permeability tensor coincide with the coordinate system of a textile, the off-diagonal components become 0. In this case, the permeability of

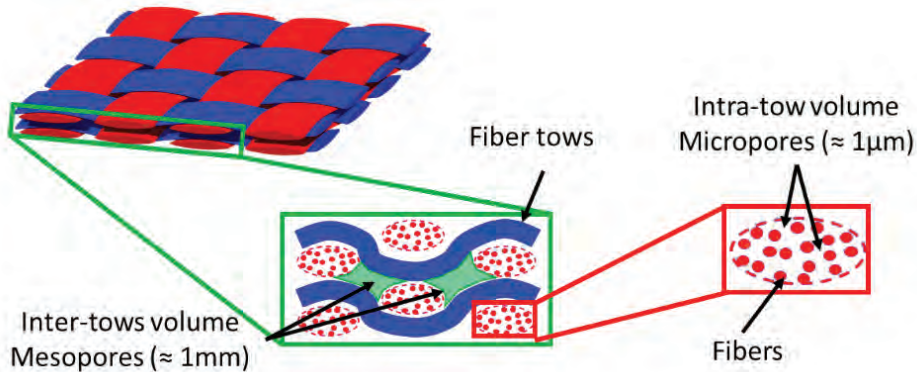


Figure 1.2 Dual-scale structure of fibrous reinforcements

the fabric can be described with the diagonal components k_{xx} , k_{yy} and k_{zz} , or a principal permeability tensor. The symbols k_{xx} and k_{yy} are typically used to denote the principal in-plane permeability components of textile reinforcements, while k_{zz} represents the transverse permeability, also known as through-thickness permeability. The permeability of isotropic reinforcements is equal in all directions, with k_{xx} , k_{yy} , and k_{zz} being the same. On the other hand, for anisotropic reinforcements, the transverse permeability k_{zz} is typically 10 to 100 times lower than k_{xx} and k_{yy} . The unit of permeability is m^2 , which can be assimilated to the surface area of a porous medium in the flow direction.

1.2 Elements of the problem

1.2.1 Research issues

Quantification of transverse permeability For new LCM process variants that favor through-thickness impregnation, knowledge of transverse permeability is critical to optimize the process and maintain a desired level of production quality and productivity. However, the measurement procedure is still far from standardization. In a transverse permeability benchmark organized in 2018, differences of approximately two orders of magnitude were observed between 28 experimental results of 26 participants obtained for the same reinforcements [13]. The challenge lies in the inherent characteristics of textiles: high deformability and small layer thickness because it is essential to ensure that the textiles can be easily adapted to the shape of the mold. Additionally, when layering textiles for preforming, nesting between layers can occur [14], which also alters transverse permeability. Consequently, evaluating the transverse permeability of textile reinforcements is more challenging compared to that of rigid porous media.

To maintain the thickness of the textile stack during the transverse permeability test, a pair of rigid support plates must be introduced. However, two additional difficulties arise. First, the flow and compression pressure applied to the sample can distort the support, leading to alterations in the fiber content of the sample. Second, the design of the support plates must allow for unimpeded through-thickness flow without causing any additional pressure drop. Therefore, it is also named the flow distribution plate. This appears to be challenging, as the support restricts the effective area of the sample for flow exchange and alters the flow pattern [15]. Therefore, the use of such apparatuses yields only apparent transverse permeability, which may vary with alterations in the testing setup, while the intrinsic transverse permeability is still obscured.

Efficient internal geometry analysis of textile reinforcement Knowledge of the internal structure of textile reinforcements is essential to study the dual-scale resin flow and identify potential sources of error in the permeability testing. X-ray Micro-computed tomography (Micro-CT) is a powerful tool to characterize the microstructure of textile composites. It has proven to be a valuable non-destructive testing method for the analysis of damage initiation and propagation within composites [16, 17]. Geometric analysis based on tomographic images has also been demonstrated to be much more accurate than traditional techniques [18]. However, errors and uncertainties can arise from two sources: the intrinsic variability of materials (irreducible aleatory uncertainty) and the processes used for in situ scanning, segmentation, and geometry reconstruction (reducible epistemic uncertainty). The latter may propagate to numerical simulations through geometry models and make the predictions unreliable. Therefore, quantifying and minimizing uncertainty represents a critical task. Until now, very few approaches have addressed the uncertainty that underlies such analyses.

In addition, the discrete step-like interface between subdomains of voxel-based images should be approximated by a smoothing surface to perform geometry analysis. Existing techniques, such as Gaussian smoothing [19], Savitzky-Golay filtering [20], and Catmull-Clark technique [21], suffer from volume shrinkage because they are based on the averaging of vertices. This results in discrepancies between the local fiber volume fraction and the actual values. The reliability of such an approximation is questionable.

High-fidelity modeling for dual-scale numerical simulation Micro-CT image sequences have been used to predict the permeability tensor of textile reinforcements using software packages developed for Digital Rock Physics (DRP) [22–24]. In these analyzes, textile reinforcements were assumed to be single-scale materials with impermeable fibrous tows. In the manufacturing process, the dual-scale structure plays a critical role in permeability and resin flow. Mesoscopic features, such as the weave pattern or the arrangement of tows, determine the overall permeability of the textile. These features dictate the pathways through which the resin flows during infusion. On the other hand, microscopic features, such as the fiber arrangement within each tow, affect local permeability on a smaller scale. As a result, the dual-scale structure can lead to non-uniform resin flow, causing defects within the composite. Nevertheless, the simulation of flow in a dual-scale reinforcement, considering spatial variability in the structures, continues to be a difficult task due to the absence of high-fidelity models. Furthermore, process-induced defects, such as air pockets and dry spots, often pose a threat to the operational safety and durability of composite parts. Software created to address these issues typically consider the injection process as resin flowing

through a homogeneous porous medium. This is oversimplified for investigating the creation of manufacturing defects. Therefore, the development of high-fidelity numerical models that can capture the dual-scale structure and spatial variability of textile reinforcements is essential for accurate prediction of resin flow and identification of potential defects. Consequently, this is another important issue that will be studied in this project.

1.2.2 Research scope

Considering the issues mentioned above, this project aims to provide an in-depth exploration of transverse flow through dual-scale textile reinforcements. This will be achieved through three interconnected aspects: evaluating the transverse flow at a macroscopic level, studying the mesoscopic structure of the textile, and creating a geometry model for numerical investigation. This research not only provides an approach to optimizing the existing transverse permeability testing method, but also advances numerical techniques for understanding the fundamentals of flow in dual-scale fabrics.

The first aspect focuses on measuring the flow through the thickness of textile samples, which is vital for accurate transverse permeability characterization. The impact of the test device on the flow pattern is studied. A dimensionless indicator, the discharge coefficient, is proposed as a means to characterize the performance of the testing apparatus. The objective is to establish a robust approach to obtain intrinsic transverse permeability while maintaining the advantages of the conventional unidirectional test method (e.g., inexpensive, simplicity of data processing, and sample preparation). The discharge coefficient serves as a metric for standardizing and comparing the results with various experimental setups. It allows researchers to quantify and account for variations in the design and configuration of the apparatus.

Subsequently, the study delves into an exploration of textile structure at both the microscale and the mesoscale levels, leading to a high-fidelity geometry modeling and meshing approach for tow-based reinforcements. The model generated by this approach, known as the Digital Material Twin (DMT), reflects the precise structure and variability of the actual material and is ready to be used in numerical investigations of multiscale flow analysis. At this stage, the work unfolds in three steps: (1) obtain *in situ* scans of the fabric through Micro-CT to analyze mesoscopic structure features; (2) establish a high-fidelity geometric model considering spatial variability that allows (3) to investigate dual-scale flow and predict the permeability of textile reinforcements. It should be noted that in Section 6, we also present the potential application of the DMT created using the newly proposed approach to numerically study the mechanical behaviors of reinforcements, despite the fact that our main focus is on investigating the flow

through dual-scale textile reinforcements.

The current research emphasizes the synergy between experimental investigations and numerical simulations to enhance overall reliability. Various reference samples were used for validation and confirmation at different stages, including rigid reference porous media and 3D printed models. The proposed framework for tomographic modeling, meshing, and numerical simulation can be an efficient tool for the investigation of flow in dual-scale materials, reducing the need for extensive experimental investigation.

This study focuses solely on the unidirectional method for assessing the transverse permeability of textile reinforcements and does not take into account the flow-induced compaction of the fabric during the experiment. In the numerical study, the current work will be limited to isothermal flows. Chemical reactions resulting from polymerization will not be considered. Furthermore, the reinforcement is assumed to be rigid and non-deformable during one simulation (no fluid–structure interaction).

1.3 Research objectives

This thesis aims to address the challenges associated with transverse flows in dual-scale textile reinforcements. Both macroscopic experimental characterization and mesoscopic analysis are considered. Several specific objectives are delineated as follows:

1. Investigating elements that affect transverse permeability measurement is the first step. This includes the effects of both the structure of the testing devices and the inherent properties of fibrous specimens. At this stage, our work aims to provide guidelines for the design of new unidirectional transverse permeability test apparatuses.
2. The second is to improve the accuracy and consistency of the transverse permeability tested with different devices. This research presents the first proof that the transverse permeability obtained with the unidirectional approach is underestimated, as demonstrated by experiments with a rigid reference porous specimen. Thus, a dimensionless indicator is suggested to quantify the performance of the devices so that the designed correcting algorithm can be applied to obtain the intrinsic permeability.
3. The third objective consists of addressing the challenges associated with the uncertainties induced by image preprocessing, segmentation, and geometry approximation in volumetric image-based geometry analysis and modeling of dual-scale textile reinforcements. An innovative Digital Material Twin model characterized by high-fidelity

geometry details is created. The model is ready to be used in numerical simulations to investigate the impregnation process through dual-scale flow simulations.

4. The final objective is to develop an open-source code to automate volumetric image-based geometry modeling and meshing for dual-scale textile reinforcements. Interoperability with other numerical environments should be provided. Therefore, users can develop their own dual-scale DMT model and use it in numerical simulations with minimal knowledge of image processing and geometry modeling.

1.4 Outline of the dissertation

The rest of the thesis begins with an exploratory review of the literature (Chapter 2) to provide the context and background of the research problems. Then, the work conducted to address the aforementioned objectives is presented through four article-based chapters:

Chapter 3 explores the relationship between the transverse permeability measurement and the test mold. The issues connected to the test mold, including the discrepancy in the fiber volume fraction due to mold deformation, flow patterns, and pressure drop induced by the mold cavity, are investigated to evaluate how the design of a unidirectional mold can affect measurement. The work presented was published in *Polymer Composites*.

In response to the factors identified in Chapter 3, Chapter 4 presents a dimensionless performance evaluation factor, named discharge coefficient, to determine the efficiency of a unidirectional transverse permeability test mold for mass transfer. A numerical procedure is suggested to create a characteristic performance map for a specific test device using the coefficient, and then an iterative framework is established to calculate the intrinsic transverse permeability. The approach is finally applied to investigate the permeability discrepancy between two different molds, located at Polytechnique Montréal and Wuhan University of Technology. The findings were published in *Composites Part A: Applied Science and Manufacturing*.

The experimental investigation of transverse permeability is limited to the macroscopic level. However, the macroscopic flow behavior is determined by the lower level structure of the textile reinforcement. Therefore, to understand the dual-scale flow behavior and the possible sources of experimental errors, it is necessary to analyze the mesoscopic structure of the textile reinforcement. Thus, Chapter 5, the third article submitted to *Composite Structures*, presents a mesoscopic geometry modeling strategy. The approach utilizes volumetric images as input and integrates stochastic resampling and spatial autocorrelation prediction techniques to address challenges related to the large volume of data in the volumetric image and the

uncertainties induced by image preprocessing, segmentation, and geometry approximation.

The creation of high-fidelity numerical models for numerical flow simulations is only possible with the geometrical information extracted from the mesoscopic analysis, as discussed in Chapter 6. This constitutes the fourth article submitted to the Journal of *Composite Science and Technology*. Additional research efforts were directed to improve the representativeness and accuracy of the numerical model. Application Programming Interfaces (API) were developed to facilitate its integration into various numerical environments, such as OpenFOAM and Abaqus. To demonstrate its applicability, numerical simulations were performed to predict the permeability of a 3D orthogonal dual-scale reinforcement. This research resulted in the development of an open-source software, *PolyTex*, specifically designed for volumetric image-based geometry modeling and meshing of dual-scale textile reinforcements.

Chapter 7 serves as the final section of this thesis. The essential findings and limitations of the current work are summarized and discussed. In addition, recommendations are presented for future research.

CHAPTER 2 LITERATURE REVIEW

This chapter presents a review of the literature that includes the background and existing challenges relevant to this project. Given that the manuscript adopts an article-based format, various concepts are described from a macroscopic perspective in this chapter. More detailed discussions of the state of the art for specific topics are provided at the beginning of each article. We first discuss the phenomena observed in the LCM process. Then, the latest advances in the experimental characterization of textile permeability are reviewed. Subsequently, the structural characterization and modeling of textile reinforcements are introduced, which is a crucial factor in controlling the flow of polymer matrices. Finally, the flow behavior in dual-scale textile reinforcements is presented to provide general background information.

2.1 Phenomena encountered in LCM

LCM processes involve various interconnected phenomena, as shown in Figure 2.1. These include the viscoelastic rheological behavior of textile reinforcements, the flow dynamics of polymer matrices, and the combined thermal and chemical aspects. Each of these components plays a critical role in ensuring complete impregnation of the reinforcing fabric with resin, without any dry spots. Therefore, it is essential to have a comprehensive understanding and precise control of each aspect to optimize part quality and minimize manufacturing defects. As the modern aerospace sector seeks alternatives to the conventional autoclave process for the more cost-effective fabrication of high-performance composites, LCM processes have found applications in some secondary structural components. Meanwhile, industries traditionally reliant on the LCM process, such as wind energy and shipbuilding, are actively trying to improve the production efficiency and quality control of large composite parts (wind turbine blades, boat hulls, etc.). These necessities have directed attention to the following three specific areas of intensive research.

2.1.1 Characterization of transverse flow

Impregnating the fibrous preform along the thickness direction is preferred due to the smaller length scale. This method effectively improves the manufacturing efficiency. However, multi-layered structures, such as the sandwich structure shown in Figure 2.2, can result in complex resin flow paths. When flow fronts converge, there is a risk of creating welding lines and potentially trapping air. To address these challenges, the knowledge of transverse flow are

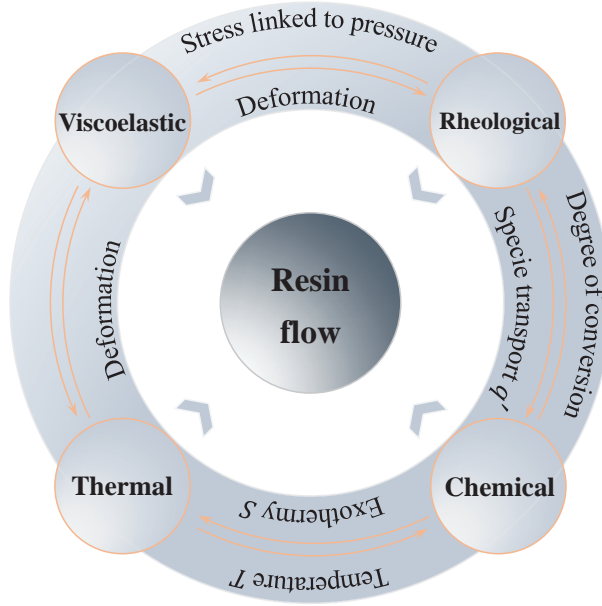


Figure 2.1 Coupling between different phenomena in LCM

necessary for resin infusion strategy optimization.

2.1.2 Quantification of textile reinforcement structure distortions

Textile reinforcements can experience structure distortions due to processes such as weaving, preforming, and molding. These distortions often manifest as tow waviness and spatial fluctuations in tow size and shape. This creates non-uniform resin flow and can lead to irregularities in resin distribution and curing, which in turn affects the mechanical properties of the final composites [25, 26]. Hence, distortions must be quantified in the design and fabrication stage.

2.1.3 Composite quality and dual-scale flow

In this context, "dual-scale flow" refers to the mesoscopic flow through the gaps between the fiber tows and the microscopic flow through the pores between the fibers inside a tow. The initial wetting of textile reinforcements is strongly dependent on the mesoscopic flow, whereas complete impregnation and prevention of microscopic voids are primarily dependent on the microscopic flow, as shown in Figure 2.3a. Additionally, the capillary force, illustrated in Figure 2.3b, may also play a critical role in the microscopic impregnation. Extensive experimental studies [27, 28] have highlighted that to achieve overall integrity of finished

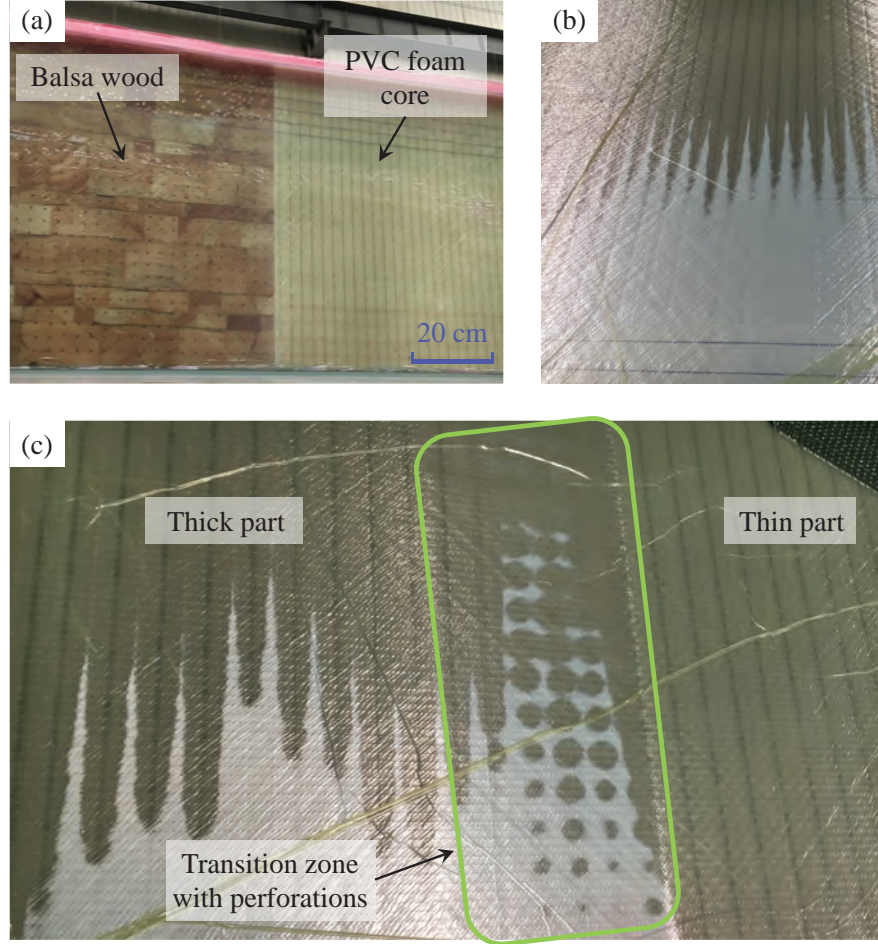


Figure 2.2 The complex flow front encountered during the manufacturing of sandwich composites: wind turbine blades utilize balsa wood and PVC foamcore sandwich composites on the shear web (a) for weight reduction. The balsa wood was perforated in the thickness direction, whereas PVC foamcore was not only perforated but also grooved on the surface to distribute resin flow; (b) serrated flow front due to grooves and (c) impregnation through the thickness because of the perforations. *Photos were taken at Sinoma Wind Power Blade Co., Ltd., China*

composites, the optimal flow front velocity [29] must be maintained to balance mesoscopic and microscopic flow. It is a challenging task, however, as a deep understanding of the dual-scale structure of the reinforcements and the flow behavior on both scales are required.

In the subsequent sections of this chapter, our attention will be directed towards conducting a brief review of the existing literature pertaining to the three domains.

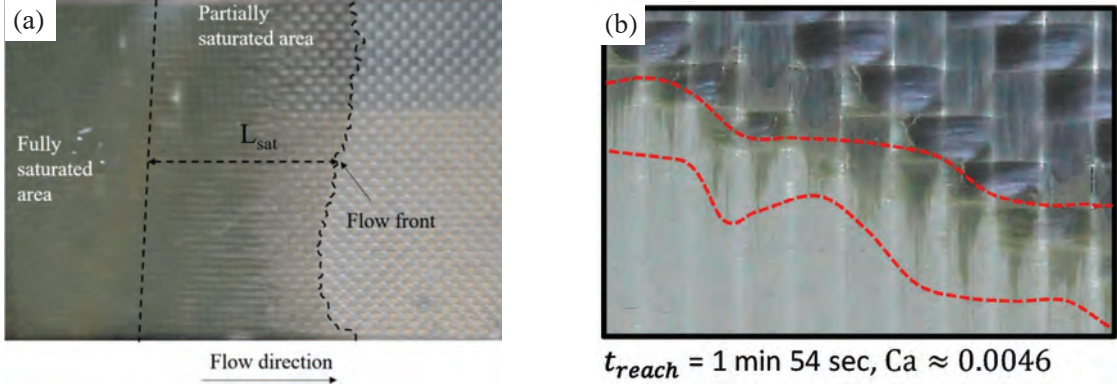


Figure 2.3 Dual-scale flow in textile reinforcements: (a) partially saturated flow with a length of L_{sat} due to the dual-scale structure of the woven fabric [30]; (b) capillary fingering along fiber tows indicated between dashed lines [31].

2.2 Characterization of textile permeability

Darcy's law (Equation 1.1) describes the linear relationship between the velocity of filtration flow in a porous medium and the pressure gradient at a macroscopic level. This implies treating the reinforced fabric as a homogeneous porous medium, which, as shown in Figure 1.2, is not actually the case. Consequently, the volume-averaged variables, pressure $\langle p \rangle^f$ and flow velocity $\langle \mathbf{v} \rangle$ are determined by:

$$\langle \mathbf{v} \rangle = \frac{1}{V} \int_{\phi V} \mathbf{v} dV \quad (2.1)$$

$$\langle p \rangle^f = \frac{1}{\phi V} \int_{\phi V} p dV \quad (2.2)$$

where ϕ and V denote the porosity and volume of the porous domain. \mathbf{v} and p denote the physical flow velocity and the fluid pressure. Furthermore, due to the regular woven structure of most textile reinforcements, the permeability tensor can be simplified to a 3×3 diagonal tensor as below:

$$\mathbf{K} = \begin{bmatrix} k_x & 0 & 0 \\ 0 & k_y & 0 \\ 0 & 0 & k_z \end{bmatrix} \quad (2.3)$$

where k_x and k_y denote the principal permeability within the layer, namely, the in-plane permeability components. k_z represents the transverse permeability, which is also known as

through-thickness permeability. A visual representation can be seen in Figure 2.4.

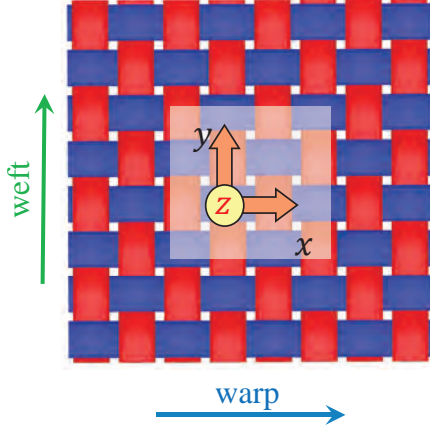


Figure 2.4 The notation used for the permeability components is usually k_x and k_y for the in-plane components, while k_z is used for the transverse permeability, as indicated by the Cartesian coordinate.

2.2.1 Classification of experimental measurement methods

Although in-plane and transverse permeability measurements share the same theoretical background, their testing procedures and setups differ significantly. This is connected to the structural characteristics of textile reinforcements:

- (a) **Length scale.** Textile reinforcements have large dimensions within the layer (measured in meters), allowing the flow front to be easily tracked. However, their small thickness, typically in the range of millimeters or even thinner, presents more challenges for tracking the flow front in the thickness direction [32].
- (b) **Deformability of preform.** In order to achieve the desired fiber volume content and avoid deformation, it is essential to provide support in the thickness direction of the fibrous material. However, this support can hinder the transverse flow and result in an underestimation of transverse permeability [15, 33].

As a result, the measurement techniques and challenges related to in-plane and transverse permeability vary significantly. Hence, we present the characterization techniques separately.

In-plane permeability

In-plane permeability measurement has attracted considerable attention in the last 30 years [34–36]. The techniques commonly used to characterize in-plane permeability are categorized

into three groups based on the flow shape of test fluids: the channel flow method (1D), the radial injection method (2D) and the three-dimensional method (3D), as illustrated in Figure 2.5.

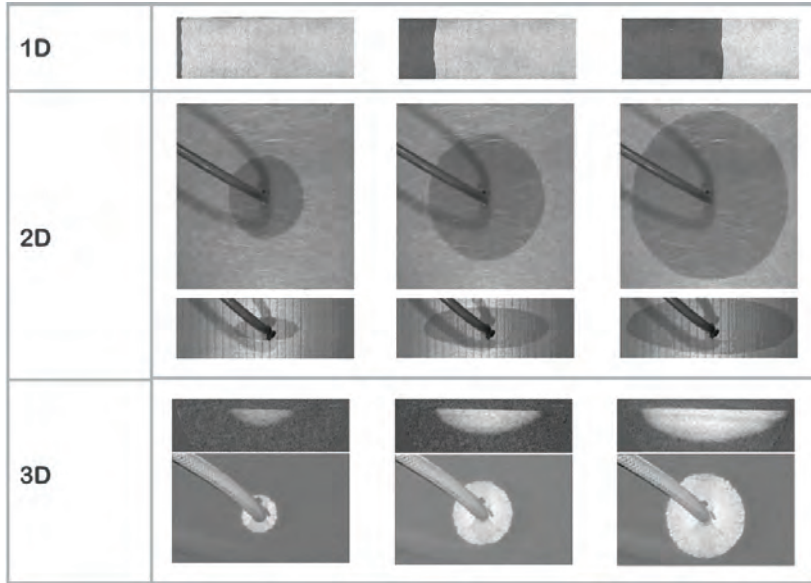


Figure 2.5 Techniques for in-plane permeability measurement: the channel flow method (1D), the radial injection method (2D) and the three-dimensional method (3D). [37]

Channel flow method (1D) The channel flow method, also known as the unidirectional method [34, 38], is the technique most commonly used to measure the in-plane permeability of textile reinforcements. Figure 2.6a shows a schematic representation of the experimental setup. Firstly, the textile reinforcement is shaped into a rectangular preform and placed between two mold halves. After clamping the mold, the test fluid is injected through the inlet, establishing a unidirectional flow. Figure 2.6b shows a photograph of the experimental setup at Polytechnique Montréal. The thickness of the test sample is regulated by calibrated shims (spacers) inserted between the mold halves, and equidistant lines are drawn on the transparent mold to facilitate the positioning of the flow front position.

The channel flow method can be carried out with saturated or unsaturated samples. In the saturated case, the sample is pre-impregnated with the test fluid. The test fluid permeates through it, driven by the pressure difference between the inlet and outlet. The flow rate is measured over time and used to calculate permeability. In the unsaturated case, the flow front can be visually tracked if the mold is transparent. Alternatively, sensors can be installed in the mold to detect the flow front. The analytical solutions for the saturated and unsaturated permeability are presented in Table 2.1. This method is straightforward in

setup and execution. However, special care should be taken to ensure that preferential flow channels between the sample and the test mold are avoided, as edge effects can lead to an overestimation of the permeability. In addition, mold deformation also affects the accuracy of measurement.

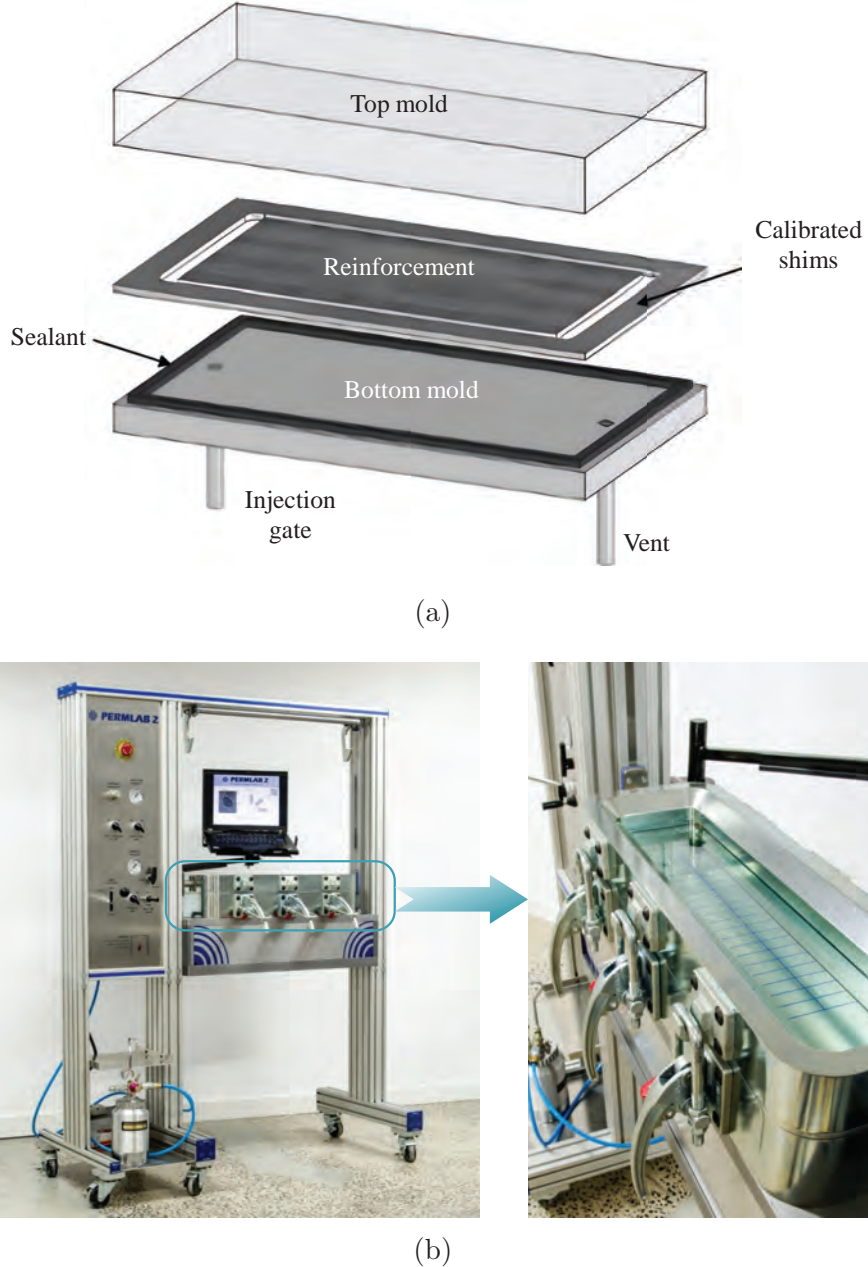


Figure 2.6 Channel flow method: (a) schematic representation of testing setup [36]; (b) In-plane permeability test device at Polytechnique Montréal.

Table 2.1 Formulas for in-plane permeability calculation

Sample state		Constant pressure	Constant flow rate
1D	Saturated	$k_{\text{sat}} = \frac{(Q \cdot \mu \cdot \Delta L)}{(A \cdot \Delta p)}$	$k_{\text{sat}} = \frac{(Q \cdot \mu \cdot \Delta L)}{(A \cdot \Delta p)}$
	Dry	$x_f(t) = \sqrt{\frac{2k(p_i - p_f)}{\mu\phi} \cdot t}$	$p_i(t) = p_f + \frac{\mu Q^2}{\phi A^2 k} \cdot t$
2D	Dry	$k_x = \frac{k_e}{k_1} = \frac{\eta\phi R_{xt}^2}{4\Delta p \cdot t} \left[2\ln\left(\frac{R_{xt}}{R_0}\right) - 1 \right]$	[39] /

Radial injection method (2D) A schematic illustration of the radial injection method is shown in Figure 2.7a. The fibrous preform is placed between two rigid molds. It is punched with a hole in the center to allow the test fluid to be injected and a two-dimensional (2D) flow pattern can be established [40]. Typically, it is performed in an unsaturated state, with a few exceptions that are carried out in a saturated condition [41]. The flow front progression is tracked over time visually [42, 43] or with sensors [44, 45]. The main advantage of the radial injection method is that it can measure in-plane permeability in both principal directions in one test and determine the orientation of the flow ellipse at the same time [46]. As shown in Figure 2.7b, a circular flow front should be observed for an isotropic fabric, whereas for anisotropic fabrics the flow front becomes elliptic. An analytical solution to determine the value of the in-plane permeability components is provided in Table 2.1. Other analytical approximations have also been found in references by Adams et al. [47], Weitzenböck et al. [46], and Um et al. [48]. In comparison, the channel flow method requires at least three tests to determine permeability anisotropy [38, 49].

Despite these advantages, the radial injection method faces several constraints. It is more complex than the channel flow method in terms of test setup, flow front tracking, and data analysis. Furthermore, to ensure sufficient flow development and to reduce the influence of the central hole on the flow, the sample must be large enough in both length and width, increasing the likelihood of test mold deformation. Many researchers, such as Heardman et al. [43] and Tan et al. [50], have attempted to identify potential sources of error and proposed strategies to calibrate radial injection setups and improve the test procedure.

Three-dimensional method (3D) The 3D method offers a comprehensive analysis of flow in three dimensions, providing a complete overview of the permeability tensor. Similarly to the radial injection method, 3D methods also require an unsaturated state for flow front

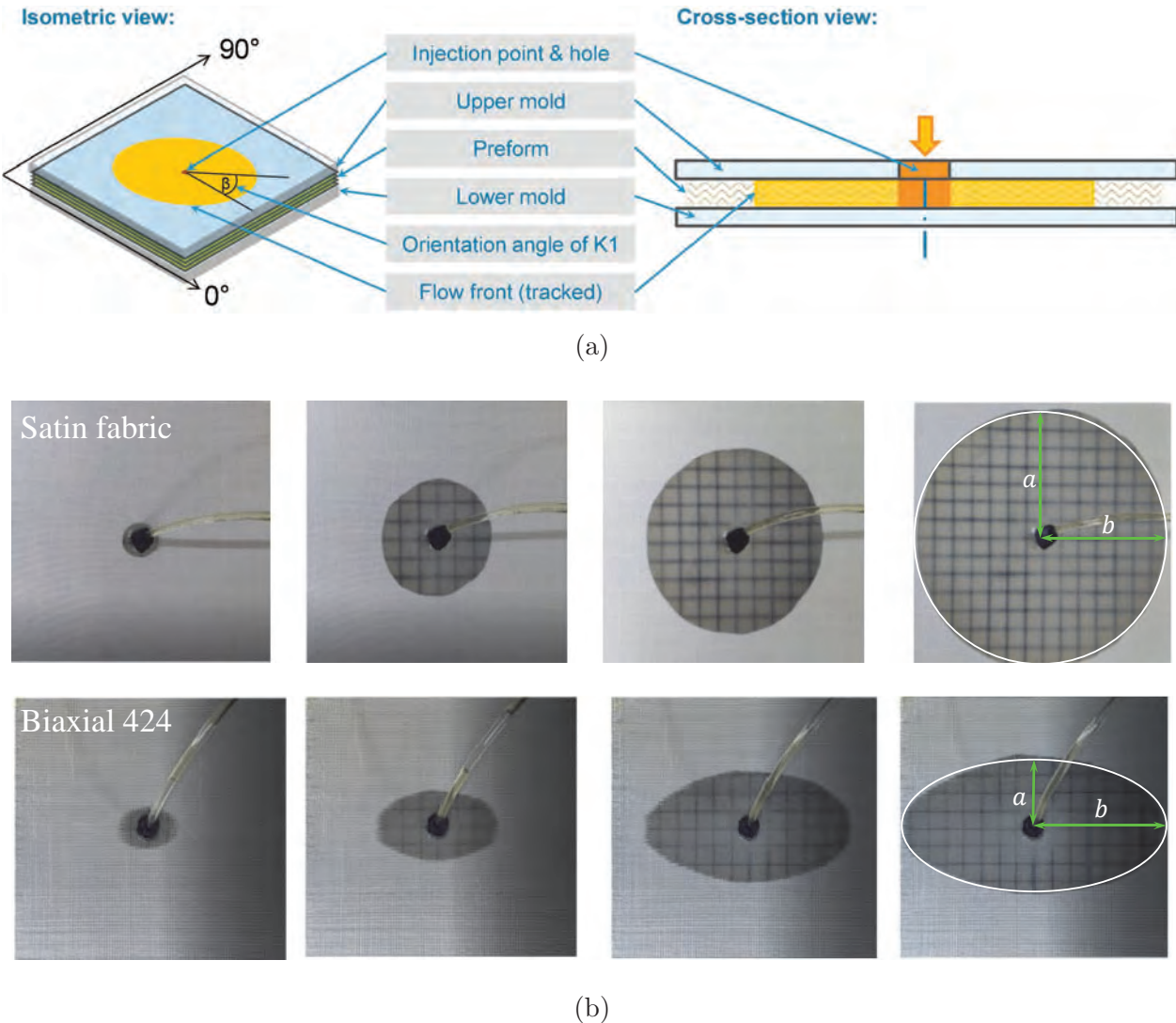


Figure 2.7 Radial injection approach for in-plane permeability measurement: (a) schematic representation of the test approach [40]; (b) the anisotropy of fibrous preforms can be measured directly with the radial injection approach [51].

monitoring. Figure 2.8a depicts a schematic diagram of the process. The test fluid is injected at the central top of the preform, and the flow front is monitored over time. Various in-situ detection sensor arrays, such as optical fibers [52], thermistors [53], and a modified version of SMARTweave [54], have been used to monitor the evolution of the flow front. These intrusive sensors, typically 0.1 to 1.4 mm in diameter [53], exhibit runners effects in the longitudinal direction and block flow in the transverse direction. Therefore, the sensors could disturb the flow front. This issue can be addressed by using non-intrusive techniques, such as ultrasound [55,56] and X-ray radioscopy [37,57,58]. Recent studies by Becker et al. [59] have

highlighted the promise of non-intrusive techniques for reliable flow front tracking. These techniques avoid the need for expensive sensors and time-consuming sensor installation and enable continuous real-time flow front tracking.

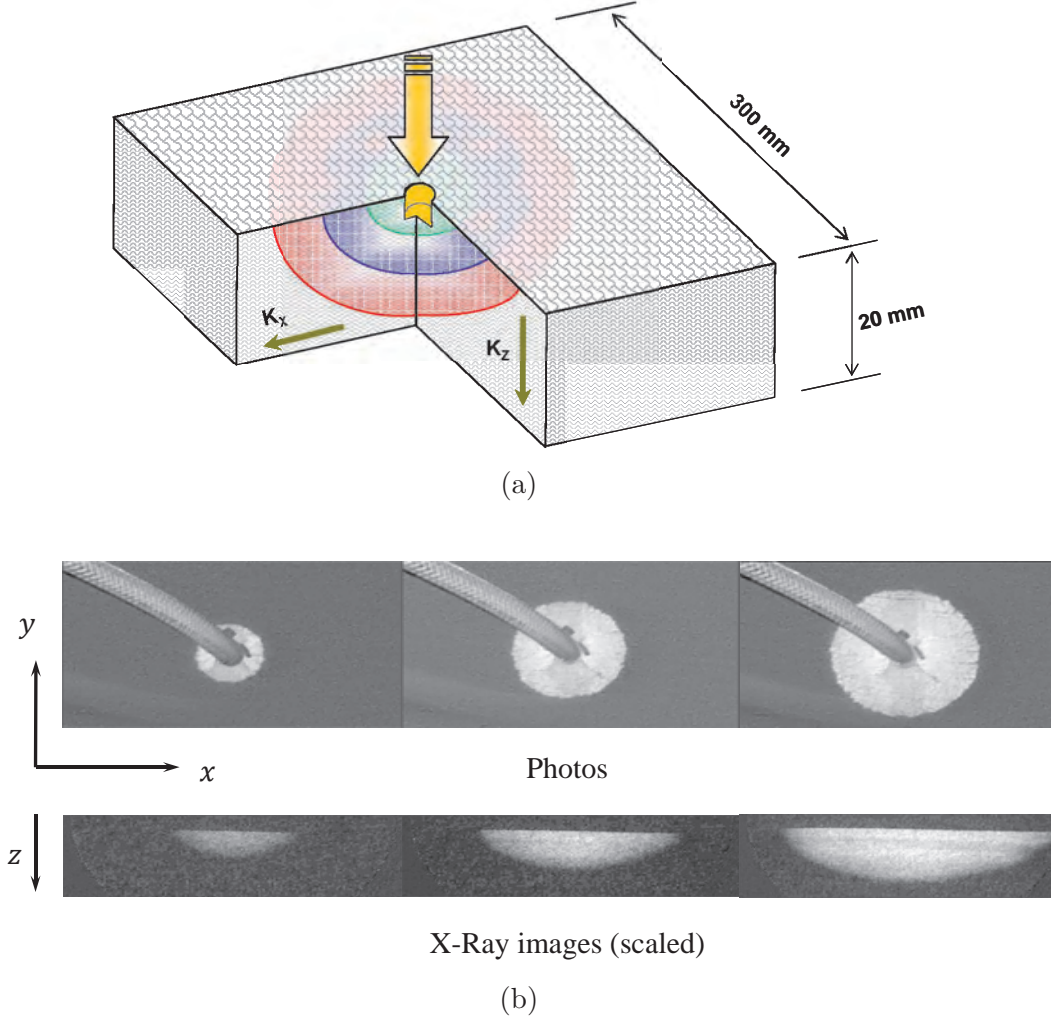


Figure 2.8 Three-dimensional (3D) method for permeability measurement: (a) schematic representation of the test approach; (b) flow front tracking with X-ray radioscopy setup for permeability measurement [37].

Analytical solutions, such as the one provided by Weitzenbock et al. [53], can be used to calculate the permeability with the experimental data collected in 3D test. Alternatively, the permeability components can be determined by matching the experimental flow front with numerical simulations iteratively, as reported by Wu et al. [60] (13% lower than the value measured directly with experiments) and Okonkwo et al. [61].

The industrial application of the 3D method still faces some challenges. The 3D flow front is

sometimes not well developed due to dual-scale flow, material variability, and nesting effects. These can result in difficulties in data interpretation. In addition, the 3D method requires that the preform has sufficient thickness. Hence, it may not result in any savings in terms of materials and time when compared to the 1D method. Moreover, previous studies [24,53] have indicated that transverse permeability is affected by the thickness of the sample, especially for thin preforms. This limits the use of the 3D method in thin preforms, which is a prevalent scenario in composites manufacturing.

Transverse permeability

Despite the fact that through-thickness impregnation is a crucial aspect of new LCM process variants, transverse permeability measurement has received less attention compared to in-plane permeability until the first international benchmark exercise on transverse permeability was launched in 2018 [13]. 26 participants in this benchmark reported 28 experimental results. As illustrated in Figure 2.9, 21 results were measured using the saturated 1D method, while the unsaturated 1D method was used for three results. Additionally, three results were obtained using the unsaturated 3D method and one result was obtained using the saturated 3D compression method. These methods are the main approaches used to characterize transverse permeability. A concise overview of these methods is presented in this section.

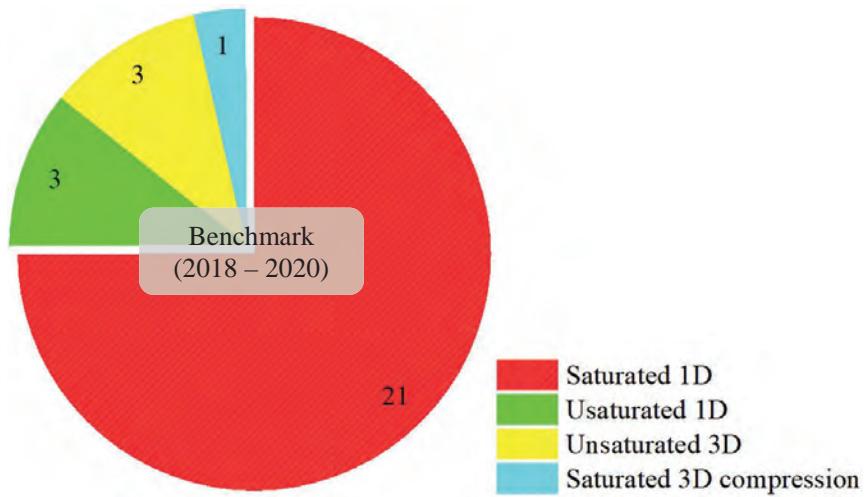


Figure 2.9 Methods for transverse permeability measurement used by participants of the first international benchmark exercise launched in 2018 [13]. The number on the pie chart indicates the number of results measured by each method.

Saturated 1D method Measurement of transverse permeability is preferably conducted in a saturated state, owing to the challenges of tracking the flow front in the thickness

direction of thin samples. Figure 2.10 (left panel) illustrates the schematic diagram of the 1D method. The sample is sandwiched between two support plates. A saturated flow is established across its thickness. This flow is maintained at a constant rate, driven by the pressure difference between the top and bottom of the sample. Subsequently, the transverse permeability is calculated in accordance with the 1D Darcy's law.

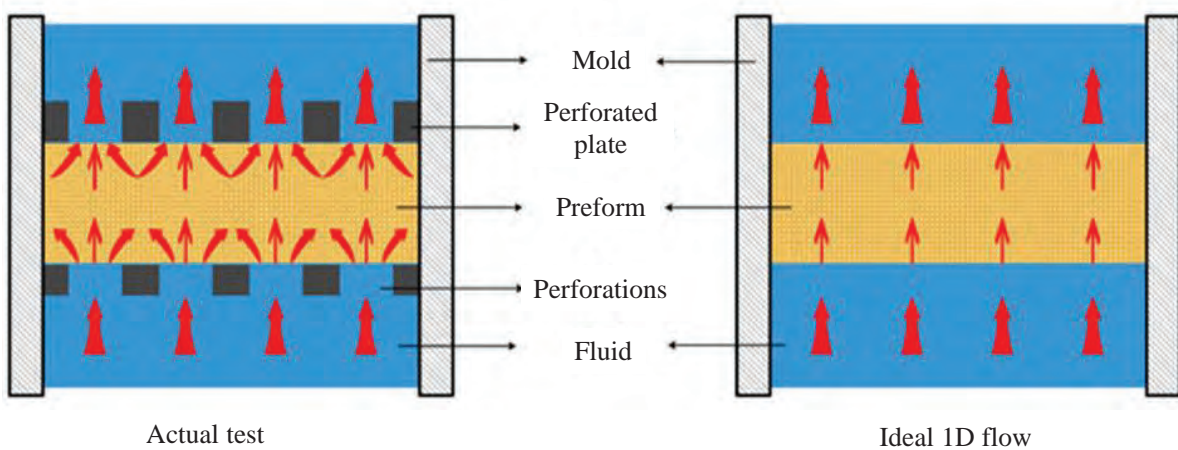


Figure 2.10 Actual flow pattern during saturated transverse permeability measurement

A fully developed unidirectional flow is essential for conducting 1D measurements. However, in contrast to the ideal 1D flow depicted in the right panel of Figure 2.10, the actual flow pattern tends to be more complex. The flow front does not remain perpendicular to the sample, and uniformity across the thickness can not achieve. The complexity arises due to the presence of perforated support plates on both sides of the sample. Consequently, the flow deviates from the intended one-dimensional flow, becoming three-dimensional. Despite its widespread use in industry and academia because of simplicity and cost-effectiveness, calculating transverse permeability using 1D Darcy's law directly may not yield accurate results.

Unsaturated 1D method In general, the unsaturated 1D method closely resembles the saturated method in terms of setup and testing procedure. The key difference lies in the fact that the test sample is not pre-saturated, and specialized techniques, such as ultrasound [59], are employed to track the flow front position. Additionally, the flow front can be observed through a transparent mold [62]. However, it may be questionable, as the flow front could be distorted by preferential flow along the edges, known as the "edge effect".

Unsaturated 3D method This is the same as the 3D method for in-plane permeability measurement presented in Section 2.2.1.

Saturated 3D compression method This method was first proposed by Comas-Cardona et al. [63]. Instead of using hydraulic pressure to drive the flow, the sample is saturated and then compressed between two rigid plates. The liquid is expelled from the sample (compression-driven), and the liquid pressure is derived from the total stress (compression stress) and the effective stress measured with sensors, following Terzaghi's principle of effective stress. The permeability is then calculated using an inverse algorithm, which matches the numerical liquid pressure under the same conditions. This approach extends the method introduced by Buntain et al. [64], originally designed for continuous measurement of the in-plane permeability of isotropic reinforcements. The saturated 3D compression method enables the quantification of transverse permeability at various fiber volume fractions within a single experiment. However, the in-plane permeability components must be known in advance for data analysis. Despite its potential, this method has seen limited practical use so far.

Other methods reported in literature In addition to the methods mentioned above, other methods have been reported in the literature. For example, Wu et al. [65] translated through-thickness permeability into an in-plane radial injection method by winding a roll of fabric tape. An inverse parameter estimation method by PAM-RTM is illustrated by Härter et al. [66]. However, these methods have not been widely adopted due to practical difficulties.

2.2.2 A brief journey through the history of permeability measurements

Since its establishment by Henry Darcy in 1856 [12] to describe fluid flow through porous materials, Darcy's law has found application in various fields. The 1980s saw the advent of LCM technologies, prompting the adoption of Darcy's law for permeability assessments of fibrous preforms. Despite the straightforward definition, permeability characterization has been a challenging task. Unlike rigid structures such as rocks, its pore structure can be altered during the processes of weaving [67,68], preforming [69,70], and resin infusion [71,72]. This results in poor reproducibility of permeability characterizations. As a result, worldwide efforts have been put into practice to develop customized characterization methods. Figure 2.11 illustrates the evolution and main milestones.

The first international benchmark [35] conducted a comparative study among 11 participants, using fabrics provided by Hexcel Corporation, all sourced from the same batch. One of the

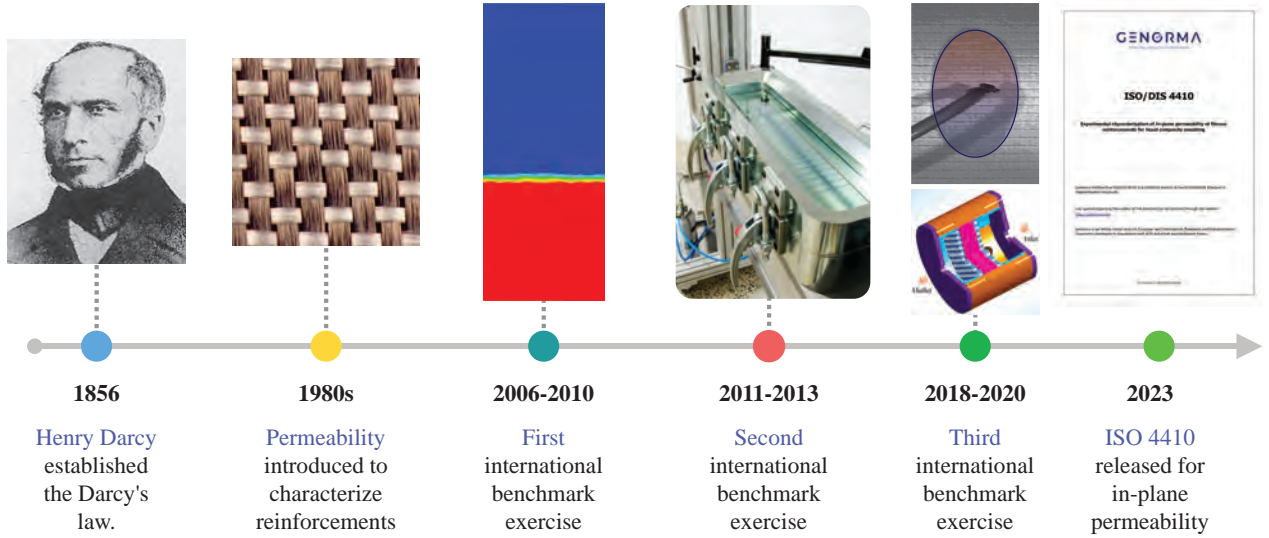


Figure 2.11 Progress and milestones in the standardization of measuring the permeability of textile reinforcement. The first global standard for assessing in-plane permeability, ISO 4410:2023 [73], was released in July 2023, as an outcome of the benchmark exercises.

fabrics, the twill carbon fiber fabric, G0986, is shown in Figure 2.12a. No specific testing protocol was prescribed. Participants were allowed to use their existing laboratory setups and procedures. This led to a variety of testing methods being used, including both channel flow and radial injection approaches, under different injection regimes (either constant pressure or flow rate). In addition, a variety of test fluids were used, including corn syrup, vegetable oil, and silicon oil. The results exhibited significant discrepancies, with errors surpassing 1000% for both in-plane permeability components, as depicted in Figure 2.12b. The errors in the anisotropy ratio k_2/k_1 also exceeded 200%. A similar trend of incomparable results was also observed in tests on another fabric made of glass fibers.

Building on the lessons learned from the first benchmark, the second benchmark incorporated comprehensive testing guidelines. The number of participants increased to 13, and they were restricted to using only the channel flow method to evaluate the in-plane permeability of the same fabrics as in the first benchmark. Two data processing methods were adopted: the squared flow front (SFF) method and the least squares fit (LSF) method proposed by Ferland et al. [34]. As depicted in Figures 2.13a and 2.13b, the results that conform to the guidelines demonstrate a decreased error margin of $\pm 22\%$ with the SFF method and even further to $\pm 20\%$ with the LSF method. This represents a significant improvement compared to the first benchmark. The error margin for the in-plane permeability k_2 of G0986 was also lowered to $\pm 17\%$ (SFF) and $\pm 16\%$ (LSF).

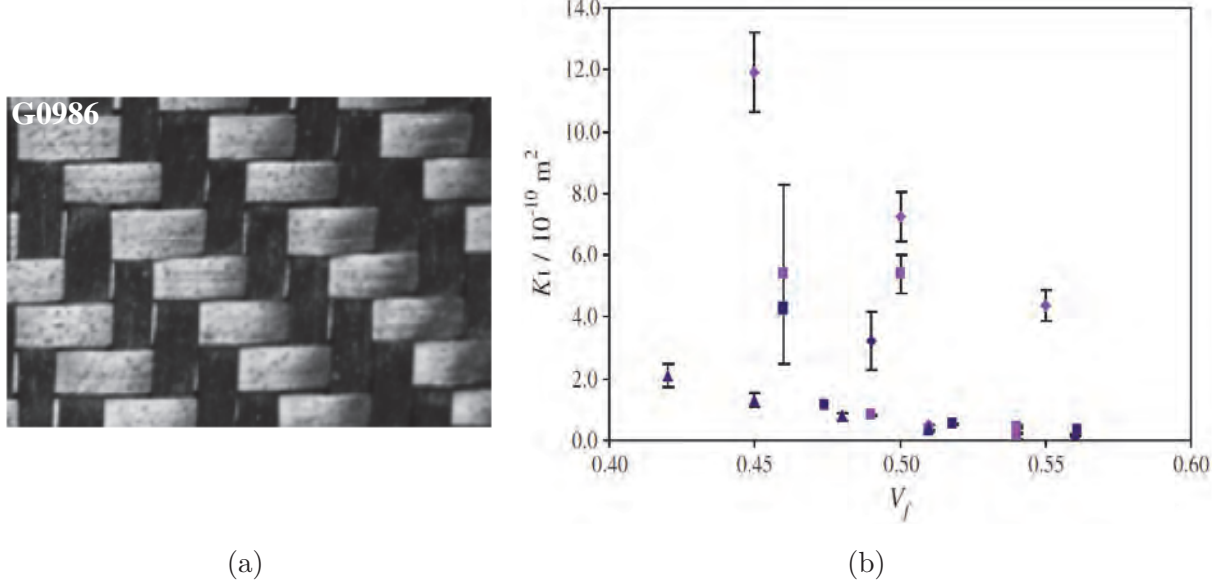


Figure 2.12 In-plane permeability K_1 for (a) twill carbon fiber fabric G0986 [36] (b) measured at the first benchmark [35].

The second benchmark underscores the importance of a robust testing protocol in improving the reproducibility and reliability of the in-plane permeability test. The two different data processing methods used did not show significant variance, yielding closely aligned average permeability values and standard deviations.

More effort was put into investigating the radial injection method in the third benchmark exercise [40]. Nineteen research institutions around the world participated, indicating a growing interest in accurately characterizing the permeability of textile reinforcements. Guidelines for fabric cutting, equipment calibration, and sample preparation were provided. However, the results indicated that the radial injection method exhibited higher error margins, reaching up to 45%, in contrast to the second benchmark, which demonstrated an approximate error level of 20%. This highlights the greater reliability of the channel flow method.

These benchmark studies laid the foundations for the standardization of permeability characterization. The first standard for assessing in-plane permeability, ISO 4410:2023 [73], was released in July 2023, as an outcome of the benchmark exercises. It provides a comprehensive guideline for the testing of in-plane permeability and specifies the testing equipment, sample preparation, and testing procedures for the channel flow method and the radial injection method. It also provides a detailed description of the data processing methods. Note that the 3D method is not included in the standard, as it is still in the early stages of development.

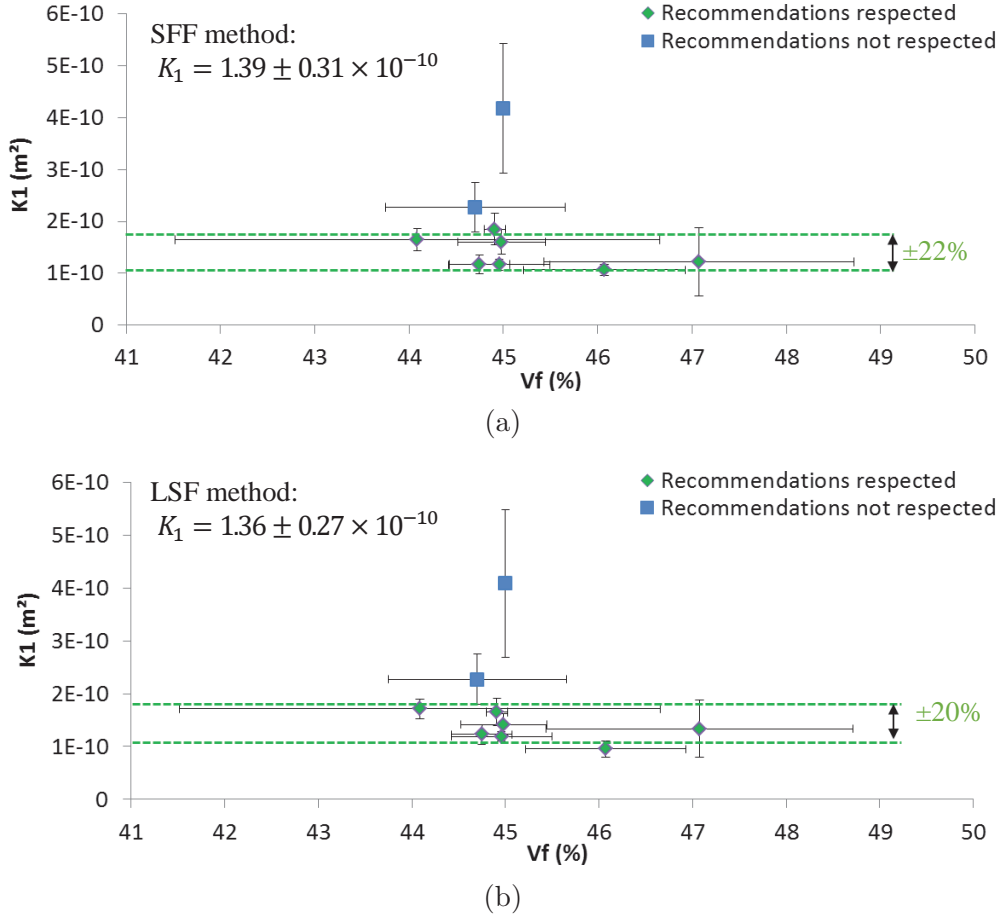


Figure 2.13 In-plane permeability k_1 for twill carbon fiber fabric G0986 measured at the second benchmark: (a) calculated with the SFF method [36]; (b) calculated with the LSF method [36].

Additionally, the first benchmark exercise focusing on transverse permeability measurements [13] was launched simultaneously with the third benchmark on in-plane permeability. The methods employed by the 26 participants have been outlined in the previous section (refer to Section 2.2.1), and the results are illustrated in Figure 2.14. It was observed that there was a significant disparity among the participants, with differences reaching up to 2 orders of magnitude. However, no definitive factors were identified as the cause of these discrepancies, given the variety of methods and setups used by the participants.

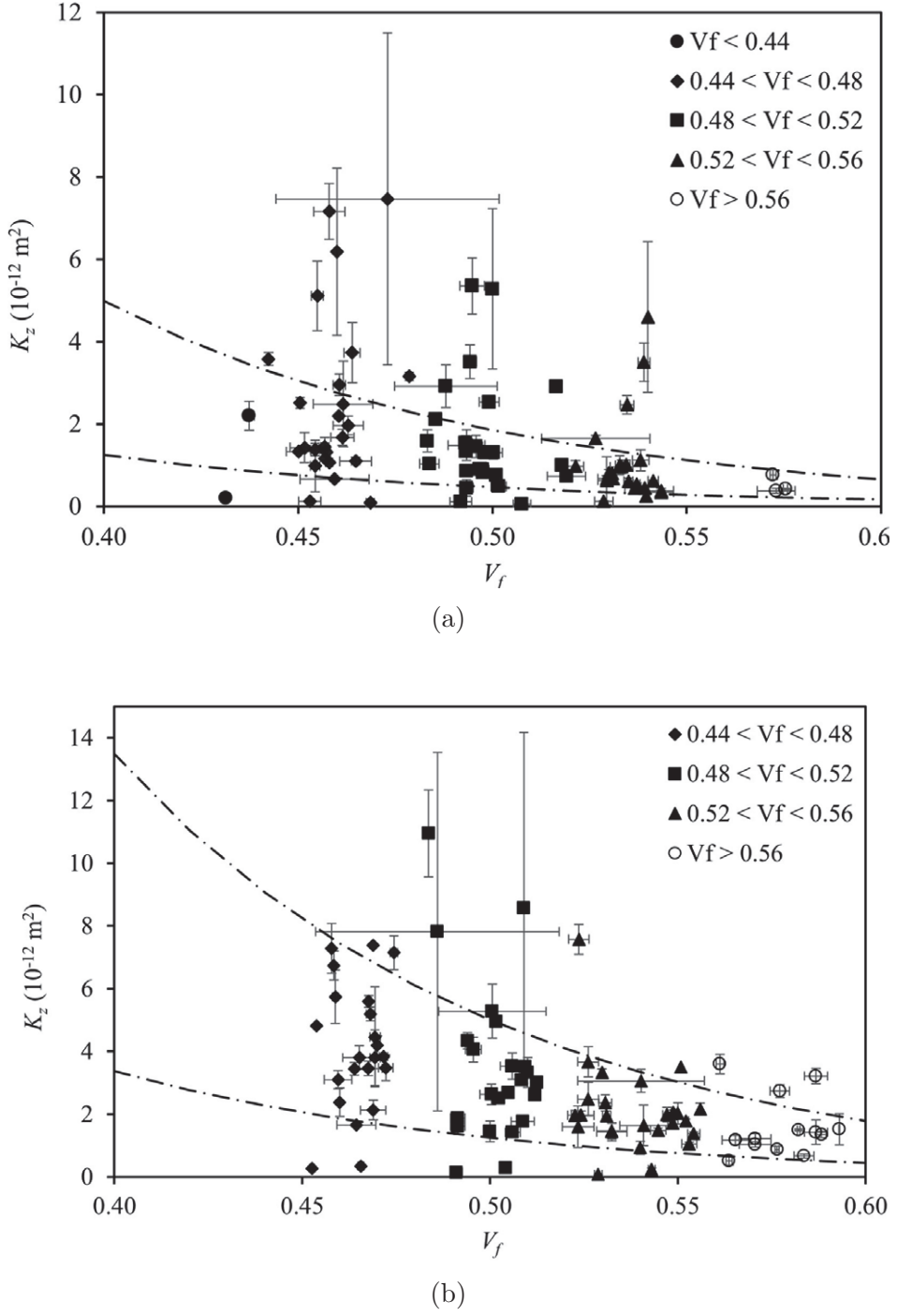


Figure 2.14 Transverse permeability at different compaction levels for all participants of the first benchmark on transverse permeability. (a) Woven fabric; (b) NCF fabric. The presence of dashed lines on the graph signifies a range of values where the ratio between the upper and lower bounds is 4 [13].

2.2.3 Summary

The need for standardization in the measurement of the permeability of textile reinforcements has reached consensus among academic and industrial communities. Although the channel flow (1D) method cannot determine both the in-plane permeability components and the angle of the permeability ellipse at the same time, it is still preferred in practice due to its simplicity, better reproducibility, and fewer disturbances during the test compared to the radial injection method. Further improvement is necessary to enhance the reproducibility of the radial injection method. The publication of the first edition of ISO 4410:2023, the international standard for in-plane permeability testing, signifies the end of a period lacking standardized testing procedures.

On the other hand, there is a lack of clarity regarding the guidelines for designing transverse permeability testing apparatuses and testing procedures, as well as the factors that impact the accuracy. This calls for further efforts to establish standardized protocols. Therefore, it constitutes one of the main research focuses of this project.

2.3 The formation, prediction and minimization of voids

2.3.1 Defects present in composites in the real world

To accurately identify the most common manufacturing defects associated with LCM processes in actual production, the author conducted a field survey at a plant of Sinoma Wind Power Blade Co., Ltd. in August 2019. Wind turbine blades, which include shells, spar cap and shear web (refer to Figure 2.15), are a well-established area of application for LCM processes. The survey tracked the manufacturing process of 68.8-meter-long wind turbine blades, models 686A and 686B.

Figure 2.16 presents our collected data on manufacturing defects in more than 350 wind turbine blades. According to this analysis, the majority of defects (70.6%) are associated with air trapping. More specifically, 29.4% of the defects are dry spots on the leading edge, also known as macroscopic voids, while the remaining 41.2% are mesoscopic and microscopic voids. Other defects make up less than 30% of the total. Consequently, it is essential to address the issue of voids in order to minimize repair costs. Otherwise, voids would promote the generation and propagation of cracks in composites and pose a severe threat to the safety service of composites [74].

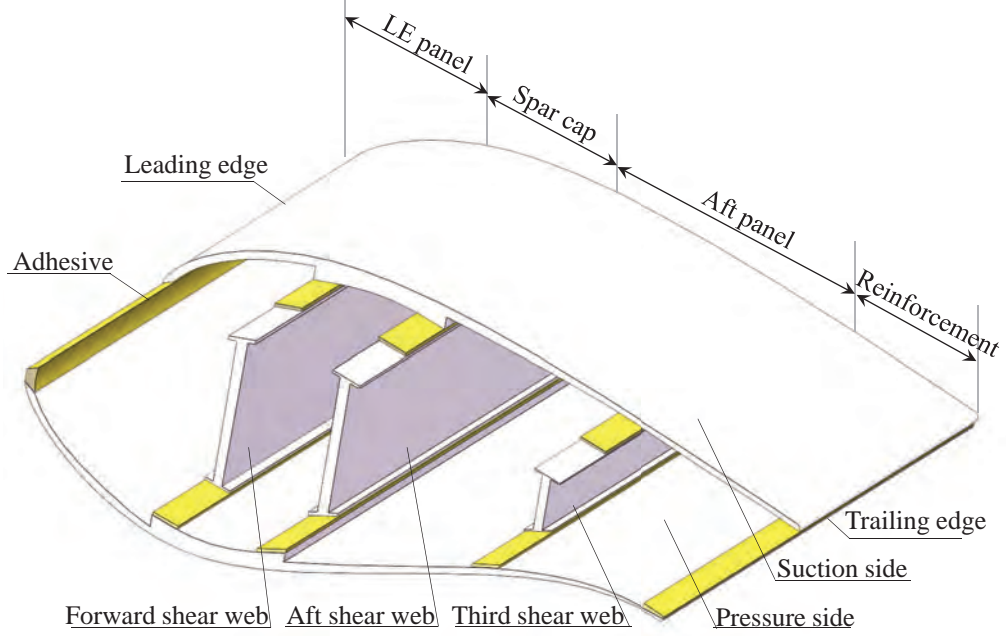


Figure 2.15 Typical structure of wind turbine blades.

2.3.2 Formation mechanism of voids

Various mechanisms contribute to the formation of voids, such as the mechanical entrapment of air, or the gas generated through chemical reactions during the curing process, and the nucleation of dissolved gases within the resin. Given that resin infusion for wind turbine blades typically occurs at low temperatures (below 40 °C), volatilization of resin components, such as styrene, is not considered a significant concern [75]. Furthermore, the resin is degassed prior to infusion to minimize void nucleation. Consequently, mechanical entrapment is recognized as the primary cause of void formation [76, 77].

As mentioned in the Introduction, dual-scale textile reinforcement consists of pores in two distinct length scales: the mesopores located between fiber tows and the micropores located within fiber tows. As illustrated in Figure 2.17, microscopic and mesoscopic voids arise due to non-uniform filling velocity fields. When the flow front velocity within the mesopores is slower than that in the fiber tows (micropores), capillary effects dominate the flow. This scenario increases the likelihood of air bubbles trapped in the mesopores. On the contrary, if the flow velocity in the mesopores is higher, air can get trapped within the fiber tows, resulting in the formation of microscopic voids.

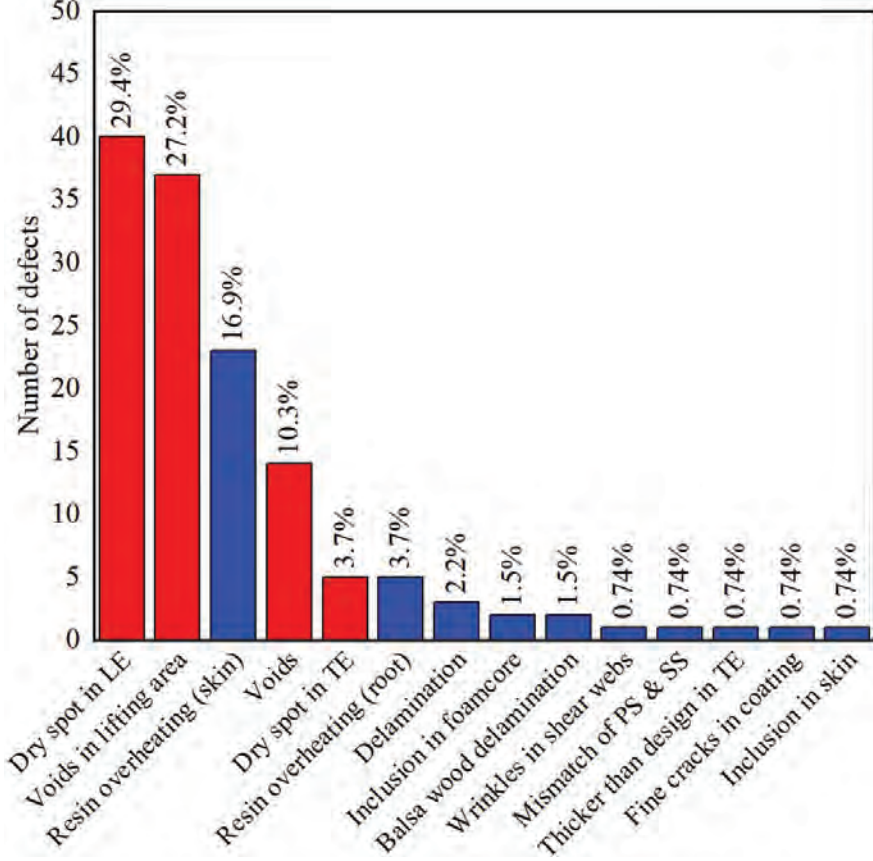


Figure 2.16 Manufacturing defects appearing on wind blades: LE stands for leading edge, TE for trailing edge, PS for pressure side of shell and SS for suction side of shell, as illustrated in Figure 2.12.

2.3.3 Voidage prediction

Many efforts have been made to predict the voidage (void content) and void distribution in composites manufactured using LCM processes. The most commonly used prediction methods fall into three categories: the empirical model, the time-difference-based model, and the numerical method based on Computational Fluid Dynamics (CFD). The latter two methods require knowledge of the structure of the textile reinforcement.

Empirical models The empirical model was developed by fitting experimental data and is described as a function of the flow front velocity v [79]:

$$\begin{aligned} V_M &= -32.28 - 11.80 \log(v) \\ V_m &= 6.35 + 2.35 \log(v) \end{aligned} \tag{2.4}$$

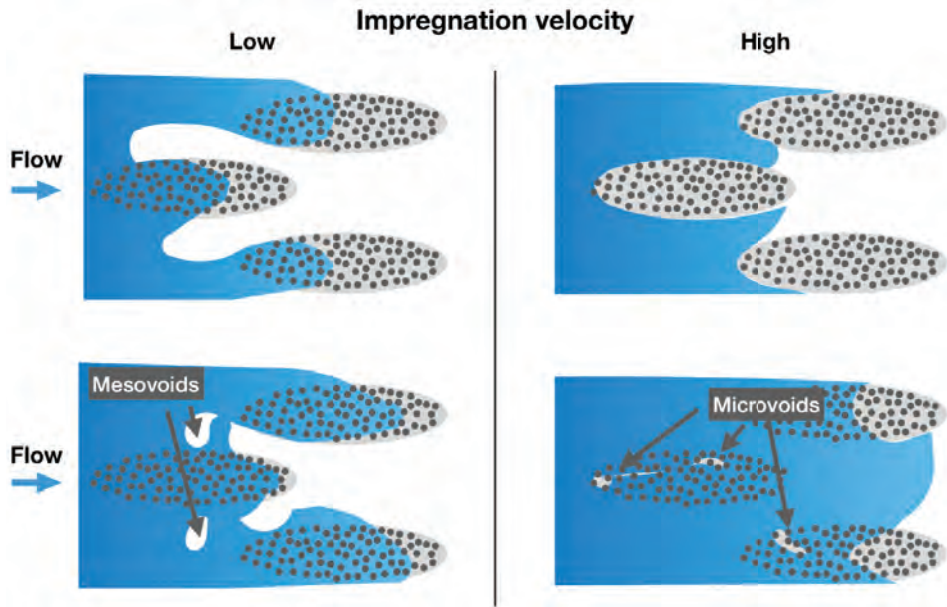


Figure 2.17 Void formation caused by dual-scale flow under (a) low and (b) high impregnation velocity [78].

where V_M stands for the mesoscopic void content, V_m the microscopic void content. The optimal flow front velocity v_{opt} , which minimizes the total void content, is expressed as:

$$v_{opt} = \frac{Ca^* \cdot \gamma \cdot \cos \theta}{\mu} \quad (2.5)$$

where Ca^* is the modified capillary number, defined as the ratio between viscosity force and capillary force, μ represents viscosity, γ is the surface tension of the resin and θ is the fiber-resin contact angle [77]. The void fraction can be represented graphically, as illustrated in Figure 2.18, as a function of the flow front velocity or the capillary number. An increase in flow front velocity (or capillary number) results in a decrease in mesoscopic voids and an increase in microscopic voids. Furthermore, below the critical value v_{opt} (or the corresponding capillary number Ca^*), the model assumes that only mesoscopic voids are present, while above this threshold, only microscopic voids are assumed to exist.

Time-difference-based models The time-difference-based model, initially proposed by Kang et al. [80], considers the architecture of textile reinforcement to predict the size and number of voids. This model accounts for air entrapment due to a non-uniform velocity field at the flow front on both the mesoscale and the microscale. The flow front velocity is determined using either Poiseuille's law (flow in mesopores) or Darcy's law (flow in micropores).

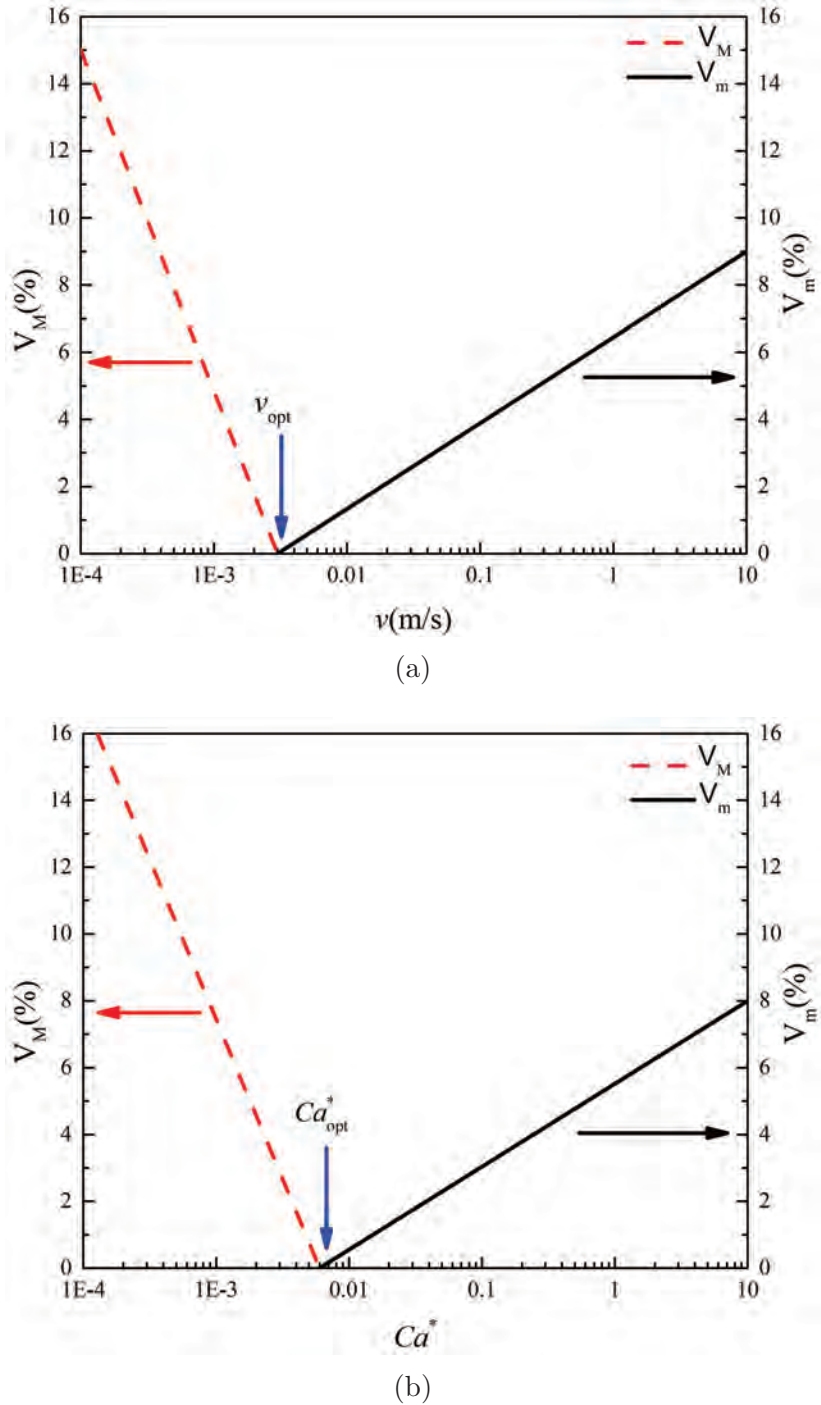


Figure 2.18 Voidage (void content) as a function of flow front velocity (a) and capillary number (b) [79].

As illustrated in Figure 2.19, the time required for the flow to reach a specified position in the fiber tow and in the channel is denoted as Δt_T and Δt_C , respectively. When the flow in

the fiber tow is slower than the flow in the channel (mesopores), namely $\Delta t_T > \Delta t_C$, microscopic voids appear in the fiber tow (Figure 2.19a). Conversely, mesoscopic voids appear in the channel (Figure 2.19b). Ideally, voids can be prevented by achieving uniform flow front velocities in both the tow and the channel (Figure 2.19c). The size and position of voids can be predicted by using the model and the ideal gas law, through correlating $(\Delta t_T - \Delta t_C)$ with injection pressure. This model has been extended to explore the impact of factors such as number of layers, fabric shear, geometric anisotropy [81], flow direction [82], and horizontal shift between fabric layers [83] on void formation in dual-scale textile reinforcements.

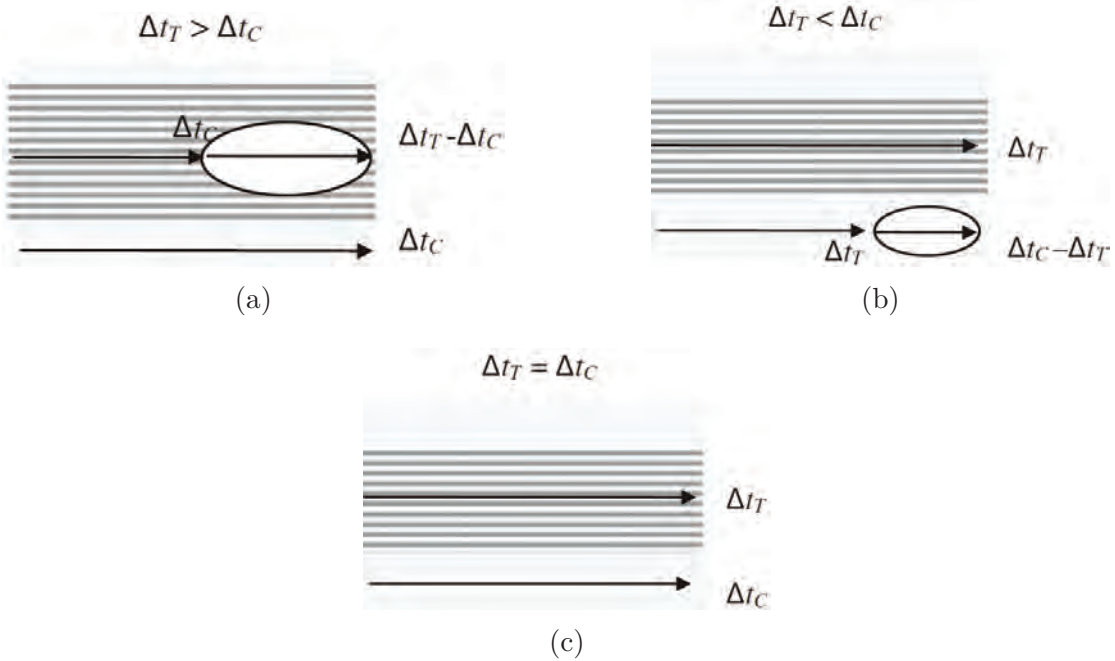


Figure 2.19 Time-difference based void prediction model (a) void formation inside the tow; (b) void formation in the channel between the tows; (c) void is prevented due to the uniform flow front [84].

Numerical method In light of significant advances in computer technology in recent decades, numerical investigations on the creation of voids based on computational fluid dynamics (CFD) have increasingly garnered attention. Lundström et al. [85] developed a three-dimensional numerical model to predict the formation of voids in a non-crimp biaxial fabric. The Navier-Stokes equations and Darcy's law are utilized, respectively, to describe the flow between and inside the tows. The capillary effect was also taken into account as a source term. The results suggest that the weave pattern and the tow geometry have a significant impact on the creation of voids. Overall, the numerical findings validated the

experimental observations outlined in the empirical model. DeValve and Pitchumani [86] performed a parametric study to analyze the process of void formation. A simplified representation of a plain weave was used as simulation model. A parametric graph, depicted in Figure 2.20, was proposed to describe the relationship between the voidage and the capillary and Reynolds numbers. The optimal processing window for actual manufacturing can be determined by the contours presented in the graph. More recently, Stokes-Brinkman [27] and Stokes-Darcy [87] formulations have also been used to predict the formation of voids in dual-scale textile reinforcements during resin infusion. These results show good agreement with the work of DeValve and Pitchumani [86].

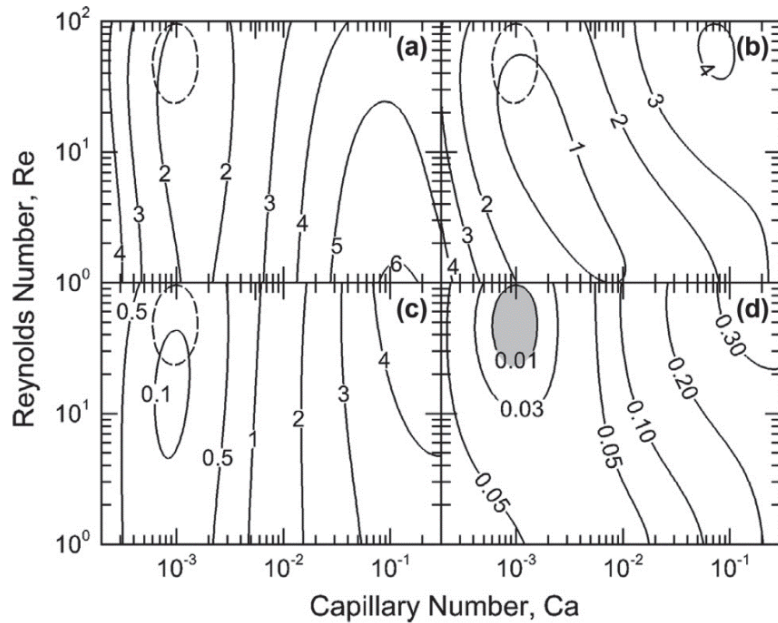


Figure 2.20 Contours of the (a) maximum final void content found in the 2D slices of the Rovcloth 2454, (b) volume-averaged final void content considering each of the two-dimensional slices, (c) dimensionless excess flow time and (d) combined parameter on a Capillary number-Reynolds number plane for the Rovcloth 2454 [86].

2.3.4 Voidage minimization

Many experience-based techniques have been proposed to reduce the void content, such as vacuuming the mold cavity [75], degassing the resin [88,89], bleeding and post-filling [90,91]. Ever since the introduction of the empirical model by Patel and Patel et al. [77], research efforts to reduce voids have been directed toward finding the optimal injection velocity. The empirical model (Eq. (2.4) and Eq. (2.5)) was successfully coupled with the fill simulation of Ruiz et al. [29] to optimize the processing parameters (that is, the injection flow rate). The

proposed numerical technique has been integrated into the commercial PAM-RTM software, which is maintained by the ESI Group [92]. Lebel et al. [93] proposed a method to predict the optimal injection velocity based on the characterization of the imbibition, which shows a promising way since there are no time-consuming tests (surface tension, contact angle, etc.) and complex dual-scale flow modeling involved. Online resin flow control strategies to maintain optimal velocity have also emerged as a prominent research field [94–97]. The results show that the voidage can be effectively reduced by controlling relevant process parameters in the impregnation and consolidation stages.

2.3.5 Summary

Investigating the creation, transport, and minimization of voids is of great importance due to the significant effect on mechanical properties of composites. Current methods for reducing voids rely primarily on empirical models and practical knowledge gained from production experience. However, these approaches are highly restricted because the internal geometry of woven fabrics cannot be explicitly considered. In comparison, computational fluid dynamics simulations have emerged as a promising approach because they allow consideration of the internal geometry of textile reinforcements, dual-scale unsaturated flow, and capillary effects at the same time. Currently, the accuracy of numerical predictions is limited by the precision of textile reinforcement geometry modeling. It is still a common practice to represent reinforcements with two-dimensional models or 3D simplified models with regular geometry. Qualitative results can be achieved through this approach. Nonetheless, it is difficult to obtain quantitative solutions that can be used to guide actual production, because the irregular geometry of textile reinforcements has a significant impact on the flow pattern.

2.4 Mesoscopic geometry modeling of textile reinforcements

The meso-level geometry of textile reinforcements, such as the weave pattern, trajectory of fiber tows, and shape of tow cross sections, plays a crucial role in determining the manufacturability (permeability, drapability, etc.) and mechanical properties (stiffness, stress concentration, etc.) of composites made from them. Therefore, mesostructural models are extensively used in numerical simulations to fill the gap between macroscopic behavior and microscopic mechanisms. A mesostructural model typically consists of one or more Representative Volume Elements (RVE)s of textile reinforcements. It allows for the prediction of macroscopic properties by upscaling and the investigation of manufacturing defect creation in the dual-scale domain.

A software used to build mesostructural models is called a Meso-Level Textile Processor (MLTP) [98, 99]. It takes geometric parameters and generates the corresponding textile model as output. The level of detail in representing the mesotexture of reinforcements in these models varies, leading to different categories:

- simplified mesostructural models,
- realistic mesostructural models, and
- digital material twins (DMT).

The following sections discuss each of these categories in detail, beginning with a brief introduction to the internal geometry characterization of textile composites.

2.4.1 Internal geometry characterization

Decades ago, analyzing the internal structure of textile composites had to go through a complicated procedure for sample preparation. This involved cutting and polishing the specimen, and then taking images using a camera [100, 101], high-resolution scanner [102–104], or microscopy [105, 106]. Finally, a limited amount of internal geometric data can be gathered by image analysis and used as input for MLTP softwares.

Non-destructive volumetric imaging techniques, especially Micro-CT, offer images of the internal structure of composites at resolutions ranging from 400 nm to 70 μm [107], thus avoiding sample damage and contamination. It provides researchers with detailed internal geometry information and help them to understand the connection between the internal structure and the macroscopic properties of composites. The use of non-destructive volumetric imaging in the characterization of textile composites serves three main purposes: (1) investigating defects and damages to analyze mechanical properties and failure mechanisms [17, 74, 108, 109]; (2) characterizing the geometric features of fiber tows for mesostructural modeling [18, 110]; and (3) analyzing the mesopore network between fiber tows to predict the permeability of fibrous preforms [111–113].

After the volumetric image is obtained, it is subjected to pre-processing to remove any unwanted noise and artifacts. The next step involves segmenting the image to identify specific phases of interest, such as the matrix and fiber tows. In studies that concentrate on geometry modeling, each fiber tow must be segmented individually, as the orientation and arrangement of tows have a significant impact on the performance of the composite material. Lastly, the measured geometry information is used as input for mesostructural model reconstructions using MLTP codes.

Table 2.2 summarizes some common image pre-processing and segmentation methods used in the literature. Various commercial software, such as VGStudio, MATLAB, Avizo, or open-source software like ImageJ and SciPy, are proficient in performing image preprocessing. However, identifying interfaces between fiber tows by segmentation is a significant obstacle. Tows are composed of the same material, making it difficult to differentiate them with X-ray. This problem is especially noticeable for carbon fiber reinforced textile composites [114].

Table 2.2 Micro-CT image pre-processing and image segmentation methods

Textile	Resolution	Smoothing	Segmentation	Software	Ref.
Plain weave	10.4 μm	-	Manual	VGStudio	[115]
	25 μm	pixel intensity averaged	Sobel operator & Structure tensor	MATLAB	[20]
	1-10 μm	median filter	threshold-texture feature morphology	-	[116]
	5 μm	1D uniform filter	Morphological gradient & Deep learning	ImageJ & SciPy	[114]
	18.6 μm	Non-local mean filter	Thresholding based on seed region growing	Avizo	[117]
5-directional braided composite	22.1 μm	✓	✓	VGStudio & ImageJ	[67]
Fiber tow	9.3 μm	Nugget effect	Implicit kriging & Indicator function	Python	[118]
3D fabric	2 μm	Median filter	Texture analysis	-	[119]
	-	Gaussian smoothing	Structure tensor & Signed distances	MATLAB	[19]

Notes:

"—" means information of the item was not given by authors;

"✓" means the item was done but the method was not given.

The structure tensor method can identify different fiber tows by analyzing the grayscale gradient of the image [119–121]. It utilizes the partial derivatives of the image f_x and f_y along the x-axis and y-axis, constructing a structure tensor \mathbf{S}_i at each pixel:

$$\mathbf{S}_i = \begin{bmatrix} f_x^2 & f_x f_y \\ f_x f_y & f_y^2 \end{bmatrix} \quad (2.6)$$

The structure tensor \mathbf{S}_i is then subjected to eigenvalue decomposition to obtain eigenvalues (λ_1, λ_2) and eigenvectors (\vec{e}_1, \vec{e}_2) . Here, the eigenvectors represent the direction of the

gradient, while the eigenvalues indicate the strength of the gradient along their respective eigenvectors. For three-dimensional volumetric images, the structure tensor is extended to:

$$\mathbf{S}_i = \begin{bmatrix} f_x^2 & f_x f_y & f_x f_z \\ f_x f_y & f_y^2 & f_y f_z \\ f_x f_z & f_y f_z & f_z^2 \end{bmatrix} \quad (2.7)$$

The structure tensor method has been found to be an effective technique for segmenting textile images that have a low fiber content. However, when dealing with samples that have a high fiber content, the interface and the grayscale gradients become less distinguishable. In these situations, it is necessary to combine the structure tensor method with other image analysis tools to achieve successful image segmentation [119, 120]. Encouragingly, with the adoption of machine learning methods in fabric image segmentation, there has been a significant improvement in the accuracy and efficiency of automated image segmentation [114, 122–125].

2.4.2 Simplified mesostructural models

The simplified mesostructural model approximates the geometry of fiber tows with regular shapes, constant cross sections, and periodically arranged unit cells. The mesostructural alterations of fiber tows that occur during weaving and preforming are not reflected. TexGen and WiseTex are two of the most widely known MLTP softwares. TexGen was developed at the University of Nottingham [126, 127] and is released as an open source code. It is positioned as a geometry modeling preprocessor for textile composites. In comparison, WiseTex, created at the Catholic University of Leuven [128, 129], stands out as a numerical toolkit. It goes beyond just modeling the internal geometry of textiles and includes features that can predict elastic properties and permeability. This is demonstrated in Figure 2.21. In addition, general-purpose Computer-Aided Design (CAD) and finite element software can also be applied to create simplified models [130–132].

These tools establish mesostructure models using a similar approach: by defining the path and cross-sectional shapes of a fiber tow (see Figure 2.22a). This allows for the convenient modeling of different weave patterns, including woven, non-crimp, knitted, and braided textiles. The path is typically defined by a sequence of node positions and is smoothly interpolated using differentiable curves. Cross sections are commonly approximated using regular shapes, such as ellipses, rectangles, power elliptical (Figure 2.22b.), and lenticular shapes (Figure 2.22c) [99, 126]. Note that for simplified models, the fiber tows do not necessarily have a constant cross-section. They can also be modeled with a smooth transition in size and shape through interpolation, such as evolving from a power ellipse to a lenticular [134].

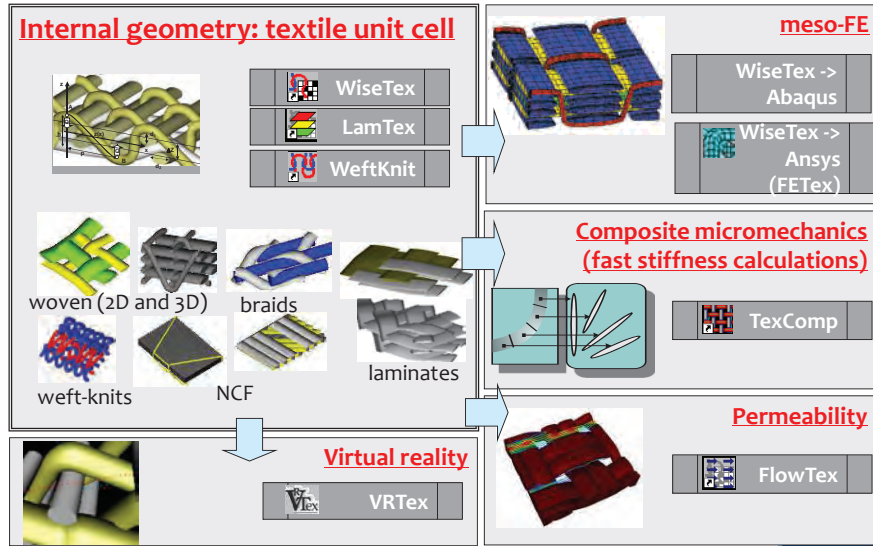


Figure 2.21 Virtual testing environment for textiles or composites built on the meso-level textile processor WiseTex [133].

2.4.3 Realistic mesostructural models

The simplified models consist of identical, periodically arranged RVEs, whereas the actual internal geometry and performance of the textile reinforcements show strong spatial discreteness [100,113,137,138]. To address this limitation, realistic mesostructural models incorporate more structural details of actual fabrics. The cross section of the fiber tows in realistic models is no longer limited to regular shapes. It can be an arbitrary closed shape. Therefore, the RVE may also not necessarily show periodicity.

Realistic models can be obtained through mesoscale numerical simulations by applying fundamental mechanical principles for transverse compression, biaxial tension, shear, bending, etc. Simplified mesostructural models are a common input for this process. For instance, WiseTex integrates mathematical models that account for deformations tow waviness, shape, and displacement [99]. Alternatively, simplified models can also serve as input for general-purpose numerical simulation software, such as Abaqus. Realistic mesostructural models can then be derived by simulations under appropriate boundary conditions. TexGen has the ability to refine simplified models based on actual test data [18]. However, the procedure can be laborious due to the significant amount of manual effort required.

Obtaining realistic mesostructural models through sub-mesoscale modeling is another commonly used approach. This can be achieved by simulations of weaving [139] and compaction [140] with filaments resolved in fiber tows. However, simulating all the fibers in each tow, which usually consists of thousands of filaments, is not feasible. The multi-chain

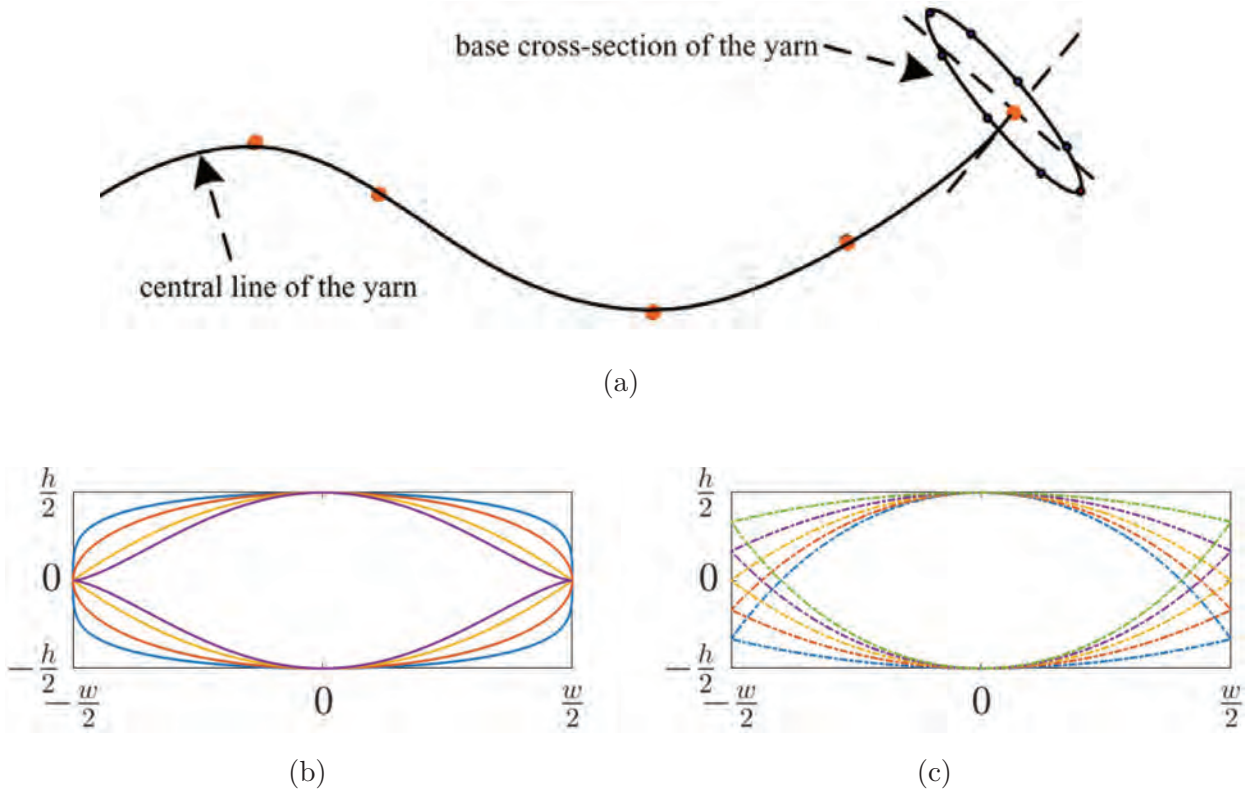


Figure 2.22 Descriptions of fiber tows in simplified models: (a) tows described by base cross sections sweeping along its path [135]; Analytical yarn cross sections modeled (b) using a power ellipse with exponents $[0.5, 1, 2, 3]$, where the colors transition from blue to purple, and (c) with a lenticular shape with distortion distance $[-h/3, -h/6, 0, h/6, h/3]$, where the colors transition from blue to green [136].

digital element method [139, 141–144] represents a tow as a collection of virtual fibers with a diameter significantly larger compared to actual filaments. Each virtual fiber is modeled as a chain of rod elements, termed a "digital chain." As the length of these rod elements approaches zero, the digital chain becomes fully flexible, effectively simulating the physical properties of a fiber. This approach enables detailed tracking of yarn paths and changes in cross-section shape during textile processes or deformation. The number of virtual fibers that can be considered sufficient for a simulation was investigated by Green et al. [140] and Daelemans et al. [145] by comparing numerical results with experiments.

2.4.4 Digital material twins

The concept of Digital Material Twin (DMT) of textile composites was proposed by Prof. François Trochu and explained in the paper by Huang et al. [110] in 2019. The goal is to de-

velop a physics-based model for textile composites that effectively captures the mesostructure of the physical component and its operating conditions to enhance the accuracy of numerical simulations. Instead of extracting limited geometric parameters from images to create a simplified model, the DMT method takes advantage of segmented image data as input directly, making full use of the information contained in the volumetric image. This allows DMT models to accurately represent the physical structure. On the other hand, realistic models only approximate the fabric's actual structure through physical simulation, and their accuracy depends on the simulation configurations. This concept has been continued by the community [123, 125].

A digital material twin should possess the following features:

- It faithfully represents the spatial variability of the modeled textile reinforcements or composites.
- Each fiber tow is reconstructed and numbered individually, while ensuring that the meso-level geometric features are maintained, acting as a mirror of the original structure (see Figure 2.23).
- The model can be used in multiscale data-driven analysis to virtually test mechanical or flow properties.

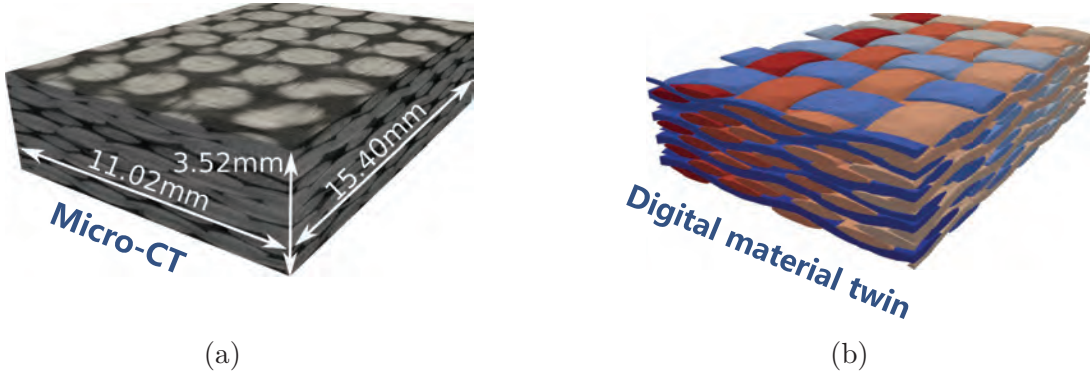


Figure 2.23 (a) Micro-tomographic image; (b) Digital material twin (voxel model) [110]

To construct a digital material twin, Micro-CT is used to capture the internal structure of textile reinforcements. This approach can be traced back to the research conducted by Anna Madra, who explored algorithms for volumetric image segmentation [122, 146], fiber tow modeling [118, 122], and geometry approximation [147]. In these works, in addition to research on learning-based segmentation techniques for processing Micro-CT scans, a method

based on dual kriging is proposed to optimize the representation of fiber tow profiles using curvature energy and applying the nugget effect in kriging for smooth surfaces [122], as illustrated in Figure 2.24.

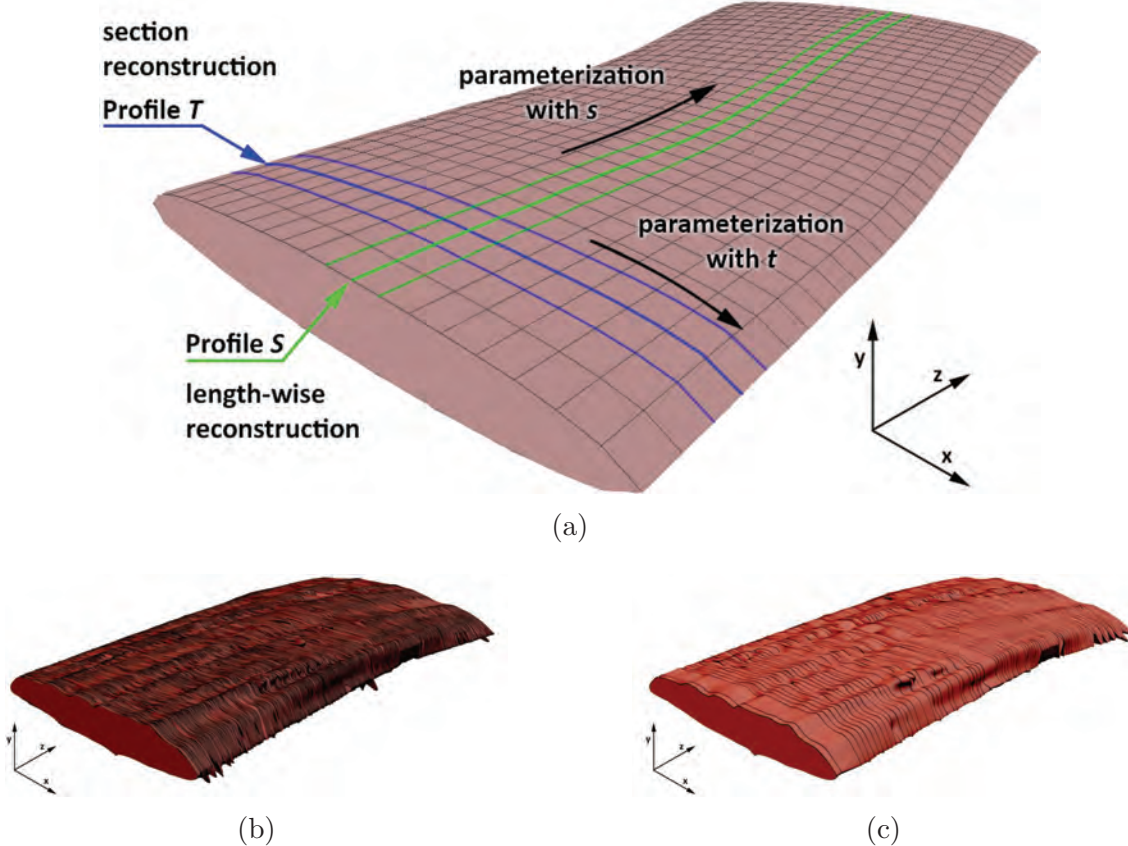


Figure 2.24 Representation of fiber tows with parametric kriging: (a) representation of tow contour with parameters (s, t) ; (b) parametric reconstruction of fiber tow surface and (c) smoothing with nugget effect [122].

Subsequently, Huang et al. [110] expanded this research to the scale of a unit cell (multiple tows) and proposed a series of methods to evaluate the accuracy of the models. The method was also applied to examine changes in the shape of fiber tows in plain weave fabrics when subjected to compression, as shown in Figure 2.25 [113, 148].

The current project aims to build upon the previous work by improving the accuracy of geometric feature extraction and the efficiency of data processing. In this project, a toolkit will be developed to automate the geometric feature analysis, digital material twin generation, and the numerical meshing process. This will allow for the use of the high-fidelity DMT models for multiscale numerical simulations.

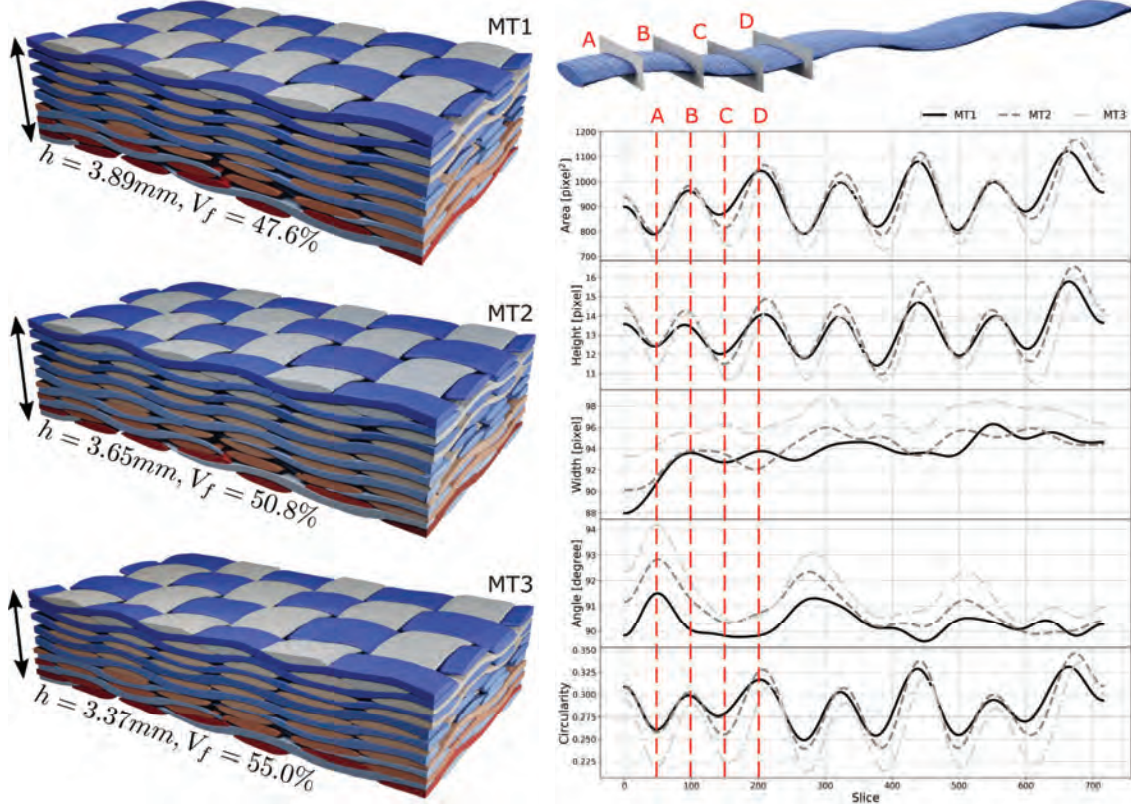


Figure 2.25 Variations of fiber tow cross-sectional area perpendicular to the horizontal plane at three compaction levels [113]

The creation of a digital material twin model is essentially a process that involves transforming volumetric image data into high-fidelity numerical models. In the past few years, many published works can also be categorized within this scope and are commonly known as image-based modeling.

Naouar et al. [120] employed the structure tensor method to segment the volumetric image of a 2D twill fabric. Subsequently, the image masks were skeletonized to obtain the centerline of each tow. The envelope surface of the fiber tow was generated and triangulated using the marching cubes algorithm, and was simplified through edge contraction. This surface was then utilized as the initial front for the advance front meshing method to generate a tetrahedral mesh of the twill fabric. In another work, Naouar et al. [119] performed the image segmentation task with a texture analysis algorithm based on the Grey Level Co-occurrence (GLC) matrix. The material is an E-glass non-crimp 3D orthogonal woven reinforcement. A prismatic mesh was generated from the segmented image sequence. This is achieved by connecting the cross sections of fiber tow with the same triangle meshes, and then the corresponding nodes are connected to generate the prismatic elements.

Wijaya et al. [20] developed a mapping algorithm to segment the weft and warp tows of a 2D woven textile with the first slice manually segmented. Similarly as Naouar et al. [119], the region of interest is discretized by creating a collection of 2D meshes along the length of each tow first and then connecting to form a structured 3D mesh. The procedure is illustrated in Figure 2.26.

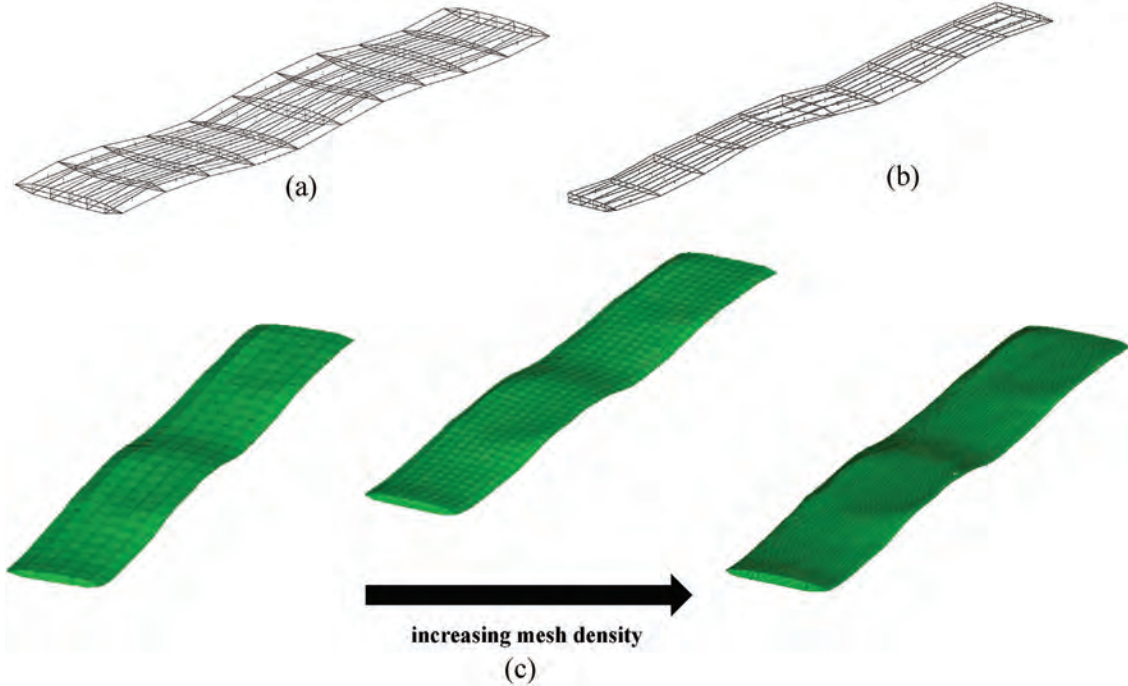


Figure 2.26 Creation of a 3D mesh for a fiber tow: (a) complete tow, (b) incomplete tow, and (c) adjusting the density of the mesh for a given fiber tow [20].

Wintiba et al. [19] utilized the conformal discretization methods previously suggested by the authors [149] to generate a conformal mesh of a 3D woven composite from Micro-CT scans. The volumetric image was segmented using the structure tensor method, with manual operations providing assistance. The interface between fiber tows and matrix phase are represented implicitly with a signed distance fields. The authors utilized the Laplacian and Gaussian filters to achieve a smooth interface. Other conformal mesh generation methods also reported by Rassineux [21] and Drach et al. [150].

Isart et al. [151] conducted a comparison between numerical simulations with simplified models, realistic models created using the multi-chain digital element method and DMT models constructed from Micro-CT image. The results show that the accuracy in predicting the elastic parameters of composites is closely related to the level of detail of the tows. As illustrated in Figure 2.27, the simplified model exhibited a discrepancy in the cross-sectional

area by more than 20%, leading to an overall fiber volume fraction in the composite that was 7% lower than the actual value and a deviation in the predicted elastic parameters from the experimental values by more than 10%. The fiber tow contours in the realistic and DMT models matched well with the Micro-CT images, with the global fiber volume fraction deviating less than 1%. The elastic parameters predicted by the latter two methods were more consistent with the experimental results.

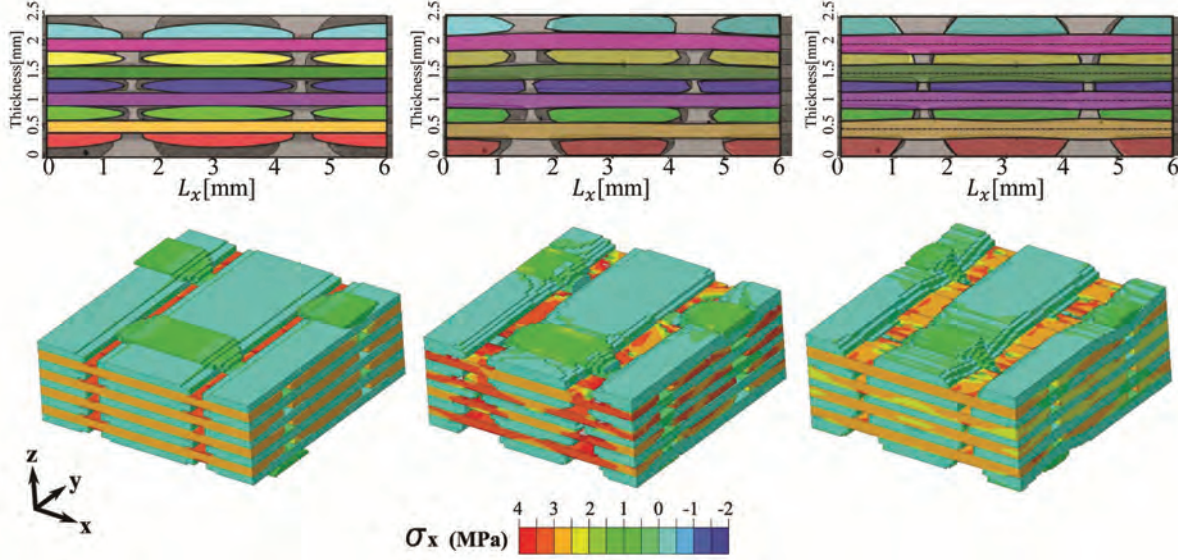


Figure 2.27 Models with different accuracy and the corresponding tensile stress field in x direction obtained through numerical simulation. The simplified model, realistic model, and DMT are shown from left to right [151].

2.4.5 Summary

In the past two decades, simplified modeling techniques have been widely employed to develop mesostructural models with regular geometry. The establishment of these models requires specifying only a few parameters, such as the width, thickness, and cross-sectional shape of the fiber tows. These models have been shown to be highly effective in analyzing the properties of textile composites. However, it has also exposed issues concerning inadequate predictive precision as a result of the simplified geometry representation.

Volumetric imaging techniques have played a crucial role in providing detailed information on the internal structure of composites. Furthermore, the use of automated segmentation techniques, especially those based on machine learning algorithms, enables users to quickly extract a large amount of geometric data from volumetric images. However, existing geometrical modeling software, primarily designed for rapid modeling with a limited number of

inputs, cannot fully utilize such a volumetric dataset.

Several image-based modeling techniques have been proposed since 2015. Leveraging the existing research findings, this project seeks to create an open-source code that can be used to generate mesostructural models using volumetric images as input. It incorporates functions that include image pre-processing, geometric modeling, and numerical meshing. The tool is designed to be easily accessible to all users, regardless of their knowledge of image processing, geometric modeling, or mesh generation. This will not only enable a more accurate estimation of permeability considering the multiscale structure and spatial variability of textile reinforcements, but will also facilitate the exploration of the manufacturing defect formation mechanisms and virtual testing of the mechanical properties of textile composites.

2.5 Volumetric image aided virtual testing of permeability

Experimental permeability tests often do not produce accurate results [13, 35, 36, 40] and can be costly and time consuming. Consequently, virtual testing methods based on Micro-CT images [152, 153] have been widely used in the last five years. The approaches are categorized into 3 groups according to how fiber tows are handled, as illustrated in Figure 2.28.

(a) Solid impermeable tow models. Treating fiber tows as solids is acceptable for virtual permeability testing, since they typically represent only approximately 10% of total flux. The problem is simplified to solve only the flow between the fiber tows. Several commercial softwares [23, 24, 112, 117] integrate solvers that can operate directly on volumetric images. This approach avoids complex mesh generation. Consequently, it has become the most widely applied method to date [23, 24, 112, 117, 154, 157, 158].

(b) Tow models considered as porous media. For issues related to the dual-scale pore network structure, such as void creation, it becomes imperative to resolve fiber tows. Considering fiber tows as porous media allows one to incorporate the flow within the tows and their spatial variability through an effective permeability tensor. Karaki et al. [159] reviewed analytical models used to estimate the permeability of tows and compared these models with experimental and numerical results in another work. The flow between the yarns can be described with Stokes' equation ($Re \ll 1$ in the LCM process), while the flow within the fiber tows is considered as the Darcy flow. Numerical methods can be categorized into two types based on the treatment of the interface. The one-domain approach considers the interface implicitly by incorporating Darcy's law as a source term of the (Navier-)Stokes equation and requires the determination of the effective viscosity. The second method describes the two

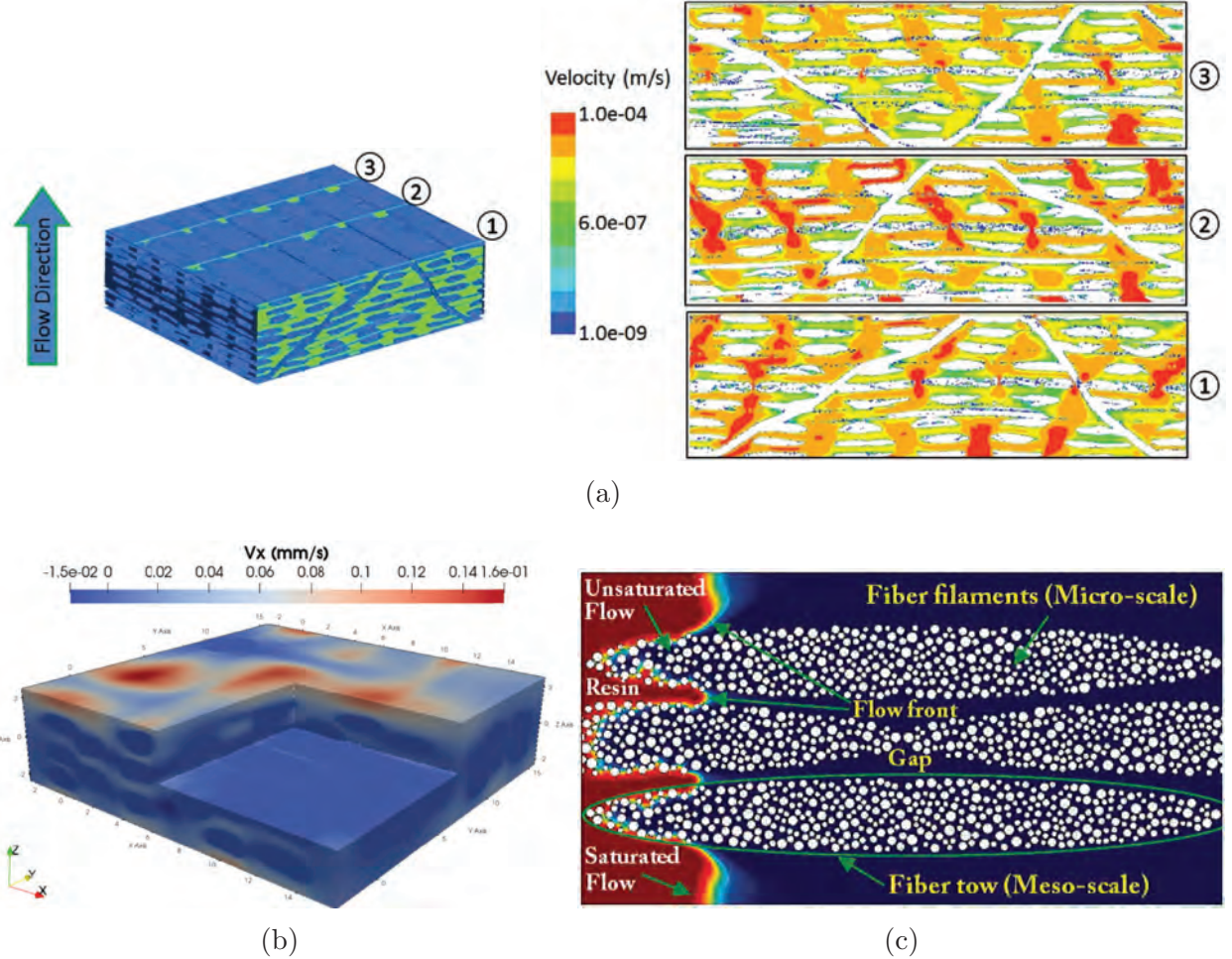


Figure 2.28 Categories of volumetric image aided permeability virtual testing according to the handling of fiber tows in the model: (a) solid tow [154]; (b) porous tow, flow along x -axis [155]; (c) fiber resolved [156].

domains using two sets of incompatible Partial Differential Equations (PDEs). Boundary conditions, such as the Beavers-Joseph boundary condition, are necessary to link the two domains. This approach is not commonly used in volumetric image-aided virtual testing because generating a dual-scale DMT model from volumetric images remains challenging [155].

(c) Filament resolved tow models. The challenges faced by this method stem primarily from two aspects. First, volumetric imaging techniques, such as Micro-CT, comprise the sample size and the imaging resolution. This results in individual fibers (μm) being indistinguishable on RVE scale scans (mm). Second, each tow of textile reinforcements contains

thousands of fibers. It is not feasible to use models that resolve all fibers in a numerical simulation. Consequently, such simulations employ either a simplified model consisting of several tows that a small number of effective fibers (with a diameter larger than that of real fibers) resolved [156, 160] or imaging a single tow only to estimate its permeability [161].

An overview of the solvers commonly employed for virtual permeability testing is presented in Table 2.3. A discussion of various solvers are presented in reference [162]. Regardless of the modeling approach chosen for fiber tows, the method to determine textile permeability follows a similar pattern. This involves extracting the volume-averaged variables $\langle \mathbf{v} \rangle$ and $\langle p \rangle^f$ from the numerical results. The permeability is then calculated using Darcy's law.

Table 2.3 Solvers commonly used for virtual permeability testing

Category	Governing equation	Software	Tow	Reference
Computational fluid dynamics (CFD)	N-S equation on discretized grid	Fluent, CFX, OpenFOAM ...	(a), (b), (c)	[163–165]
Voxel based direct N-S solvers (VBS)	N-S equation on volumetric images	VGStudio, Avizo, etc.	(a)	[154, 166] [23, 157]
Lattice-Boltzmann method (LBM)	Boltzmann equation on voxel mesh	OpenLB ...	(a)	[167, 168]
Pore network modeling (PNM)	Poiseuille's law	OpenPNM Avizo ...	(a)	[169, 170]
Semi-analytical solvers (SAS)	Analytical up-scaling	/	/	[171]
Empirical models (EMP)	Kozeny-Carman etc.	/	/	[112, 172] [173]

* N-S: Navier-Stokes;

** (a) solid tow; (b) porous tow; (c) filament resolved.

CHAPTER 3 ARTICLE 1: ON THE DESIGN OF TEST MOLDS BASED ON UNIDIRECTIONAL SATURATED FLOWS TO MEASURE TRANSVERSE PERMEABILITY IN LIQUID COMPOSITE MOLDING

Bin Yang, Wei Huang, Philippe Causse,
Cédric Béguin, Jihui Wang, François Trochu

Published in *Polymer Composites* on 02/10/2022

3.1 Chapter overview

This chapter presents a study published in *Polymer Composites* that examines the various factors that influence the precision of transverse permeability measurements with the unidirectional method. We analyze factors related to both the test device and the sample. Our research introduces a new concept to quantify the influence of these factors on the accuracy of the test, providing guidance for the design of test devices and the optimization of testing processes. The findings indicate that a well-designed structure can prevent device deformation. The most significant factor that affects the test is the design of the flow distribution plates. However, since flow distribution plates are crucial for the unidirectional test setup to maintain sample thickness, Chapter 4 proposes additional methods to mitigate their impact on the tests.

3.2 Abstract

Impregnating fibrous preforms through thickness has become a main feature of some Liquid Composite Molding process variants. Thus, the evaluation of transverse permeability is critical to optimize the fabrication and reduce manufacturing defects. Some problems connected with the design of testing devices need to be addressed to perform a reliable characterization. In this study, the efficiency of a typical one-dimensional testing device to measure transverse permeability is evaluated numerically and experimentally. The paper introduces a novel methodology to identify the optimal mold configuration and evaluate the flow pattern inside the mold cavity. A dimensionless number called the “fill coefficient” is also proposed to evaluate quantitatively the effect of the mold structure on the transverse flow pattern. The measured transverse permeability is shown to increase with lower fill coefficients for saturated and unsaturated flows. The intrinsic transverse permeability is obtained when the fill coeffi-

cient is equal to one. The proposed methodology is verified by experiments performed in an existing tool. This confirms that the measured transverse permeability can be significantly affected by the above mentioned factors.

Keywords: Liquid Composite Molding; Mold deformation; Flow distribution; Preform; Transverse permeability;

3.3 Introduction

Liquid Composite Molding (LCM) is a family of composite manufacturing processes, in which a liquid resin is injected into a mold cavity to impregnate a fibrous preform. Several new LCM process variants were developed over the years, such as vacuum-assisted Liquid Resin Infusion (LRI) with a distribution medium [174], Compression Resin Transfer Molding (C-RTM) [11] and Flexible Injection (FI) [10]. In these processes, an empty open space is filled by resin above the preform, followed by through-thickness impregnation. Therefore, knowledge of transverse permeability (k_z) is critical for process design and optimization, which characterizes the resistance of a fibrous preform to a transverse liquid flow through its thickness.

Thanks to its simplicity, the unidirectional test method is widely used to determine transverse permeability. In the latest international benchmark, twenty-eight experimental results were reported by 26 different participants, among which 22 were measured using this method [13]. This approach is carried out by establishing a unidirectional transverse flow through a stack of fibrous reinforcements (the “preform”) in the mold cavity. A typical example of a testing device is shown in Figure 3.1. The preform (white in the inset of Figure 1a) is laid out and compressed to the desired fiber volume fraction between two perforated plates (red). The test liquid or gas [175, 176] enters in the mold cavity from a bottom inlet gate, flows through the holes of the lower perforated plate into the fibrous reinforcement, and then out of the sample through the upper perforated plate to leave finally the mold cavity from the outlet gate in the mold cover. The transverse permeability mold and data acquisition system provide experimental data (flow rate Q , pressure drop ΔP , etc.) to derive the k_z permeability from the one-dimensional Darcy’s law [12]:

$$k_z = \frac{Q}{A} \cdot \frac{h_f}{\Delta P} \cdot \mu \quad (3.1)$$

where μ denotes the viscosity of the test fluid, A the flow area and h_f the thickness of the fibrous reinforcement (usually defined as the distance between the two perforated plates

under and above the specimen).

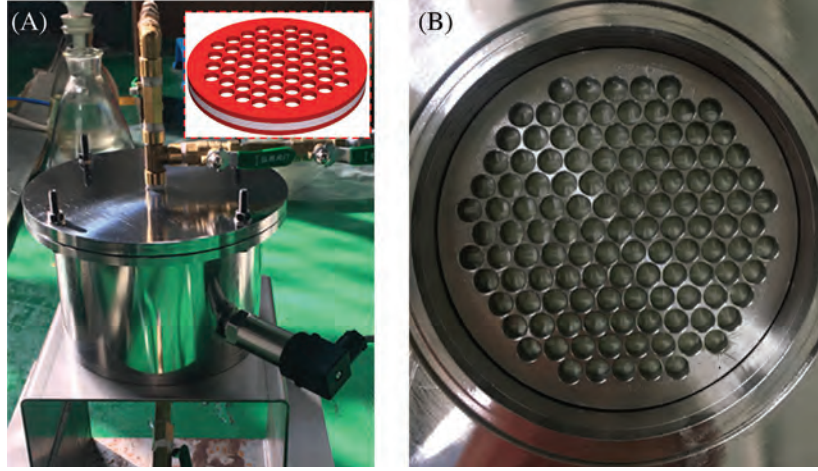


Figure 3.1 Example of one-dimensional transverse permeability test mold: (a) tool with pressure sensors near the inlet and outlet. (b) Perforated plate.

Several unidirectional transverse permeability test molds have been described in the scientific literature to evaluate the transverse permeability of fibrous reinforcements [15, 62, 177–179]. However, the characterization of k_z remains a challenge. Differences of about two orders of magnitude were observed between experimental results with the same fibrous reinforcements and test liquid [13], although much lower variations (usually under 20%) are expected for measurements with the same measurement system. The observed discrepancy is due to several factors such as material variability, difference in test molds and measurement procedure. Another common source of error is the edge effect, namely the preferential boundary layer flow between the preform and the vertical cavity wall. This can be prevented by using specimens precisely cut with customized tools [24], adding seals on the sample perimeter [14, 180, 181] or considering separately the flow at the edge of the tested specimen [182].

Summing up the challenges reported in the scientific literature, the following issues appear:

1. *Discrepancy in fiber volume fraction.* Not much attention was paid in published articles to assess the possible deformations of the perforated plates due to pressure induced by sample clamping or liquid injection. This may change the thickness and fiber volume fraction of the specimen and hence alter its transverse permeability. Therefore, it is worth analyzing the deformation behavior to limit the fiber volume fraction discrepancy to an acceptable range when designing a new mold. Note that it can also be used to correct the cavity height of an existing mold.
2. *Flow patterns in the cavity.* In the one-dimensional method, calculating the transverse

permeability by Darcy's law implies that the sample is considered homogeneous and crossed by a unidirectional transverse flow at the macroscopic level of Darcy's equation. Otherwise, as illustrated in Figure 3.2, an in-plane flow is involved, giving a flow rate generated by coupling the in-plane and transverse flows. The transverse permeability cannot be determined precisely in such a case. Fibrous reinforcements are usually not rigid enough to be self-supported. Therefore, support plates are introduced, which create a three-dimensional flow profile as shown in Figure 3.2. This affects the measured transverse permeability and might explain the poor reproducibility of test results for different testing devices. As a matter of fact, depending on the configuration of the test mold, the in-plane flow created varies from device to device. A parametric study is conducted in this article to connect partial unidirectional flows with k_z measurements. This leads to introduce a dimensionless number called the "fill coefficient" to evaluate the efficiency of test molds. A similar analysis is reported by Ferland et al. [34] for one-dimensional unsaturated in-plane permeability measurements, who showed that several geometrical features in testing equipment might have a significant influence on the measured permeability.

3. *Pressure drop of the test device.* The pressure drop without specimen in an empty mold should always be negligible in front of the one created by the fibrous reinforcement. A similar verification was also carried out by Ferland et al. [34] for in-plane permeability measurements.
4. *Material and/or specimen properties.* The variability of measurements is usually attributed to discrepancies in textile architecture, nesting between plies and/or sample preparation. Up to now, not much attention was given to investigate the effect of other material properties such as that of the preform in-plane permeability on k_z measurements. However, the in-plane permeability of the fibrous reinforcement may play a role for anisotropic textile reinforcements because of the in-plane flow caused by perforated plates. Another concern is connected with the thickness of the specimen, which may affect the development of the flow pattern in the sample.
5. *Effective flow area.* Another difficulty is connected with the flow area A used in Eq. (3.1) to evaluate the transverse permeability since the flow is not perpendicular to the preform due to the presence of perforated plates. In the scientific literature, the flow area is usually referred to as the area of mold cavity cross-section [183], the actual open space [184], or a value between the two precedent ones [177, 185]. However, the methodology followed to determine the effective flow area was not fully investigated so far, although it can affect directly permeability. A similar investigation on effective flow

area can be found in [186], which investigates the transverse gas permeability through preprints.

6. Flow induced compaction. This issue studied by Klunker et al. [14] and Becker et al. [187] is based on Terzaghi's law [188], which states that the total stress applied to a porous material saturated with liquid is equal to the sum of pore pressure plus the load on its skeletal portion. Although a linear pore pressure profile is obtained according to Darcy's and Terzaghi's laws, nonlinear pressure distributions were observed by Klunker et al. [14] and Ouagne et al. [178]. Fluid induced compaction results in the highest fiber volume fraction at the outlet while the lowest appears at the inlet [14, 187].

This article focuses on the first four issues connected with the test mold (1, 2, 3) and with the dimension and anisotropy in permeability of the fibrous specimen (4). The investigation seeks to evaluate how the design of a unidirectional mold and material properties affect the accuracy of transverse permeability measurements. A new approach is proposed to assess the performance of unidirectional test devices while finding an optimal perforated plate design to minimize mold deformation. This could be possibly used to improve the reproducibility of tests performed with different molds. Since this work concentrates only on the impact of the test device on measurement accuracy, some causes of variability in measurements connected with the preform are neglected, such as nesting, local variability, edge effect and so forth. The analysis is performed at the macroscopic level of Darcy's equation. Namely, textile reinforcements are regarded as homogeneous porous media, and the microscopic uneven flow caused by their mesostructure is not considered. Besides, flow induced compaction is also neglected in experimental validations because the injection pressure used is much lower than the compaction pressure required to achieve the target fiber volume fraction.

In summary, the rest of this article is organized as follows. After a review of the scientific literature on transverse permeability in Section 2, investigation on mold deformation behavior

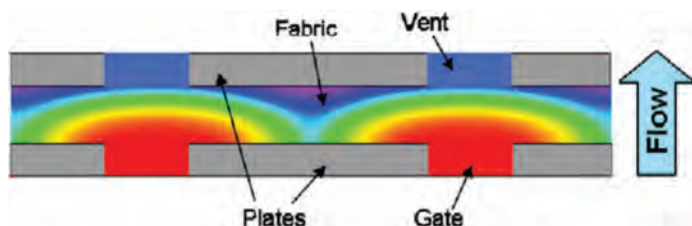


Figure 3.2 The fibrous preform being held between two perforated plates, this figure shows typical non-unidirectional flow patterns created by perforations [15]. Convergent and divergent flows can be observed in zones of the specimen facing impermeable parts in the perforated plates.

is presented in Section 3. A relationship is proposed to connect the fiber volume fraction with preform compressibility and the open space ratio of the perforated plates to identify the optimal design configuration. In Section 4, parametric studies are conducted based on unsaturated and saturated flow simulations to evaluate a new dimensionless number, the “fill coefficient”, devised to assess the performance of designed measurement tool. Section 5 presents an experimental verification on the accuracy of an existing k_z mold. The main results are summed up in Section 6 to provide guidelines to design more robust k_z test molds based on through-thickness flows.

3.4 Review of literature

Transverse permeability test devices based on one-dimensional Darcy’s law are usually made out of transparent plastic [62], aluminum [62, 177] or stainless steel [24, 189, 190]. The shape of the mold cavity cross-section can be constantly square or circular. Its size ranges from 79 mm to 150 mm [14, 62, 166, 178, 185, 191–193]. Among the difficulties encountered in the design of unidirectional test molds, the deformation behavior and the effect of non-unidirectional flow patterns represent two main issues. This is connected with the configuration of perforated plates, which turns out to be a critical feature in unidirectional test molds. Inappropriate evaluation of the role of perforated plates may prevent from accurately controlling the global fiber volume fraction and alters the streamlines inside the mold cavity.

Table 3.1 summarizes geometrical configurations of perforated plates reported in the scientific literature, including the material, shape, thickness, size and density of perforations. No specific optimization or analysis were reported on these existing devices so far. The packing pattern and size of perforations differ from one another. In most published articles on k_z permeability, the mold is considered to be sufficiently stiff [194] to control the cavity height. Although this may be the case, this analysis provides a model to identify the optimal configuration of perforated plates.

Local fiber volume fraction can also be disturbed significantly (up to 26%) as noted by Graupner and Drechsler [195], because the outermost preform layers may bend in the open spaces of the perforated plates when a compaction force is applied. These authors added a sintered metal porous plate between the perforated plates and the preform to prevent fiber bending. Comparing k_z results with and without the sintered porous structure, they concluded that changes in local fiber volume content can be neglected [182]. Nevertheless, the transverse permeability of sintered porous plates and of the measured fabric were not reported in their investigation. For this approach to be valid, the porous plate should be at least two orders of magnitude more permeable than the measured preform. In fact, no study

Table 3.1 Configurations of perforated plates reported in the scientific literature.

Authors	Material	Shape	Thickness (mm)	Dimension of perforations (mm)	Number of perforations
Visconti et al. [180]	Metal net	Not specified	0.7	10 × 10 (square)	5
Li et al. [189]	Stainless steel	Rectangular	10	Φ 5	225
Li et al. [183]	Stainless steel	Rectangular	Not specified	Φ 6/Φ 2	49/35
Klunker et al. [14]	Steel	Circular	Not specified	Φ 8	95
Huang et al. [24]	Stainless steel	Circular	6.5	Φ 7.5	60

was yet conducted on the minimum permeability of flow distribution layers, nor on a way to evaluate quantitatively, as proposed in this article.

The presence of perforated plates or other similar flow distribution media creates a three-dimensional flow profile as discussed above, because of the limited flow exchange area between the free flow and the porous specimen. This is not consistent with the theoretical background, the one-dimensional Darcy's equation, which is used to derive the transverse permeability from experimental data. Scholz et al. [15] studied the non-unidirectional flow by numerical simulations with LIMS software [196]. As illustrated in Figure 3.2, the liquid flow in the cavity is divergent instead of along the thickness direction. In order to eliminate the unwanted in-plane flow and generate a more unidirectional flow, Wu et al. [184] placed an impermeable Mylar sheet with a 2.54 cm (1 inch) hole in the center between every two fabric layers, while Li et al. [183] machined two different sizes of perforations in the perforated plates to increase its open space.

Another approach was reported in the scientific literature with highly permeable flow distribution layers laid out above and below the preform. Note that a metallic mesh [15, 24] or a screen [184] have been used for that purpose. However, the permeability of the distribution layer and the size of the grid should be balanced, because too coarse a grid could lead to nesting between the preform and the distribution layers [110]. Another difficulty with this approach stems from its possible deformation if the distribution layers are not sufficiently stiff.

In summary, most researchers assumed that the perforated plates are highly permeable and have no influence on the pressure drop [14, 194]. For the required unidirectional flow, some

of the measures mentioned above were taken only intuitively. No index can be used to evaluate the performance of test molds so far. The combination of these effects leads to poor test reproducibility of transverse permeability, as confirmed by the significant differences observed in the latest transverse permeability benchmark [13].

3.5 Cavity deformation for unidirectional mold with perforated plates

The deformation of the perforated plates resulting from specimen compaction pressure or injection pressure may vary the average thickness of the specimen, and hence affect transverse permeability characterization, which is a function of fiber volume fraction. The more open spaces exist in the two perforated plates, the easier it is to establish a transverse flow. However, this reduces the stiffness of perforated plates and may cause significant cavity deformation. Conversely, insufficient open spaces increase the resistance to the flow, and introduce another drift in k_z measurements. To keep a balance between the open spaces and cavity deformation, mechanical analysis is carried out here followed by flow behavior analysis in next section to assess a proper range of geometric parameters for appropriate design of k_z molds.

Different configurations of circular perforated plates are analyzed based on two design parameters: the thickness of the plate and the packing pattern of perforations. Compressibility results carried out for the two benchmark fabrics [13] are used to determine the typical range of compaction pressure. The fluid injection pressure was not considered. The fluid pressure is equally applied on both sides of perforated plate since the pressure drop at perforated plate is negligible. Then the deformation behavior of the mold cavity is evaluated by finite element analysis. Finally, a two-dimensional model based on dual kriging interpolation [110, 197] is proposed to take into account the average deflection of perforated plates and correct, if needed, the thickness of test samples. In the end, a corrected value of k_z permeability is obtained as a function of actual cavity height.

3.5.1 Compressibility of engineering fabrics

The two typical fibrous reinforcements are a non-crimp glass multi-axial fabric produced by Saertex (NCF, 45°/90°/0°/45°, areal density of 444 g/m²) and a twill glass woven fabric supplied by Hexcel (WF, areal density of 295 g/m²) [13]. Square pieces of 100 mm × 100 mm are cut and stacked visually with the same orientation. Both dry and wetted compressibility is measured using a universal test machine (UTM, CRT-30kN, Shenzhen Riger Instrument Co., Ltd). The preform was fully saturated with PMX-200-100cs silicone oil for saturated

tests. The stress evolution after compliance correction is plotted in Figure 3.3 against fiber volume fraction in dry and wet modes. Each test is repeated five times and averaged. The upper and lower bounds of the error bars represent the maximum and minimum values for each set of experiments. Higher stiffness and similar compaction response between the dry and wet tests can be observed in the behavior of the NCF glass fabric. In contrast, the wet compaction pressure of the less rigid WF fabric is much lower than the dry one due to lubricating effects. Figure 3.3 shows that 270 kPa of compression pressure is required to reach a fiber volume fraction of 57%. In practice, the fiber volume fraction of composite parts rarely exceeds this value. Therefore, the maximum effective stress acting on perforated plates is taken as 600 kPa($> 540 \text{ kPa} = 270 \text{ kPa}/50\%$) in this analysis because the open space ratio in perforated plates stands usually around 50%.

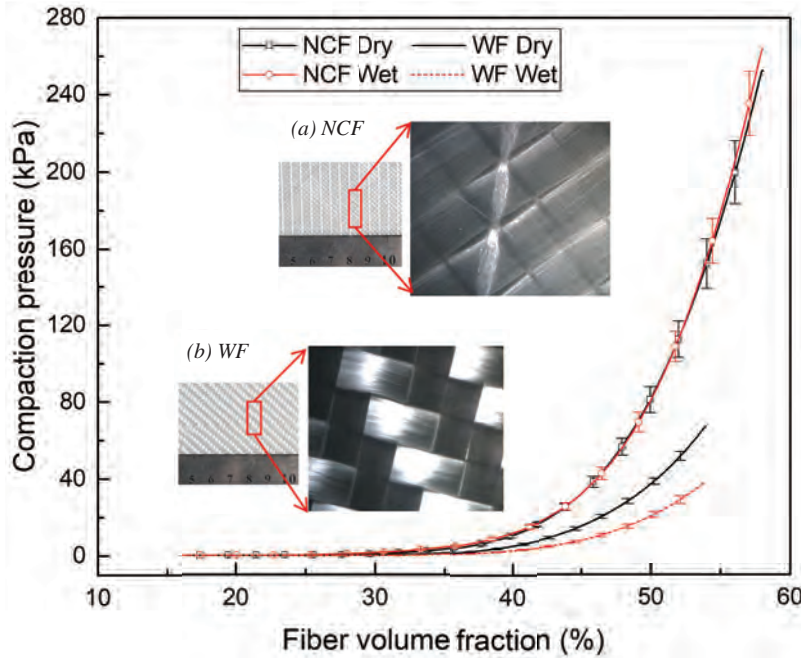


Figure 3.3 Dry and wet compressibility measurement for the two benchmark fabrics (measured at Wuhan University of Technology).

3.5.2 Simulation of perforated plate deformation

Hexagonal packing patterns are used for the arrangement of perforations, because it allows achieving a larger open space ratio compared to square packing. The geometrical model, the finite element mesh and boundary conditions are shown in Figure 3.4a. Thanks to symmetry, only a one-sixth circular sector model needs to be used in the calculations. The mesh is fine enough to obtain a detailed representation of the stress distribution for each kind of

perforations. Fixed boundary conditions are imposed on the edge (support width, see Figure 3.4a) and a uniform pressure is applied on the bottom surface. The plate considered in our analysis has a radius of 57 mm to support a sample with an area of 100cm^2 in addition to the area required to fix the perforated plate. Two materials are investigated numerically with standard mechanical properties: aluminum (Young's modulus: 70.0 GPa; Poisson's ratio: 0.33) and stainless steel (Young's modulus: 190.0 GPa; Poisson's ratio: 0.265). Different configurations of perforated plates are obtained by adjusting the perforation spacing and size.

To estimate the fiber volume fraction, the mean deflection is calculated from the node displacements in the thickness direction predicted by numerical simulation. The mean deflection of the aluminum perforated plates under an even-distributed load is plotted in Figure 3.4b as a function of thickness t and open space ratio φ . As the open space ratio increases and thickness decreases, the deformation shows a significant increasing trend. Moreover, thickness plays a more significant role than the open space ratio. The deflection increases significantly for a thickness lower than 6 mm.

In Table 3.2, the maximum and mean deflections are compared for different perforation spacing and diameters while keeping nearly similar ratios of open space. The deflections remain similar and independent of the perforation spacing and diameter for the aluminum and stainless steel perforated plates. Therefore, a deflection model for different perforation patterns may consider only one independent variable, namely the open space ratio, instead of two (hole spacing and diameter). Moreover, the maximum and mean deflections are shown to be inversely proportional to the elastic modulus of the materials.

Table 3.2 Deflections for similar open space ratios and different perforation patterns.

Open space ratio	Hole spacing	Hole diameter	Max. deflection ^a		Mean deflection ^a	
			Aluminum	Stainless steel	Aluminum	Stainless steel
55.0%	8.0 mm	7.5 mm	0.373 mm	0.134 mm	0.074 mm	0.026 mm
54.9%	7.0 mm	6.5 mm	0.374 mm	0.139 mm	0.076 mm	0.028 mm
55.1%	6.5 mm	6.0 mm	0.390 mm	0.145 mm	0.085 mm	0.031 mm

^a Deflection under 600 kPa acting on the 4-mm-thick perforated plate.

After having obtained the mean deflections for each configuration from the stiffness analysis illustrated in Figure 3.4b, all the data points are used to construct a parametric model of

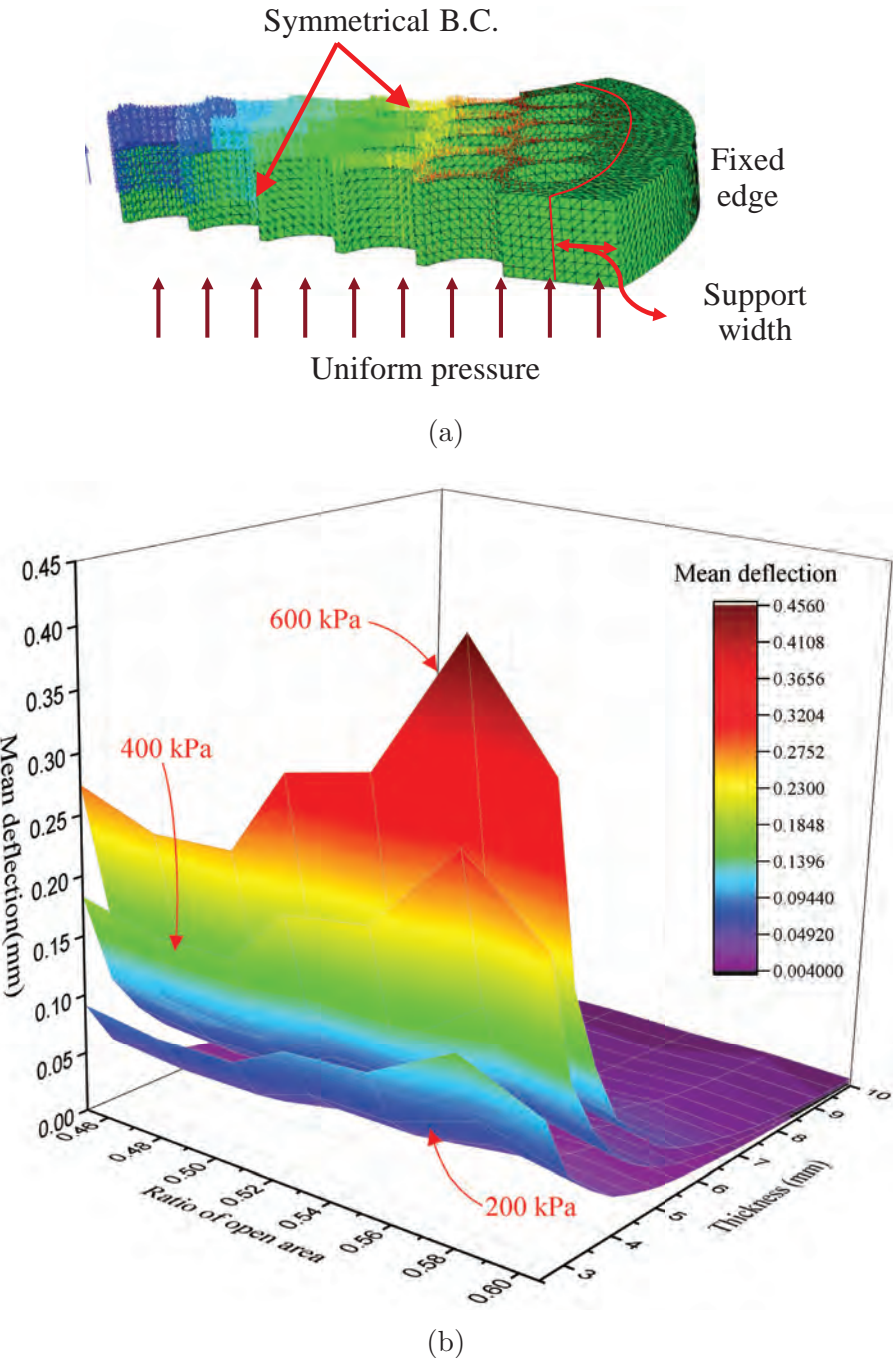


Figure 3.4 Analysis of perforated plate deformation: (a) boundary conditions for the 3D stiffness finite element analysis of a circular sector. (b) Mean deflection as a function of the open space ratio and plate thickness for the three pressure levels considered (aluminum).

cavity deformation $\mathbf{D}_f(t, \varphi)$ in Eq. (3.2) below based on dual kriging parametric surface interpolation [110, 197]. The line vectors $\mathbf{k}_1(t)$ and $\mathbf{k}_2(\varphi)$ are vector containing the drift and covariance functions of each kriging profile, and \mathbf{T} and \mathbf{M} are the dual kriging matrices along each interpolating direction (see Appendix A for more details on parametric surface kriging). Numerical calculations of the mean deflection at 100 kPa were carried out for $n = 17$ thickness values $t_i \in [2, 10], 1 \leq i \leq 17$ and $m = 7$ open space ratios $\varphi_j \in [45\%, 60\%], 1 \leq j \leq 7$. A total of $n \times m = 119$ mean deflection data points (t_i, φ_j) are obtained for $1 \leq i \leq 17$ and $1 \leq j \leq 7$, which are stored in a 17×7 matrix \mathbf{D}_{base} . More details on parametric surface interpolation based on dual kriging are given in Appendix A.

The average deflection $\mathbf{D}_f(t, \varphi)$ in millimeter of perforated plates as a function of $\mathbf{D}_{base}(mm)$ writes as follows:

$$\mathbf{D}_f(t, \varphi) = \mathbf{k}_1(t)^\top \cdot \mathbf{T}^{-1} \cdot \mathbf{D}_{base} \cdot M_\varphi^{-1} \cdot \mathbf{k}_2(\varphi) \quad (3.2)$$

where $\mathbf{k}_1(t)$, \mathbf{T} are matrices consisting of functions of perforated plate thickness t in millimeter, M_φ^{-1} and $\mathbf{k}_2(\varphi)$ are matrices consisting of open area of perforated plate φ as shown in Appendix A. Note also that the elastic analysis carried out by finite element approximation is linear with respect to the external load, namely here the uniform compaction pressure $P(kPa)$ applied on perforated plates. Hence, the mean deflection of perforated plates depends linearly on P . Therefore, the compaction pressure P may appear in the deflection model as a linear coefficient as follows:

$$\mathbf{D}_f(t, \varphi, P) = P \cdot \mathbf{k}_1(t)^\top \cdot \mathbf{T}^{-1} \cdot \mathbf{D}_{base} \cdot M_\varphi^{-1} \cdot \mathbf{k}_2(\varphi)/100 \quad (3.3)$$

Thus, after taking into account the mean deformations of the two perforated plates, the corrected average cavity height becomes:

$$H = h_f + 2 \cdot \mathbf{D}_f(t, \varphi, P) \quad (3.4)$$

Finally, the mean deflection of perforated plates gives the mean fiber volume fraction and transverse permeability, respectively:

$$V_f = \frac{n \cdot \rho_A}{H \cdot \rho} \times 100\% \quad (3.5)$$

$$k_z = \frac{Q}{A} \cdot \frac{H\mu}{P_{in} - P_{out}} \quad (3.6)$$

where n is the number of fabric layers, ρ_A the areal density of the fibrous reinforcement (kg/m^2), H the cavity height after correction (m) and ρ the fiber density (kg/m^3). The proposed correction models for V_f and k_z allow characterizing more accurately the transverse permeability. Note that only the central matrix \mathbf{D}_{base} in Eq. (3.3) must be recalculated when the material of perforated plates changes. This model is implemented in Section 5 to illustrate its application to an existing k_z mold.

3.6 Through-thickness flow pattern

In this section, the flow pattern inside the mold cavity is investigated by taking into account the configuration of perforated plates and dimensional issues connected with the specimen. The geometrical models of the mold cavity generated for the stiffness analysis are used to conduct flow analyses in both unsaturated and saturated modes. A way to ensure the generation of quasi one-dimensional flow in the test mold is proposed, together with a quantitative criterion to evaluate the performance of transverse permeability test molds.

3.6.1 Theory

The analytical solution giving the fill time t_{1D} at constant pressure for fully unidirectional porous unsaturated flows writes as follows [34]:

$$t_{1D} = \frac{(1 - V_f) \mu}{2k_z \cdot \Delta P} \cdot h_f^2 \quad (3.7)$$

where V_f denotes the fiber volume fraction and h_f the thickness of the specimen. The liquid is constrained to flow through the open spaces in the perforated plates and through the open spaces in the fibrous reinforcement. The solid part of the plates limits contacts between the specimen and the liquid. This changes the pressure distribution in the sample and modifies the flow paths of liquid particles during the experiment. Therefore, Figure 3.2 shows a non-fully unidirectional flow in the specimen. This changes the actual fill time of the fibrous sample compared to the one-dimensional solution of Eq. (3.7). Hence a new dimensionless number called the “fill coefficient” was introduced as the ratio of the actual impregnation time of the cavity from the holes of the lower perforated plate over the fill time required in a unidirectional impregnation to evaluate quantitatively the effect of perforated plates on the flow pattern.

Since the perforated plates cover the bottom and top of the preform, to fill the specimen, only the open spaces in the lower perforated plate is considered as inlet gates on the bottom

plane of the sample and the holes in the upper perforated plate model vents on the top plane of the specimen. Mold filling simulation carried out with PAM-RTM [198] gives the time t_{sim} needed to fill the preform. Hence the fill coefficient was defined as:

$$F = \frac{t_{sim}}{t_{1D}} \quad (3.8)$$

Ideally speaking, unidirectional filling should be the fastest way to fill a fibrous preform with a surface runner as injection port on the bottom side of the test sample. Thus, the fill coefficient measures the relative mold filling efficiency with respect to a full unidirectional through-thickness impregnation. A fill coefficient greater than 1 indicates a lower efficiency compared to a perfectly unidirectional filling. Note that the efficiency of a transverse permeability test mold can also be affected by the in-plane permeability when a three-dimensional flow front profile is created. For anisotropic fabrics, it is possible to achieve the same efficiency as in the unidirectional filling because the surface layer of the preform act as a flow distribution medium. Locally, there is a skin effect with significant in-plane velocity, then flow becomes unidirectional when the distance to the plate increases (in the core of the preform). Therefore fill coefficient could also be used to measure the deviation of flow from quasi-unidirectional and as an index to measure the accuracy of transverse permeability tests. It facilitates the comparison of flow patterns for different geometrical configurations of perforated plates, and hence allows evaluating the efficiency of a transverse permeability test mold with respect to this issue.

Note that saturated flow simulations are also carried out in Section 4.6 to show that the fill coefficient is also suitable to evaluate saturated flow patterns. It is important because the most common methods to measure k_z are based on one-dimensional saturated flows [24], although unsaturated tests have also been conducted by several investigators [13, 32, 199].

3.6.2 Geometrical models

(a) Geometrical models for unsaturated filling analysis

As shown in Figure 3.5a, the unsaturated filling analysis can be simplified in PAM-RTM as follows: a pressure boundary condition is assigned to the area in contact with the holes of the perforated plates, namely the inlet pressure is set at 100 kPa relative pressure, and the outlet at 0 kPa. The model is discretized using tetrahedral elements, and the fiber volume fraction is set to 50%. The viscosity of the test liquid is considered constant at 0.1 Pa · s. Convergence analysis was conducted before the parametric investigation to ensure the independence of the numerical solutions from the mesh size for the filling and saturated flow simulations.

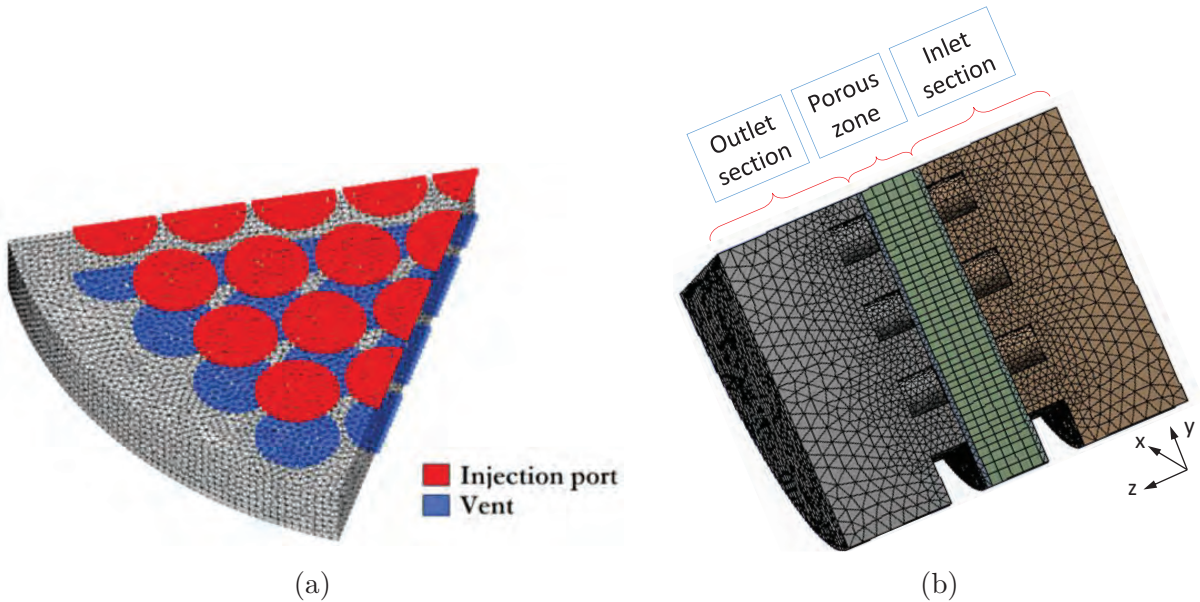


Figure 3.5 Geometrical models and boundary conditions used to conduct filling and saturated flow simulations: (a) boundary conditions (pressure inlet of 100 kPa in red and outlet at 0 Pa in blue) for filling flow simulations with PAM-RTM. (b) Mesh of the geometrical domain considered for the saturated steady state flow simulations including the preform, the two perforated plates, the flow distribution layers under and above the specimen and part of the inlet and outlet mold cavity. The pressure is 100 kPa in the bottom inlet surface and 0 Pa in the upper outlet surface.

(b) Geometrical models for saturated flow analysis

The transverse permeability is usually measured in saturated flow experiments, because of the difficulty of tracking a transverse flow front through thin laminates [13,199]. Therefore, it is critical to ensure that the fill coefficient can also accurately assess saturated flow patterns in the k_z molds. To verify this, steady state laminar flow simulations were also performed with the software ANSYS Fluent [200]. Figure 3.5b shows the 3D geometrical domain for saturated flow simulation. The mesh was refined around the perforations to improve accuracy. It considered not only the specimen (porous domain) like in filling simulations, but also the Hagen Poiseuille flow through cylindrical holes of the perforated plates. The thickness of the preform remains 7mm. The $z = 0\text{mm}$ plane corresponds to the base of the fibrous sample on the inlet side, and the $z = 7\text{mm}$ plane lies on the top of the preform on the outlet side. The same material properties and boundary conditions are specified as in the unsaturated filling simulations. Besides, a no-slip wall boundary condition is specified on the inner circumferential wall surface of the cavity.

3.6.3 Effect of perforations

As the most widely used flow distribution media, perforated plates can affect the fluid exchange between the flows in the preform and in the empty cavity through the hole diameter, the width between holes and the packing pattern. To evaluate the effect of perforations, the open space ratio remains at a similar level for different plate configurations. Unless otherwise specified, hexagonal packing patterns of perforations in the perforated plates were used to achieve a maximum open space for the transverse flow. The parametric investigation conducted is summarized in Table 3.3, in which only the hole spacing and diameter change. The first configuration in Table 3.3 is chosen as a reference case to investigate the effect of width between holes. Various widths are selected by adjusting the distance between neighboring perforations. The thickness of the preform is supposed here to be 7 mm, and the preform is assumed to be isotropic with a principal permeability of $3.0 \times 10^{-12} \text{ m}^2$.

Table 3.3 List of simulation cases considered to study the effect of perforations.

No.	Hole spacing	Hole diameter	No. of holes	Support width	Open space ratio
1	8.0 mm	7.5 mm	127	5 mm	54.97%
2	7.0 mm	6.5 mm	169	5 mm	54.94%
3	6.5 mm	6.0 mm	199	5 mm	55.12%
4	4.5 mm	4.0 mm	439	5 mm	54.05%
5	4.0 mm	3.5 mm	583	5 mm	54.95%

Figure 3.6a plots the fill coefficients obtained for the cases of Table 3.3 as a function of the number of holes. The fill coefficient decreases from 7 to 3 from 127 to 583 perforations. When the hole spacing and diameter decrease, the fill coefficient decreases even if the open space ratio does not change. However, when the number of holes increases nearly five times, the fill coefficient drops only by 55%, but still remains much greater than one. Hence the in-plane flow is not significantly reduced. Note that the fabrication of perforated plates becomes then more difficult and expensive because of the reduced hole size and larger number of holes. In contrast, Figure 3.6b shows that a significant improvement can be obtained by reducing the support width as defined in Figure 3.4a. This is especially true for support widths lower than 4 mm. In this analysis, it was achieved by increasing the inter-hole distance. Note also that the fill coefficient becomes even lower than in the configuration with 583 small holes (see Figure 3.6a).

Most of the perforations encountered in the scientific literature follow a hexagonal packing

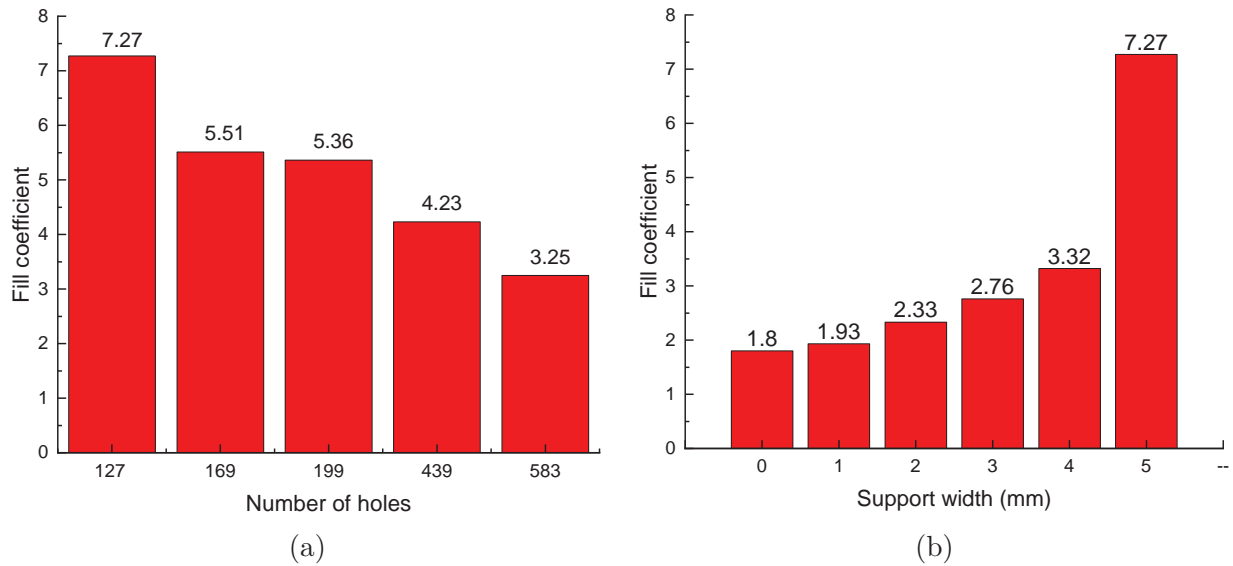


Figure 3.6 Effect of two geometrical parameters on flow patterns for a 7 mm thick preform:
(a) number of perforations for nearly the same open space ratio and reduced hole diameters.
(b) Support width (for simulations based on the configuration of Table 3.1).

pattern. The holes adjacent to the edge of the plate are not evenly distributed due to the limited area and need to reserve a space to hold the fixture (referred to as “support width” hereinafter). This results in more in-plane flow near the edge than in the center, and affects the flow pattern in the cavity. A perforated plate model with evenly distributed perforations near the edge was created as reference in Figure 3.7b. The central hole is located in the center of the plate, and the second round of perforations follow a hexagonal pattern. Starting from the third round, the number of holes doubles for each new round.

Figure 3.7 shows results of filling simulations for a 20 mm thick preforms (instead of 7 mm like in Figure 3.6) and displays the transverse velocity field inside the test cavity. When the preform is filled, the velocity field in the thickness direction appears in Figure 3.7c and Figure 3.7d. Although the structure is asymmetric in Case a, the velocity field only slightly changes. In Case b, the velocity field in all cross-sections is almost the same. In both cases, the sudden change in velocity leading to a non-unidirectional flow mainly occurs near the edge of the cavity, but the affected area is larger in Case a. This shows that perforated plates with uniformly distributed holes near the edge, even with a larger hole diameter, decrease the fill coefficient from 1.58 to 1.31, and hence create a more unidirectional flow through the preform.

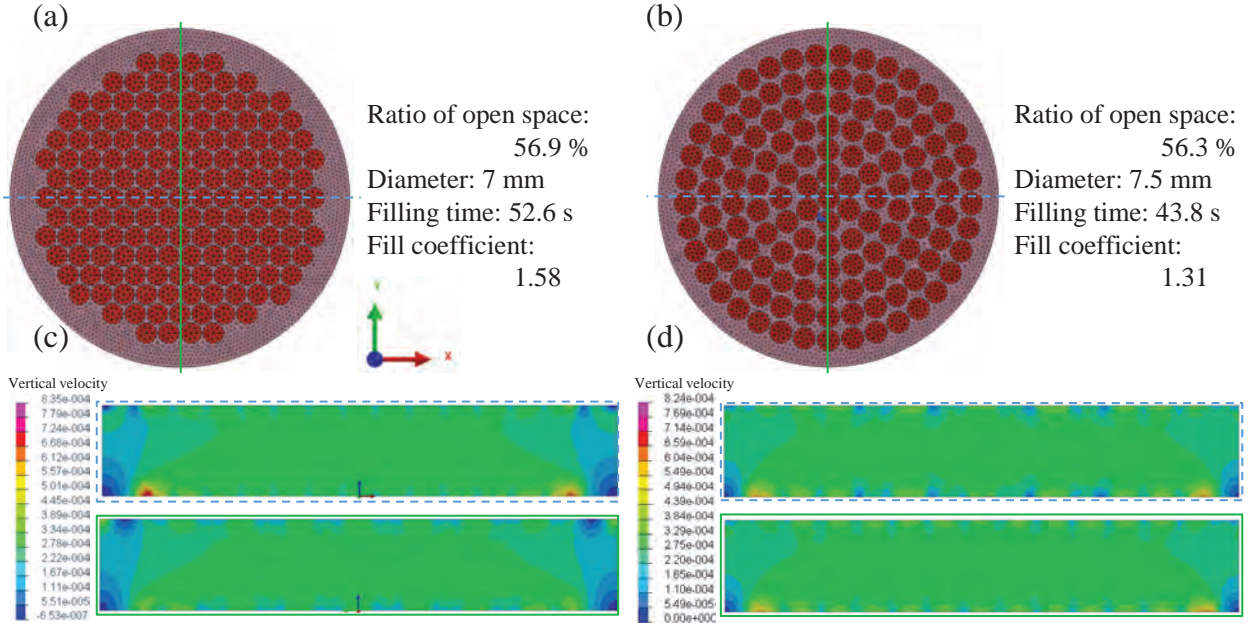


Figure 3.7 Influence of hole packing calculated for a 20 mm thick preform: (a) non-uniform distribution of perforations near the edge of the mold cavity. (b) Uniformly distributed perforations. (c) Vertical transverse velocity fields in the XZ and YZ planes in case A. (d) Vertical transverse velocity fields in the XZ and YZ planes in case B. The vertical velocity decreases near the edges of the mold cavity. The decrease spreads more in case A, which is consistent with the larger fill coefficient obtained (1.58 vs. 1.31 in case B).

3.6.4 Effect of sample and material properties

In one-dimensional transverse permeability measurements, the geometrical dimensions and the flow properties of fibrous samples, namely here their thickness and in-plane permeability, are rarely taken into account in the analysis of transverse flows. For instance, the difference in measured transverse permeability for samples of different thicknesses is often attributed to nesting [62], while the in-plane permeability is generally ignored [185]. However, in-plane flows may occur due to the presence of perforated plates as shown in Figure 3.7c. For that purpose, perforated plates with holes of diameter 7.5 mm and a hole spacing of 8.5 mm as in the existing k_z mold of Section 5 were chosen to carry out numerical simulations. The open space ratio is 52.4% in this analysis.

(a) Preform thickness

Figure 3.8a shows a top view of the geometrical model and plots the fill coefficient as a function of sample thickness. The flow domain in the preform was discretized with tetrahedral elements, and the vent was set at a relative pressure of 0 kPa (with respect to the atmospheric

pressure). The principal permeability of the preform is isotropic with $k_x = k_y = k_z = 3.0 \times 10^{-12} \text{ m}^2$. The baseline indicates a fill coefficient $F = 1$. As shown in this figure, when the thickness is less than 15 mm, F decreases significantly when thickness grows. If thickness continues to increase, the decrease of F slows down, but does not stabilize until the preform thickness reaches 50 mm. With the same configuration of perforated plates and boundary conditions, the velocity field is displayed in Figure 3.8b at the specified cross-section for preform thicknesses of 4 mm, 20 mm, and 70 mm respectively. This shows that the velocity inside the preform becomes more uniform for a larger specimen thickness. Hence, increasing the preform thickness to improve the one-dimensionality of the flow decreases the fill coefficient.

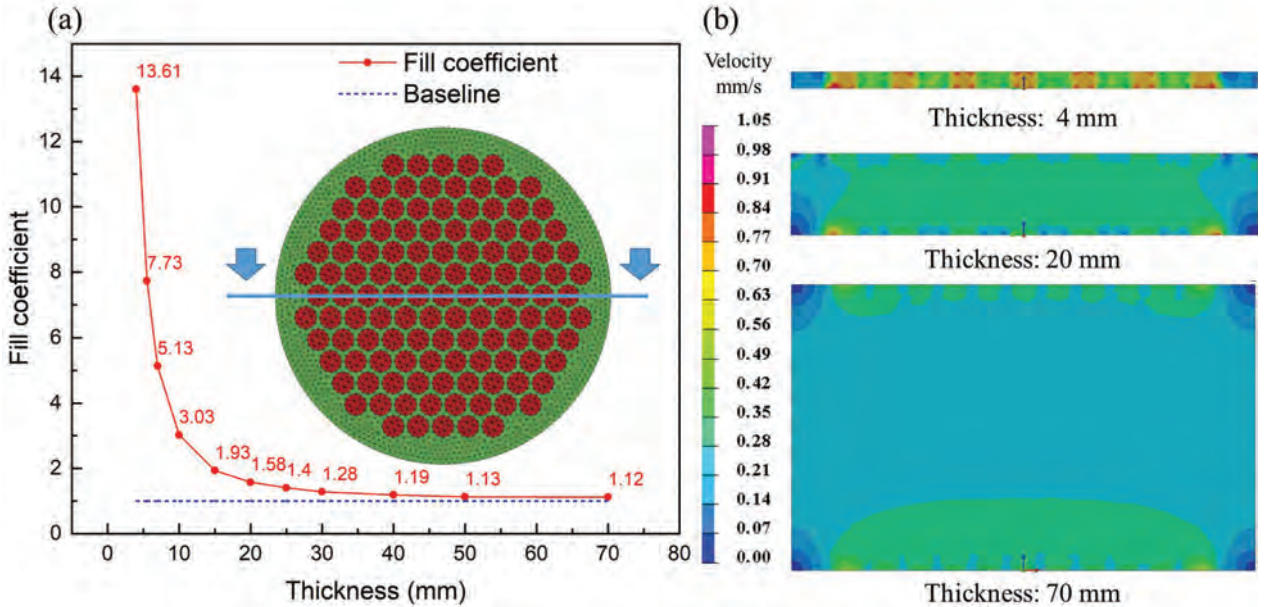


Figure 3.8 (a) Results of numerical simulations for the existing tool to investigate the relationship between the fill coefficients and preform thickness. As expected, larger preform thicknesses give smaller fill coefficients. (b) Transverse velocity in the cross-section shown by arrows in (a). In each case considered, the velocity is divided equally into 15 color levels from the minimum to the maximum values. As thickness increases, the zones of larger transverse flow velocity become relatively smaller with respect to the whole flow domain.

Moreover, since composite parts are mostly thin shell structures, it is worth keeping test samples as close as possible to the thickness of parts fabricated by resin injection. Therefore, using thick preforms is not necessarily recommended and the effect of thickness itself on transverse permeability, neglecting nesting, is worth to be investigated.

(b) Preform in-plane permeability

Fibrous reinforcements may possess an isotropic or anisotropic flow behavior. The in-plane flow may play a significant role when the actual flow deviates from a unidirectional Darcy flow pattern since in-plane permeability is usually one or two orders of magnitude higher than the transverse permeability. The principal permeability values of the preforms analyzed here are summarized in Table 3.4. The thickness of specimens always remains 7.0 mm.

Table 3.4 Influence of permeability on the fill coefficient.

$k_x = k_y$	k_z	Anisotropy	1D fill time	Actual fill time	Fill coefficient
$3.0 \times 10^{-11} \text{ m}^2$	$3.0 \times 10^{-11} \text{ m}^2$	1	0.41 s	2.01 s	5.12
$3.0 \times 10^{-12} \text{ m}^2$	$3.0 \times 10^{-12} \text{ m}^2$	1	4.08 s	20.8 s	5.10
$3.0 \times 10^{-13} \text{ m}^2$	$3.0 \times 10^{-13} \text{ m}^2$	1		208 s	5.09
$3.0 \times 10^{-12} \text{ m}^2$	$3.0 \times 10^{-13} \text{ m}^2$	10		63 s	1.54
$3.0 \times 10^{-11} \text{ m}^2$	$3.0 \times 10^{-13} \text{ m}^2$	100		47.4 s	1.16
$3.0 \times 10^{-10} \text{ m}^2$	$3.0 \times 10^{-13} \text{ m}^2$	1000		44.0 s	1.08

Table 3.4 shows that the fill coefficient is greater or approximately equal to one, but never less than one, even if the in-plane permeability is three orders of magnitude larger than k_z . Therefore, for an anisotropic preform with a larger in-plane than transverse permeability, the in-plane flow can compensate for delays in fill times due to longer flow paths. Hence, when the fill coefficient nearly equals one for anisotropic preforms with larger in-plane than transverse permeability, this does not necessarily mean that the transverse flow is unidirectional. It only means that the measured transverse permeability is close to the value that would be measured in a perfectly unidirectional injection.

3.6.5 Flow distribution layer

The solid part of perforated plates is the main cause of the deviation from a quasi-unidirectional flow on the Darcy scale because it blocks the liquid flow and creates more complex flow patterns. Nevertheless, a rigid perforated plate is essential to precisely control the fiber volume fraction of fibrous samples since it is not rigid enough to be free standing. It is possible to use a Flow Distribution Layer (FDL) between the preform and the perforated plates to facilitate the spread of the liquid flow on the preform surface [15, 24].

To verify this hypothesis, a geometrical model with FDLs was created as illustrated in Figure 3.9. In addition to the yellow part representing the preform, two layers of elements (in pink

and blue) are added to model FDLs of thickness 0.5 mm. The same boundary conditions are applied as in the previous analysis. The principal permeability of the isotropic preform is assumed to be $3.0 \times 10^{-12} \text{ m}^2$ with a thickness of 4 mm. Figure 3.9 shows that the fill coefficient decreases significantly when the FDL permeability increases. The flow pattern becomes very close to the ideal unidirectional case with a fill coefficient close to 1 when the FDL permeability is three orders of magnitude larger than that of the fabric.

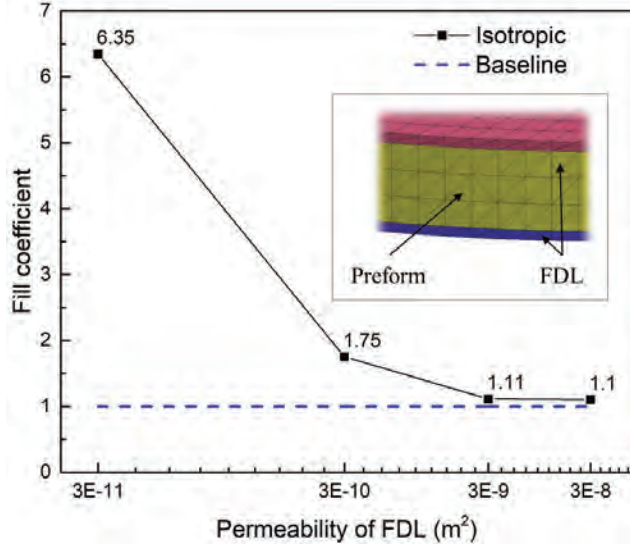


Figure 3.9 Fill coefficient as a function of an isotropic flow distribution layers (FDL) permeability. The principal permeability of the 4-millimeter-thick isotropic preform is $3.0 \times 10^{-12} \text{ m}^2$

Note that a new problem may be introduced by the FDL because of possible nesting between the fabric and the FDLs. Huang et al. [24] developed an iterative algorithm to estimate the nesting depth between FDLs and fabric, Δh , from 3D images sequence generated by micro-CT scans. This approach was adopted in the present study to account for the nesting depth between FDLs and fabric when calculating the height H of the specimen as below:

$$H = h_f + 2 \cdot \mathbf{D}_f(t, \varphi, P) + \Delta h \quad (3.9)$$

Using H in Eq. (3.5) and Eq. (3.6) allows correcting the fiber volume fraction and the corresponding transverse permeability.

3.6.6 Saturated flow analysis

The FDL layers are modeled separately as porous zones under and above the 7 mm thick specimen. The same perforated plate configuration is used as in Section 4.4. In the porous zones, namely the preform and the FDLs, a source term S_i for the i -th (x , y , or z) momentum equation is added to Navier-Stokes equation [200]:

$$S_i = - \left(\sum_{j=1}^3 \mathbf{D}_{ij} \mu v_j + \sum_{j=1}^3 C_{ij} \frac{1}{2} \rho |v| v_j \right) \quad (3.10)$$

where $|v|$ denotes the magnitude of the liquid velocity, \mathbf{D}_{ij} and C_{ij} are prescribed 3×3 matrices representing the viscous and inertial resistances, respectively. In the case of a homogeneous preform with FDLs, we get:

$$S_i = - \left(\frac{\mu}{K} v_i + C_2 \frac{1}{2} \rho |v| v_j \right) \quad (3.11)$$

where K and C_2 are the permeability and inertial resistance coefficients, respectively. The inertial resistance coefficient C_2 may be calculated by the following formula [201]:

$$C_2 = 2 \frac{C_f}{\sqrt{K}} \quad (3.12)$$

where the principal permeability K of the isotropic preform is $3.0 \times 10^{-12} \text{ m}^2$ and the dimensionless drag constant $C_f = 0.55$ [201]. In our case, the liquid velocity not being high (Reynolds number less than 1), the inertial resistance - the second term on the right hand side of Eq. (3.11) can be neglected compared to the viscous resistance (the first term on the right hand side of Eq. (3.11)).

Two cases without and with FDLs were simulated in Figure 3.10 and give fill coefficients of 5.1 and 1.1, respectively. The lower fill coefficient is obtained by adding FDLs of permeability $K_{FDL} = 3.0 \times 10^{-8} \text{ m}^2$ above and below the preform. Figure 3.10 displays the transverse velocity component w in the thickness direction along the z -axis by varying the transparency and colour as a function of velocity in the entire domain. When $F = 5.1$, the velocity in Figure 3.10c exhibits periodic values reflecting the periodic hole distribution. The velocity decreases gradually from the middle of the cavity to the edge. In contrast, when $F = 1.1$ as shown in Figure 3.10b, the distribution of the transverse velocity component w between the perforated plates exhibits a good uniformity except in the FDL layer, where it has a larger magnitude, hence facilitating the liquid flow through the bottom and top surfaces of

the specimen.

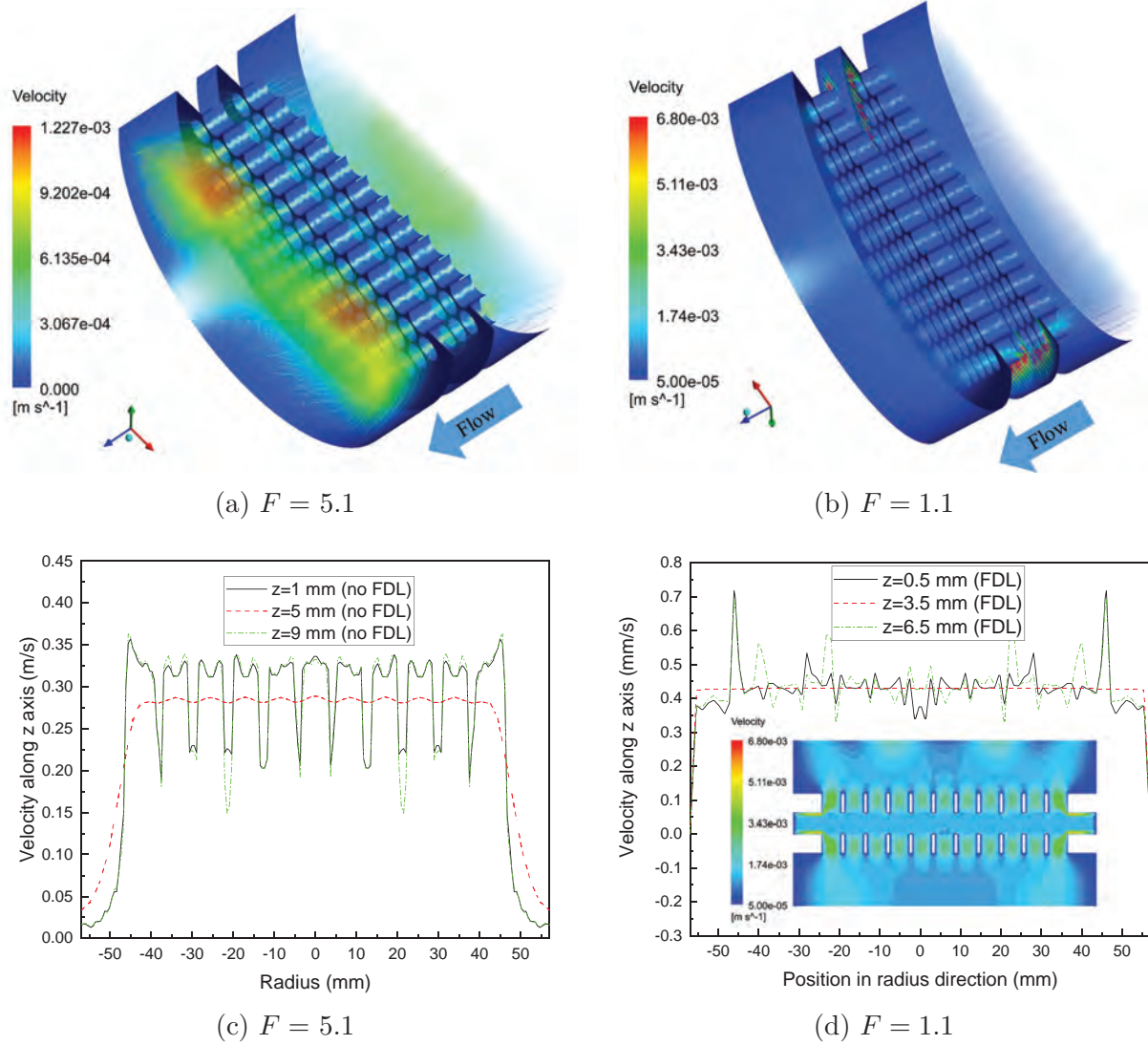


Figure 3.10 Transverse velocity distribution inside the mold cavity: (a) 3D view obtained by volume rendering for $F = 5.1$. (b) 3D view obtained by volume rendering for $F = 1.1$. (c) Transverse velocity component w along the z -axis for $F = 5.1$. (d) Transverse velocity component w along the z -axis and cross-sectional view of the flow pattern for $F = 1.1$.

The velocity component w along the z axis is extracted at $z = 0.5$ mm, 3.5 mm and 6.5 mm in both cases and shown in Figure 3.10c and Figure 3.10d. In these figures, the abscissa denotes the radius of the concentric circle where the sampling point is located. When $F = 5.1$, a very small velocity develops near the wall because of the impermeable edge of the perforated plate. The flow in the cross-sections $z = 0.5$ mm and $z = 6.5$ mm gets its maximum velocity in alignment with the center of the perforations, which is approximately equal to two times the

minimum axial velocity in the same cross-section. Even in the mid-surface of the specimen ($z = 3.5$ mm), the velocity component still fluctuates with the position of perforations, but with much less intensity.

In the case of FDLs, the velocity fluctuations in the three cross-sections are significantly reduced, and the velocity on the wall is only slightly lower than in the middle of the specimen (see Figure 3.10d). The velocity remains constant in the mid-surface of the preform ($z = 3.5$ mm). The cross-section view of the flow pattern in the mold cavity in Figure 3.10d shows that the liquid passes through the perforated plate and then quickly spreads out on the surface of the preform, thus creating a quasi-unidirectional flow in the specimen.

It is also worth noting that the flow rate is lower in the case of a larger fill coefficient. At the cross-sections where $z = 0.5$ mm, 3.5 mm and 6.5 mm, the average axial Darcy velocity is 0.35 mm/s, 0.34 mm/s and 0.37 mm/s when $F = 5.1$ compared to 0.42 mm/s, 0.42 mm/s and 0.43 mm/s when $F = 1.1$, respectively. The latter shows a good agreement with the analytical solution at 0.428 mm/s, obtained by Darcy's law, while a decrease of approximately 20% is observed in the mass flow rate for the former. Therefore, the measured transverse permeability obtained in that case is underestimated by 20%. This confirms the validity of the fill coefficient for transverse saturated permeability tests. It also confirms that the factors affecting the fill coefficient influence the accuracy of transverse permeability measurements as well.

3.6.7 Pressure drop in empty mold

The pressure drop in the k_z mold caused by an empty mold cavity with perforated plates was investigated by carrying out saturated numerical simulations. The same mold geometry as the one in Section 4.6 was tested. As a function of flow rate, the pressure drop in the empty mold was 21.5 Pa, 43.1 Pa, 64.6 Pa and 86.1 Pa for fluid velocities of 2 mm/s, 4 mm/s, 6 mm/s and 8 mm/s. To achieve the same injection velocity, a pressure gradient in the order of $10^5 \sim 10^6$ Pa/mm should be established in a typical textile reinforcements. The ratio of the pressure drop in the empty mold to that in typical textile reinforcements converges to a constant and keeps lower than 0.05%. Therefore, the pressure drop in an empty mold can generally be neglected.

3.7 Experimental verification

As introduced in Section 4, both saturated and unsaturated simulations show that longer flow paths than the specimen thickness are created because of the perforated plates. Therefore,

the measured transverse permeability is significantly underestimated and can be evaluated by the proposed dimensionless number. The greater is the fill coefficient compared to 1, the more is the measured transverse permeability underestimated. Two sets of experiments with and without FDLs are conducted to verify this result. Using the average displacement of the perforated plates, the correction model of fiber volume fraction proposed in Section 3 is also applied here to demonstrate its use in one practical case. Note that in this case the average deformation of the test device is expected to be less than 0.5% of the preform thickness, because the transverse mold considered here was designed with the geometric parameters detailed in Section 3.

A S-glass satin weave fabric (SF) of areal density 220 g/m² from Nanjing fiberglass research and design institute is tested with PMX-200-100cs silicone oil, a substitute fluid specified in Benchmark III [13]. The fabric contains 18 tows/cm in the warp direction and 14 tows/cm in the weft direction. Each circular specimen has a diameter 114 mm and consists of 17 layers of SF fabric. The sample area is used as effective flow area to calculate the transverse permeability in all tests. Fiber volume fractions are adjusted by different combinations of calibrated shims. A rigid metal screen was used as FDL to facilitate the flow distribution and reduce the fill coefficient in one group of the test. It is woven with metal wires of diameter 0.25 mm and regarded as non-deformable. There are 40 meshes per inch, and the size of each mesh is 0.385 × 0.385 mm. In the experiments with FDLs, one layer of FDL is placed below and one above the fibrous sample. Since the FDL mesh is miniature, nesting between the FDL and the fabric can be neglected ($\Delta h = 0$ in Eq. (3.9)).

The experiments use an existing tool made of 304 stainless steel shown in Figure 3.1. The injection pressure of 0.1 MPa is provided by a pressure pot and stabilized by a regulator. Commercial pressure sensors MIK-P300 with a specified accuracy of $+/- 0.25\%$ for a range of pressure values from 0 to 0.6 MPa (Hangzhou Meacon Automation Technology, China) are installed near the outlet and inlet to monitor the liquid pressure in the cavity. A digital balance measuring mass accurately (± 0.01 g) up to 3000 g (AH-A+r, Shenzhen Anheng Electronic Weighing Apparatus Co., Ltd, China) is placed under the outlet to record the mass flow rate. The perforated plate is also made of 304 stainless steel with holes of diameter 7.5 mm, hole spacing of 8.5 mm and 52.4% open space ratio. The plate thickness is 7 mm. The upper and lower perforated plates are identical. The geometrical model of perforated plates given in Sections 5.4, 5.5 and 5.6 was devised from the geometry of this existing tool to facilitate the comparison of simulations with experiments.

Each series of tests was repeated five times. The average values are plotted in Figure 3.11 with the upper and lower bounds of errors bar representing the maximum and minimum

values the five replicates. The average fiber volume fractions are 48.3%, 50.0%, 52.0%, and 53.7%, which correspond to sample thicknesses of 3.05 mm, 2.93 mm, 2.82 mm, and 2.72 mm, respectively. Figure 3.11 shows that the measured transverse permeability with FDLs is between 20% to 30% larger than that without FDLs. This is consistent with the information inferred from the saturated flow analysis of Section 4.6. It also confirms that it is possible to disperse the liquid on the sample surface with FDLs, thus creating a quasi-unidirectional Darcy flow.

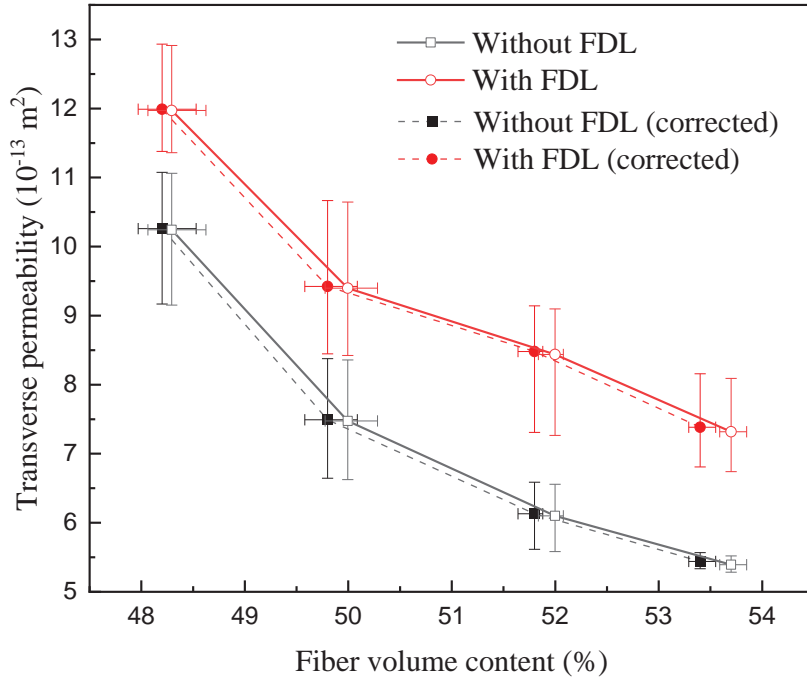


Figure 3.11 Typical transverse permeability experimental results obtained with a 1D test device compared with measurements with flow distribution layers (FDL) after correcting for perforated plate deformation.

According to the compressibility test for the S-glass satin weave fabric, achieving the above mentioned fiber volume fractions requires an effective stress acting on both perforated plates of 231 kPa, 315 kPa, 435 kPa, and 611 kPa. Therefore, the deflection of each perforated plate can be calculated by Eq. (3.3) with the known structural parameters for the different pressure values. The corrected fiber volume fractions given by Eq. (3.5) are 48.2%, 49.8%, 51.8%, and 53.4%, which becomes 0.1%, 0.2%, 0.2%, and 0.3% smaller, respectively, than the nominal values. As expected, the correction on the fiber volume fraction for the mold considered here is rather small, especially because it was designed following the approach detailed in Section 3. This is not necessarily the case for all transverse permeability test molds.

Figure 3.11 shows in dash line the relationship between the fiber volume fraction and transverse permeability after correcting for the cavity thickness by Eq. (3.6). The corrected transverse permeability increases slightly. For perforated plates made of honeycomb or aluminum, the corrections on fiber volume fraction and permeability would be more critical.

Although the correction for deformation could be neglected for this test mold, the difference in Figure 3.11 between the experimental transverse permeability measured with and without FDLs is significant. The transverse permeability with FDL is 16.9%, 25.8%, 38.3% and 35.7% higher than these without FDL for fiber volume fractions of 48.2%, 49.8%, 51.8% and 53.4%, respectively. This experimental observation is consistent with the results of the saturated flow simulations carried out in Section 4.6.

3.8 Conclusion

By limiting the investigation to Darcy flows, creating a quasi-unidirectional through-thickness flow in a fibrous preform is required to perform accurate transverse permeability measurements. As investigated in this article, the measurement accuracy is closely connected with the geometric structure of the test device. A new approach is proposed to assess the performance of unidirectional test devices while optimizing the design of perforated plates to minimize mold deformation. By providing general guidelines, this work can improve the accuracy of transverse permeability measurements.

The optimal configuration of perforated plates takes into account the deformation of the cavity under the mold clamping pressure and/or the injection pressure. The average deformation of the specimen was modelled as a function of the perforated plate thickness, the open space ratio and the compaction pressure. As illustrated in the experimental validation section, it can also be used to correct the cavity height in existing molds.

A numerical parametric study was conducted to assess the performance of unidirectional test devices. Mold filling simulations were carried out with PAM-RTM, and saturated flow simulations with Fluent. This showed that significant in-plane flows occur in textile reinforcements. As verified experimentally, this can underestimate transverse permeability by up to 30 % in the cases analyzed. Thus, a new dimensionless number called the “fill coefficient” was proposed to measure the relative filling efficiency of the mold compared to a full unidirectional through-thickness impregnation and the accuracy of transverse permeability. Applying this approach for different device configurations, a fill coefficient greater than 1 indicates a lower efficiency than the unidirectional case. Besides, saturated flow simulations show that the fill coefficient is also suited to evaluate saturated flow patterns. This is important since

the most common unidirectional methods are based on saturated flows. The results show that reducing the hole diameter, increasing the open space ratio, using a more uniform hole packing in the perforated plates and secondary Flow Distribution Layers (FDL) are possible corrective actions to improve the performance of the test device to create quasi-unidirectional flows. Among them, as verified by experiments, FDLs turn out to be the simplest and most effective solution. However, this requires ensuring that the permeability of the FDL is at least three orders of magnitude higher than that of the specimen. In addition, because of the in-plane flow caused by perforated plates, note that the thickness of the specimen and the in-plane permeability of the fibrous reinforcement may also affect the transverse permeability measurement.

Although with FDLs, it is possible to remain consistent with Darcy's law and measure the transverse permeability in quasi-unidirectional flow conditions, the selection of an appropriate FDL could be an interesting topic in future investigations. It need not only be metallic. Rigid porous foams (ceramic or else) could provide interesting alternatives to prevent nesting between the FDLs and the textile specimens. However, Graupner and Drechsler [195] reported that the same nesting problem also exists when perforated plates are used, which still remains an open problem.

Acknowledgments

This research was partially funded by the Department of *Mechanical Engineering of Polytechnique Montréal* and by the *Natural Sciences & Engineering Research Council of Canada* (NSERC) (Discovery Grant). Authors also gratefully acknowledge the financial support of the composite laboratory by the *Research Center for High Performance Polymer and Composite Systems* (CREPEC), the “*Fonds de recherche du Québec - Nature et technologies*” (FRQNT) and the *Department of Mechanical Engineering of Polytechnique Montreal*. Authors would like to express their sincere thanks to Christian-Charles Martel, technical assistant at Polytechnique Montreal, for his high quality support in the laboratory. This research was also partially funded at Wuhan University of Technology by the *Fundamental Research Funds for Central Universities* (2019-JL-003). The help of Hao Zhang, a master degree student at Wuhan University of Technology, is highly appreciated for the experiments.

Appendix A - Model of plate deformation interpolated by parametric surface kriging

The deflection data obtained from the stiffness analysis at 100 kPa shown in Figure 3.4b are used to build a parametric surface interpolation model of the cavity deformation by parametric surface kriging [110, 197]. Deflection calculations were carried out for $n = 17$ thickness values $t_i \in [2, 10], 1 \leq i \leq 17$ and $m = 7$ open space ratios $\varphi_j \in [45\%, 60\%], 1 \leq j \leq 7$. A total of $n \times m = 119$ data points (t_i, φ_j) are obtained for $1 \leq i \leq 17$ and $1 \leq j \leq 7$. In kriging, a general correlation model between data points is constructed by assuming that the statistical correlation between observations (here the three parametric coordinates of surface points) depends only on their Euclidean distance h in the subspace of parameters $(t, \varphi) \in [2, 10] \times [45\%, 60\%]$, which is called the intrinsic hypothesis in kriging.

As illustrated in Figure 3.12, the thickness t of the perforated plate and the open space ratio φ are used as parameters along each interpolation profile so that the kriging interpolation can be directly expressed as a function of these two parameters. Two different correlation functions (also called “generalized covariances” in kriging) $K_1(h)$ and $K_2(h)$ are used here for each variable t and φ respectively:

$$\begin{cases} K_1(h) = |h|^3 & \text{cubic covariance} \\ K_2(h) = |h| & \text{linear covariance} \end{cases}$$

The kriged interpolation proposed as deflection model of the perforated plates depends on the plate thickness and open space ratio φ as follows:

$$\mathbf{D}_f(t, \varphi) = \mathbf{k}_1(t)^\top \cdot \mathbf{T}^{-1} \cdot \mathbf{D}_{\text{base}} \cdot \mathbf{M}^{-1} \cdot \mathbf{k}_2(\varphi) \quad (3.13)$$

where \mathbf{T} and \mathbf{M} are the dual kriging matrices along profiles 1 and 2, respectively:

$$\mathbf{T} = \begin{bmatrix} & 1 & t_1 & t_1^2 \\ |t_i - t_j|^3 & : & : & : \\ & 1 & t_n & t_n^2 \\ 1 & \dots & 1 & 0 & 0 & 0 \\ t_1 & \dots & t_n & 0 & 0 & 0 \\ t_1^2 & \dots & t_n^2 & 0 & 0 & 0 \end{bmatrix} \quad \mathbf{M} = \begin{bmatrix} & 1 & \varphi_1 \\ |\varphi_i - \varphi_j| & : & : \\ & 1 & \varphi_m \\ 1 & \dots & 1 & 0 & 0 \\ \varphi_1 & \dots & \varphi_m & 0 & 0 \end{bmatrix}$$

and the vectors of drift and covariance $\mathbf{k}_1(t)$ and $\mathbf{k}_2(\varphi)$ are defined as follows along each kriging profile:

$$\mathbf{k}_1(t) = [|t - t_1|^3 \quad \cdots \quad |t - t_n|^3 \quad 1 \quad t \quad t^2]^\top \quad (3.14)$$

$$\mathbf{k}_2(\varphi) = [|\varphi - \varphi_1| \quad \cdots \quad |\varphi - \varphi_m| \quad 1 \quad \varphi]^\top \quad (3.15)$$

The matrix \mathbf{D}_{base} contains the deflection values at the positions (t_i, φ_j) for the 119 simulations performed at a given uniform compaction pressure of 100 kPa. The matrices \mathbf{T} and \mathbf{M} do not depend on the unknown deflection, but only on the finite number of parameter values selected as thickness and open space ratio to conduct the numerical simulations.

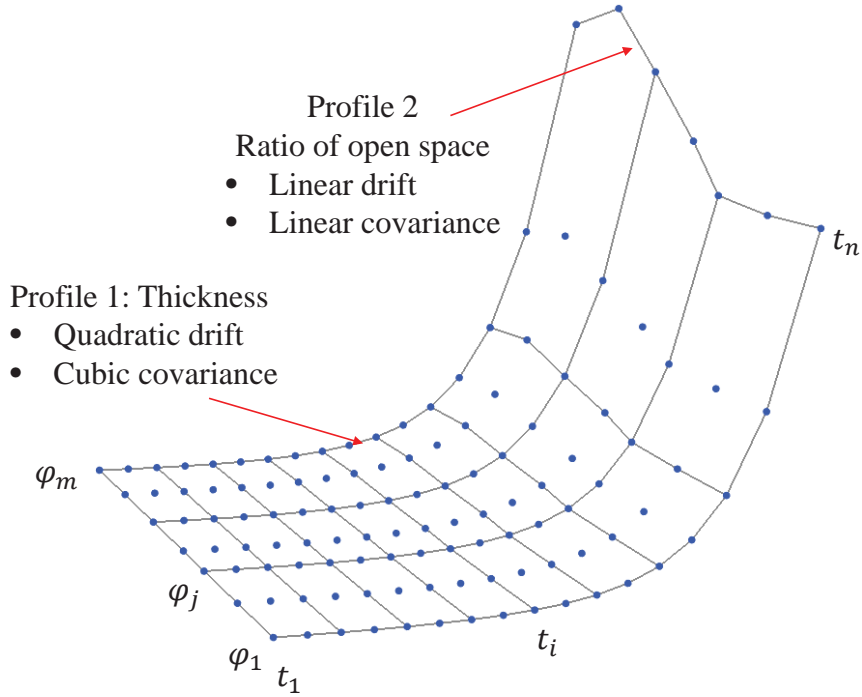


Figure 3.12 Kriging profiles for parametric surface kriging of the deflection field under a 100 kPa load.

CHAPTER 4 ARTICLE 2: PERFORMANCE EVALUATION OF UNIDIRECTIONAL MOLDS USED FOR MEASURING SATURATED TRANSVERSE PERMEABILITY OF ENGINEERING TEXTILES

Bin Yang, Yixun Sun, François Trochu,
Cédric Béguin, Jihui Wang, Philippe Causse

Published in *Composites Part A: Applied Science and Manufacturing* on 03/09/2023

4.1 Chapter overview

This chapter and Chapter 3 together addressed the first issue summarized in Chapter 1: accurately quantifying the transverse permeability of textile reinforcements. Chapter 3 examines the factors that influence testing from the perspective of device design, while this chapter focuses on evaluating the performance of different testing devices. The goal is to reduce the impact of the device structure on the test and to improve the consistency of the results obtained from various testing setups. The proposed procedure for characterizing intrinsic transverse permeability can serve as a basis for numerically predicting permeability using the high-fidelity DMT model developed in Chapters 5 and 6.

4.2 Abstract

Transverse permeability measurement of engineering textiles by state-of-the-art approaches revealed considerable discrepancies between different test devices. The absence of performance analysis protocols makes quantifying error sources challenging. This work addresses this issue by providing approaches for evaluating performance of unidirectional test devices and obtaining transverse permeability from conventional saturated tests. Firstly, experiments are presented to illustrate how flow distribution plates affect flow capacity and lead to underestimation of permeability. To quantify this effect and describe device performance, a dimensionless descriptor, discharge coefficient, is introduced. The latter appears to depend on mold geometry and sample thickness and anisotropy. An iterative framework is then established to obtain intrinsic transverse permeability through simulations or using the descriptor. Two molds were investigated with actual textiles. The first underestimated permeability by up to 51%, whereas the second by 36%, resulting in inconsistency. Comparatively, the proposed approach significantly improved measurement accuracy and consistency

for both molds.

Keywords: Engineering textiles; Transverse permeability; Mold performance; Iterative framework;

4.3 Introduction

In sectors such as automotive, low-cost, high-volume production is key for textile reinforced thermoset and thermoplastic composites to find practical applications, but achieving defect-free fabrication is technologically challenging. Transverse impregnation plays a key role in efficiently manufacturing composites by modern *Liquid Composite Molding* (LCM) techniques because it provides a much shorter flow path than in-plane directions [202,203]. Hence, it is of high practical significance to determine the capability of textile reinforcements in establishing through-thickness flow. This is quantified by transverse permeability according to Darcy's law [12]:

$$\vec{u} = -\frac{\mathbf{K}}{\mu\varphi} \cdot \vec{\nabla}p \quad (4.1)$$

where \mathbf{K} is the permeability tensor (m^2) depending on fabric architecture and fiber volume fraction, \vec{u} is the physical velocity of the test fluid (also known as intrinsic average velocity [204], m/s), φ is the porosity of specimen, μ is the dynamic viscosity of fluid in $\text{Pa} \cdot \text{s}$ and p fluid pressure in Pa. A survey conducted by the National Physical Laboratory in 2016 confirmed the interest in standardizing the transverse permeability measurement [205].

Methods developed to determine the transverse permeability of engineering textiles fall primarily into two categories. The first category, referred to as unidirectional method or 1D method, involves establishing a quasi-unidirectional through-thickness flow across a fibrous preform sandwiched between two rigid flow distribution plates (e.g., perforated plate [24, 206–208], aluminum honeycomb [185] and porous media [182]). The transverse permeability can be determined knowing the pressure gradient and liquid flow rate. Typically, the test mold is cylindrical (see Figure 4.1) [14, 189, 206, 207]. Few investigations used square molds [183], or special devices to continuously alter the compaction level of textile samples [178, 209]. A number of devices also integrated sample thickness [13, 207] and textile layer position [208] tracking systems to evaluate the effect of hydrodynamic compaction [14] induced by injection pressure of the test liquid.

The second category includes various 3D methods that relate the principal permeability with

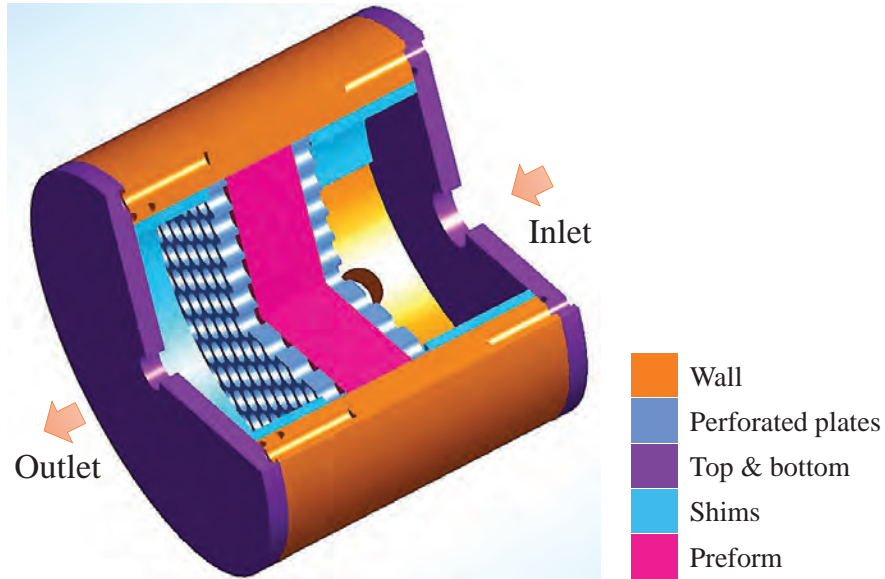


Figure 4.1 Schematic diagram of a typical unidirectional transverse permeability test device.

the flow front position of a 3D transient flow through a textile specimen [52, 53, 210, 211]. The permeability tensor can be obtained in this case either analytically by solving governing equations [54, 210] or numerically by matching the actual flow front on a case-by-case basis [61, 211]. Due to the complexity in flow front tracking and data analysis, 22 out of the 28 tests reported by 26 participants in an international benchmarking project (hereafter referred to as Benchmark III) [13] were obtained by the unidirectional approach with saturated flow conditions.

Transverse permeability measurement remains challenging, as evidenced by results of Benchmark III: experimental results obtained with the same textiles showed differences of about two orders of magnitude. Even after excluding the possible outliers, the maximum value was still roughly four times larger than the minimum. In spite of this, the single-factor analysis failed to identify any significant error sources [13]. The challenges are primarily caused by the following two aspects:

One is connected with the test mold, data analysis, and operational guidelines. Among them, a fully calibrated test mold forms the basis for a more extensive error source analysis. Research [15, 206] demonstrated that flow distribution plates in 1D molds may lead to permeability underestimation since they alter flow path and reduce mass transfer efficiency. Neither experimental evidence of the underestimation nor a method for 1D mold calibration has been published to date. This makes it difficult to quantify the efficiency of test molds.

The other is related to the material. The inherent variability of materials, partly caused

by manual handling, dual-scale structure [212] and layer nesting [62, 213] are well-known factors that contribute to the inconsistency between measurements. Besides, the deformable nature of engineering textiles makes rigid sample holders necessary to maintain fiber volume fraction. As a result, in-plane flow is introduced. The specimen permeability anisotropy and thickness may play a role in this case [206]. Furthermore, microstructure variations may also appear due to flow-induced compaction [14, 207, 208].

Therefore, it is imperative to determine the efficiency of a 1D test mold for mass transfer to improve measurement accuracy. It is usually related to the cross-sectional area of test molds or the open space of flow distribution plates. For instance, Merhi et al. [185] described a transverse permeability test in which the fiber bed (140 mm in diameter) was sandwiched between two distribution plates of 100 mm in diameter. For permeability calculations, the area of the plates, rather than the sample area, was used as an estimation of the limited flow transfer capability. Similar approximation was also adopted by Huang et al. [24], Swery et al. [177], and Studer et al [193]. A rigorous theoretical analysis is, however, required for accurate assessment. Furthermore, the flow exchange capability may also vary depending on the specimen, as will be demonstrated in this study.

The current work aims to improve the accuracy and reproducibility of the conventional 1D method by quantifying and correcting the effect of test devices on the measured transverse permeability. The paper is organized as follows: experimental evidence is first presented in Section 4.4 to illustrate the issues associated with conventional 1D test methods. A dimensionless number, discharge coefficient, is introduced as a performance descriptor to assess mold efficiency. Section 4.5 presents a numerical procedure for building the characteristic performance map of a test mold. In Section 4.6, we propose a method for determining intrinsic permeability from conventional 1D measurements for isotropic materials based on the performance descriptor. Section 4.7 extends the method to anisotropic materials and validation experiments are conducted with a fibrous textile. Finally, the approach is applied to investigate the discrepancy in permeability tested by two different unidirectional molds in Section 4.8.

4.4 Evidence for permeability underestimation of the conventional 1D method

4.4.1 Equipment and method

Permeability tests were conducted with an existing unidirectional testing device (see Figure 4.2a) that was previously used for Benchmark III. The specimen was held between a pair of 6.5-millimeter-thick metallic flow distribution plates. As shown in Figure 4.2b, the perfora-

tions in the plates are arranged in a hexagonal pattern and are not present near the edges of the plate. This leads to an open space ratio (γ_p) of 35.1%. The testing fluid enters the mold from the bottom inlet at a controlled flow rate and leaves from the top at atmospheric pressure. Injection pressure is monitored by sensors on the bottom of the mold. The testing fluid was XIAMETER® PMX-200 100cst silicone oil (density 964 kg/m³). Its viscosity μ (Pa · s) was determined using Eq. (4.2) obtained by fitting experimental results against temperature T :

$$\mu = 0.001e^{6.061}T^{-0.473}, 21^\circ\text{C} < T(\text{°C}) < 26^\circ\text{C} \quad (4.2)$$

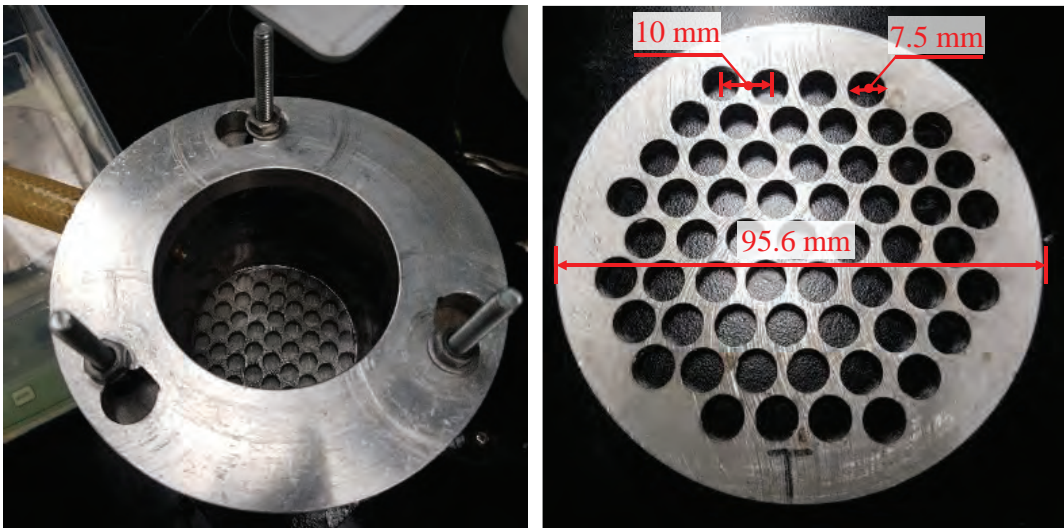


Figure 4.2 Transverse permeability test mold at Polytechnique Montréal (a) and its perforated plate of 6.5 mm in thickness (b).

The apparent transverse permeability k_z^a was computed according to Darcy's law from the measured pressure drop ΔP (Pa) and liquid volume flow rate Q (m³/s):

$$k_z^a = \frac{Q}{A} \cdot \frac{h\mu}{\Delta P} \quad (4.3)$$

where A (m²) is the mold cavity cross-sectional area (area of the perforated plates) and h (m) the sample thickness controlled by distance between two flow distribution plates. The equivalent permeability of the flow distribution plates K_p was estimated using the model derived [214] based on Hagen-Poiseuille relation:

$$K_p = \frac{n_h \pi R^4}{8A} \quad (4.4)$$

where n_h is the number of the holes, R the hole radius. K_p can thus be estimated as $6.2 \times 10^{-7} \text{ m}^2$, between 3 and 5 orders of magnitude higher than typical textile reinforcements. This indicates that additional pressure drop caused by the perforated plates is negligible. It agrees with the report of Barnett et al. [209], although it may need to be considered in some limiting cases (extremely low thickness or high permeability).

4.4.2 Permeability of reference porous medium

A reference isotropic porous medium made of sintered ceramic balls of 0.2 mm diameter (Figure 4.3a) was tested with the unidirectional mold to quantify the mold performance. It has the advantage of being much more rigid than engineering textiles. This allowed comparing the results obtained with and without flow distribution plates, as depicted in Figure 4.3. The transverse permeability measured with perforated plates (Figure 4.3b) is referred to as apparent permeability k_z^a , which can be influenced by a deviation from unidirectional flow caused by the plates. In comparison, the value measured in freestanding condition (Figure 4.3c) is referred to as the intrinsic permeability k_z , since a quasi-unidirectional flow satisfying 1D Darcy's law can be established in this case.

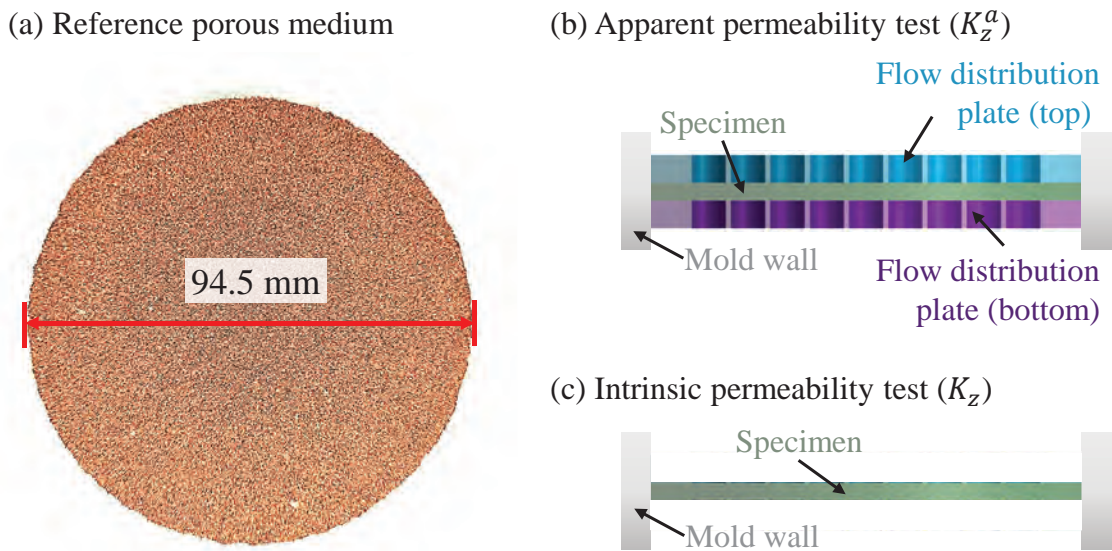


Figure 4.3 Reference porous medium (a) and two test configurations: apparent permeability test with flow distribution plates (b) and intrinsic permeability test in freestanding conditions (c).

Two specimens of the reference porous medium with different thicknesses, 11.6 mm and 25 mm, were tested. The samples were machined to a diameter of 94.5 mm. The gap between

the specimen and the mold wall was sealed to prevent any edge effect. Each sample was tested with and without distribution plates. Experimental results are reported in Figure 4.4. In each case, an almost perfectly linear relationship between flow rate and pressure drop ($R^2 \sim 0.999$) is observed. This confirms that possible unfavorable effects, such as flow-induced compaction and nesting effect, were avoided. The presence of the perforated plates can then be considered the only important factor in analyzing experimental results and evaluating the testing procedure.

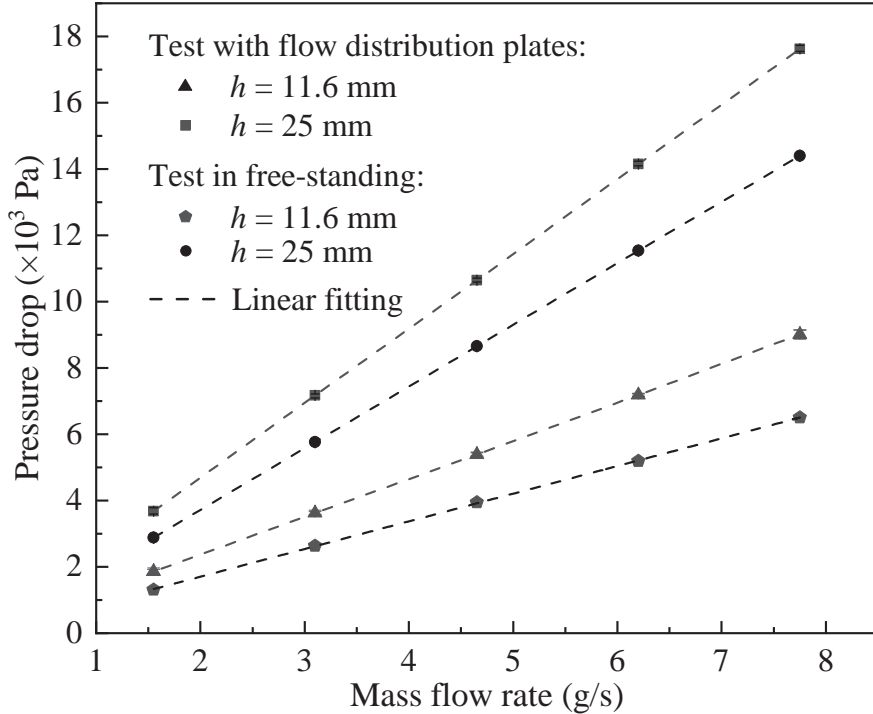


Figure 4.4 Measured pressure drop across the thickness direction for the reference porous specimens with thickness (h) of 11.6 mm and 25 mm.

Permeability is an intrinsic property that should not depend on the operational conditions of measurements. However, the values reported in Table 4.1 for the reference material contradict this concept in two aspects:

- 1) The apparent permeability is specimen thickness sensitive. Significant inconsistency (18%) in apparent permeability was observed for specimens of different thickness. In comparison, the intrinsic permeability is in good agreement (the 4% difference is possibly induced by machining).
- 2) The presence of flow distribution plates leads to considerable permeability underestimation. As expected from the difference in pressure drop (Figure 4.4), the intrinsic permeability is

43% and 26% higher than the corresponding apparent permeability for the thinner and thicker specimens, respectively.

Table 4.1 Transverse permeability of the reference porous medium.

Sample thickness	Apparent permeability $k_z^a (\times 10^{-10} \text{ m}^2)$	Intrinsic permeability $k_z (\times 10^{-10} \text{ m}^2)$	Relative error $(k_z - k_z^a) / k_z^a$
11.6 mm	1.41 ± 0.030	2.02 ± 0.015	43%
25.0 mm	1.67 ± 0.027	2.11 ± 0.005	26%

The underestimation could be caused by (1) additional pressure drop through the perforated plates and (2) limited fluid exchange capacity between the specimen and the free flow zone due to perforated plates. As the pressure drop associated with the devices is negligible, the second one becomes critical for accurate permeability characterization. It is, however, necessary to use flow distribution plates as holders since actual textiles are deformable and compressible. In the following, the impact of the plates on the measurement will be quantified numerically to eventually propose a correction strategy.

4.4.3 Performance of unidirectional molds

A performance descriptor named the discharge coefficient C_d is introduced to evaluate the flow capacity and performance of unidirectional molds. It is simply computed as the ratio of the apparent discharge Q^a (m^3/s) measured through a given test mold with flow distribution plates to the theoretical discharge Q^{1d} for unidirectional Darcy flow at the same pressure gradient:

$$C_d = \frac{Q^a}{Q^{1d}} = \frac{k_z^a}{k_z} \quad (4.5)$$

The above definition is thus equivalent to $k_z = \frac{k_z^a}{C_d}$, considering C_d as a correction factor to obtain the intrinsic permeability from the apparent permeability. With the measurement data on the reference material, the corresponding discharge coefficient C_d of 69% and 79% can be obtained for the thinner and the thicker specimens, respectively. It should finally be noted that for any similar test mold, the discharge coefficient takes values between 0 and 1 and is expected to decrease when the open space ratio of the perforated plates is reduced. As will be shown later, the discharge coefficient is not a constant for a specific device but also depends on characteristics of the porous sample.

4.5 Numerical characterization of 1D experimental setup

4.5.1 Motivation

The motivation of this research is to establish a robust approach to obtain intrinsic permeability while maintaining the advantages of the conventional method (e.g., inexpensive, simplicity of data processing and sample preparation). The method consists of quantitatively evaluating the performance of test devices by computing the discharge coefficient using numerical simulation. The unidirectional flow rate is calculated using Darcy's law while the apparent flow rate Q^a is predicted using numerical simulation. The latter is detailed in this section. In Sections 4.6 and 4.7, the method is then applied to predict the characteristic performance map of 1D molds and identify the intrinsic transverse permeability from apparent measurements.

4.5.2 Governing equations

The numerical domain consists of two solid-free subdomains (upstream and downstream) and a porous zone representing the fibrous preform, as illustrated in Figure 4.5. Assuming constant porosity φ and single phase flow, the volume-averaged mass and momentum conservation equations for flow in porous media are as follows:

$$\nabla \cdot (\rho \vec{u}) = 0 \quad (4.6)$$

$$\nabla \cdot (\rho \vec{u} \vec{u}) = -\vec{\nabla} p + \nabla \cdot \mu \left[(\vec{\nabla} \vec{u} + \vec{\nabla} \vec{u}^T) - \frac{2}{3} \nabla \cdot \vec{u} \vec{I} \right] + \rho \vec{g} - \left(\mathbf{K}^{-1} \varphi \mu \vec{u} + \frac{\varphi^2 C_2}{2} \rho |\vec{u}| \vec{u} \right) \quad (4.7)$$

where ρ , μ and \vec{u} are, respectively, the density, viscosity, and intrinsic average velocity of the fluid. p denotes the static pressure, \vec{I} the identity tensor and \vec{g} the gravitational acceleration. The last two terms of Eq. (4.7) in the bracket of the right-hand side describe the viscous and inertial resistance of flow in porous media. In this research, the inertial resistance is neglected ($C_2=0$) because of the low Reynolds number ($Re < 1$) for practical resin flow in engineering textiles. Note that in the solid-free subdomain where $\varphi = 100\%$ and permeability $\rightarrow \infty$, Eq. (4.6) and Eq. (4.7) reduce to standard Navier-Stokes equations for single phase flow.

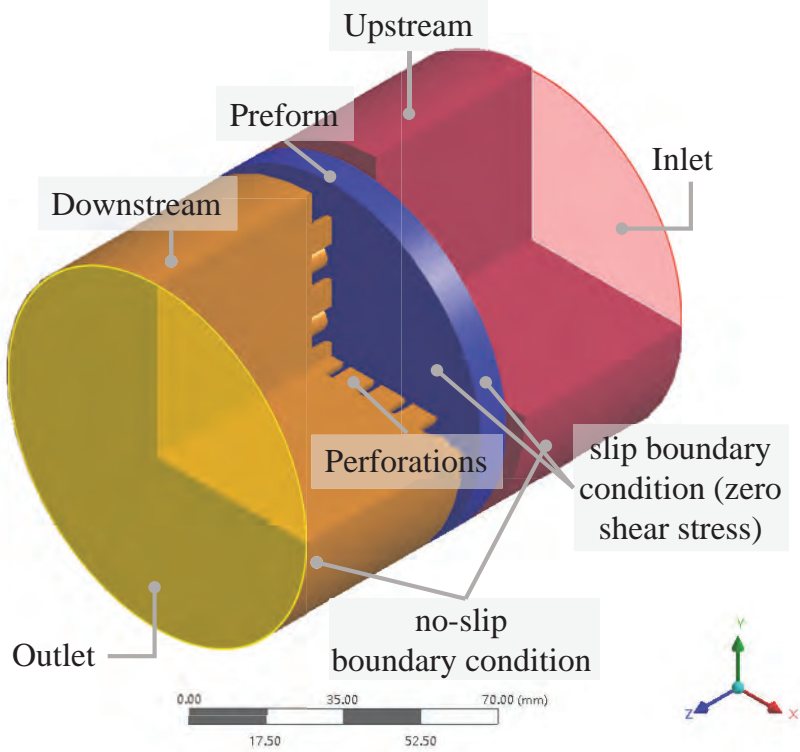


Figure 4.5 Geometrical model and boundary conditions for 3D flow simulation.

4.5.3 Geometrical model and boundary conditions

The geometrical model and the boundary conditions are also described in Figure 4.5. The analysis takes into account the geometrical features of the mold, the thickness, and the permeability anisotropy of the specimen as the flow pattern might be altered by these factors [206]. The dimensions are the same as the device described in Figure 4.2. Pressure boundary conditions are assigned to the inlet and outlet. The domain is discretized in a non-conforming hexahedral-dominated mesh. Mesh sensitivity analysis was conducted by considering different grid resolutions to ensure the independence of the numerical solutions from the mesh size. The mass and momentum conservation equations are discretized by the second-order upwind scheme. The Semi-Implicit Method for Pressure Linked Equations (SIMPLE) algorithm [215] is employed to decouple the pressure–velocity linkage to solve the incompressible flow problem. The convergence criterion was set to be 10^{-5} for all residuals. The simulations were performed with ANSYS Fluent.

The flow is assumed to be Newtonian, isothermal, and incompressible. Besides, previous knowledge of the in-plane permeability of the preform is required to complete the simulation. Nevertheless, it will be shown in Section 4.7.5 that the numerical results are not sensitive

to in-plane permeability with acceptable errors. The other properties needed to run the simulation are viscosity and density of the test fluid.

4.6 Correction of permeability measurements with isotropic materials

This section presents the use of the discharge coefficient for correcting the permeability of isotropic materials. A parametric study is first conducted to predict the performance of the setup for varying test conditions. The approach is then validated using experimental data previously acquired with the reference porous medium.

4.6.1 Numerical evaluation of mold performance

The apparent flow rate through an isotropic porous sample was predicted at a constant pressure gradient numerically for permeability ranging from $1 \times 10^{-13} \text{ m}^2$ to $1 \times 10^{-10} \text{ m}^2$, and specimen thickness from 1.5 mm to 60 mm. The corresponding discharge coefficient is reported in Figure 4.6 with permeability underestimation Δ_k representing the relative difference between the apparent and intrinsic permeability:

$$\Delta_K = \frac{k_z - k_z^a}{k_z^a} \times 100\% = \frac{1 - C_d}{C_d} \times 100\% \quad (4.8)$$

It can first be noted that the discharge coefficient does not vary with permeability values, as shown by the superimposed markers corresponding to numerical simulation in Figure 4.6. This is not surprising because the pressure drop of the plates is negligible and because the porous sample is isotropic. In that case, the permeability tensor reduces to a scalar and the apparent flow rate Q^a varies linearly with permeability for given pressure difference and sample thickness. Since the theoretical flow rate Q^{1d} is also proportional to k_z , the discharge coefficient varies only with the sample thickness as indicated by the trend line. This numerically built performance indicator agrees well with the data points derived from experiments presented in Section 4.4.3 (red star markers).

Figure 4.6 also indicates that the underestimation of transverse permeability can exceed 100% for isotropic specimens with a thickness less than 5 mm. The discharge coefficient increases with specimen thickness as the effect of the perforated plates diminishes and flow tends to get closer to unidirectional conditions. This is consistent with our previous numerical study [206], which showed that apparent permeability could only approach the intrinsic permeability of a specimen when sample thickness exceeds 50 mm. However, such test condition seems impractical for actual fabric characterization due to increased material and time costs.

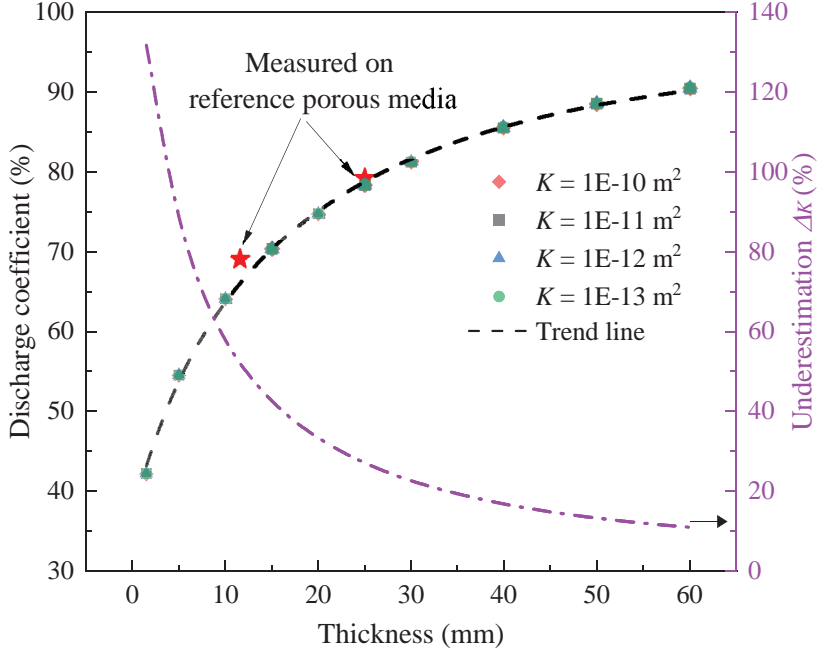


Figure 4.6 Discharge coefficient (scatters) and transverse permeability underestimation for isotropic materials as a function of sample thickness for the test device shown in Figure 4.2. Red stars indicate experimental measurements whereas all other markers correspond to numerical simulations.

4.6.2 Permeability correction and validation

Figure 4.7 compares the measured apparent and intrinsic permeability, and the corrected value obtained by applying Eq. (4.8) with the numerically determined C_d . For the two reference samples, the corrected permeabilities are similar and in quite good agreement with intrinsic values. The largest difference of 4% is observed for the thinner specimen, which may be due to the slightly uneven specimen thickness caused by machining. Overall, results indicate that the apparent permeability measured by the conventional test can be adequately corrected with the C_d performance indicator, demonstrating the validity of the proposed approach.

4.7 Correction of permeability measurements with orthotropic materials

In this section, the approach for permeability correction is extended to orthotropic materials. We first show that the result of the permeability test is influenced by anisotropy of the sample so that this parameter must be considered when modelling the performance of the mold. Two iterative frameworks are then presented for permeability correction based on the discharge

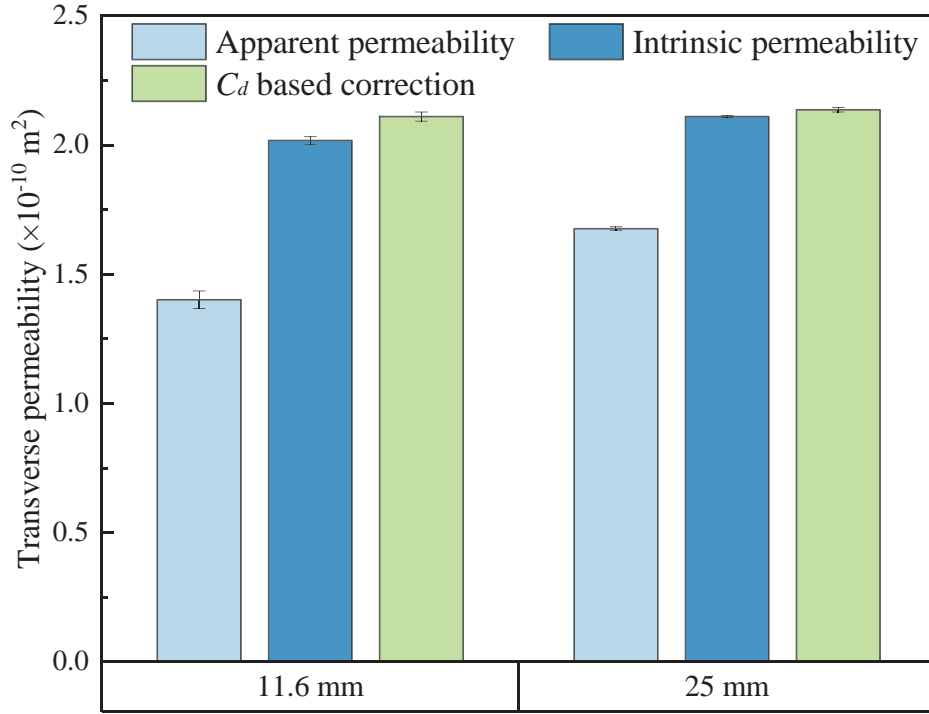


Figure 4.7 Comparison of apparent, intrinsic, and identified transverse permeability based on numerically determined discharge coefficient for the reference porous medium.

coefficient and validated with tests on a typical fibrous fabric.

4.7.1 Influence of global permeability anisotropy

Common fibrous preforms exhibit a quasi-orthotropic behavior. If the coordinate system is chosen to coincide with the principal directions of the material, the permeability tensor reads:

$$K = \begin{bmatrix} k_x & 0 & 0 \\ 0 & k_y & 0 \\ 0 & 0 & k_z \end{bmatrix} \quad (4.9)$$

In-plane permeability components k_x and k_y are usually significantly higher than k_z . This is considered by global permeability anisotropy α_g defined as:

$$\alpha_g = \frac{\sqrt{k_z k_y}}{k_z} \quad (4.10)$$

The anisotropic behavior influences the permeability test by altering the flow pattern in the sample. This is shown in Figure 4.8b, which plots the intrinsic average velocity magnitude

in a cross-section located at the center of the mold (the visualization zone covering one full and two half perforations as shown in Figure 4.8a). To obtain these numerical results, the transverse permeability was kept constant ($1 \times 10^{-11} \text{ m}^2$) while the in-plane permeability was taken equal ($k_x = k_y$) and selected to achieve the given anisotropy. In all simulations, the pressure gradient across the sample was 2000 Pa/mm. The solid part of perforated plates, which is impermeable, is represented in gray in Figure 4.8b.

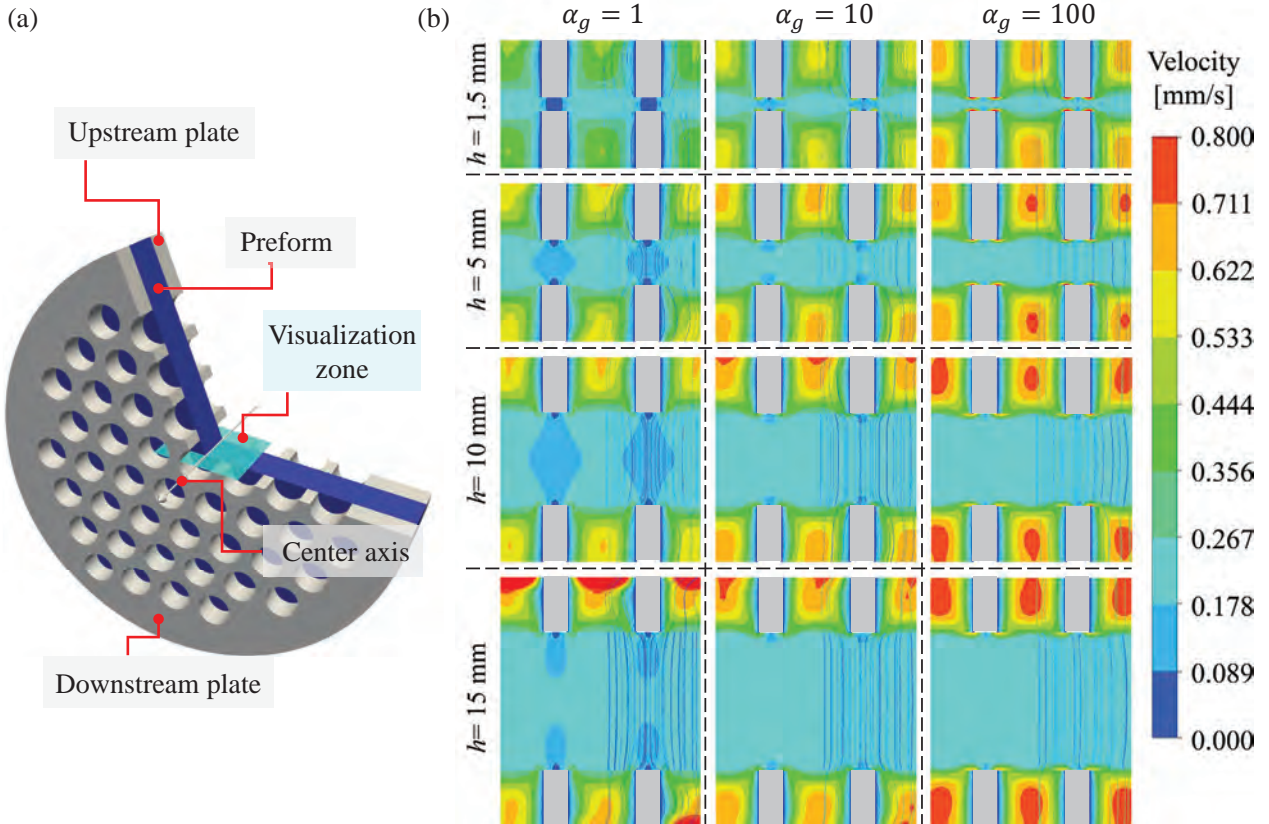


Figure 4.8 Parametric investigation of fluid exchange through distribution plates for different preform thickness h and anisotropy α_g : the magnitude of intrinsic average velocity vector in the visualization zone of (a) is shown in (b) superimposed with streamlines (only shown on the right half of each subplot). The gray color in (b) represents the solid part of perforated plates which is impermeable.

The four left panels of Figure 4.8b were obtained with an isotropic material ($\alpha_g = 1$) and corresponds to results already presented in Figure 4.6. As can be seen, the fluid in the porous medium between the impermeable part of the perforated plates is nearly stagnant for the case with the thinnest sample ($h = 1.5 \text{ mm}$). When the thickness increases, the stagnant zone decreases and a flow redistribution can be observed so that the intrinsic average velocity tends to become uniform in the mid-plane of the sample. For a given preform thickness,

increasing global permeability anisotropy facilitates in-plane flow redistribution in the vicinity of the plates and the averaged flow becomes unidirectional more rapidly. In the case of thickest sample and highest global permeability anisotropy ($h = 15$ mm and $\alpha_g = 100$), the intrinsic average velocity field is almost uniform in a large part of the sample and flow conditions are quite close to quasi-unidirectional because the sample itself plays a role of flow distribution media that offsets the limited flow exchange capacity induced by perforated plates. Consequently, the apparent transverse permeability measured with an orthotropic material depends not only on the device but also on the global permeability anisotropy and thickness of the specimen.

4.7.2 Evaluation of mold performance

Following the approach of Section 4.6.1, the characteristic performance map of the mold was numerically characterized for a wide range of specimen thickness and global permeability anisotropy. As shown in Figure 4.9, the discharge coefficient for $\alpha_g > 1$ is significantly enhanced compared to isotropic case at the same thickness because higher in-plane permeability facilitates flow redistribution. However, the effect of global permeability anisotropy becomes less noticeable once α_g is greater than 50. Note that the two in-plane permeability components, k_x and k_y , are assumed to be equal. As for the isotropic material, other simulations also confirmed that the discharge coefficient is not affected by the absolute value of transverse permeability if the thickness and anisotropy are same. Besides, a simulation performed with $k_x = 10k_y = 10k_z$ shows that the discharge coefficient is quite similar to the one for $k_x = k_y$ with an error less than 2%. It is then reasonable to consider that Figure 4.9 describes the performance of the test device for any orthotropic preform.

A simple analytical model was proposed to relate the performance descriptor C_d to the open space ratio γ_p of a flow distribution plate (with perforations in hexagonal pattern) and the thickness and global permeability anisotropy of the specimen. It is given by:

$$C_d(h, \alpha_g) = \frac{(1 - \gamma_p)h}{h + \frac{E}{\sqrt{\alpha_g}}} + \gamma_p \quad (4.11)$$

In this general model, the only unknown E is a constant to be determined by making use of the data obtained from either numerical simulations or experiments. As shown by the dashed lines in Figure 4.9, the model represents the predicted discharge coefficient quite precisely ($E=13.6$, $R^2 = 0.99$). In addition, the model is bounded between the open space ratio of the distribution plate and 1. This is consistent with the fact that when $h \rightarrow 0$, the flow can only develop in perforations, whereas it approaches a 1D ideal flow for $h \rightarrow \infty$.

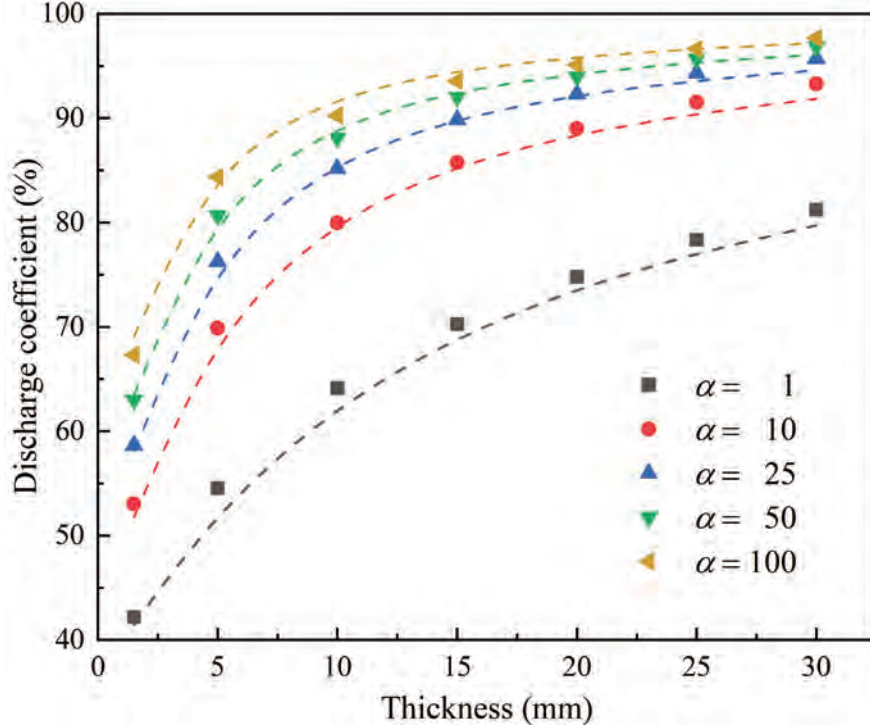


Figure 4.9 Characteristic performance map for the mold presented in Figure 4.2.

4.7.3 Iterative framework for transverse permeability identification

For anisotropic materials, the discharge coefficient C_d cannot be computed directly since the anisotropy is a priori unknown. To tackle this issue, two iterative frameworks are presented here.

(1) Numerical-based approach

This method consists of running a series of flow simulations for each test. Its principle is rather similar to past work on 3D unsaturated tests that matched simulation results with the experimental flow front to identify the material permeability [61, 211] except it matches the experimental and numerical flow rates. It uses a numerical model that replicates the test conditions (mold geometry, pressure drop, etc.). The apparent permeability measured by the conventional method is used as initial value for transverse permeability in the first simulation. It is then updated iteratively using Eq. (4.12) to minimize the residual R_{nu} :

$$k_{z,i+1} = \frac{Q_{exp}}{Q_i} \times k_{z,i} \quad (4.12)$$

$$R_{nu} = \frac{Q_{exp} - Q_i}{Q_{exp}} \times 100\% \quad (4.13)$$

where Q_{exp} is the experimental flow rate, Q_i is the flow rate predicted by simulation and i stands for the i -th iteration. The output (when $R_{nu} < 0.5\%$) is referred to as numerically identified permeability to distinguish from intrinsic transverse permeability measured directly by experiment. This strategy is summarized below:

Algorithm 1: Numerical based approach

Input : $P_{in}, P_{out}, k_x, k_y, k_z^a$

Output: k_z^{nu}

```

1  $k_x, k_y \leftarrow$  in-plane permeability;
2  $k_z \leftarrow k_z^a;$ 
3 Read full-scale numerical mesh;
4 Impose boundary conditions  $P_{in}$  and  $P_{out}$ ;
5 while True do
6   Solve Eq.(4.6) and Eq.(4.7);
7   Calculate numerical flow rate;
8   Residual checking: Eq.(4.13);
9   if Residual > 0.5% then
10    Update  $k_z$  according to Eq.(4.12);
11    Continue;
12  else
13     $k_z^{nu} \leftarrow k_z;$ 
14    return  $k_z^{nu};$ 
15  end
16 end

```

(2) Discharge coefficient-based approach A series of simulations is first performed to establish the characteristic performance map of the mold and determine the model parameter E in Eq. (4.11). Then the initial discharge coefficient C_d^0 is computed with the sample thickness and the initial permeability anisotropy α_g^0 using apparent transverse permeability:

$$\alpha_g^0 = \frac{\sqrt{k_z k_y}}{k_z^a} \quad (4.14)$$

The transverse permeability is then updated iteratively using the newly computed discharge coefficient $C_d(t, \alpha_i)$, following evaluation of residual R_{Cd} :

$$\alpha_g^i = \frac{\sqrt{k_z k_y}}{k_z^i} \quad (4.15)$$

$$R_{Cd} = \frac{k_z^i - k_z^{i-1}}{k_z^i} \times 100\% \quad (4.16)$$

This approach can greatly facilitate the post-processing of experimental data compared to the previous one. The performance of the test mold is obtained through an initial parametric study and no additional simulation is needed once the model parameter E is determined. The method is summarized in Algorithm 2 below.

Algorithm 2: C_d based approach

Input : k_x, k_y, k_z^a, h
Output: $k_z^{C_d}$

```

1  $\alpha_0 \leftarrow \frac{\text{sqrt}(k_x \times k_y)}{k_z^0};$ 
2  $C_d^0 \leftarrow C_d(t, \alpha^0);$ 
3 i = 0;
4 while True do
5   ++ i;
6    $k_z^i \leftarrow \frac{k_z^a}{C_d^{i-1}};$ 
7   Residual  $\leftarrow$  Eq.(4.16);
8   if Residual > 0.5% then
9      $\alpha_i \leftarrow \frac{\text{sqrt}(k_x \times k_y)}{k_z^i};$ 
10     $C_d^i \leftarrow C_d(t, \alpha^i);$ 
11    Continue;
12  else
13    return  $k_z^{C_d} = k_z^i;$ 
14 end
15 end

```

4.7.4 Validation

A 3D orthogonal glass textile TG96N (3250 g/m², Texonic Inc.) was characterized with the experimental setup to show the validity of the two iterative methods for anisotropic fibrous reinforcements. A first series of tests were conducted following the conventional method. As summarized in Table 4.2, four fiber volume fractions were considered by changing the cavity

thickness while keeping the number of fabric layers constant. Each sample was weighted to evaluate the actual fiber volume fraction and each experiment was repeated three times with fresh samples. 4.2 also shows the in-plane permeability along the warp and weft directions that were derived from the experimental results of Karaki et al. [212].

Table 4.2 Transverse permeability test configurations of TG96N.

V_f	Without secondary FDL		With secondary FDL		In-plane permeability (10^{-11} m^2)	
	h (mm)	n	h (mm)	n	k_x	k_y
53%	9.45	4	10.58	4	14.2	7.0
56%	8.94	4	10.08	4	11.2	4.54
59%	8.49	4	9.64	4	8.36	2.62
62%	8.10	4	9.23	4	5.74	1.25

* The thickness of the two layers secondary flow distribution layers is included.

To validate the approach, a second series of tests were performed to measure directly the intrinsic permeability following the approach proposed by Huang et al. [24]. It consists of placing a highly permeable secondary Flow Distribution Layer (FDL) between perforated plates and sample. The FDL distributes fluid on the entire cross-section rapidly and create unidirectional flow in the tested specimen. However, some nesting is inevitable between the fibrous preform and the FDL so that the actual fiber volume fraction is reduced and the transverse permeability is overestimated. Huang et al. [24] characterized the nesting between the FDL and the preform by micro-computed X-ray tomography at different levels of compaction. This analysis allowed relating the effective thickness of secondary FDL h_s (in millimeter) with the fiber volume fraction V_f through the following fitting function:

$$h_s = 3.49 \times 10^6 e^{-35.52V_f} + 3.43 \times 10^{-1} \quad (4.17)$$

Note that Eq. (4.17) was obtained for a different type of woven fabric. However, the 3D fabric considered here possesses a similar compaction behavior and the experiments were conducted with the same secondary FDL as reported by Huang et al. As a first approximation, Eq. (4.17) was directly used in the present study without reproducing the Micro CT experiments and analysis.

Figure 4.10 presents the apparent permeability of TG96N and its intrinsic permeability obtained following Huang's method and the two newly proposed approaches. Before correction,

the permeability measured with secondary FDL is between 52% and 107% larger than the apparent permeability without secondary FDL (Figure 4.10a). The former was overestimated due to the lower fiber volume fraction induced by nesting, while the latter was underestimated because of the presence of perforated plates. The data with secondary FDL was processed with Huang's method and presented in Figure 4.10b as a reference value to validate the two iterative frameworks. As reported, the two iterative approaches yield nearly the same result, indicating that they are equivalent. In addition, the intrinsic permeabilities obtained by the new approaches are quite close to those determined by Huang's approach. This strongly suggests that the two iterative approaches are valid.

Although Huang's method can eliminate the overestimation due to the nesting between sample and secondary FDL, one must first use volumetric imaging technology to obtain the model. Moreover, the model is expected to differ from one fabric or secondary FDL to another. Therefore, it can be expensive and time-consuming. This is another reason that motivates the development of the general approach reported in this work.

4.7.5 Sensitivity analysis

(1) Errors in in-plane permeability: In-plane permeability is a required input for the iterative algorithms. To mimic the measurement error of in-plane permeability, this analysis varied the in-plane permeability in a range of $\pm 20\%$ while keeping transverse permeability constant in numerical identification. The investigation included two thickness levels (5 mm and 10 mm) and the global permeability anisotropy ranges from 1 to 100. The change in identified transverse permeability is less than 3% and decreases gradually as global permeability anisotropy increases. Considering typical textiles exhibit global permeability anisotropy ranging from 10 to 100, error in in-plane permeability shows only limited impact. (2) Alignment of perforated plates: The numerical analyses presented so far assumes the upper and lower perforated plates are fully aligned. It is not always the case in practice. This could possibly modify the flow pattern within the sample. The holes in the perforated plates usually follow a hexagonal packing pattern to maximize the open space ratio, as illustrated in Figure 4.2. The maximum misalignment angle is then considered as 30 degrees because of symmetry. Two extreme conditions, i.e., the perfectly aligned and the 30° misaligned perforated plates, were investigated numerically with the proposed algorithm based on the experimental result of the reference porous medium. The transverse permeability identified is plotted in Figure 4.11 as a function of the mass flow rate of the test liquid. Only 0.1% increase in the identified transverse permeability was obtained for the case with misaligned perforated plates. The authors tried to verify this experimentally but no difference could be observed.

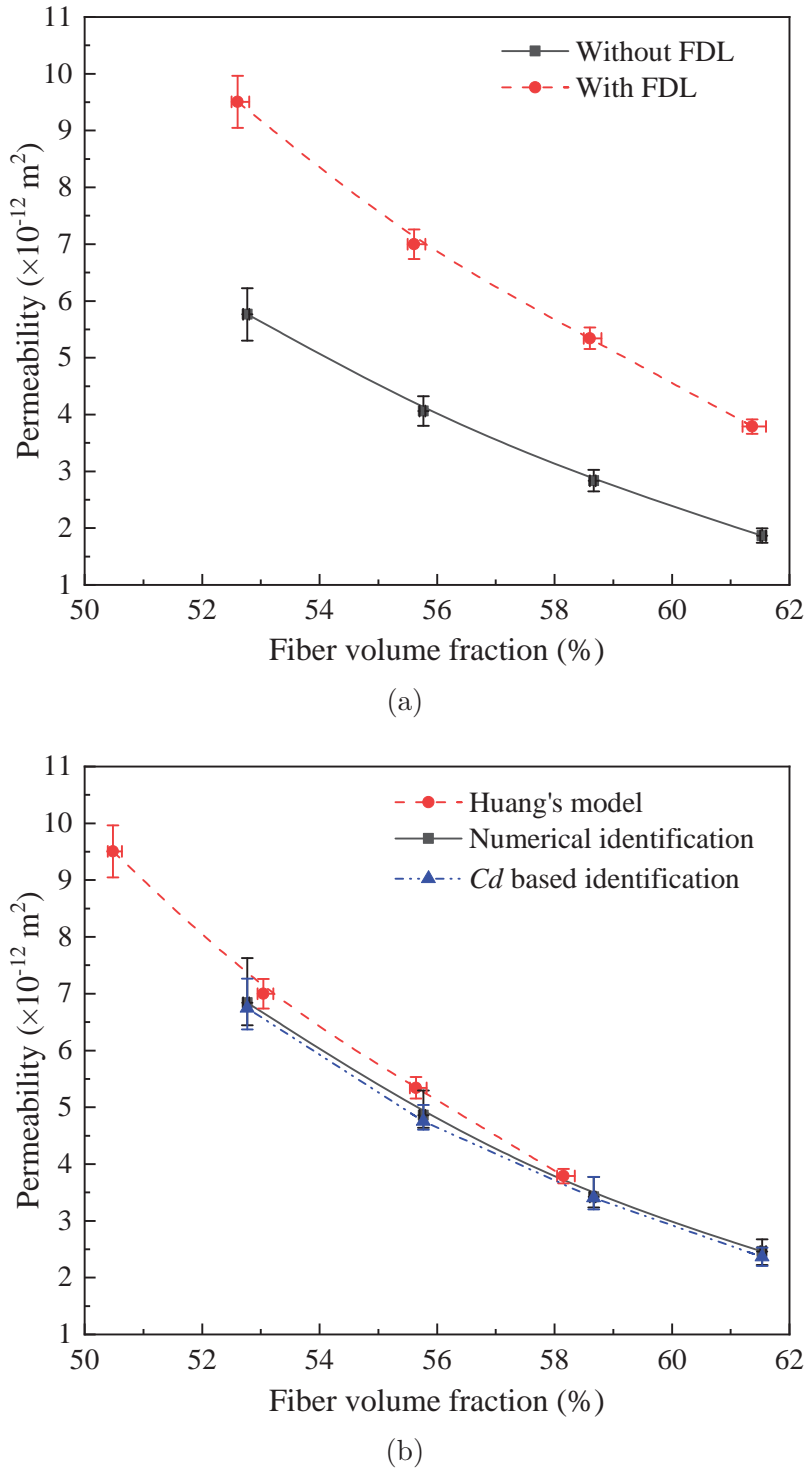


Figure 4.10 Transverse permeability of TG96N: (a) raw data with and without secondary flow distribution layers; (b) corrected values with Huang's model and the two newly proposed iterative frameworks.

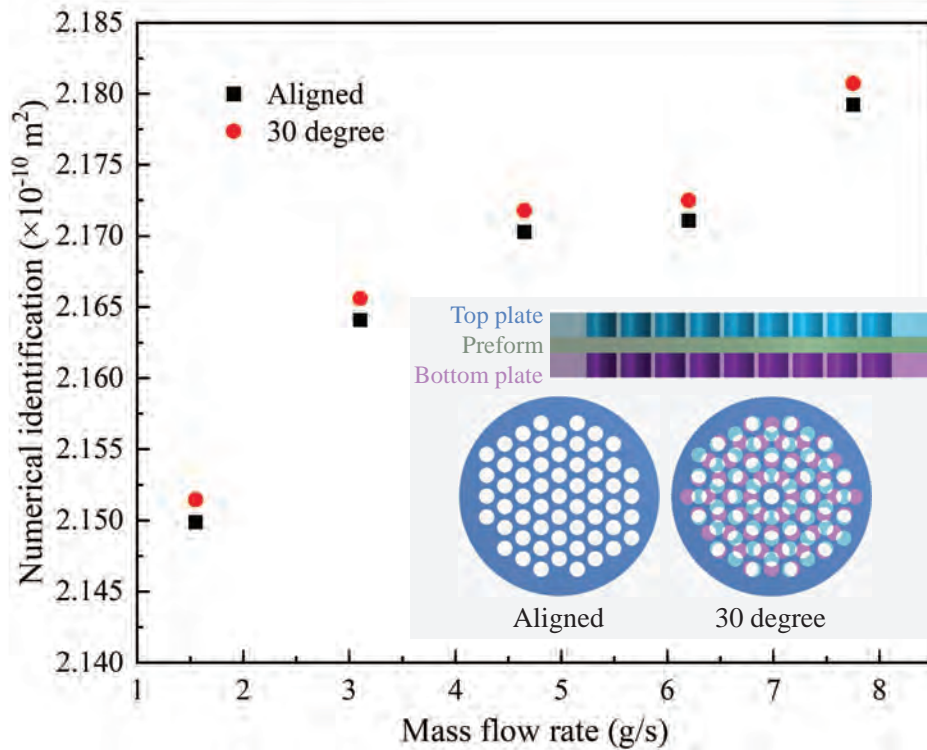


Figure 4.11 Comparison of numerically identified permeability for aligned and not aligned perforated plates: two extreme conditions for hexagonal packing holes as depicted by the inset.

4.8 Effect of test device on transverse permeability characterization

In this section, previous results obtained by two participants of Benchmark III [13] are re-analyzed to illustrate the usefulness of the correction method and the effect of test devices on transverse permeability characterization.

4.8.1 Mold description and analysis of performance

The setups used at Polytechnique Montreal (Figure 4.2) and Wuhan University of Technology (Figure 4.12) were investigated. The test principle is similar and both molds use perforated plates to control fiber volume fraction. However, some differences exist:

1. *geometry*: the diameter of the mold is 95.6 mm for Montreal and 114 mm for Wuhan.
2. *perforated plates*: the open space ratio of perforated plates in Montreal is 35.1% and 52.4% in Wuhan. The centroid distance between perforations is also different (see Figure 4.2 and Figure 4.12).

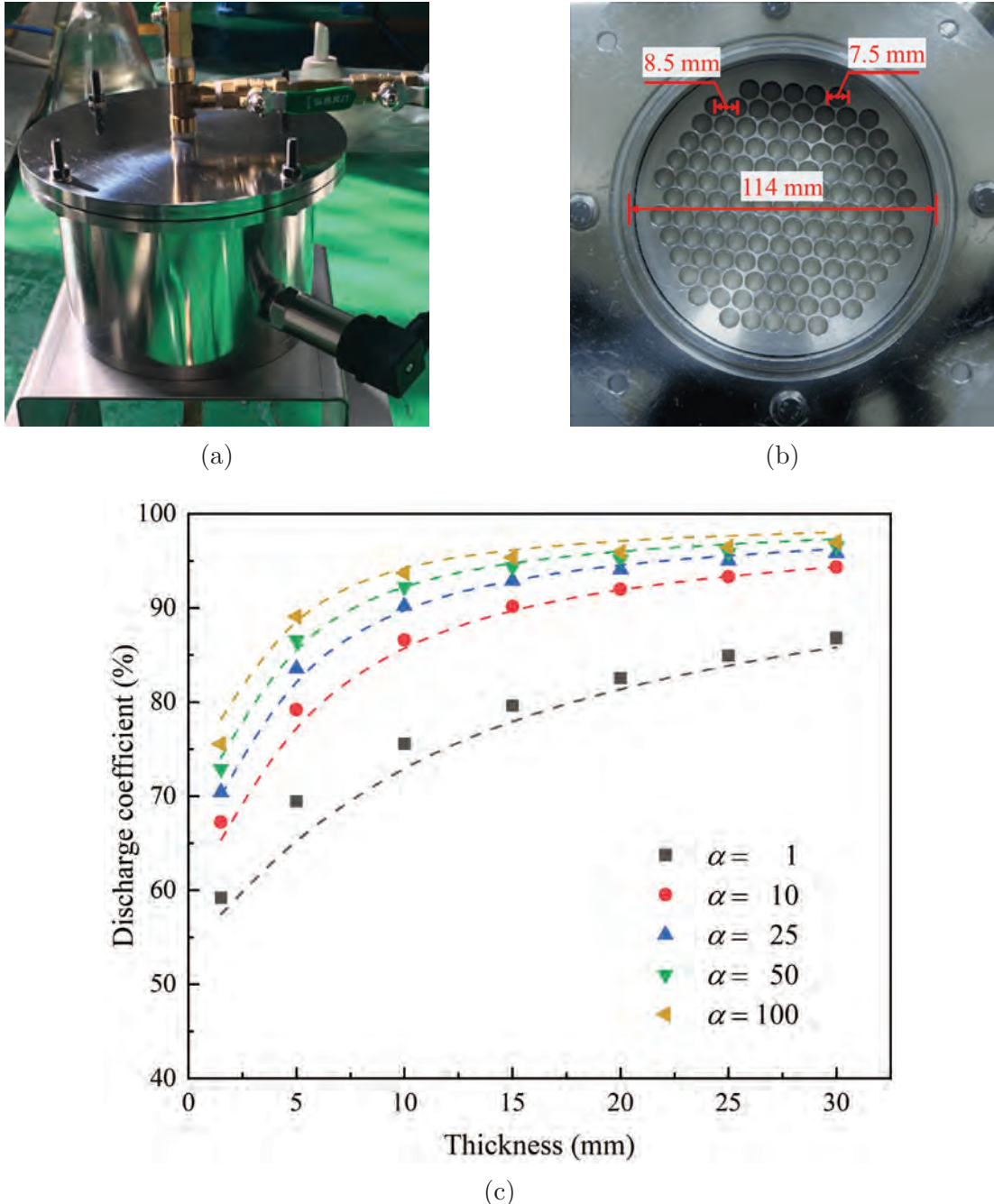


Figure 4.12 Transverse permeability test mold of Wuhan University of Technology (a) and its perforated plate of 7 mm in thickness (b); Characteristic performance map of the mold (c).

3. *pressure monitoring*: only one pressure sensor is mounted near the inlet for the mold in Montreal since fluid leaves the mold at atmospheric pressure. In contrast, one more pressure sensor was installed at outlet to monitor outflow pressure because the mold in

Wuhan is closed with a top cover.

The characteristic performance map for the Wuhan device is presented in Figure 4.12c. The minimum discharge coefficient is 59.2% ($t = 1.5$ mm, $\alpha = 1$), while it is 42.2% for the one in Montreal. The discharge coefficient of the device in Wuhan is constantly higher than that of the Montreal device (see Figure 4.9 and Figure 4.12c). This is consistent with the inherent difference in mold structure: the open space ratio of perforated plates in Wuhan is higher than that in Montreal (52.4% vs. 35.1%). It can be concluded that the Wuhan setup is more efficient. However, its discharge coefficient is still significantly lower than 1 for practical test conditions.

4.8.2 Permeability and measurement consistency

Experimental data from the two participants of Benchmark III were compared and reprocessed with the proposed approach. The textiles are non-crimp glass fabric produced by Saertex (NCF, 45°/90°/0°/45° of areal density 444 g/m²) and twill glass woven fabric supplied by Hexcel (295 g/m²). The in-plane permeability of the two fabrics was derived by polynomial fitting (see Table 4.4) from the results of Technische Universität Clausthal [216]. The test configurations are summarized in 4.3. Each test was repeated five times with fresh samples. Refer to [13] for more details on the benchmark materials and test guidelines.

Table 4.3 The transverse permeability test configurations for Benchmark III.

Devices	Woven fabric			Non-crimp fabric		
	V_f	h (mm)	n	V_f	h (mm)	n
Polytechnique Montréal*	45.1 ± 0.06 %	5.29	21	46.8 ± 0.10 %	5.29	14
	49.3 ± 0.04 %	5.29	23	51.2 ± 0.07 %	4.48	13
	53.1 ± 0.06 %	4.48	21	55.2 ± 0.08 %	4.48	14
Wuhan University of Technology	45.0 ± 0.32 %	3.01	12	46.7 ± 0.37 %	3.01	8
	48.4 ± 0.24 %	3.01	13	50.0 ± 0.31 %	2.80	8
	51.9 ± 0.49 %	3.01	14	54.8 ± 0.34 %	3.20	10

Note: All the benchmark tests in Montreal and Wuhan were performed without secondary flow distribution layers.

The apparent and identified transverse permeability are plotted in Figure 4.13a for the woven fabric and Figure 4.13b for the non-crimp fabric. Only the identified permeability using the

Table 4.4 In-plane permeability of the two benchmark fabrics.

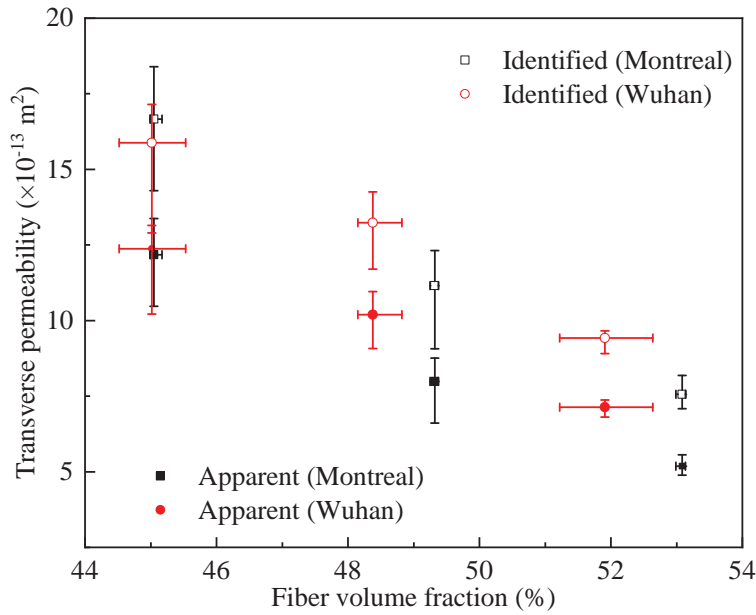
Non-crimp fabric			Woven fabric		
V_f	Permeability in 10^{-11} m^2		V_f	Permeability in 10^{-11} m^2	
46.8%	k_x	5.54	45%	k_x	6.56
	k_y	4.45		k_y	1.36
50.5%	k_x	3.79	49%	k_x	4.13
	k_y	2.99		k_y	0.64
55.0%	k_x	2.15	53%	k_x	2.61
	k_y	1.64		k_y	0.369

numerical-based approach is presented since the two iterative frameworks provide equivalent results. Figure 4.13 shows that the apparent permeability of the two institutes is in good agreement. The values obtained by Wuhan tend to be higher but the difference is small considering the variability observed during the international benchmark. However, good repeatability does not necessarily mean the measured apparent permeability is accurate. Result shows that the identified permeability is significantly higher than apparent permeability. For woven fabrics tested in Montreal, the apparent permeability is 36.8%, 39.7%, and 45.8% lower than intrinsic values (for fiber volume fractions from low to high), while it is 28.3%, 29.8%, and 32.0% in Wuhan. For non-crimp fabric, the underestimation is 44.7%, 50.8%, 50.4% in Montreal and 34.6%, 36.3%, 34.3% in Wuhan. Overall, the amount of correction is higher for Montreal for all cases since the Wuhan setup possesses a larger open space ratio and is more efficient. It is also important to note that the number of plies (and hence thickness) was higher in Montreal which tends to increase the discharge coefficient. Additionally, it was observed that the correction is of greater importance for non-crimp fabric because of its low global permeability anisotropy.

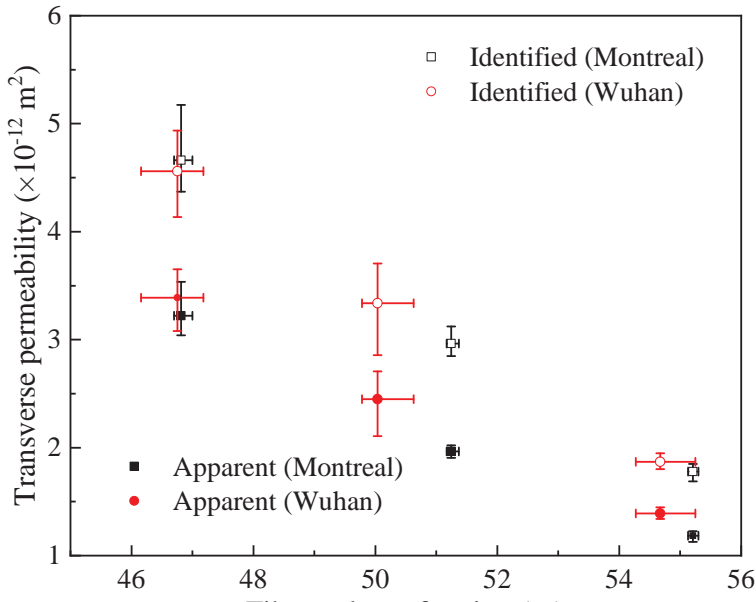
To facilitate comparison, the apparent and identified permeability was adjusted to a nominal fiber volume fraction V_f using the following equation (derivation in Appendix A):

$$k_z^{V_f} = k_z^a \cdot \frac{V_f^{a2}}{(1 - V_f^a)^3} \cdot \frac{(1 - V_f)^3}{V_f^2} \quad (4.18)$$

where V_f^a is the actual fiber volume fractions and $k_z^{V_f}$ the permeability for the nominal fiber volume fractions V_f . Three nominal fiber volume fractions are chosen here as the median



(a)



(b)

Figure 4.13 The apparent and the identified permeability of (a) woven and (b) non-crimp fabric.

values of the two institutes. They are 45%, 49%, and 53% for woven fabric and 46.8%, 50.5%, and 55% for non-crimp fabric. The apparent and identified permeability at nominal fiber volume fractions are presented in Figure 4.14a for the woven fabric and Figure 4.14b

for the non-crimp fabric. The identified permeability improved significantly in consistency. The maximum difference in average permeability of the woven fabric decreases from 18% (apparent permeability at $V_f^a = 53\%$) to 10% (between identified permeability). For non-crimp fabric, the difference in apparent permeability is 4%, 9%, and 10% for the fiber volume fraction of 46.8%, 50.5%, and 55%. It decreases to 3%, 0.4% and 0.6% after reprocessing. This again confirms the validity of the proposed algorithm in improving the consistency of transverse permeability measured with different devices. It also shows that geometrical differences in test molds may lead to apparently inconsistent results.

4.9 Conclusion

This study investigated the impact of flow distribution plates used in conventional 1D transverse permeability test devices for characterization of engineering textiles in saturated conditions. A general approach has been proposed to predict and model the performance of the test mold and correct the measured permeability value. Validation experiments were also conducted by measuring the intrinsic permeability of an isotropic reference porous medium and an anisotropic engineering textile. The key results are summarized as follows:

The underestimation of transverse permeability using the conventional unidirectional method was experimentally demonstrated for the first time by introducing a rigid reference porous medium. This effect was quantified by a dimensionless mold performance descriptor named discharge coefficient.

Using numerical simulation, the discharge coefficient was shown to depend on the geometry of the test device (open spaces in the flow distribution plates and cavity thickness) and on the anisotropy of the tested material. A simple analytical model was proposed to relate the mold performance to these key parameters.

An iterative framework was presented to identify the intrinsic transverse permeability from the conventional 1D test, either based on a series of numerical simulations or on the discharge coefficient model. The two approaches give equivalent results and agree well with the intrinsic permeability. The discharge coefficient approach is more promising, as it reuses the performance map and no additional simulation is required. The approach was finally applied to investigate the permeability discrepancy between two different molds. The discharge coefficient shows a strong positive correlation with the open space ratio of flow distribution plates. Permeability underestimation of the first mold is up to 46% for woven fabrics and 51% for non-crimp fabrics. In comparison, the second mold underestimates up to 32% and 36%, respectively. The iterative framework successfully improved the reproducibility of the

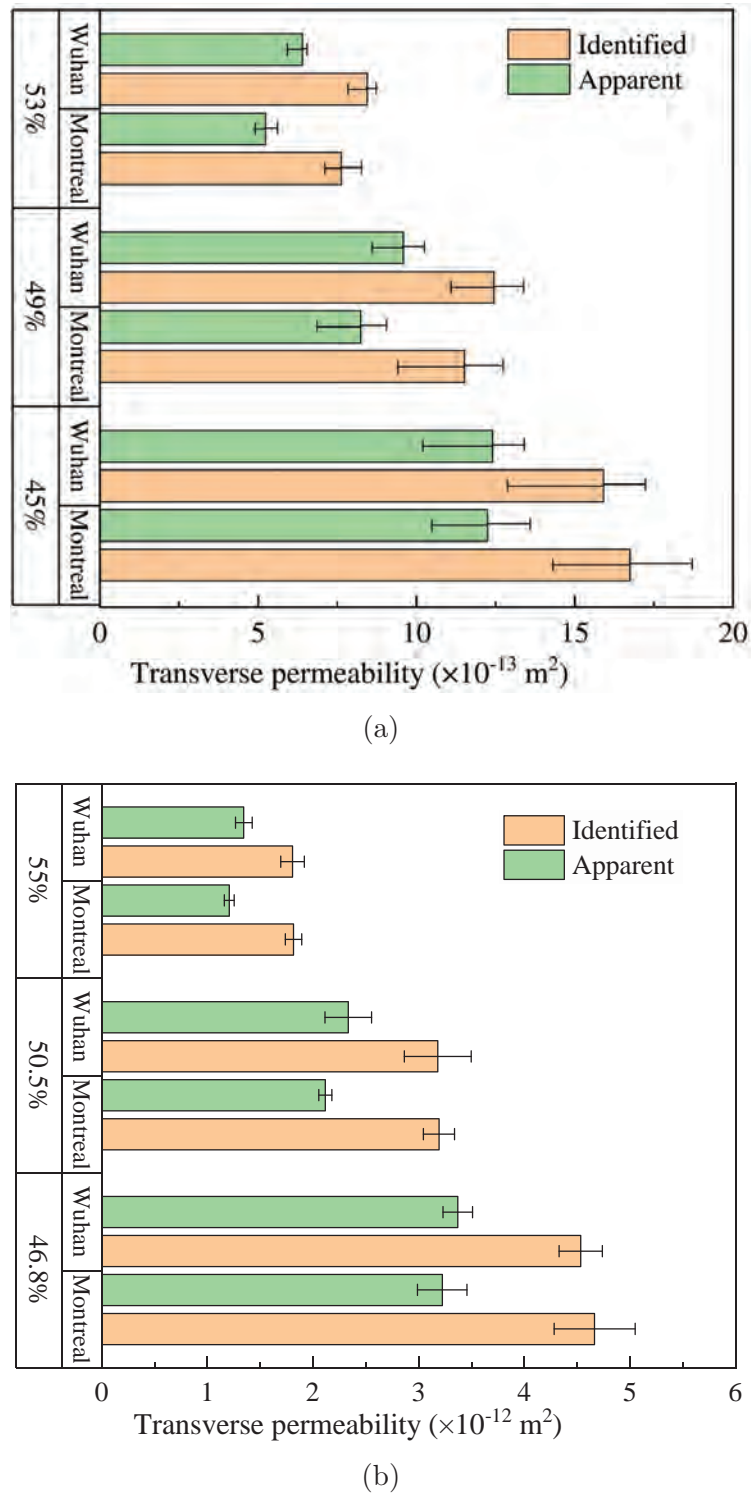


Figure 4.14 The apparent and identified permeability of (a) woven fabric and (b) non-crimp fabric after being corrected to nominal fiber volume fractions.

two molds and eliminated underestimations.

Overall, the concept of discharge coefficient can be applied to any testing device based on 1D saturated flow and is promising for improving measurement consistency between different setups. It could be used to refine the analyses conducted during the recent benchmark that only considered the effect of perforated plate geometry and sample thickness separately [13]. Future investigations could also consider other types of distribution medium (such as honeycomb or sintered structures) to provide guidelines for highly efficient mold design.

Acknowledgments

This research was partially funded by the *Department of Mechanical Engineering of Polytechnique Montreal* and by the *Natural Sciences & Engineering Research Council of Canada* (NSERC) (Discovery Grant). Authors also gratefully acknowledge the financial support from the *Research Center for High Performance Polymer and Composite Systems* (CREPEC) and the *Fonds de recherche du Québec - Nature et technologies* (FRQNT). This research was also partially funded at Wuhan University of Technology by *Fundamental Research Funds for Central Universities* (2019-JL-003). Authors would like to express sincere thanks to Christian-Charles Martel and Steve Dube for their support in the laboratory.

Appendix A

Kozeny-Carman [217] model expresses the permeability as a function of fiber volume fraction V_f as follows:

$$k = \frac{r_f^2}{4k} \cdot \frac{(1 - V_f)^3}{V_f^2}$$

where r_f is fiber radius and k is Kozeny constant, which varies with V_f . The term $r_f^2/4k$ can be considered constant when the variation of V_f is limited to a small range. This gives the following equations for the actual and nominal fiber volume fractions V_f^a and V_f , and the corresponding permeability k_z^a and $k_z^{(V_f)}$:

$$k_z^a = \frac{r_f^2}{4k} \cdot \frac{(1 - V_f^a)^3}{V_f^{a2}}, \quad k_z^{V_f} = \frac{r_f^2}{4k} \cdot \frac{(1 - V_f)^3}{V_f^2}$$

This leads to the correction equation Eq. (4.18).

CHAPTER 5 ARTICLE 3: TOMOGRAPHIC MODELING AND INTERNAL STRUCTURE ANALYSIS OF ENGINEERING TEXTILES: A PARAMETRIC APPROACH

Bin Yang, Cédric Béguin, Philippe Causse,
Yuwei Feng, Jihui Wang

Submitted to *Composite Structures* on xx/xx/2024

5.1 Chapter overview

The internal geometry of the textile reinforcements on different scales determines the flow pattern of the liquids within them. This chapter aims to establish a method for analyzing and modeling the mesostructure of textile reinforcements using tomographic imaging. The detailed structural information obtained by the proposed method can help to understand the relationship between the variability of the measured transverse permeability discussed in Chapters 3 and 4, and the structure of the reinforcements. Additionally, it can also be used to develop DMT models to predict the flow rate and the flow pattern under a given condition. The content of this chapter serves as the theoretical foundation for Chapter 6.

5.2 Abstract

Tomographic modeling of textiles is a very attractive tool for numerical investigation of composites because of its ability of the ability to reveal the internal architecture of the material. However, reliability is notably dependent on the accuracy of the geometrical modeling, which is challenged by the volume, preprocessing, and segmentation of the volumetric image and the geometry approximation of the fiber tows. This paper addresses this issue using a parametric approach that relies on statistical resampling and spatial autocorrelated prediction. The proposed strategy involves three stages: first, an explicit representation of each fiber tow is derived from the segmented dataset through kernel density estimation-based resampling in the parametric domain, which is subsequently mapped back to the physical domain according to spatial autocorrelation of known information. It allows for depicting tow surfaces with varying levels of detail depending on the number of selected key points during resampling. Second, the tow trajectory is parameterized and subjected to a smoothing process, thereby identifying the local fiber orientation as its tangent vector. Finally, the normal cross-sections

of tows are solved as intersecting implicit planes with a parametric tubular surface thanks to the parametric representation. This enables the assessment of spatial architectural variability in textiles with tows of significant waviness. The examination was carried out by contrasting the proposed approach with existing techniques at different stages. The results show that the reconstructed geometry is consistent with the scanned image and confirm that the proposed method is reliable and efficient.

Keywords: Textile reinforcements; Mesostructural modeling; Stochastic resampling; Internal structure analysis;

5.3 Introduction

Engineering textiles woven from fiber tows are widely used as reinforcements in high-performance composites. Simulation at the mesoscale has proven valuable for understanding their mechanical and percolation performance, as it bridges the gap between the micromechanisms and the macrobehavior. However, it remains challenging to accurately predict manufacturing defects and mechanical properties on the mesoscale due to the spatial variability and complexity of real fabric architecture. Volumetric imaging techniques are widely used to obtain detailed mesoscopic geometry of engineering textiles, for example, the weave pattern, the tow trajectory, and the spacing between them [113, 115, 218]. These can then be fed into Textile Geometrical Preprocessors (TGP), such as TexGen [18] and WiseTex [128], to generate realistic mesoscopic models of composites. Realistic models exhibit better representability [18, 67] over ideal models based on numerous assumptions and simplifications, which in turn leads to better numerical accuracy [151, 166, 219]. Additionally, it has the advantage of not requiring expertise in image processing. However, this method is either unable to fully exploit the vast amount of information contained in volumetric images, resulting in models with low level of detail, or the processing is extremely time consuming since extensive manual intervention is required.

Recent years have seen a rise in tomographic mesoscopic structural modeling of engineering textiles using a data-driven approach [218, 220]. The resulting textile models are referred to as *Digital Material Twins* (DMT) [110, 123] because they reflect the exact structure and material variability of the physical part and are ready to be used for virtual testing [19, 20, 113, 119, 123, 148, 221]. To generate a DMT, the initial step involves identifying the subdomains within the volumetric image, namely the matrix and fiber tows. This can be achieved through segmentation techniques such as manual or thresholding segmentation [110, 114], learning-based approaches [114, 123, 222], or structural tensor methods [121]. These techniques result

in a geometric representation of fiber tows, either as a point cloud of tow surfaces or as a cluster of voxels. It leads to two families of algorithms for textile geometry modeling: explicit and implicit methods.

The explicit method represents the surface of a 3D object with parametric surfaces, point clouds, or triangular meshes. Madra et al. [122] were among the first to create image-based geometrical models of single fiber tow with a parametric surface. Huang et al. [110] performed a further analysis of fiber tow morphology (such as cross-sectional circularity, area, etc.) utilizing this parametric framework. In fact, this is a key benefit of the explicit method. It facilitates the implementation of differential geometry operations. Moreover, advances in learning-based segmentation techniques make it more reliable and efficient to retrieve the geometry of textiles explicitly from images, as shown in [123, 222, 223]. The present study extends the research of Madra et al. and Huang et al. by integrating stochastic methods to enhance the robustness and efficiency of the approach. A streamlined procedure is developed for the analysis of internal structures and geometry modeling of textiles.

On the other hand, the interface between subdomains can be defined implicitly as the zero-level isosurface \mathcal{S} of a scalar field x as F : $\mathcal{S} = \{x \in \mathbb{R}^3 \mid F(x) = 0\}$. This is usually represented by discrete voxels labeled by the scalar. In fact, volumetric images themselves are such a scalar field. The boundaries between subdomains (fiber tows and matrix) can be determined by the isosurface of gray-level values in sufficiently high-resolution images. However, it is practically infeasible for mesoscopic scanning due to the compromise between sample size and scanning resolution [224]. The interfaces, particularly those between tows composed of the same material, are usually blurred. Consequently, an appropriate implicit scalar field has to be reconstructed after segmentation. In most cases, signed distance functions [19, 225], tow labels [110], and probability maps obtained by learning-based segmentation algorithms [118, 226] are used. According to Wintiba et al. [19], smoothing operations on an implicit representation can be automated more easily than on its explicit counterpart. However, an explicit representation is still required for geometrical analysis and the determination of element-wise properties locally to achieve accurate numerical predictions.

The discrete step-like interface between the subdomains of the volumetric images should be approximated by a smoothing surface mesh to perform geometrical analysis and create a conformal mesh [19, 227]. Therefore, smoothing techniques, such as Laplacian and Gaussian smoothing [19], Savitzky-Golay filtering [20], and the Catmull-Clark technique [21], were widely applied. An inherent problem is that these smoothing algorithms suffer from volume shrinkage, as they are based on the averaging of vertices. Consequently, a dilation algorithm is required to counteract volume shrinkage, as shown in [21, 227]. Thus, the efficiency of data

processing is further reduced. The accuracy of such an approximation is also questionable. The smoothing-dilation process could result in geometric distortions, as illustrated in the current study.

In addition, tomographic modeling experiences error and uncertainty due to two main factors. Firstly, the intrinsic spatial variability of materials introduces an irreducible aleatory uncertainty. Second, the processes involved in *in situ* scanning, segmentation, and model reconstruction contribute to a reducible epistemic uncertainty [223]. The second type of uncertainty may propagate to numerical simulations through geometry modeling, making the predictions unreliable. Therefore, quantifying and minimizing uncertainty represents a critical task. Very few modeling approaches have addressed the uncertainty that underlies the tomographic geometric modeling of engineering textiles so far. Another challenge that impedes the application of tomographic models is the efficiency of the modeling approach. The accuracy of modeling can generally be improved by using high-resolution volumetric images. However, this is often accompanied by a high computational cost and low processing efficiency.

The current research develops a geometric modeling strategy for engineering textile using volumetric images. It integrates stochastic resampling and spatial autocorrelation prediction techniques. This approach aims to address the challenges related to the large volume of volumetric images and the uncertainties induced by preprocessing, segmentation, and geometry approximation of fiber tows. A 3D orthogonal textile was subjected to Micro CT imaging, as explained in Section 5.4, which provided input data to apply the proposed method. The geometrical modeling procedure was considered to be a fundamental problem related to point-cloud parameterization, clustering, stochastic resampling, and geometry modeling. Section 5.5 details the mathematical formulations that underlie these fundamental concepts. By mapping the envelop surface of a fiber tow onto a parametric domain, the problem was reduced to 2D. This enables anisotropic morphological operations while reducing handling complexity. In this section, we also address the determination of tow trajectories and normal cross-sections, particularly for fiber tows with considerable waviness. Finally, we demonstrate and compare the proposed approach with other existing techniques in Section 5.6. The spatial variation of the internal textile architecture was examined, such as the local orientation and the cross-sectional area of the fiber tows. As an advantage of the proposed approach over existing techniques, it prevents volume shrinkage when smoothing the tow surface. Therefore, dilation algorithms are no longer required. The proposed approach offers several benefits compared to existing methods. It effectively avoids volume reduction during smoothing of the tow surface and enables accurate extraction and reproduction of local geometric features using DMT models.

5.4 Material characterization

An orthogonal 3D woven glass textile, TG96N, from Texonic Inc. was used to illustrate the proposed tomographic modeling approach. It consists of three different yarns: straight warp and weft yarns are orthogonal and bound together by the wavy binder yarns (see Figure 5.1). Nikon XTH 225 was used to perform the observations with a voxel size of $22^3 \mu\text{m}^3$. The size of the *Region of Interest* (ROI) shown in Figure 5.2a contains six-unit cells. To maximize the field of view, the scanning resolution is lower than in other investigations that focus on analyzing microscopic structures [147]. This compromise is deemed necessary to create mesoscopic models that reflect the variability of actual reinforcements, as discussed in [228]. The fiber volume fraction of the specimen is 57 %.

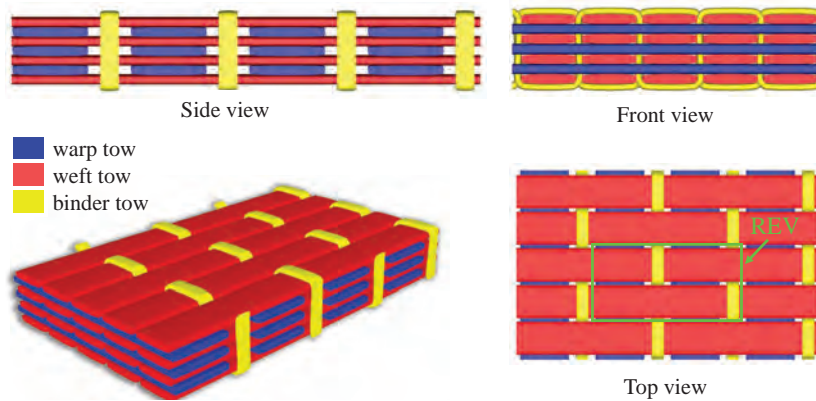


Figure 5.1 Woven structure of the 3D orthogonal textile TG96N from Texonic Inc.

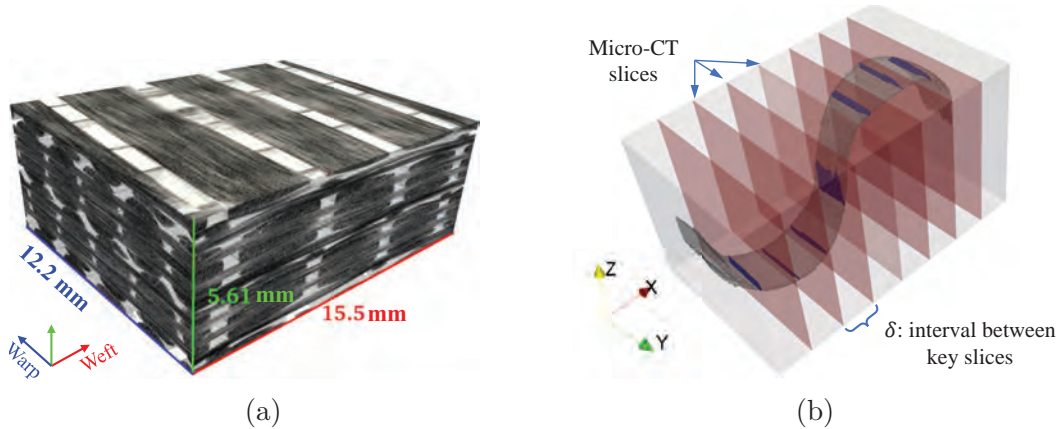


Figure 5.2 Textile internal architecture characterization: (a) The Region of Interest (ROI) subjected to subsequent analysis; (b) Schematic of Micro-CT slices. These Micro-CT slices do not always align perpendicularly with the fibers within the tow.

A semi-automatic segmentation method was implemented in ImageJ [229] to obtain the input data for ROI reconstruction. It consists of three steps: (1) manual segmentation of key Micro-CT slices by an interval of δ (see Figure 5.2b); (2) mathematical morphology interpolation between key slices; (3) interactive correction of the interpolation results. Different interpolation functions were used depending on the trajectory of the fiber tows. The segmented 3D point clouds provide an explicit representation of each tow contour that can then be used for denoising, geometrical modeling, and spatial variability analysis. Although only TG96N was presented here, the proposed approach should be applicable to any tow-based textile.

5.5 Methodology

5.5.1 Parametric representation of tow geometry

The geometry of a fiber tow can be approximated as an envelop surface \mathcal{S} embedded in a 3D space \mathbb{R}^3 , as illustrated in Figure 5.3a. It is assumed that:

- the envelop surface is watertight and distinctive, enabling a clear distinction between matrix and reinforcement or between different tows,
- it is a smooth surface with a degree of continuity greater than 1. Hence, differential geometry tools can be applied for data manipulation.

On each Micro-CT slice, the cross-section of a fiber tow can be approximated by a polygon, as shown in 5.3b. The vertices of all polygons on the Micro-CT slices constitute a point cloud dataset describing the envelope surface. To facilitate morphology analysis and geometry reconstruction, the point cloud was parameterized onto a planar parametric domain Ω by a function $\mathbf{r}: \mathcal{S} \rightarrow \Omega$ (see Figure 5.3c):

$$\mathbf{r}(s, t) = \begin{pmatrix} x^w(s, t) \\ y^w(s, t) \\ z^w(s, t) \end{pmatrix}, \quad (s, t) \in \Omega \quad (5.1)$$

where x^w, y^w and z^w are functions of the coordinates (s, t) in the parameter space.

In this study, the parameter s represents the normalized arc length starting ($s = 0$) and ending ($s = 1$) at a cutting point, where the polygon intersects the positive x^l -axis of the local coordinate originating at the centroid of the cross-section (see Figure 5.3b). The centroid is determined by analyzing the image momenutum, as reported by Vanaerschot et al [230]. The

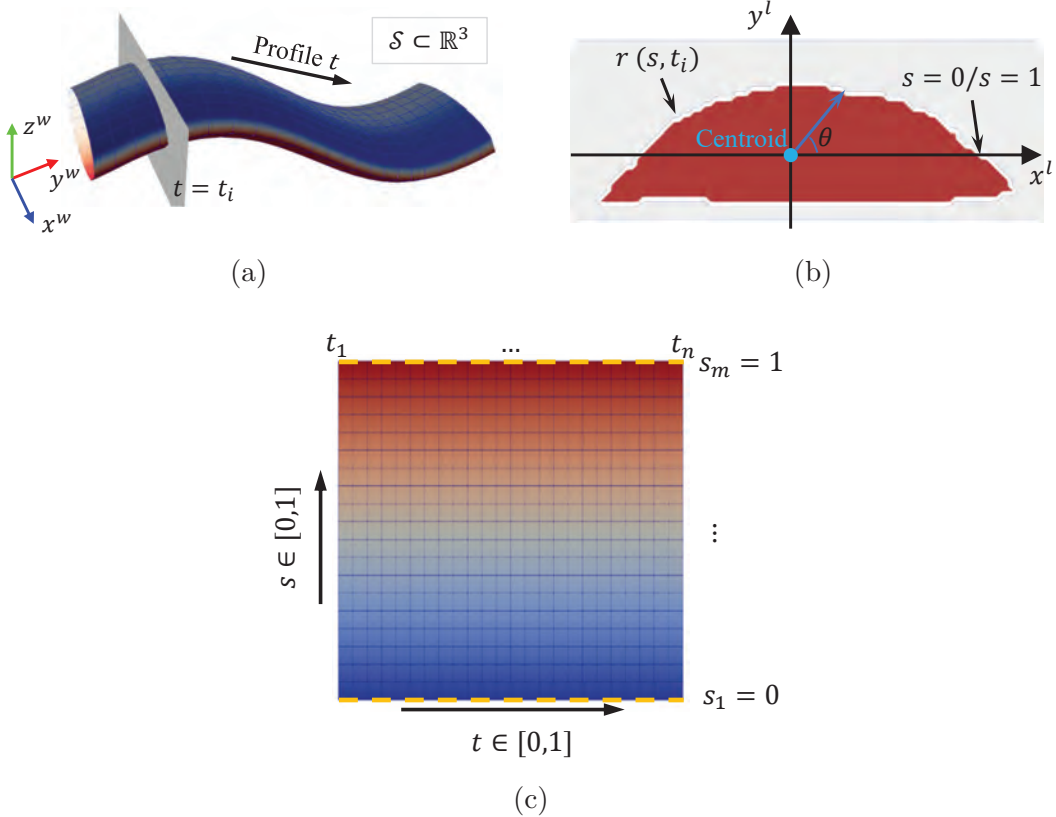


Figure 5.3 Parametric representation of fiber tows: profile t along the axial direction (a) and profile s in the radial direction (b) are mapped on to a rectangular parameter domain Ω with different resolution (c). The dashed line in (c) represents the cutting path along which the tow surface is unfolded.

parameter t represents the normalized length of the fiber tow (see Figure 5.3a). Consequently, the tow surface is transformed into the parameter domain $\Omega : [0, 1] \times [0, 1]$ and is described by n cross-sections, each of them is approximated by a polygon with m vertices, as shown in Figure 5.3c. In the following, x^w , y^w , and z^w are represented as x , y , and z for the sake of simplicity.

5.5.2 Point cloud clustering and resampling

The parametric representation requires an equal number of points, which may not be evenly spaced, to describe each cross-section. Therefore, selecting a limited number of points capable of capturing geometry features while remaining unaffected by segmentation noise is crucial. To achieve this, the point cloud of each fiber tow (Figure 5.4a) is initially parameterized and then decomposed into multiple clusters using univariate analysis on the normalized radial

distance s . The statistical technique employed for this purpose is the Kernel Density Estimation (KDE). It is used to estimate the probability density function $\hat{f}_h(s)$ in the parameter space:

$$\hat{f}_h(s) = \frac{1}{N} \sum_{i=1}^N K_h(s - s_i) \quad (5.2)$$

where N is the size of the point cloud. The kernel function K_h is centered on the variable to be estimated and puts more weight on points close to it. The kernel function in this work was predetermined to be Gaussian:

$$K_h(s - s_i) = \frac{1}{\sqrt{2\pi}h} e^{-\frac{(s-s_i)^2}{2h^2}} \quad (5.3)$$

where h is a hyper-parameter called bandwidth. It controls the smoothing range that K_h performed and was initialized with Scott's rule of thumb [231].

The distribution of the point cloud shown in Figure 5.4a is estimated in the parameter space using the suggested method. The result is shown in Figure 5.4b. Points located in regions subject to sharp changes are associated with high probability density, while points in regions with fewer changes show a low probability density. This provides a geometric signature for fiber tows. The point cloud is then clustered using the local minima of the probability density function as boundaries and the local maxima as cluster centers, as shown in Figure 5.4c. The choice of bandwidth significantly influences the number of clusters. A decrease in bandwidth captures finer details but may also introduce more noise, whereas a larger bandwidth smooths out more details, potentially obscuring subtle features.

An adaptive approach for filtering and resampling point clouds is established on this basis. The approach involves eliminating low-frequency elements (spatial redundancy and noise) within each cluster. The cluster centers are used to describe the overall geometry. Consequently, each cross-section is represented by an equal number of control points, as shown in Figure 5.4d. The representative fidelity of the resampled point cloud can be adaptively adjusted via bandwidth. Given that both the clustering and resampling of point clouds are performed within the parameter space, the resultant coordinates of the resampled points also reside in this space. Besides, the resampled points may not be a subset of the input dataset. The methodology for mapping these points back to the geometric space is detailed in Section 5.5.3.

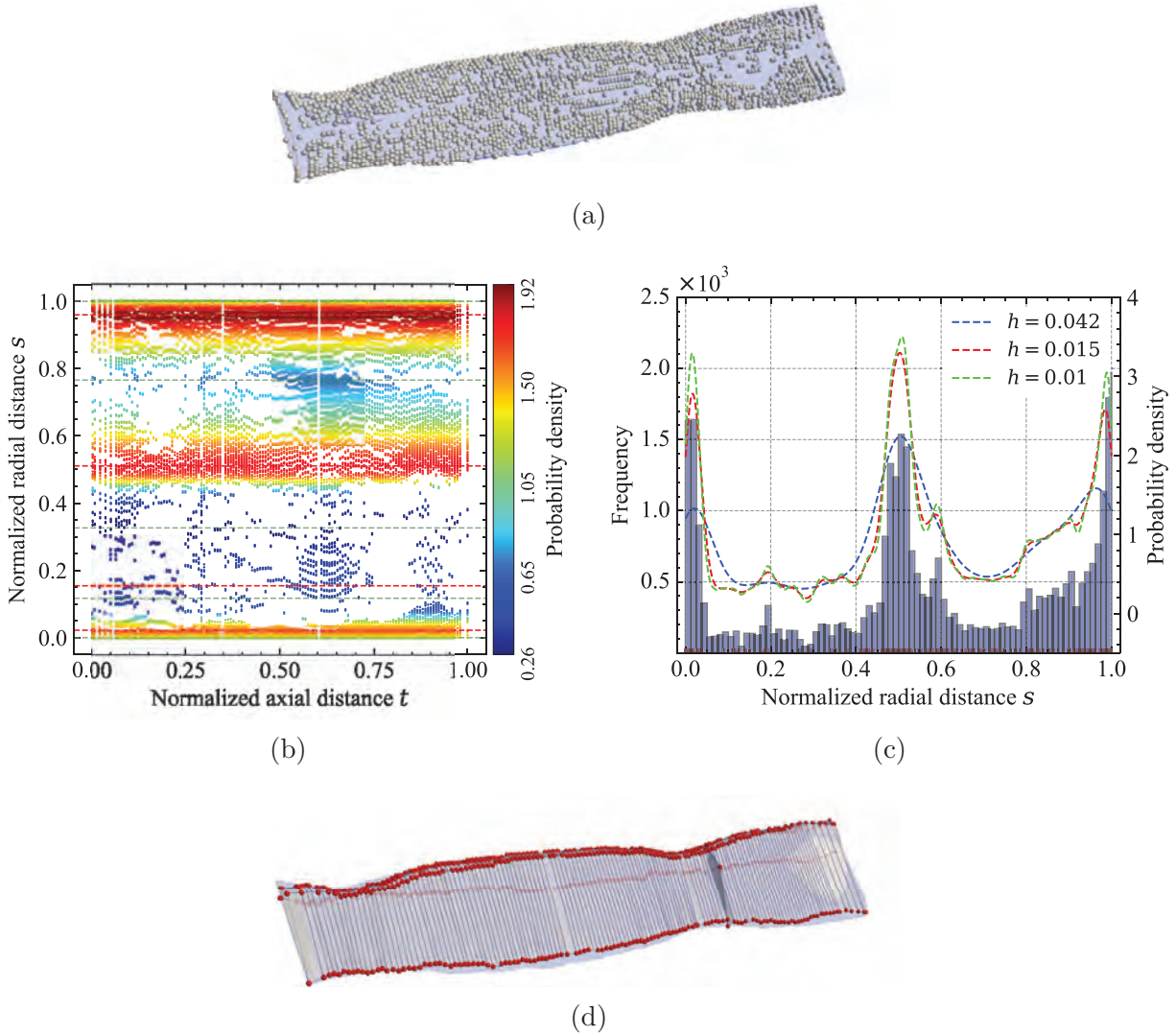


Figure 5.4 Illustration of point cloud clustering and resampling: (a) A fiber tow represented by a point cloud consisting of 11088 points in geometric space $(x, y, z) \in \mathbb{R}^3$; (b) Distribution of points and associated probability density in parameter space $(s, t) \in \Omega$; (c) Impact of bandwidth h on probability density estimation using Gaussian kernel; (d) Fiber tow profile reconstructed with the cluster centers. Kriging-based estimator is used to map the resampled point cloud back to the geometric space. Red and green horizontal lines in (b) represent the cluster centers and boundaries. Only four clusters are decomposed here for illustration purposes.

5.5.3 Reconstruction of tow geometry

According to the parametric representation defined in Section 5.5.1, the envelop surface of a fiber tow can be represented by Eq. (5.1). Nonetheless, it is generally not feasible to find a simple analytical function to approximate a real fiber tow geometry with sufficient

accuracy. From a statistical point of view, the coordinate (x, y, z) of the points describing a fiber tow can be considered as the possible realizations of random variables $x(s, t)$, $y(s, t)$, and $z(s, t)$. These random variables establish a connection between the geometric and parameter spaces, and enable the estimation of the corresponding positions of the cluster centers in the geometric space from the known points. Estimators of these random variables are established by a linear combination of the individual covariance between the point to be estimated and each of those known values C_i and a trend (local mean represented by a polynomial):

$$w(s, t) = \sum_{i=1}^N \lambda_i C_i + \sum_{i=0}^{m'-1} \sum_{j=0}^{n'-1} \mu_{ij} s^i t^j, \quad w = x, y, \text{ or } z \quad (5.4)$$

where N denotes the size of the point cloud. m' and n' represent the degree of s and t in the trend term. The weights $[\lambda_1 \dots \lambda_N \mu_{00} \dots \mu_{ij} \dots \mu_{m'n'}]$ are solved by minimizing the variance of estimation with unbiasedness constraint. For the parametric method presented in Section 5.5.1, the formulation of the estimator reads:

$$w(s, t) = \mathbf{k}_1(s)^\top \cdot \mathbf{A}_s^{-1} \cdot \mathbf{P}_w(s, t) \cdot \mathbf{A}_t^{-1} \cdot \mathbf{k}_2(t), \quad w = x, y, \text{ or } z \quad (5.5)$$

where $\mathbf{k}(s)$ and $\mathbf{k}(t)$ are the covariance vectors of s and t , respectively:

$$\mathbf{k}_1(s) = \begin{bmatrix} \text{Cov}(s, s_1) & \dots & \text{Cov}(s, s_m) & 1 & \dots & s^{m'-1} \end{bmatrix}^\top \quad (5.6)$$

$$\mathbf{k}_2(t) = \begin{bmatrix} \text{Cov}(t, t_1) & \dots & \text{Cov}(t, t_n) & 1 & \dots & t^{n'-1} \end{bmatrix}^\top \quad (5.7)$$

The matrix \mathbf{P}_w contains the coordinate component of known points and a number of zeros:

$$\mathbf{P}_w = \begin{bmatrix} w(s_1, t_1) & \dots & w(s_1, t_n) & & \\ \vdots & \vdots & \vdots & \mathbf{0}_{m \times n'} & \\ w(s_m, t_1) & \dots & w(s_m, t_n) & & \\ & \mathbf{0}_{m' \times n} & & \mathbf{0}_{m' \times n'} & \end{bmatrix} \quad (5.8)$$

\mathbf{A}_s and \mathbf{A}_t are the coefficient matrices expressed as:

$$\mathbf{A}_s = \begin{bmatrix} & 1 & \dots & s_1^{m'-1} \\ \mathbf{C}_{ij} & \vdots & & \vdots \\ & 1 & \dots & s_m^{m'-1} \\ 1 & \dots & 1 & \\ \vdots & \vdots & & \mathbf{0}_{m' \times m'} \\ s_1^{m'-1} & \dots & s_m^{m'-1} & \end{bmatrix}, \quad \mathbf{A}_t = \begin{bmatrix} & 1 & \dots & t_1^{n'-1} \\ \mathbf{C}_{ij} & \vdots & & \vdots \\ & 1 & \dots & t_n^{n'-1} \\ 1 & \dots & 1 & \\ \vdots & \vdots & & \mathbf{0}_{n' \times n'} \\ t_1^{n'-1} & \dots & t_n^{n'-1} & \end{bmatrix} \quad (5.9)$$

for $1 \leq i, j \leq (m \times n)$

in which the stationary covariance matrix \mathbf{C}_{ij} is as follows ($p = s$ for \mathbf{A}_s and $p = t$ for \mathbf{A}_t):

$$\mathbf{C}_{ij} = \begin{cases} \text{Cov}(p_i, p_j) & i \neq j \\ \sigma^2 & i = j \end{cases} \quad (5.10)$$

σ^2 measures the variance of the estimation error and is proportional to the gap between the estimated value and the ground truth. As a matter of fact, the closer the cross-sections of a fiber tow are, the more similar the profiles will be. Thus, an assumption, called the intrinsic hypothesis, is introduced. It states that the relationship of two points depends only on the distance between them. Hence, let:

$$\mathbf{C}_{ij} = K(|p_i - p_j|) \quad (5.11)$$

This is called generalized covariance, where $|p_i - p_j|$ is the distance in the parameter domain Ω ($p = s$ or $p = t$). Depending on the shape of the profile, different generalized covariance and trends can be selected. The continuity of the parametric surface is determined by the order of the generalized covariance and the trend. This formulation is referred to as dual kriging [232, 233].

Note that $\mathbf{r}(s, t)$ is reduced to a parametric kriging equation for a space curve when one of the parameters (s or t) is assigned as a constant. For example, the parametric equation of a horizontal line in Figure 5.3c can be obtained by specifying s , while t should remain constant to acquire the parametric equation of a vertical line. This feature is further employed to parameterize fiber tow trajectories and determine the cross-sections that are perpendicular to the tows.

5.5.4 Tow trajectory and local orientation

The image skeleton technique, implemented in ImageJ [229], is used to extract the trajectory of fiber tows. Subsequently, the trajectory is parameterized with the normalized length of fiber tows, t , the same as for the axial direction of the fiber tow envelope surface:

$$w(t) = \sum_{i=1}^n b_i K(|t - t_i|) + \sum_{i=0}^{n'-1} a_i t^i, \quad w = x, y, \text{ or } z \quad (5.12)$$

where the coefficient a_i and b_i are the solution of the linear system:

$$\begin{bmatrix} & 1 & t_1^{n'-1} \\ K(|t_i - t_j|) & \vdots & \vdots \\ & 1 & t_n^{n'-1} \\ 1 & \dots & 1 \\ \vdots & \dots & \vdots \\ t_1^{n'-1} & \dots & t_n^{n'-1} \end{bmatrix} \cdot \begin{bmatrix} b_1 \\ \vdots \\ b_n \\ a_0 \\ \vdots \\ a_{n'} \end{bmatrix} = \begin{bmatrix} w_1 \\ \vdots \\ w_n \\ \mathbf{0}_{n' \times 1} \end{bmatrix} \quad (5.13)$$

The local orientation of fiber tows can then be determined by the derivatives of the parametric curve equations $(x'(t), y'(t), z'(t))$.

5.5.5 Normal cross-sections of fiber tow

It is essential to determine the cross-sectional profiles that are perpendicular to a fiber tow (see Figure 5.5c, hereafter referred to as normal cross-sections) to quantify the spatial variability of textiles in geometry and material properties. Thanks to the parametric representation, the problem is simplified as the intersection of a plane with a number of iso-parametric curves. As mentioned in previous sections, the parametric surface equation $\mathbf{r}(s, t)$ is reduced to a parametric equation for a curve lying on the tow surface when s is fixed:

$$\mathbf{r}(s_i, t) = \begin{pmatrix} x(s_i, t) \\ y(s_i, t) \\ z(s_i, t) \end{pmatrix}, \text{ for } s \in [0, 1] \quad (5.14)$$

The tangent vector $\vec{n} = (A, B, C)$ of a given point on the trajectory (x_c, y_c, z_c) can be obtained by taking the derivatives of the parametric equation of the trajectory. Hence, the plane \mathcal{P} on which the normal cross-section lies can be expressed as:

$$\mathcal{P}: A(x - x_c) + B(y - y_c) + C(z - z_c) = 0 \quad (5.15)$$

Thus, a series of points describing the profile of the normal cross-section is determined by solving:

$$e(s_i, t) = A(x(s_i, t) - x_c) + B(y(s_i, t) - y_c) + C(z(s_i, t) - z_c), \text{ for } s \in [0, 1] \quad (5.16)$$

As proposed by Limaiem and Trochu [234], the intersecting segment $(t, t+\Delta t)$ can be found by $e(s_i, t) \cdot e(s_i, t+\Delta t) \leq 0$ since the plane \mathcal{P} divides the space into three regions that correspond to $e(s_i, t) = 0, > 0$ and < 0 . The intersecting segment is then recursively subdivided until the desired accuracy is achieved. The golden section search algorithm is used to accelerate the recursive subdivision process. One major benefit of this approach is that the resulting intersecting points are sorted and can be readily used for geometry analysis. Figure 5.5d shows an example of the identified normal cross-sections.

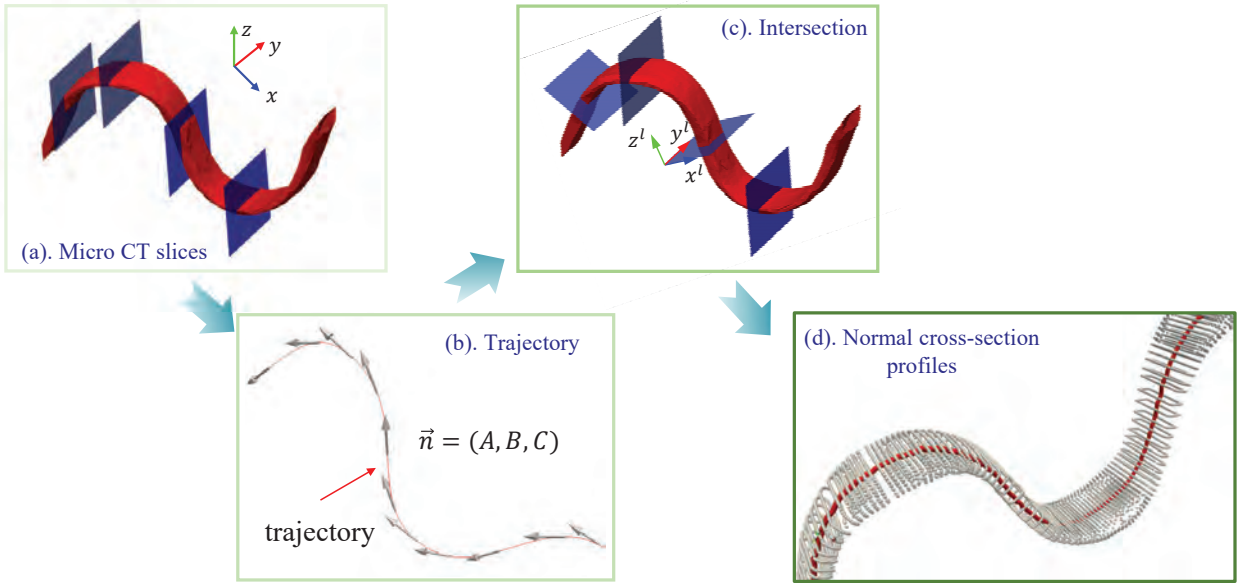


Figure 5.5 Normal cross-section identification: (a) envelop surface of a fiber tow segmented from Micro-CT slices; (b) trajectory of tows with its tangent identified; (c) intersection detection between an implicit plane (defined by the trajectory tangent \vec{n} and its origin) and the parametric surface of fiber tow; (d) the identified normal cross-sections that are perpendicular to the tow trajectory.

5.5.6 Geometry smoothing

Another attractive feature of this parametric approach is its ability to achieve a smooth representation of the geometric shape being considered, whether it is a surface or a curve. For a parametric surface, the diagonal elements of Eq. (5.10), σ^2 , serves as a smoothing factor. The surface passes through all points in the given point cloud when $\sigma^2 = 0$, while deviating from them when $\sigma^2 > 0$ and the parametric surface is smoothed. The smoothing of the fiber tow trajectory can also be achieved by replacing the first n diagonal elements of the matrix coefficient in Eq. (5.13) with a value greater than 0. By adjusting this value, the strength of smoothing can be controlled. Additional advantages provided by this smoothing technique is further discussed in Section 5.6.

5.5.7 Code implementation

An open-source Python package named *PolyTex* was developed based on the methodology outlined in this paper. This package incorporates the techniques described here and is easily accessible to users. Examples can be found in the online documentation [235]. Sample scripts are also provided as supplementary data. Furthermore, *PolyTex* also offers specialized helper functions designed for image-based geometric modeling and analysis of textile reinforcements.

5.6 Comparative analysis and case study

5.6.1 Effects of point clustering on geometry approximation

The KDE-based point cloud clustering method offers the benefit that points for describing the cross-section profiles of a fiber tow can be resampled based on the variation of its geometry. This improves the efficiency of data storage and processing compared to using equidistant points. Figure 5.6a illustrates two methods for implementing point cloud clustering and resampling. It can be applied to the entire dataset, namely clustering and resampling globally. On the other hand, it can be applied locally in a moving window that is sliding in the axial direction.

Figures 5.6b - 5.6e present a qualitative assessment in which the shape of a weft tow, approximated using resampled points (depicted in red), is superimposed onto the reference structure (shown in gray). Differences between the two are highlighted with dashed ellipses. The geometries shown in Figures 5.6b and 5.6c were derived by global clustering and resampling with $m = 30$ (each tow cross-section was approximated with a polygon of 30 vertices) and $m = 50$, respectively. The geometries in Figures 5.6d and 5.6e were obtained by clustering

and resampling locally with $m = 50$ and $m = 100$ using the moving windows illustrated in Figure 5.6a with colors.

For both approaches, the difference in structure between the resampled geometry and the reference decreases as m grows. This is anticipated due to the increased density of vertices used to approximate fiber tow cross-sections. When m is constant (e.g., $m = 50$), the moving window method (Figure 5.6d) exhibits fewer discrepancies compared to the global method (Figure 5.6c). This superiority arises from the localized nature of the moving window method. By concentrating on smaller sections at a time, it captures local geometry variations more accurately.

Quantitative evaluation was also performed by comparing the cross-sectional area, height and width of the tow with the manually measured ground truth values, as illustrated in Figure 5.6f. Increasing m from 30 to 50 leads to a decrease in the relative error of 2% for the global method. The deviation of the moving window method is 1% less than that of the global method for $m = 50$. The reference structure can be fully replicated with $m = 100$. However, this seems unnecessary, as approximating the cross-sections with 30 points still maintains a relative error lower than 4% for all geometry features.

5.6.2 Geometry smoothing

Envelop surface of fiber tow The newly proposed geometric smoothing technique is compared with two widely used algorithms, Laplacian [19] and Taubin [236]. Their impact on the volume and shape of the object being smoothed is assessed. As indicated in Figure 5.7a, a rugged geometry model of a weft tow that was segmented directly from Micro-CT images serves as input in this case study. Laplacian smoothing leads to a significant shrinkage in volume as the number of iterations increases. In contrast, the Taubin algorithm achieves comparable smoothing effects with fewer iterations and avoids volume reduction. Nonetheless, both techniques introduce distortions in the smoothed geometry, especially at the ends of the tow, as illustrated in the insets in Figure 5.7a.

The method proposed in this study is the most efficient in preventing volume reduction and maintaining geometric features at various values of smooth factor. Shrinkage is prevented by the proposed method for several reasons. First, the kriging estimator is formulated by minimizing the variance of the estimation errors. Second, the estimated values are calculated as a weighted linear combination of the known dataset, as shown in Eq. (5.4). Lastly, the method searches for the combination that results in zero estimation error, adhering to the "unbiased" constraint.

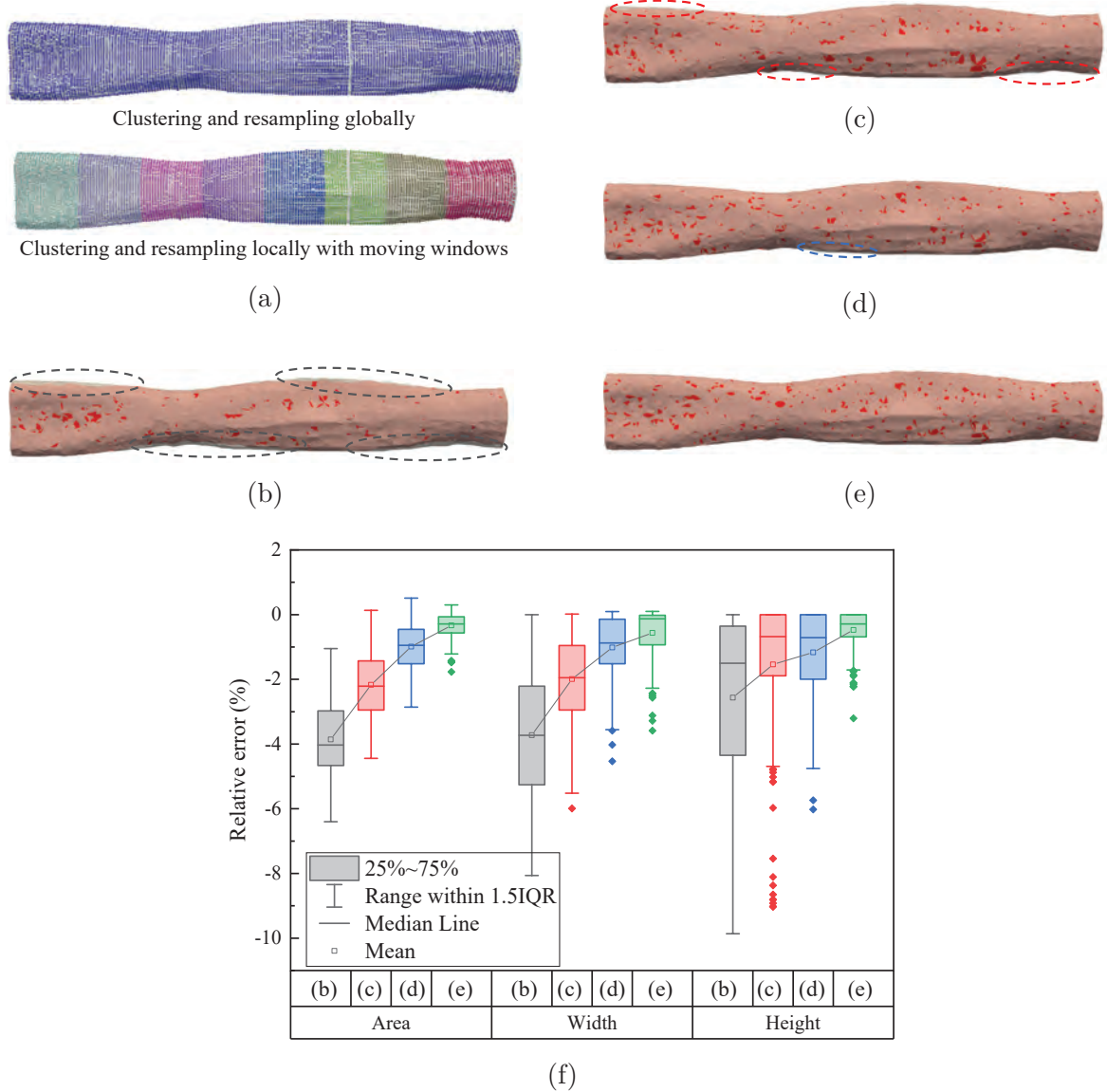


Figure 5.6 Effect of point cloud clustering on geometry approximation accuracy: (a) Point clustering and resampling globally considering the entire tow or locally with a moving window (indicated by different colors) sliding along the axial direction; Global clustering with (b) $m = 30$ (each tow cross-section approximated with a polygon of 30 vertices) and (c) $m = 50$; Local clustering with (d) $m = 50$ and (e) $m = 100$; The geometry approximated with the resampled points (in red) is overlaid onto the reference fiber tow structure (in gray). (f) Derivation of geometry features from ground truth for the cases shown in (b) - (e).

The geometry features of a fiber tow show significant differences in the axial and radial directions. The axial morphology changes periodically with the textile weave pattern, whereas the radial structure is closely related to the contact of the adjacent tows. Therefore, achieving

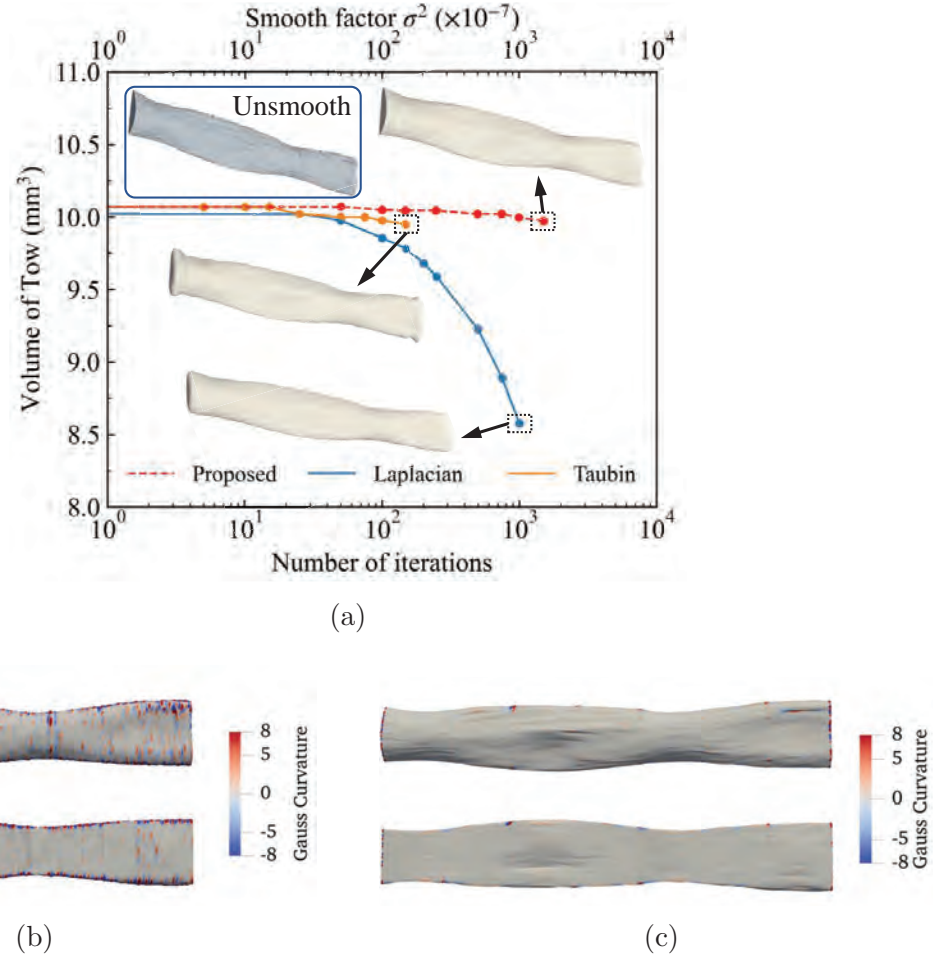


Figure 5.7 Tow surface smoothing: (a) Tow volume versus iterations (or smooth factor σ^2 for the proposed method) for various smoothing algorithms. Anisotropic smoothing along the radial direction (b) or the axial direction (c) of a fiber tow using the proposed method. No smoothing is applied to the perpendicular direction. Both the top and bottom views of the tow are shown and visualized with Gaussian curvature.

satisfactory smoothing in both directions can be challenging. The proposed method achieves anisotropic smoothing by assigning different smoothing factors to the radial and axial directions. Figures 5.7b and 5.7c show the fiber tow that was smoothed along the radial and axial directions, respectively, with a smooth factor of $\sigma^2 = 10^{-4}$. No smoothing is applied to the other direction, making it more rugged. This preserves the fiber tow geometry along a specific direction while simultaneously achieving smoothing along the other. It is tailored to match the inherent directional properties of the fiber tows.

Tow trajectory A comparative analysis was conducted with three established curve smoothing filters: the Savitzky-Golay (SG) filter, the Fast Fourier Transform (FFT) filter, and the median filter. Data from a binder tow trajectory were utilized for this analysis. Figure 5.8a illustrates the trajectory without smoothing (referred to as "Raw"), showing sharp localized fluctuations. The parametric equation constructed using kriging faithfully mirrors the initial shape of the tow trajectory at a smoothing factor of $\sigma^2 = 0$. As σ^2 increases, smoothing is progressively introduced. Local serrations are effectively eliminated with $\sigma^2 = 0.2$. Further increasing the smoothing factor to 10 enhances the smoothing effect. However, it also causes deviations from the initial trajectory, which can result in a loss of essential details and a misrepresentation of local fiber directions.

The Savitzky-Golay filter fits a polynomial function within a moving window and uses it to estimate smoothed values. Hence, its effectiveness in suppressing spurious fluctuations depends on the selection of window size (win) and polynomial degree (deg). As shown in Figure 5.8b, with the parameters configured to $\text{win} = 31$ and $\text{deg} = 3$, the level of smoothing achieved is comparable to the kriging approach with $\sigma^2 = 0.2$. However, achieving optimal smoothing results with the Savitzky-Golay method requires fine-tuning of two parameters, which is not a straightforward task.

The challenges encountered by the FFT and median filters are evident in Figures 5.8c and 5.8d. The FFT filter operates in the frequency domain and acts as a low-pass filter by attenuating high-frequency noise. Figure 5.8c shows that sequentially reducing the cutoff frequency to 2.0, 1.0, and 0.5 Hz exhibits increased smoothness. However, both endpoints of the trajectories show varying degrees of underfitting. On the other hand, when the median filter is applied to the z -coordinates of sinusoidal-shaped binder tow trajectories, straight lines are observed at the peaks and troughs of the waveform. However, in the y -direction, an adequate level of smoothing is not achieved.

5.6.3 Tow trajectory and local orientation

As illustrated in Figure 5.9a, the trajectories of the fiber tows were extracted and labeled separately. Each trajectory specifies the position of an individual tow within the 3D textile structure and corresponds to a continuous and differentiable parametric equation. Hence, the local fiber orientation can readily be determined from the tangent of the trajectories, as shown in Figure 5.9b. Unrealistic fluctuations can be observed on the fiber tow trajectory extracted directly from the volumetric image (see Figure 5.8a ("Raw")).

The smoothing technique proposed in this study successfully reduces these fluctuations, as illustrated in Figure 5.10. The left panel and the right panel show Region I (depicted in

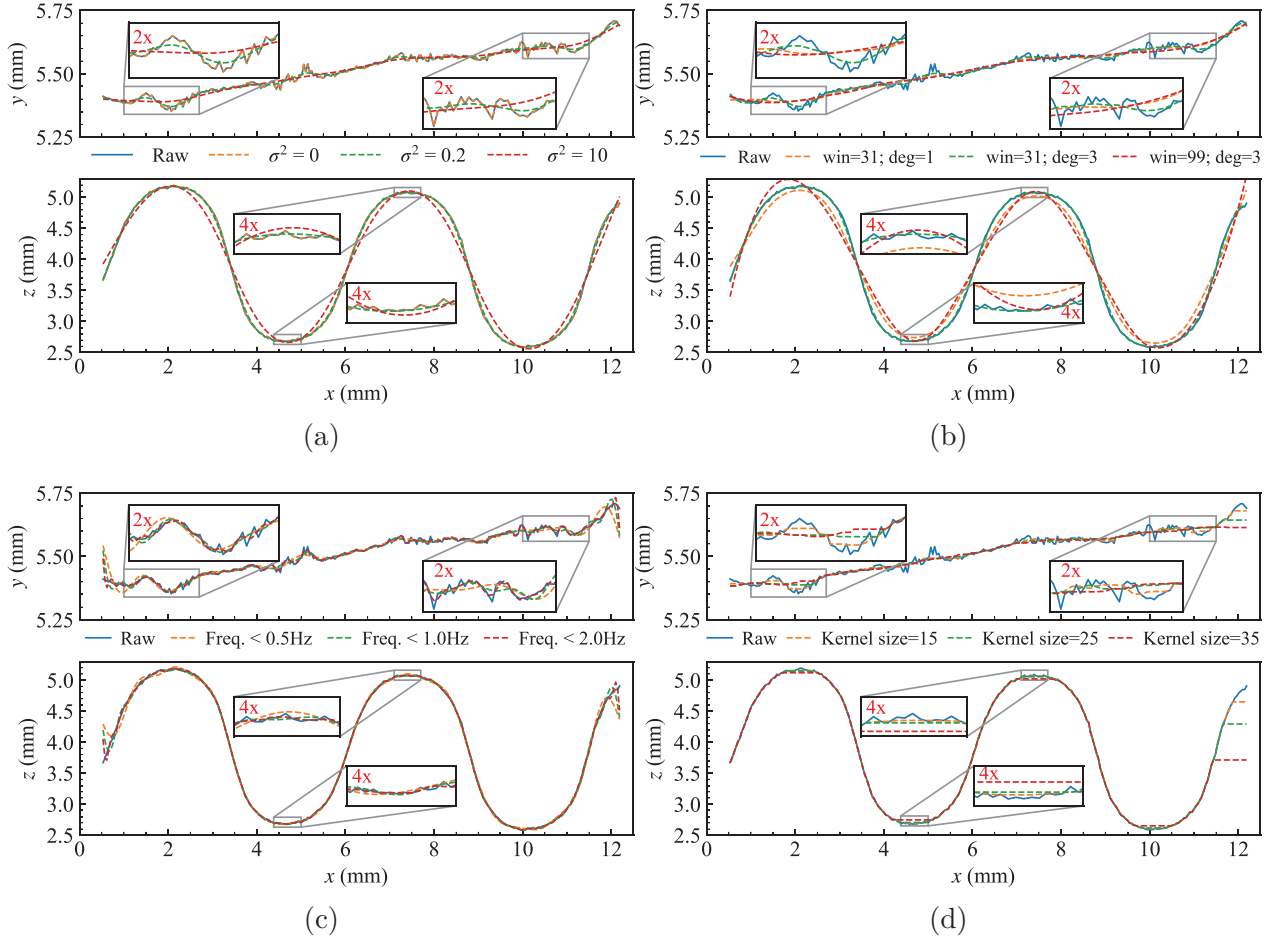


Figure 5.8 Suppression of spurious fluctuations in a binder tow trajectory using various techniques: (a) kriging; (b) Savitzky-Golay filter; (c) Fast Fourier Transform (FFT); (d) Median filter. The insets labeled “2x” and “4x” indicate curves enlarged by a factor of 2 and 4, respectively.

red, representing part of the binder tow trajectory) and Region II (depicting part of the weft tow trajectory in brown) that indicated in Figure 5.9b, respectively. It can be observed that as the smoothing intensity (σ^2) increases, local fluctuations are effectively suppressed, regardless of whether the trajectory is curved or straight. This facilitates the determination of the local fiber orientations. Note that it is important to choose the smoothing intensity carefully to avoid obscuring any local waviness that exists in a real fabric.

5.6.4 Normal cross-sections of fiber tow

An assessment of the normal cross-sections acquired through the proposed method was conducted by comparing it with two established techniques: the mesh trimming method and

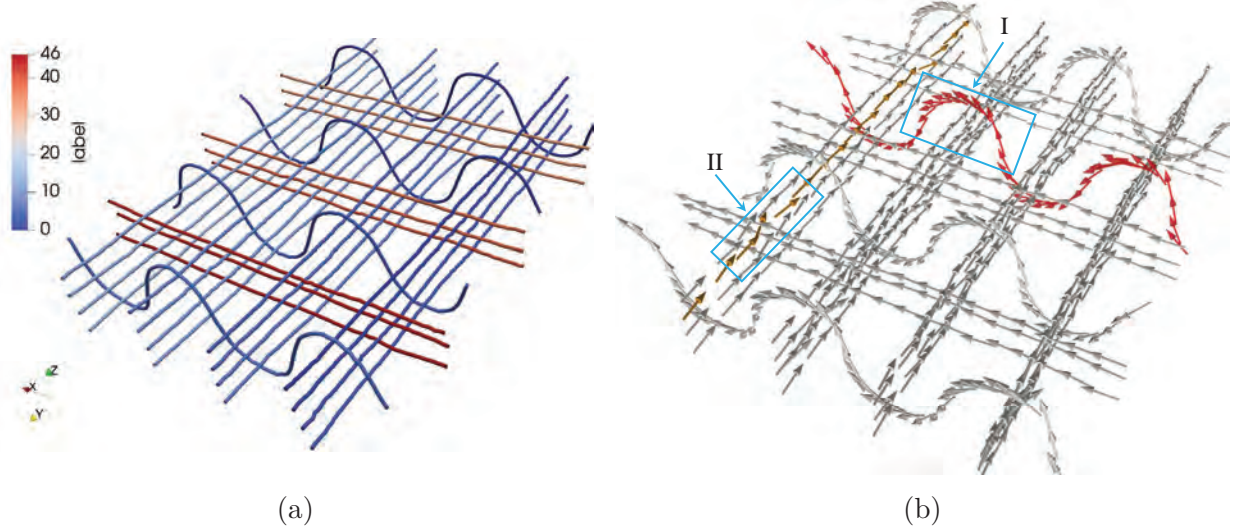


Figure 5.9 Fiber tow trajectories (a) and local orientations (b) in a single layer of the textile shown in Figure 5.2a.

the projection method. The former involves using a tool mesh to crop a target mesh, as shown in Figure 5.11a. In our case, the tool mesh is the envelop surface of a fiber tow. The target mesh to be trimmed is the normal plane determined by a point on the tow trajectory and the associated tangent vector. This tool is implemented using a Python package named PyVista [237]. It serves as a standard for assessing different methods. The projection method directly projects the segmented cross-sections on the Micro-CT slices onto the normal plane (Figure 5.11b).

Figure 5.12(a) - (d) shows the cross-sectional area for four different binder tows. The area obtained directly from segmented tow profiles on Micro-CT slices shows considerable overestimation (reaching up to 465%) compared to those obtained through the mesh trimming technique. This discrepancy occurs because the Micro-CT slices represent only the non-perpendicular cross-sections to the trajectory. As indicated by insets I and III in Figure 5.11c, those cross-sections show significantly larger area than normal cross-sections at the same positions, while in the case shown in inset II, the two types of cross-sections completely overlap. Hence, the degree of overestimation shows a significant correlation with the shape of the fiber tows. This underscores the importance of algorithms for accurately identifying the normal cross-sections in textile internal structure analysis.

The proposed method demonstrated favorable results, closely matching with the area achieved using the mesh trimming method. The maximum deviation is approximately 10%, whereas the average deviation is around 1.5%. One notable advantage of the proposed approach is

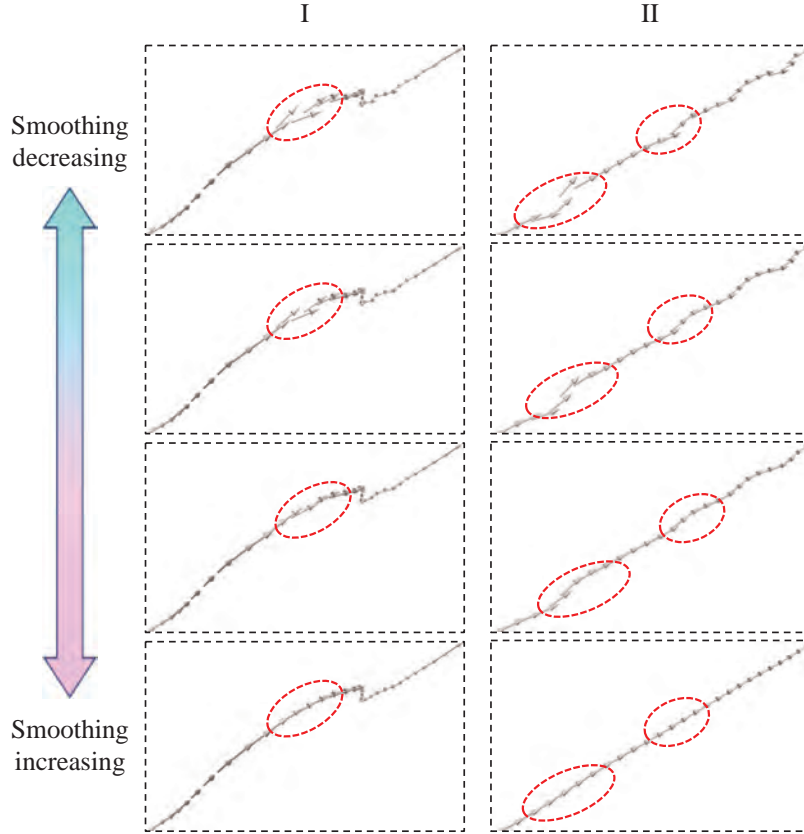


Figure 5.10 Effect of smoothing strength using the proposed method on local fiber orientations. I and II correspond to the regions labeled in Figure 5.9b.

that it eliminates the need for a mesh of fiber tow surface and normal planes. Therefore, the accuracy of the estimation is no longer affected by mesh resolution, a common challenge associated with the mesh trimming technique. The projection method offers more accurate measurements compared to the one measured directly on Micro-CT slices. Nevertheless, there are cases where a significant overestimation of around 45% is detected.

The analysis of warp and weft tows is shown in Figure 5.12e and Figure 5.12f, respectively. The area obtained from all the different methods showed good agreement. The maximum deviation between the methods was 6% for warp tows and 5% for weft tows. Once again, the proposed method showed a very good consistency with the mesh trimming technique (maximum deviation < 2.7%).

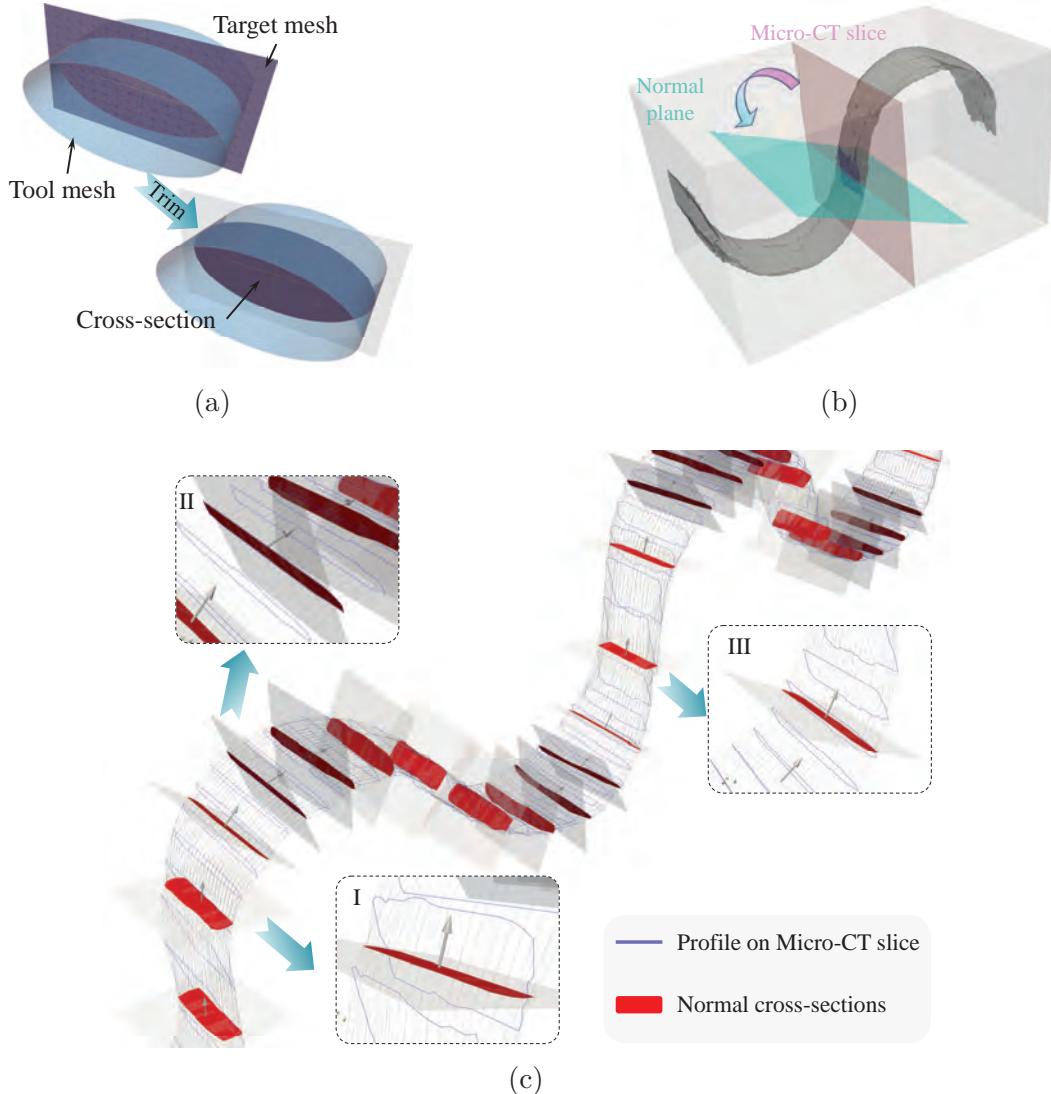


Figure 5.11 Illustration of mesh trimming method (a) and projection method (b) for cross-sectional profile identification and local cross-section area calculation; (c) a comparison between the normal cross-sections determined with the proposed method and the profiles obtained directly from Micro-CT image slices.

5.6.5 Textile geometry modeling

The proposed method provides the trajectory and local geometry features, such as the cross-sectional area, width, and height of the fiber tows. Thus, the spatial variation of textile internal structure can be accurately captured. Sections 5.6.1 and 5.6.4 provided a quantitative analysis of the proposed analysis methods at the fiber tow level. In this section, a qualitative examination is presented at the Representative Elementary Volume (REV) level.

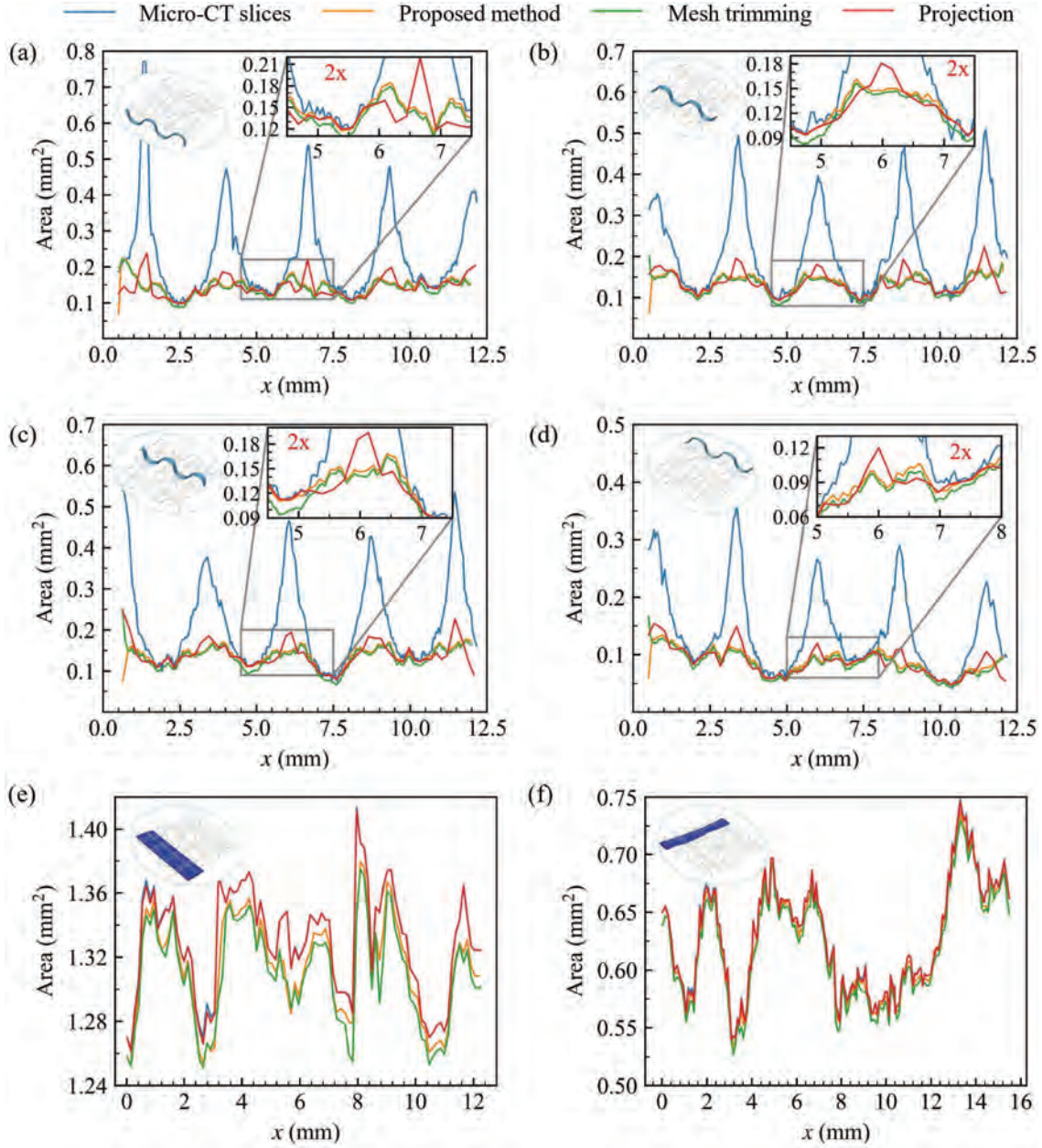


Figure 5.12 Comparison of local cross-sectional area determined by various methods: (a) - (d) correspond to binder tows located at the positions indicated by the insets in the upper-left corner. A portion of the curves were magnified two-fold and presented in the inset located in the upper right corner of each subplot. (e) and (f) correspond to a warp tow and a weft tow located at the positions indicated by the insets in the upper-left corner.

Geometry information obtained through the proposed method was first fed to a textile geometrical preprocessor, TexGen, to create mesoscopic models of the textile at different levels of detail. Figure 5.13a shows the simplified geometric model that was created with the av-

verage height and width of the fiber tows. It generally adheres to the 3D orthogonal weave structure. Figure 5.13b shows a more realistic geometry model. This model incorporates additional nuances in the textile structure, as the local geometry variability of the textile was provided to TexGen. Compared to Figure 5.13d, the realistic model shows a significant improvement in describing the shape of the fiber tows (see Figure 5.13e). One issue observed in generating a realistic model using TexGen is that providing more detailed local geometric information leads to an increased occurrence of fiber tow intersections, where different tows occupy the same spaces.

Figure 5.13c introduces the digital material twin model (DMT) derived directly from Micro-CT scans with the method presented in this paper. It captures intricate details of the actual structure. The spatial geometry information was fully utilized. Compared to simplified and realistic models, the DMT model faithfully reproduces the actual structure of the real textile, as illustrated in Figure 5.13f. More details and tutorials on the generation of image-based DMT models are provided in the PolyTex package documentation [235]. Thanks to the application programming interfaces (APIs) provided by PolyTex, the DMT models are readily usable for dual-scale flow simulation in OpenFOAM or mechanical analysis with Abaqus.

5.7 Conclusion

This study introduces a parametric method to analyze the internal structure and model the geometry of textile reinforcements based on volumetric images. By estimating the distribution density of point cloud that represents fiber tows within the parameter space, this method simultaneously reduces noise and achieves clustering and resampling based on the geometry signature of fiber tows. This allows for establishing high-fidelity model of a fiber tow with an equal number of points for each cross-section. The mapping between the geometric space and the parameter space is established with parametric kriging, which is constructed by a weighted linear combination of the known dataset.

This parametric approach brings two additional benefits. First, it adjusts the estimation variance to achieve smoothing of the envelope surface and the trajectory of the fiber tows. Compared to commonly used smoothing algorithms (Laplacian and Taubin algorithms for surface smoothing and Savitzky-Golay algorithms, fast Fourier transform, and median filters for curve smoothing), the proposed smoothing tool excels in smoothing performance and geometry preservation. The case study shows that it avoids volume shrinkage. This is of primary importance as the volume of fiber tows determines the local fiber fraction. Additionally, it enables anisotropic smoothing for the axial and radial directions of a fiber tow. Second, the normal cross-sections can be identified by intersecting implicit planes with the

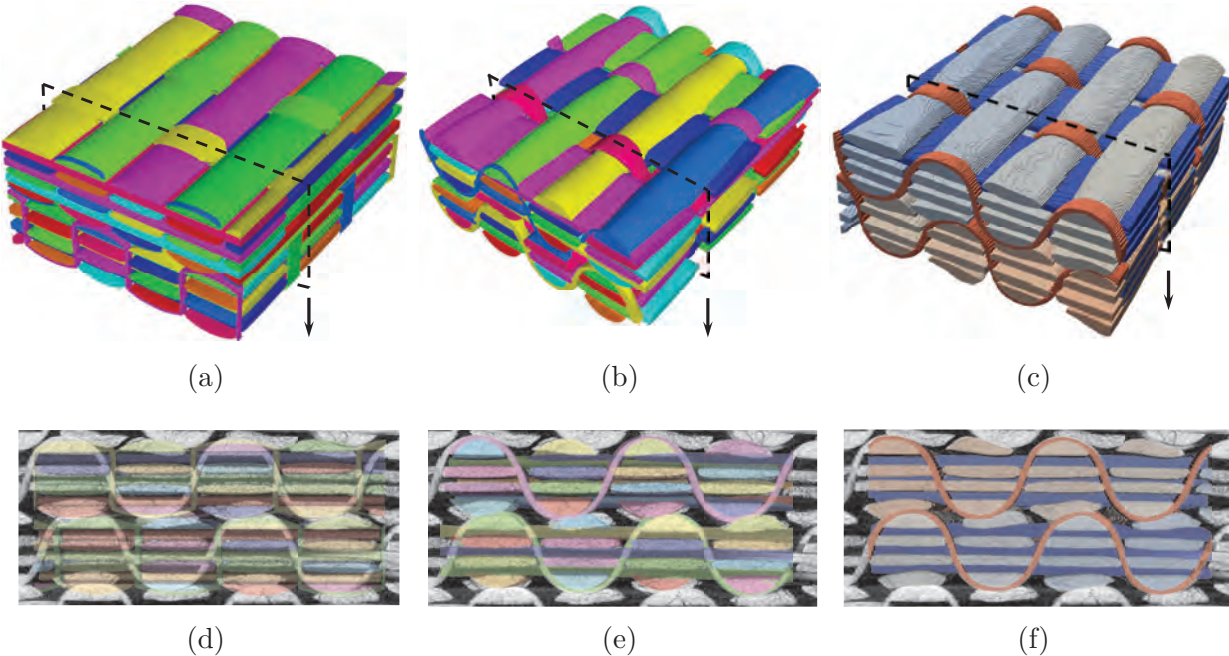


Figure 5.13 Internal geometric modeling of the 3D orthogonal textile reinforcements shown in Figure 5.2a using various methodologies: (a) the simplified and (b) the realistic geometry models created with TexGen; (c) the digital material twin model created with the proposed method. (d) - (f): Visual comparison of the cross-sections indicated by the dashed frames. The selected cross-sections are overlaid with the corresponding micro-CT image.

parametric surface of a fiber tow thanks to the parametric representation. Therefore, analyzing the internal structure and spatial architectural variability with the obtained normal cross-sections becomes a natural progression. The precision of geometrical modeling was examined qualitatively and quantitatively.

A high-fidelity model of a 3D orthogonal fabric was generated using the proposed approach. The model is termed a Digital Material Twin (DMT) as it faithfully replicates the actual structure. Geometric information was also used to create simplified and realistic models with TexGen. Although TexGen models have less intricate details compared to DMT, TexGen is capable of modeling fabric patterns using a reduced number of parameters. **The proposed method could serve as a complement to TexGen for situations where high-fidelity DMT models are required.**

The analysis procedures have been implemented in an open source Python Library for textile geometry modeling named *PolyTex*. A key component of our future research will involve the application of such models to numerical simulations to predict permeability and investigating

the mechanisms that contribute to the formation of manufacturing defects.

5.8 Acknowledgements

The authors acknowledge the contributions of our late colleague, Prof. François Trochu. His insights, expertise, and dedication to this research were instrumental and have profoundly influenced the work. The authors also express their gratitude to Dr. Wei Huang from Wuhan University for his advice on image processing and Prof. Vladimir Brailovski for access to X-ray microtomography at École de Technologie Supérieure (ÉTS), Montreal. This research was partially funded by the Natural Sciences & Engineering Research Council of Canada (No. 06629) and by the Department of Mechanical Engineering of Polytechnique Montreal. The authors also appreciated the financial support from the Research Center for High Performance Polymer and Composite Systems and the Fonds de recherche du Québec - Nature et Technologies (FRQNT). This research also received partial funding from Wuhan University of Technology through the Fundamental Research Funds for Central Universities (2019-JL-003).

CHAPTER 6 ARTICLE 4: OPEN-SOURCE TOOL FOR MICRO-CT AIDED MESO-SCALE MODELING AND MESHING OF COMPLEX TEXTILE COMPOSITE STRUCTURES

Bin Yang, Yuwei Feng, Cédric Béguin,
Philippe Causse, Jihui Wang

Submitted to *Composites Science and Technology* on xx/xx/2024

6.1 Chapter overview

In this chapter, we bring together the research findings discussed in Chapter 5 and create an open source Python package, *PolyTex*. It is intended for automatic geometrical analysis and generation of digital material twins from volumetric scanning data of textile reinforcements. This chapter presents the architecture, data specifications, and functionality of the package. Object-oriented programming principles have been adopted. The toolkit is released as an open source project. This enables material scientists to predict composite behaviors through high-fidelity digital material twins to address engineering challenges, without necessitating expertise in image processing and mesh generation.

6.2 Abstract

Volumetric image-based modeling of textile reinforcements and composites is favored over ideal geometric modeling because of its ability to represent complex structure in sufficient detail. Although several approaches were devised, there is still a scarcity of dedicated tools capable of effectively transferring pertinent information from images to high-fidelity models. This work presents the open source project, *PolyTex*, a Python-based object-oriented application that establishes a streamlined and reproducible workflow for such tasks. Dual kriging serves as the foundational theory for the parametric approach developed to represent, simplify, and approximate the morphology and topology of fiber tows. The code takes two types of input, either an explicit representation of tow geometry using point clouds or implicit representations, such as image masks representing fiber tows separately with grayscale values. Tailored APIs allow for smooth integration between *PolyTex*'s modeling capabilities and the simulation environments offered by OpenFOAM and Abaqus. Case studies on virtual testing of textile permeability were presented to demonstrate this capability. The modular

and object-oriented design makes *PolyTex* a highly reusable and extensible tool that allows users to create a customized pipeline.

Keywords: Textile reinforcements; Geometry modeling; PolyTex; Digital material twin; Permeability prediction;

6.3 Introduction

Volumetric image-based modeling [19, 122, 238] of mesoscale structures is a pivotal methodology for investigating the properties of textile reinforcements and composites. In contrast to textile modeling with idealized assumptions in yarn cross-sections and trajectory, the models generated by image-based approach can capture the intricate material variability, offering a more faithful representation of the physical counterparts. Such models are henceforth denoted to Digital Material Twins (DMT) [110, 123].

Studies have shown that employing DMT results in enhanced precision in predicting the properties of composites. Isart et al. [151] performed a comparative analysis that included idealized models, models created using the digital unit cell method, and models based on Micro-CT images. The authors identified a strong correlation between the representativeness of the models, particularly the accuracy of representing the cross-sectional shapes of fiber tows, and the accuracy of predicting the elastic constants of the composites. The cross-sectional area of the fiber tows in the idealized model deviated by over 20%, resulting in deviation between the predicted elastic constants and experimental values larger than than 10%. In contrast, the predicted values using image-based models were nearly identical to those of experiments. Moreover, Liu et al. [239] emphasize that errors in analyzing the damage and failure of composites using idealized models are further exacerbated due to the significant influence of local details in the shapes of fiber tows on damage behavior. [19], [67], and [240] also confirm the advantages of volumetric image-based modeling.

The benefits also extend to the prediction of textile processability. Ali et al. [23, 241] employed image-based DMT models to predict the permeability of woven fabrics. The result reveals that spatial variability in permeability induced by internal geometry changes can be accurately reflected. Authors [24, 157] also demonstrated that the predicted permeability with image-based models closely aligned with experiments. Regarding the drapability of textile reinforcements, Naouar et al. [119] showed that DMT models, compared to an idealized model, can better capture the internal structure of a 3D orthogonal woven fabric. Therefore, the numerical simulations of the compression response exhibited better consistency with the experimental results.

A common procedure for creating digital material twins involves several steps: preparing samples (either dry preforms or composite laminates), capturing and segmenting the volumetric images, extracting geometry features, and generating numerical meshes. To successfully accomplish this task, expertise in the fields of image processing, numerical discretization, and computer programming is required.

Image segmentation serves as the foundation for subsequent analysis and the creation of DMT models. It involves segmenting the volumetric image into multiple targets, namely matrix and fiber tows, and identifying the interfaces between them. Segmentation techniques can be classified into three categories: manual segmentation [110, 242], traditional segmentation techniques (such as threshold segmentation [20, 241, 243], structural tensor method [119, 121, 240, 244], etc.), and machine learning segmentation algorithms [122, 123, 222, 223, 245]. Manual segmentation is often employed as a benchmark to assess the accuracy of the latter two approaches. Today, there are a variety of tools available for image segmentation in both commercial domains (such as VG Studio [24, 67, 115], Dragonfly [245, 246], GeoDict [23, 241], etc.) and open source domains (such as ImageJ / FIJI [109, 247], 3D slicer [248], LabelMe [249], etc.).

However, despite the fact that several approaches have been devised for the extraction of geometrical features [110, 115, 122] and the generation of numerical meshes [19–21], effectively transferring pertinent information from images to models remains a challenging task. For instance, in current image-based permeability predictions, it is common practice to treat fiber tows as solids, as there is no need for morphology analysis and meshing for each fiber tow. This approach can lead to minimal errors (about 10% [250, 251]) in predicting permeability. However, it prevents the possibility of investigating the intra- and intertow fluid exchange [252]. This dual-scale effect has fundamental implications for process-induced issues such as void formation [74] and residual stresses [253]. Furthermore, it is also essential to have a multiscale model that precisely represents the geometric morphology of fiber tows within a fabric for the study of the failure mechanisms of composites [239]. As far as the authors are aware, there are currently no publicly accessible tools that can fill this gap.

This work presents a new open source project *PolyTex* for geometrical analysis, modeling, and high-fidelity mesh generation. This Python package can be easily installed on different operating systems, guaranteeing its compatibility across platforms. It provides a comprehensive, reproducible, and object-oriented framework that establishes a streamlined workflow for such tasks. Dual kriging serves as the foundational theory for the parametric approach developed to represent, simplify, and approximate the morphology and topology of the actual fiber tows. The modular architecture and object-oriented design make *PolyTex* a highly reusable

and extensible tool that allows users to create a customized pipeline for their own task. The design principle prioritizes the flexibility of input data and emphasizes data persistence and incremental modifications. The former enables users to import data from various sources, including image masks and point clouds. The latter ensures the storage and management of data in a traceable and reproducible manner, facilitating incremental modifications. Additionally, tailored APIs support cross-tool interoperation, allowing seamless integration with the simulation environments provided by *OpenFOAM* and *Abaqus*.

The rest of the paper begins by introducing the code's design philosophy, data structures, and object-oriented workflow. Subsequently, a brief summary of the underlying theory is given. Finally, case studies are presented to demonstrate the use of Digital Material Twins (DMT) models generated by *PolyTex* in textile permeability predictions. In this article, the inline code and function parameters are portrayed in a monospaced **typewriter font** for a clear differentiation from regular text. Software names are denoted in *italicized font*, and file paths are enclosed within "double quotation marks".

6.4 The design of *PolyTex*

PolyTex adheres to the principles of object-oriented programming, structuring the image-based geometry modeling process of textile composites into three hierarchical levels: primitive and parametric geometries, **Tow**, and **Textile** objects. As shown in Figure 6.1a, the **Textile** class serves as the top-level class. It is designed to manage multiple instances of **Tow** objects and perform operations at the textile level. Each **Tow** instance forms an individual building block of the textile structure (the individual threads that make up the textile). It contains the geometric and physical information of the tow and provides methods for data processing and analysis by calling the underlying modules implemented in the primitive geometry classes.

Customized interfaces are essential to enable *PolyTex* seamless integration with various numerical environments. As depicted in Figure 6.1b, *PolyTex* includes interfaces with *Abaqus* and *OpenFOAM*. Additionally, the code allows one to export geometrical analysis results to *TexGen* for simplified model creation. It also functions as a converter, transforming *TexGen* voxel models into *OpenFOAM* case files. Furthermore, *PolyTex* can utilize pre-processed images generated by image processing software such as *ImageJ* as input. More information on these features is provided in Section 6.5.

The following script illustrates the use of *PolyTex* package, abbreviated to **ptx**. First, a textile instance, denoted as **tex_inst**, is created using **ptx.Textile**. The subsequent step loads an explicit input data set (see Section 6.5.1 for the specifications of input data) with function

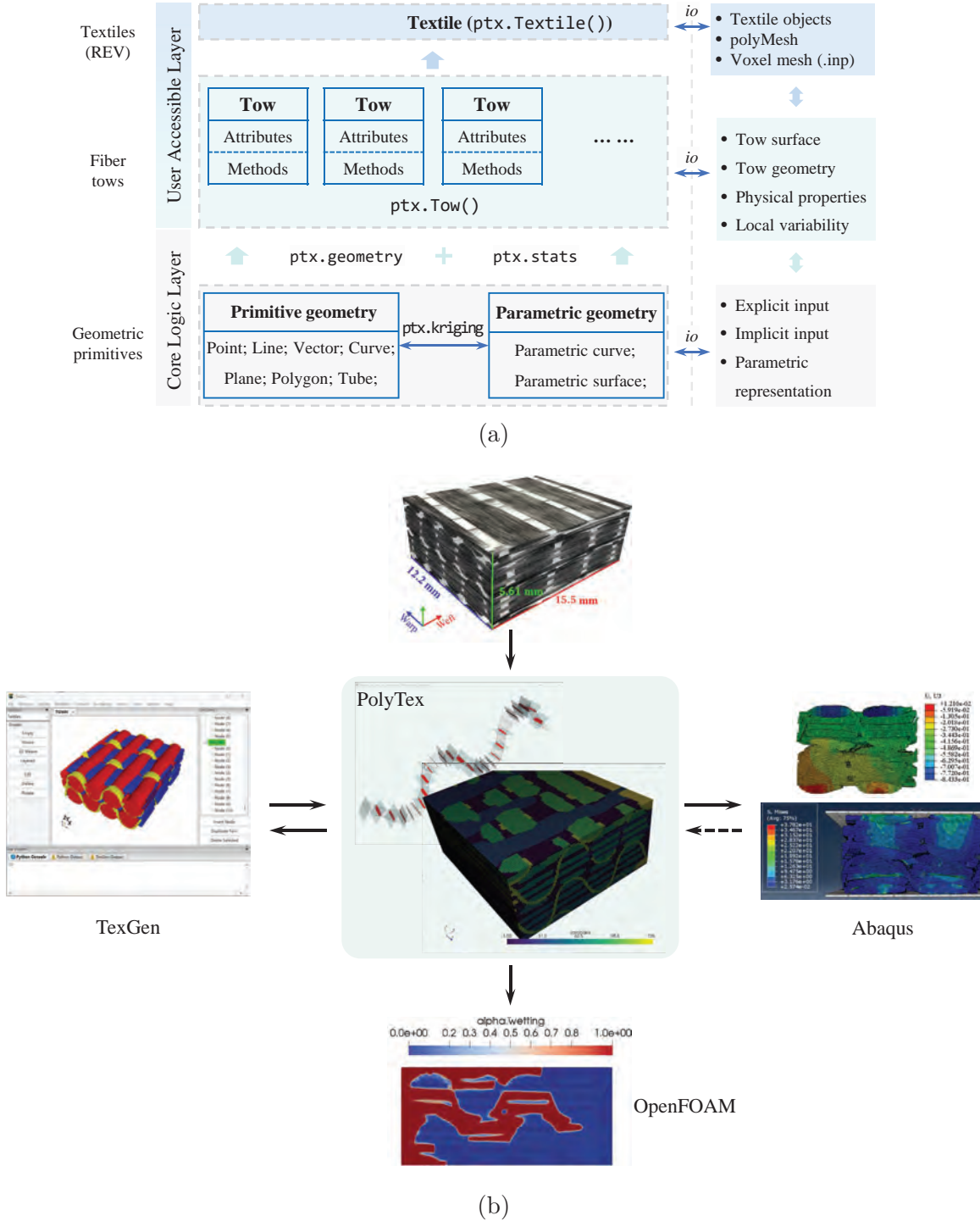


Figure 6.1 Design of the object-oriented textile modeling code, *PolyTex* (abbreviated to *ptx*): (a) hierarchical and modular architecture; (b) customized interfaces to various software. Implemented features are represented by solid line with arrows, while features to be added in the future are represented by dashed arrows.

`ptx.read_explicit_data` and returns the point cloud that represents the tow. Following that, an instance of `Tow`, noted as `tow_inst`, is established using `ptx.Tow` and added to the `Textile` instance `tex_inst` using the `add_tow` method.

```

1 import polytex as ptx
2
3 tex_inst = ptx.Textile(name="TG96N_Vf57")
4
5 coordinates = ptx.read_explicit_data(
6     "file/path/to/explicit/dataset.zip",
7     type="zip")
8
9 tow_inst = ptx.Tow(
10     surf_points=coordinates,
11     order="xyz",
12     rho_fiber=2550,
13     radius_fiber=6.5e-6,
14     length_scale="mm", tex=2200,
15     name="weft_0")
16
17 tex_inst.add_tow(tow, group=tow.name.split("_") [0])

```

Table 6.1 encapsulates the key attributes and methods associated with the `Tow` and `Textile` classes. In the `Tow` class, attributes include `name` (fiber tow identifier for indexing), `coordinates` (housing fiber tow spatial data), and `geom_features` (comprising geometric attributes), etc. The methods include functionalities such as resampling, smoothing, computation of normal cross-sections, etc. The `Textile` class features attributes such as `items` (containing `Tow` components), `layer` (representing textile layer information) and `mesh` (the generated mesh). The associated methods facilitate operations such as managing fiber tows, meshing, and exporting data in various formats. For a detailed description of the available functionalities, please refer to the online documentation of *PolyTex* [235].

Only essential interfaces are exposed to users through the `Tow` and `Textile` classes, while the underlying modules related to primitive geometry and parametric geometry for geometric operations and data computations are hidden. The hierarchical structure makes the data manipulation process straightforward so that end users can easily implement the modeling process and developpers can add new functions. In addition, the object-oriented workflow driven by its classes provides a straightforward process for data processing and analysis. This approach facilitates efficient use of the package, emphasizing simplicity and coherence throughout the workflow.

Table 6.1 Attributes and methods of the `Tow` and `Textile` classes

Tow class		Textile class	
Attributes	Methods	Attributes	Methods
<code>name</code>	<code>resampling(krig_config, ...)</code>	<code>name</code>	<code>add_tow(tow, group=None)</code>
<code>coordinates</code>	<code>smoothing(drift, cov, ...)</code>	<code>items</code>	<code>meshing(bbox, voxel_size, ...)</code>
<code>geom_features</code>	<code>normal_cross_section(algorithm, ...)</code>	<code>layer</code>	<code>export_as_openfoam(fp, ...)</code>
<code>orientation</code>	<code>save(save_path)</code>	<code>n_tows</code>	<code>save(path=None, ...)</code>
<code>tex</code>	<code>from_file(path)</code>	<code>mesh</code>	<code>from_file(path)</code>
...

6.5 Data handling and structural representation

6.5.1 Specifications of input data

Figure 6.2a shows a coordinate system with the point of origin situated at the upper-left corner of the first slice of the volumetric image. The coordinate system is configured in such a manner that the positive x -axis extends towards the right, in alignment with the warp tows. Similarly, the positive y axis extends downward, following the direction of the fabric thickness, and the positive z axis extends backward, parallel to the direction of the weft tows. In this coordinate system, the fiber tow geometry resulting from segmentation of a volumetric image can be represented either explicitly or implicitly. The explicit method represents the surface of each fiber tow with point clouds [110, 122], as shown in Figure 6.2b. It provides a key advantage by allowing the analysis of fiber tow morphology directly, including cross-sectional circularity, area, and other related parameters. In addition, it facilitates the implementation of differential geometry operations. In contrast, the interface between tows can also be implicitly defined as the zero-level isosurface \mathcal{S} of a scalar field x : $\mathcal{S} = x \in \mathbb{R}^3 \mid F(x) = 0$. The variable x is commonly defined as a signed distance [19, 225], or as probability maps obtained from machine learning-based segmentation methods [118, 226]. The scalar field can be readily converted into image masks that represent fiber tows separately with different grayscale values (see Figure 6.2d).

PolyTex accommodates both types of input data. Figure 6.2c illustrates the storage format of point cloud data when expressing the geometric shapes of fiber tows explicitly. The contour of a fiber tow on a given slice is represented by an arbitrary number of feature points.

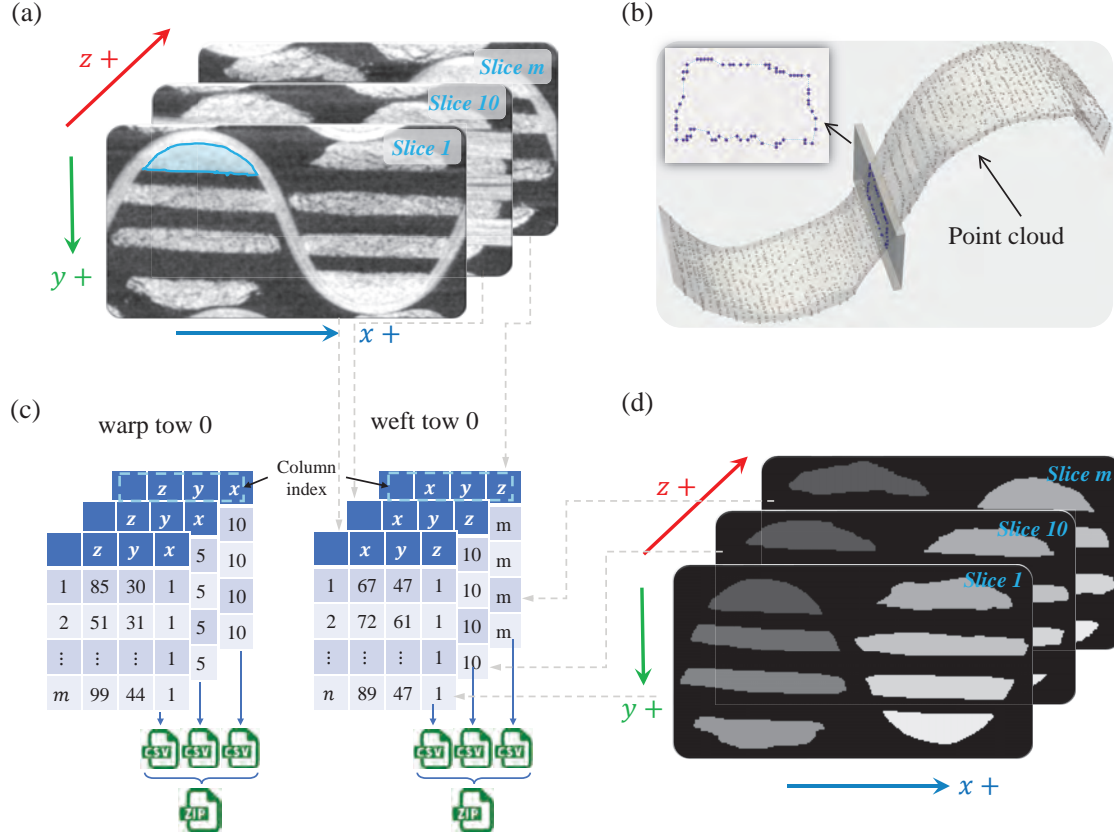


Figure 6.2 Data structure of input dataset for *PolyTex*: (a) Volumetric image of a composite in the provided coordinate system, where the matrix is depicted in darker tones, and the fibers are represented in lighter shades. The weft tow 0 is highlighted in blue; (b) typical fiber tow represented by point cloud; (c) the data structure used to store the input dataset of a point cloud; (d) segmented masks associated with the weft tows shown in (a), the matrix is left in black; With the coordinate system defined in (a), the fiber tow geometry obtained after segmentation can be represented either by point cloud explicitly or by image masks implicitly. *PolyTex* can handle both types of input data.

These points, arranged either clockwise or counterclockwise, are stored as a table in a CSV (comma-separated values) file. The table specifies the row index (first column) along with the corresponding x , y , z coordinates for each feature point. Note that the last column must represent the coordinate component parallel to the longitudinal direction of the fiber tows, serving as a label for the feature points belonging to the same slice of the volumetric image. In order to enhance data transfer efficiency, the CSV files that contain sectional contour information of the same fiber tow are compressed into a ZIP archive. This compressed file can then be directly read by the provided functions in *PolyTex*.

The spacing between image slices that were subjected to segmentation (segmentation inter-

vals) is not required to be uniform, providing flexibility and efficiency for adapting to diverse contexts. The data structure, which resembles volumetric images, aligns with the format exported during manual segmentation using *ImageJ*. This compatibility facilitates integration across existing toolsets. In addition, it maintains an intuitive geometric representation for easy comprehension.

When an image mask is used as input data (implicit dataset), *PolyTex* converts it into point cloud data with the function `pk.mesh.from_image()`, as explicit representation allows denoising, resampling, and morphology analysis in parameter space. Supplementary datasets and scripts are available as references for both representation methods. Note that beyond the representation illustrated in Figure 6.2a, equivalent coordinates can be used to depict the morphology of the fiber tows. However, strict adherence to the right-hand rule is imperative.

6.5.2 Morphological features

The morphological features of the fiber tow cross-sections play a crucial role in various applications. For instance, in numerical simulations, accounting for the changes in the relevant parameters due to variations in the fiber volume fraction requires knowledge of the cross-sectional area. Additionally, the centerline is frequently employed to determine the direction of a tow and describe the weave pattern of the fabric.

Morphological analysis of fiber tows is automated and can be accessed through `tow_inst.geom_features`. As illustrated in Figure 6.3a, the returned morphological features encompasses parameters such as area, perimeter, width, height, rotated angle, circularity and centroid coordinates for each cross-section, presented in the form of a pandas DataFrame. Figure 6.3b provides an illustration of the definitions of these parameters, except that the circularity is computed in the following manner:

$$\text{Circularity} = \frac{4\pi A}{P^2} \quad (6.1)$$

where A is the area determined using the shoelace algorithm and P is the perimeter of the cross-section.

6.5.3 Data persistence

As depicted in Figure 6.4, users employing *PolyTex* for textile modeling have the flexibility to save data at different stages. For example, the results of morphological analysis can be saved as `.geo` files, while the denoised and resampled point cloud data can be stored as

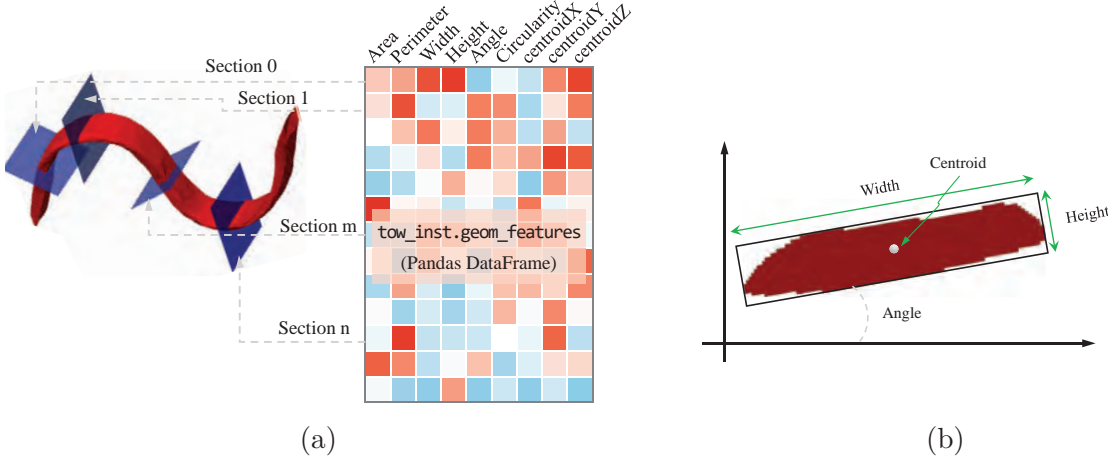


Figure 6.3 Morphological features of each fiber tow are calculated and stored in a Pandas DataFrame (a) with parameters defined in (b) and Eq. 6.1.

.coo files or .stl triangular surface meshes for visualization and data exchange with other applications. Similarly, instances of the `Tow` class and the `Textile` class can be saved as files in the `.tow` and `.tex` formats, respectively. *PolyTex* provides functions for saving and loading these data, as well as customized handlers for data analysis. This eliminates the need to perform repetitive tasks. Instead, users can simply load the previously saved data to make incremental updates. This data persistence scheme provides an efficient method for collaboration and data sharing between users. With the input information and analysis results included, collaborators can effortlessly load, track, and reproduce the analyses.

6.5.4 Cross-tool interoperation

The purpose of creating DMT is to better understand the performance of textiles and textile composites through numerical simulations. Numerical mesh serves as a crucial component extensively used during the modeling, computational, and analytical phases in various programs. APIs for *OpenFOAM* and *Abaqus* have been implemented. Additionally, a VTK XML unstructured grid, commonly identified by the extension `.vtu`, can also be saved. The 3D visualization interfaces are also provided through a Python wrapper for VTK called *PyVista* [237]. With the three formats acting as intermediaries, convenient conversions to other formats can be achieved using commercial software such as HyperMesh or open source tools such as meshio [254].

Table 6.2 presents a comparison of the three formats. The VTK unstructured grid allows for the storage of spatial field information, such as fiber volume fraction and fiber tow orientation.

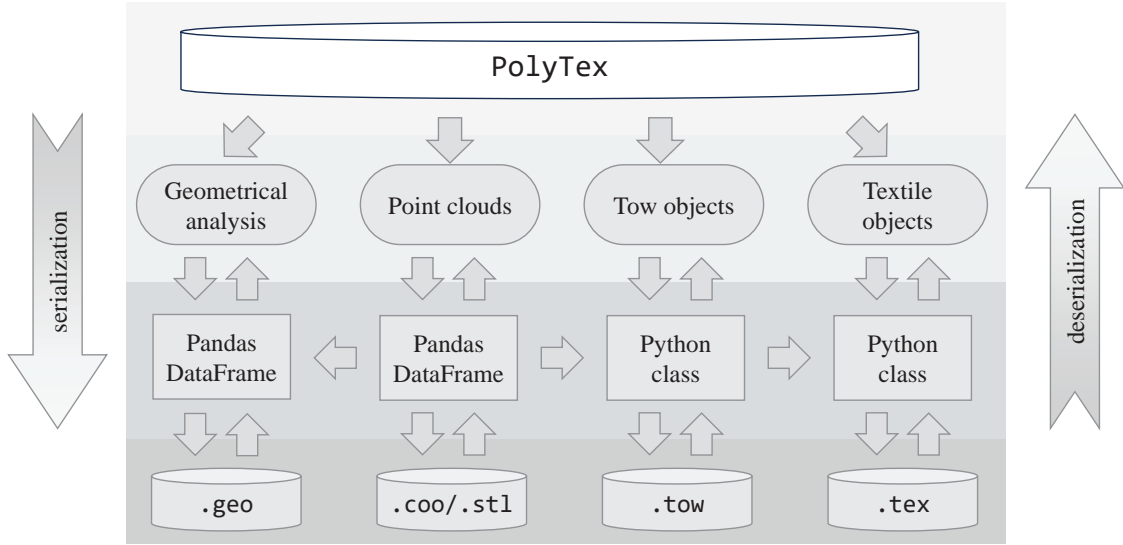


Figure 6.4 Object serialization and deserialization at different stages of analysis aid in reducing repetitive work and facilitate data sharing.

tion, as point data arrays or cell data arrays in conjunction with node coordinates and cell connectivity within a single file, facilitating data transfer and storage. It is also compatible with the open source visualization software *ParaView* [255], which is widely used in the field of computational mechanics.

In contrast to the typical data structure of grid data, *OpenFOAM* polyMesh organizes the mesh data in a series of files in the "./constant/polyMesh/" directory. Each file contains a specific type of information. However, the connectivity of the nodes for 3D cells is not explicitly stated, but rather determined by the connection of cell faces. See Appendix 6.10 for more details. Cell data arrays are transformed into volume fields and saved in the directory "./0/", as depicted in Figure 6.5. The file "./0/D" represents the Darcy coefficient, which is further elaborated in Section 6.6.

The *Abaqus* input is composed of three files: a .inp file that includes information on nodes, elements, boundary conditions, and material definitions, a .eld file that contains cell data arrays, and a .ori file that contains orientation vectors for fiber tows. These files are the same as those generated by TexGen [256]. Hence, the tutorials that demonstrate the process of conducting simulations in *Abaqus* with the input for the TexGen project can also be used for the one generated by *PolyTex*.

To generate a mesh, the user needs to specify the bounding box and resolution of the grids by calling `tex_inst.meshing()`. The resolution is defined by the desired size of the element in the *x*, *y* and *z* directions. Upon execution, a mesh object is attached to `tex_inst`

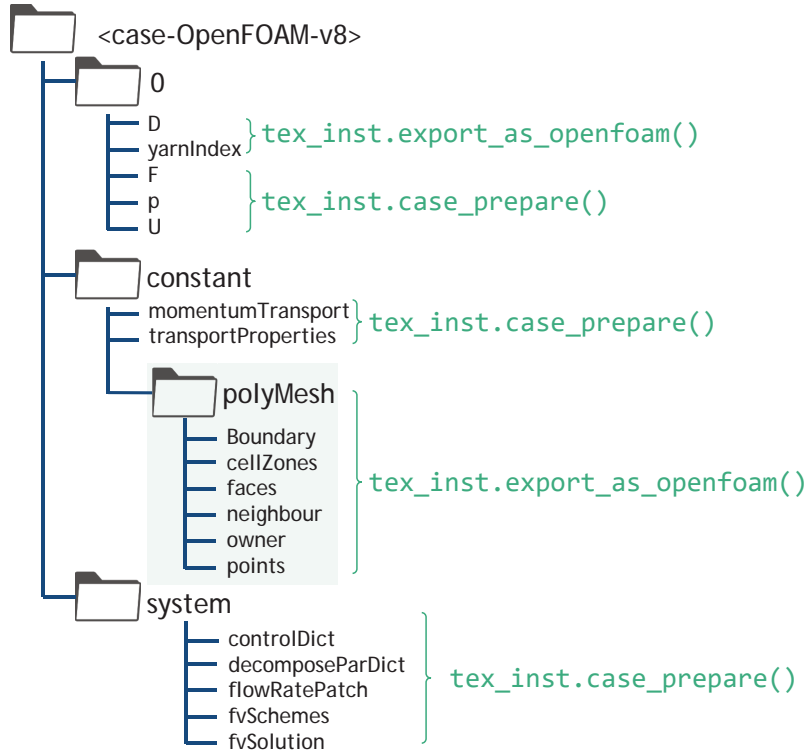


Figure 6.5 File structure of OpenFOAM case template prepared automatically by calling `tex_inst.export_as_openfoam()` and `tex_inst.case_prepare()`

and can be accessed by `tex_inst.mesh` or saved as VTK unstructured grid by invoking `tex_inst.export_as_vtu("file/save/path/filename.vtu")`. Similarly, the mesh can be exported as OpenFOAM or Abaqus input files by calling `tex_inst.export_as_openfoam()` or `tex_inst.export_as_abaus()`, respectively. Besides, a case template is provided. The file structure of the case template is shown in Figure 6.5. Once the mesh is generated, users can call `tex_inst.case_prepare()` to prepare a case that is ready to run in OpenFOAM v8 and then modify the case template to suit their needs.

Under any circumstances, it is consistently recommended to perform a sensitivity analysis to assess the optimal grid resolution for a specific simulation. Currently, only the voxel mesh is supported. In Appendix 6.10, a comparison of data structures and numbering rules for node, face, and cell connectivity of hexahedral elements is provided in these three formats. The support for conformal mesh will be added in future releases.

Table 6.2 3D mesh data structure for VTK unstructured grid, polyMesh, and Abaqus inp Formats

Mesh type	File format	Data structure	Extension	Connectivity (face)	Connectivity (cell)
VTK unstructured grid	ascii & binary	XML	.vtu	implicit	explicit
OpenFOAM	ascii	File Assembly	-	explicit	implicit
Abaqus	ascii	ASCII	.inp, .ori, .eld	implicit	explicit

6.6 Theory

Comprehensive information regarding the theoretical principles underlying *PolyTex* is available in the literature [257]. In this context, we present a summary of essential concepts and methods implemented in the package for the sake of completeness.

6.6.1 Robust noise reduction and data resampling

PolyTex introduces a robust noise reduction approach, incorporating stochastic filtering based on kernel density estimation (KDE). Then, the input point cloud is resampled based on the probability density function (PDF) estimated by KDE for each fiber tow (see Figure 6.6a). The filtering and resampling process allows effective noise reduction and improved modeling fidelity. See [257] for more details.

6.6.2 Geometry representation with kriging

The modeling of textile geometry encompasses representing and manipulating point clouds, spatial curves, and surfaces. The theoretical underpinning for *PolyTex* relies on dual kriging, a robust method to represent known positions (samples) and estimate non-sampled values. In particular, it provides the estimation variance, serving as a metric for the accuracy of each individually estimated value. The geometry of an object $G(x)$, such as a curve shown in Figure 6.6b, is considered as the sum of the contributions of a drift and a random fluctuation:

$$G(x) = \underbrace{a(x)}_{\text{drift}} + \underbrace{W(x)}_{\text{fluctuation}} \quad (6.2)$$

The term $a(x)$ is a deterministic function representing an average value and $W(x)$ is a prob-

abilistic random function. x denotes position vector. The fluctuation is connected to a generalized covariance $K(h)$ between known positions, for instance x and y . h is the distance between x and y , as shapes are especially likely to be correlated if x and y are close. Hence, unlike deterministic methods, kriging is a method based on statistical models that includes spatial autocorrelation (relationship statistics between measured points).

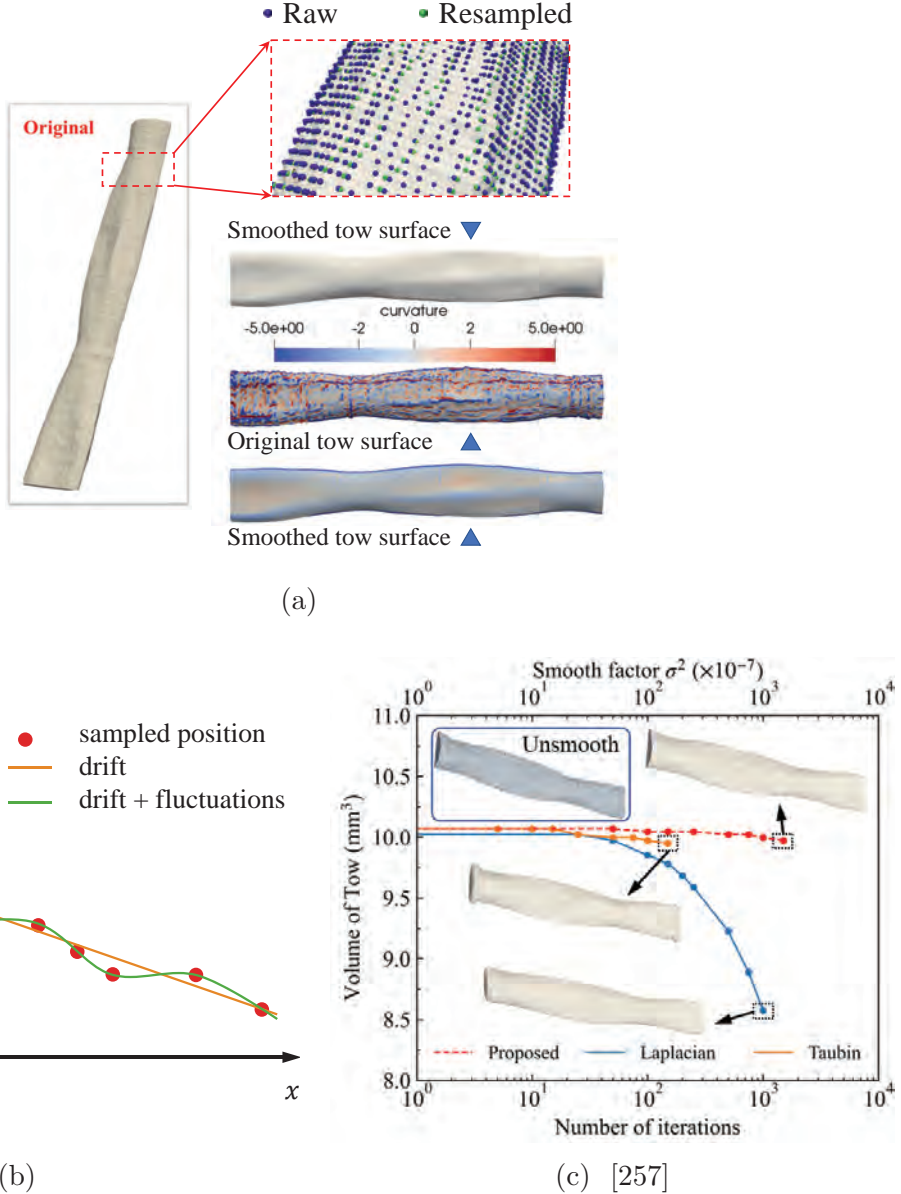


Figure 6.6 Illustration of the procedure for fiber tow geometry modeling: (a) stochastic point cloud resampling and data smoothing; (b) concepts of parametric kriging for geometry modeling; (c) The behavior of tow volume vs. iterations (or smooth factor for the proposed method) for the selected algorithms.

Table 6.3 Summary of drift and generalized covariance functions available in *PolyTex*

Drift function			Generalized covariance
	Curve (1D)	Surface (2D)	
Constant	$a(x) = a_0$	$a(x) = a_0$	/
Linear	$a(x) = a_0 + a_1x$	$a(x, y) = a_0 + a_1x + a_2y$	$K(h) = h$
Quadratic	$a(x) = a_0 + a_1x + a_2x^2$	$a(x, y) = a_0 + a_1x + a_2y + a_3x^2 + a_4y^2 + a_5xy$	/
Cubic	/	/	$K(h) = h^3$

Note: Generalized covariances with even powers in h are not admissible and lead to singular kriging matrices.

A kriging estimator T_x of $G(x)$, when we know the outcome of $G(x_i)$ for $1 \leq i \leq N$, is constructed as a linear combination of random variables $G(x_i)$:

$$T_x(G(x_1), \dots, G(x_N)) = \sum_{i=1}^N \lambda_i(x) \cdot G(x_i) \quad (6.3)$$

where the N weight coefficients, $\lambda_i(x)$ for $1 \leq i \leq N$, are determined by minimizing the variance of the estimation with the unbiasedness constraint. The options available in *PolyTex* for drift and generalized covariance are summarized in Table 6.3. The combination of drift and covariance functions can be selected according to the shape of the object to be modeled.

The discrete step-like interface between subdomains composed by voxels in the volumetric images should be approximated by a smoothing surface mesh to perform geometrical analysis and to create a conformal mesh [19, 227]. It is achieved by adjusting the generalized covariance functions with a smoothing factor. Note that, unlike commonly used smoothing techniques, volume shrinkage induced by smoothing is avoided because:

- the estimator is constructed by minimizing estimation variance ("best");
- estimated values are weighted "linear" combinations of known values;
- it searches the combination with zero mean estimation error ("unbiased").

Therefore, the volume compensation algorithm is no longer necessary, which improves the efficiency of data processing and reduces data approximation errors. Figure 6.6c compares

the volume and geometry variations of a weft tow with different smoothing strengths. Taubin algorithm [236] guarantees that the smoothing process does not cause substantial contraction in fiber tow volume, although it does cause distortion in the geometry. Laplacian smoothing causes notable volume contraction. In contrast, our proposed method achieves the most effective performance in terms of preserving both volume and geometry during the smoothing process.

6.6.3 Normal cross-section identification

The determination of the local properties of fiber tows relies on the geometric information of their normal cross-sections, in particular for the wavy tow shown in Figure 6.7. Two methods are provided to obtain the normal cross-sections. The default is based on the intersection of a parametric surface (the tow surface) and an implicit plane (determined by the local orientation of a fiber tow trajectory), thanks to the availability of the analytical equations (the kriging estimator Eq. (6.3)) for each fiber tow:

```
1 cross_section, plane = tow_inst.normal_cross_section(algorithm="kriging", plot=True)
```

Figure 6.7b shows the identified normal cross-sections through the visualization interfaces provided within *PolyTex*. Users can decide whether to visualize the results with the boolean switch "plot", as demonstrated by the code above. The other option for the parameter "algorithm" is "pyvista". It wraps the mesh clip function in the *PyVista* package (`Polydata.clip_surface()`). In contrast to the *PyVista* approach, the suggested algorithm does not require triangular meshes for fiber tows and cross-sectional planes, leading to improved computational efficiency. Local geometric information of fiber tows, including area A , width, height, and circularity for each identified cross-section, is calculated and stored in the variable `tow_inst`. It is automatically invoked when spatial properties of the tow are required, such as discretization of the numerical domain.

6.6.4 Local permeability

Many analytical models have been proposed in the literature for estimating the longitudinal ((k_{\parallel}^{tow})) and transverse (k_{\perp}^{tow}) permeability of fiber tows [159]. These models usually relate permeability to the local fiber volume fraction of a fiber tow, the radius of the filaments, and the maximum fiber volume fraction for a specific fiber packing pattern. This enables the derivation of permeability tensors for fiber tows in the local coordinate system \mathcal{F}^l :

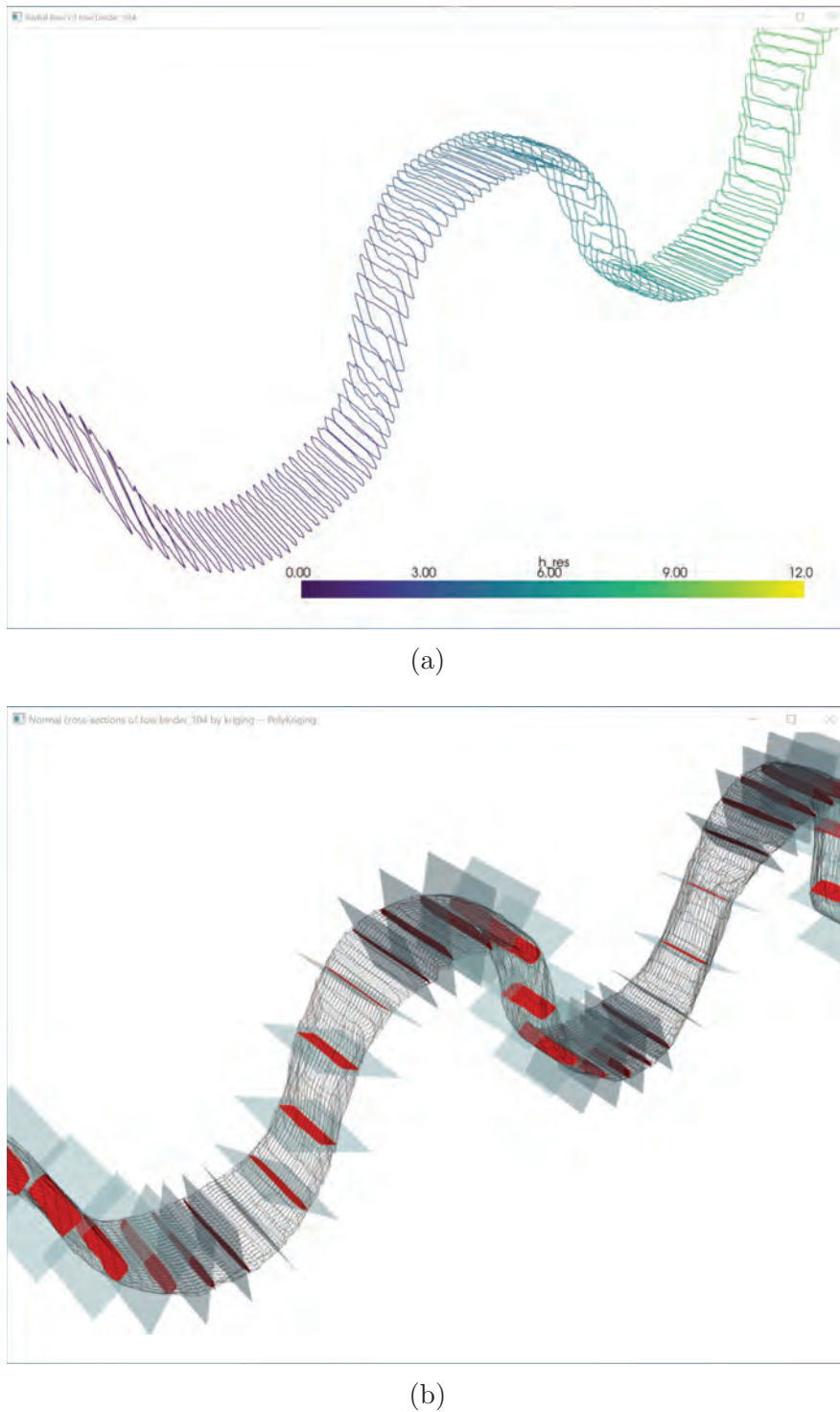


Figure 6.7 (a) presents the cross-sections of a fiber tow extracted from image slices directly, which may not necessarily be perpendicular to the orientation of the wavy tow. *PolyTex* offers two algorithms that can automatically determine normal cross-sections and compute geometric information, such as area and circularity, for each cross-section. (b) Normal sections determined using the newly proposed kriging-based method. (a) and (b) are two of the visualization interfaces provided by *PolyTex*. Users can decide whether to visualize the results upon invoking relevant functions.

$$\mathbf{K}^l = \begin{bmatrix} k_{||}^{tow} & 0 & 0 \\ 0 & k_{\perp}^{tow} & 0 \\ 0 & 0 & k_{\perp}^{tow} \end{bmatrix} \quad (6.4)$$

At present, the *PolyTex* framework incorporates two sets of equations proposed by Gebart [258] and Drummond and Tahir [259] for the estimation of $k_{||}^{tow}$ and k_{\perp}^{tow} . The former provides more accurate estimates at low fiber volume fractions, while the latter is better suited to estimate the permeability of fiber tows with fiber volume fractions exceeding 60% [159].

Permeability tensors in the world coordinate system \mathcal{F}^w are typically required in most simulation softwares. Therefore, finding a rotation matrix \mathbf{R} between the local coordinate system \mathcal{F}^l and the world coordinate system \mathcal{F}^w becomes essential. It is determined by minimizing the following loss function with the Kabsch algorithm [260]:

$$L(\mathbf{R}) = \frac{1}{2} \sum_{i=1}^n \|\mathbf{a}_i - \mathbf{R}\mathbf{b}_i\|^2 \quad (6.5)$$

where \mathbf{a}_i and \mathbf{b}_i represent the principal axes of the local and world coordinate systems within the world coordinate system. The local permeability tensor in \mathcal{F}^w can be determined as follows:

$$\mathbf{K}^w = \mathbf{R}\mathbf{K}^l\mathbf{R}^T \quad (6.6)$$

6.7 Case studies

This section illustrates the application of Digital Material Twin (DMT) models, which is generated using the code and approach provided in this manuscript. Specifically, DMT models are developed for a 3D orthogonal fabric from Texonic Inc., TG96N, and used for virtual testing of transverse permeability. The woven structure is illustrated in Figure 6.8a. The DMT model allows tows to be accounted for as a porous medium rather than a solid. The result is compared with the ones predicted with the models created by *TexGen*. A physical model was also created by 3D printing to replicate the DMT. This physical model serves as a reference sample for the experimental validation of numerical results. As the physical model is much more rigid than a real fabric, it ensures that factors such as flow-induced deformation do not affect the permeability experiment.

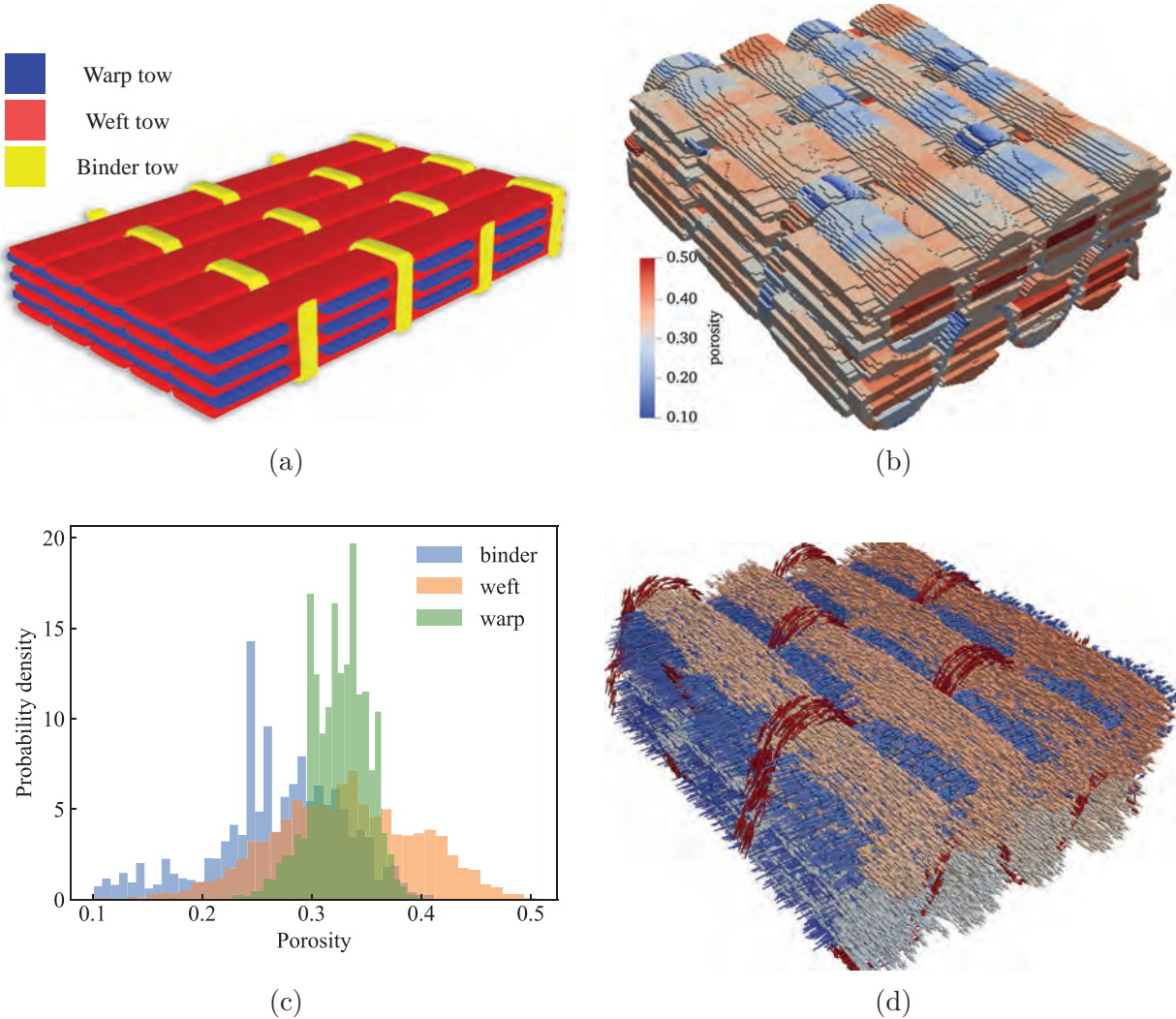


Figure 6.8 Digital Material Twin (DMT) model of a 3D orthogonal textile reconstructed from a volumetric image scanned with a resolution of $22\text{ }\mu\text{m}$. The size of the model is $11.4 \times 13.12 \times 5.35\text{ mm}$. (a) woven structure; (b) the DMT model discretized with hexahedral elements; (c) porosity distribution of warp, weft and binder tows; (d) fiber orientations. The elements for mesopores are hidden to clearly show the fiber tows.

6.7.1 Digital material twin

Figure 6.8b shows the DMT model that has been discretized with hexahedral elements. The model consists of two layers of the textile, with 18 warp tows, 32 weft tows, and 8 binders. The porosity of each element is illustrated, revealing that the DMT model effectively represents the local variations. This is particularly evident at the intersecting points where the porosity experiences a significant decrease. Although collectively forming the textile, the warp, weft, and binder tows exhibit different porosity distributions. As illustrated in Figure 6.8c, the

porosity of binder tows is lower than that of warp and weft tows. This is to be expected because the woven structure is maintained with the binders by exerting force on the warp and weft tows. Furthermore, the porosity of the weft tows is more dispersed than the others. As shown in Figure 6.8b, each layer of textile contains four layers of weft tows. The top and bottom weft tows are constrained by the binders and experience compression when in contact with other textile layers. As a result, their porosity is considerably lower than that of the two middle layers. Consequently, weft tows can be categorized into two types. In contrast, warp tows are always distributed between weft tows and do not interact directly with binders, resulting in the most concentrated distribution of porosity. The variation of local fiber orientations is also well reproduced in the DMT model, as illustrated in Figure 6.8d. This information is crucial for both flow and mechanical simulations.

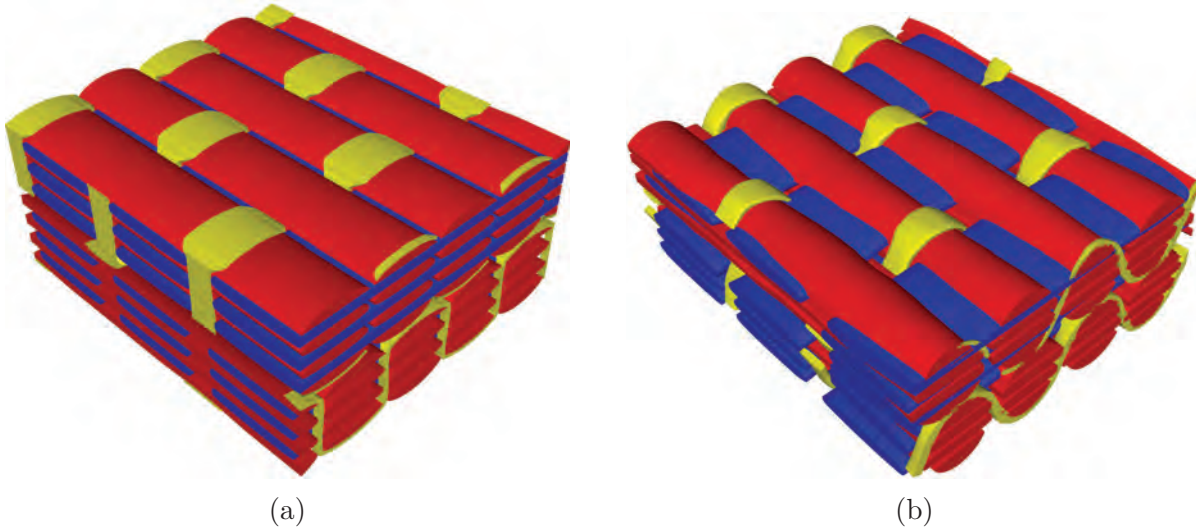


Figure 6.9 TexGen-created models of TG96N: (a) An idealized model featuring constant tow width, height, and spacing. The "Refine" option in TexGen was utilized to automatically adjust yarn cross-sections for the desired layer thickness; (b) A realistic model created with the geometrical analysis results from *PolyTex*, capable of replicating spatial variability to a certain extent.

A comparison was conducted between the permeability predictions with the DMT and two models created with TexGen. Figure 6.9a presents the idealized model (hereafter referred to as the "ideal model"), in which each tow possesses a constant cross-section with fixed width and height. The model was adjusted to achieve the desired layer thickness. Conversely, the TexGen model depicted in Figure 6.9b (hereafter referred to as the "realistic model") employs the geometrical analysis results obtained with *PolyTex*. Consequently, the variation in the tow cross-sectional shapes is captured and is similar to the DMT model.

6.7.2 Governing equations

Coupling the Navier–Stokes equations with the Darcy-Forchheimer model stands out as one of the most widely adopted approaches for describing fluid flows in regions partially occupied by porous media. Assuming a constant porosity (no flow-induced deformation), denoted as φ , the coupled equation can be written as:

$$\nabla \cdot \vec{u} = 0 \quad (6.7)$$

$$\frac{\partial \vec{u}}{\partial t} + \nabla \cdot (\vec{u} \vec{u}) = -\vec{\nabla} \frac{p}{\rho} + \nabla \cdot \frac{\mu}{\rho} (\vec{\nabla} \vec{u} + \vec{\nabla} \vec{u}^T) + \frac{S}{\rho} \quad (6.8)$$

$$S = - \left(\varphi \mu_e \mathbf{D} \vec{u} + \frac{\rho \varphi^2 \mathbf{F}}{2} |\vec{u}| \vec{u} \right) \quad (6.9)$$

The Darcy-Forchheimer model serves as the source term S . \mathbf{D} and \mathbf{F} represent second-order tensors that denote the Darcy and Forchheimer coefficients, respectively. \vec{u} and ρ are the intrinsic average velocity and density of the fluid. p denotes the static pressure. t the pseudo-time (iterations for steady-state simulation). Eq. (6.8) is commonly referred to as the Navier-Stokes/Darcy-Forchheimer equation. In the solid-free subdomain where $\varphi = 100\%$, the permeability approaches ∞ and Eq. (6.8) converges to the standard Navier-Stokes equations. This modeling strategy enables a unified numerical framework that captures both macroscopic and microscopic phenomena.

The Darcy coefficient is defined as $\mathbf{D} = (\mathbf{K}^w)^{-1}$ where \mathbf{K}^w is the intrinsic permeability tensor of fiber tows determined according to Section 6.6.4 with the Gebart model [258]. The permeability tensors (part of the DMT model shown in Figure 6.8b) are visualized in Figure 6.10 with ellipsoid glyph. The ellipsoids are directionally scaled according to the local permeability components. Therefore, the longer the principal axis of an ellipsoid, the higher the permeability in the direction of fiber tows. The permeability distribution exactly mirrors that of fiber tow porosity and orientation. Ochoa-Tapia and Whitaker [261] determined that the connection between effective viscosity and dynamic viscosity μ is $\mu_e = \mu/\varphi$. For practical resin flow in textile reinforcements, the viscous resistance in fiber tows is much greater than the inertial resistance due to the low Reynolds number ($Re < 0.1$). Therefore, the Forchheimer coefficient \mathbf{F} is set to $\mathbf{0}$. The equations are solved in OpenFOAM. The transverse permeability is then calculated according to Darcy's law [12].

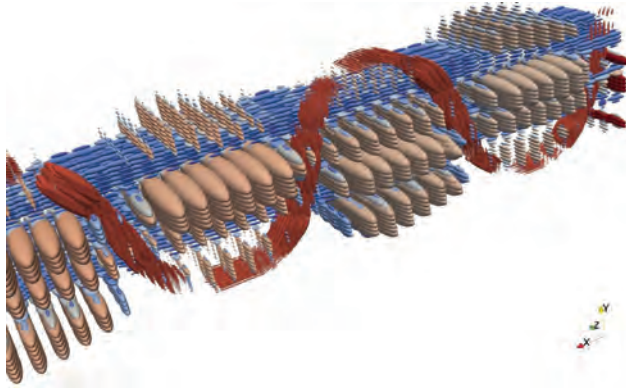


Figure 6.10 Spatial variation of fiber tow permeability rendered with ellipsoid tensor glyph. Only a portion of the DMT model shown in Figure 6.8b is presented to more clearly display the permeability distribution.

6.7.3 Boundary conditions

The boundaries of the numerical domain are labeled on the basis of their positions in the Cartesian coordinate system, as shown in Figure 6.11. The transverse permeability k_z is predicted by setting the upper ($Z+$) and lower ($Z-$) boundaries as inlets and outlets, respectively. An injection pressure of 1000 Pa is specified at the inlet. No backward flow is allowed at the outlet. The other boundaries are specified as non-slip walls. The simulations with the ideal model are subjected to the same boundary condition.

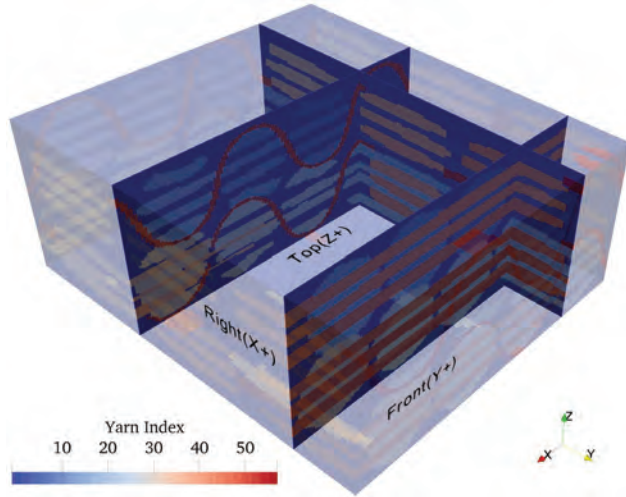


Figure 6.11 The boundaries of the numerical domain are referred to as right ($X+$), left ($X-$), front ($Y+$), back ($Y-$), top ($Z+$) and bottom ($Z-$) according to their positions in the Cartesian coordinate system. To predict transverse permeability, an injection pressure of 1000 Pa is specified at the top ($Z+$) and 0 Pa at the opposing boundary.

6.7.4 Result and discussion

Figure 6.12a presents the pressure contour for the dual-scale simulation with the DMT model. The pressure decrease is more pronounced in the micropores than in the mesopores. This discrepancy reflects the arrangement of the fiber tows. Additionally, Figure 6.12b shows the corresponding streamlines. It emphasizes that the flux passing through the fabric is primarily caused by the flow in the mesopores, since only a minimal number of streamlines are observed passing through the fiber tows.

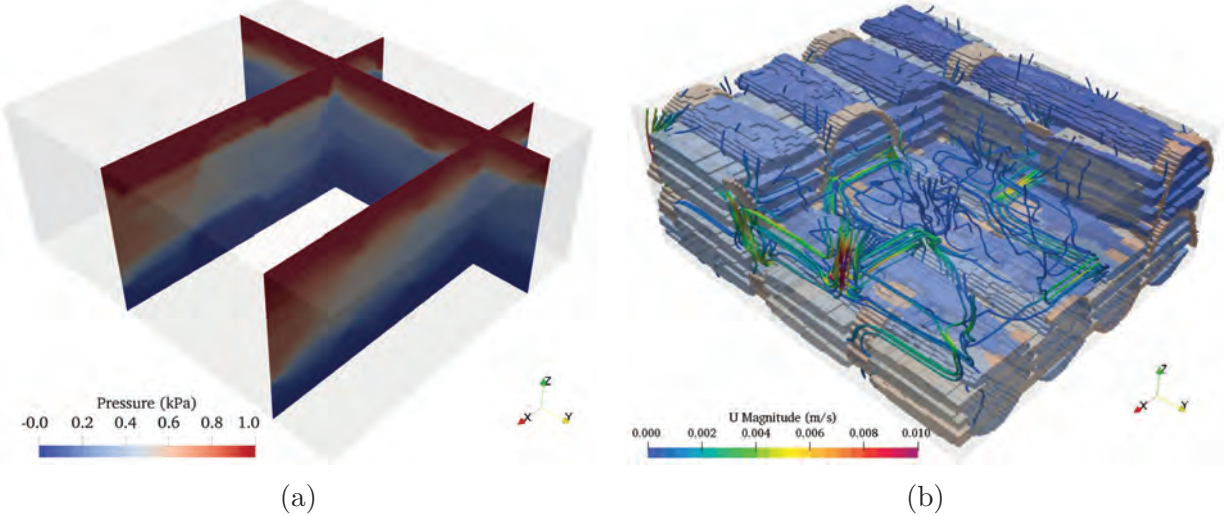


Figure 6.12 Dual-scale flow simulation with DMT models: (a) pressure contour across the thickness and (b) streamlines.

Figure 6.13 presents a quantitative analysis of the transverse permeability k_z^{tex} virtually tested with the ideal, realistic, and DMT models. A reference value is obtained experimentally for the 3D printing sample ($1.78 \times 10^{-11} \text{m}^2$, see Appendix 6.11 for the configurations for printing and permeability testing) to establish a baseline. The ideal model consistently predicts the highest permeability values for both solid and porous tow models, suggesting an overestimation due to the inability to fully account for the complexity of real-world microstructure. The realistic model, which integrates more microstructural characteristics, indicates a closer approximation to the experimental observations. The DMT approach yields the closest k_z to the reference, with a value of $2.07 \times 10^{-11} \text{m}^2$ for the solid tow model. This value is 14% higher than the reference. This comparison demonstrates that the more detailed information incorporated into the numerical model, the less deviation there is from the predictions. Hence, the DMT model demonstrates superior performance in predicting permeability.

The observed discrepancy between the predicted permeability with DMT and the reference

can be attributed to several factors. First, the thermal contraction of the printed material causes a reduction in the volume of the sample. Second, the gravitational force induces sagging during the printing and cooling phases. Such deformations disrupt the internal porous structure, potentially reducing the interconnected pores and impeding fluid flow. This discrepancy may also originate from numerical errors. Nevertheless, an error margin of 14% is considered acceptable, especially considering that the experimental error of transverse permeability tests generally falls within this range.

The numbers above the bars in Figure 6.13 represent the increase in the predicted permeability from solid to porous models. This difference is also visualized with the vertical lines. The contribution of porous tows to the total flux is 3.7%, 15.3%, and 6.7% for the ideal, realistic, and DMT models, respectively. Such models can also be used to calculate two-phase flow [262] inside textiles, which is important for understanding the formation of manufacturing defects. This particular capability addresses the limitations of current image-based permeability predictions commonly found in the literature [23, 24].

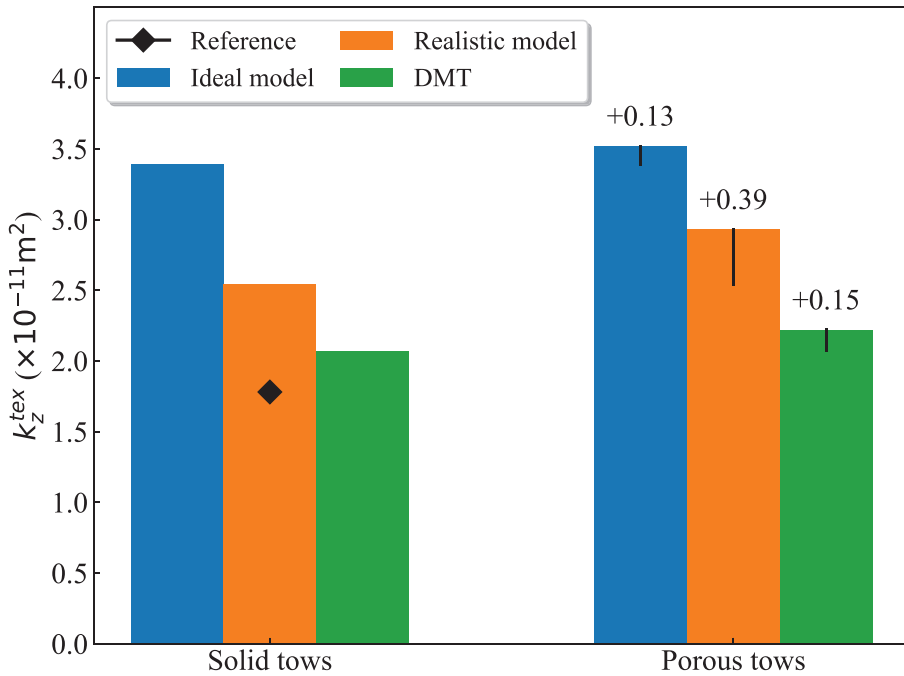


Figure 6.13 Comparison of transverse permeability predicted with ideal (Figure 6.9a), realistic (Figure 6.9b) and DMT (Figure 6.8) models. A reference value was obtained experimentally with a 3D printed sample of the DMT model to establish a baseline for the comparison.

6.8 Conclusion

This work introduces a new numerical tool specifically designed for geometric analysis, modeling, and high-fidelity mesh generation of textile reinforcements based on volumetric images. This open-source project, named PolyTex, features a purpose-designed hierarchical object-oriented structure. This enables a streamlined and efficient workflow. Researchers and engineers can better predict composite properties using the generated Digital Material Twin (DMT) model, as it excels at capturing the intricate internal structure of actual textiles. The tool provides a concise and well-documented interface to users and offers a range of advantages:

- **Input Flexibility.** *PolyTex* accepts two widely used data structures as input: either an explicit representation of tow geometry using point clouds (data obtained through manual segmentation tools such as *ImageJ*), or implicit representations, such as image masks - a common output format from machine learning-based image segmentation methods or conventional thresholding.
- **High-fidelity geometry representation.** The unbiased estimation property inherent in the kriging method minimizes errors throughout the geometrical modeling process. A substantial amount of pertinent information from the volumetric image can be automatically transferred to the generated geometric model.
- **Data persistence and incremental modifications.** The object-oriented principle, formulated for the purpose of storing and managing raw and processed data together with processing parameters, guarantees the traceability and reproducibility of the work process. Furthermore, distinct data persistence methods were devised at various stages, allowing incremental modifications using the preserved data.
- **Cross-tool interoperability.** Tailored APIs allow smooth integration between *PolyTex*'s modeling capabilities and the simulation environments offered by *OpenFOAM* and *Abaqus*. The generated numerical simulation files retain the local variability of the fiber tows concerning parameters such as fiber volume fraction and permeability. This enables dual-scale simulations that closely mimic the actual structures. Case studies on virtual testing of permeability were presented to demonstrate this capability and illustrate the use of DMT models.

Overall, the open-source project developed in this work can serve as a valuable resource for various specialized research problems and applications. For example, future work could

use DMT models to study the impact of dual-scale resin flow and textile architecture on the formation of manufacturing defects (voids) and on the development of residual stresses during processing.

Data availability

The complete source code for the *PolyTex* project can be found on GitHub (<https://github.com/binyang424/polytex>). The source code is publicly available under the GNU General Public License. The code for the case study is available for download as Supplementary Data. Additionally, the *PolyTex* project website provides demo data on how to use the code.

Acknowledgements

The authors would like to acknowledge the contributions of our late colleague, Prof. François Trochu. His insights, expertise, and dedication to this research were instrumental and have profoundly influenced the work. The authors are grateful for the foundation he provided us. The authors also wish to express their gratitude to Dr. Yang Chao from Wuhan University of Technology for his assistance in the development of the *Abaqus* interface.

6.9 Appendix

6.10 Mesh file specifications

The conventions for representing hexahedral meshes in the VTK unstructured grid, *Abaqus* input (.inp), and *OpenFOAM* polyMesh formats are shown in Figure 6.14. In both the VTK unstructured grid and the *Abaqus* inp, hexahedral elements are explicitly defined using node connectivity. The VTK unstructured grid format starts by numbering nodes from 0, while the *Abaqus* inp starts from 1. Figure 6.14b also shows the manner in which element faces are ordered in *Abaqus* format. Correctly defining the faces is essential to specify the contact between fiber tows.

The description in *OpenFOAM* polyMesh differs significantly. Hexahedral meshes are structured on a face-based basis in polyMesh. Figure 6.14c illustrates that a mesh comprises two types of faces: internal faces that connect two elements, and boundary faces that connect to a single element. The nodes on each face are arranged counterclockwise and the node ids are stored in a file named **faces** (see Figure 6.5). The element towards which the normal vector

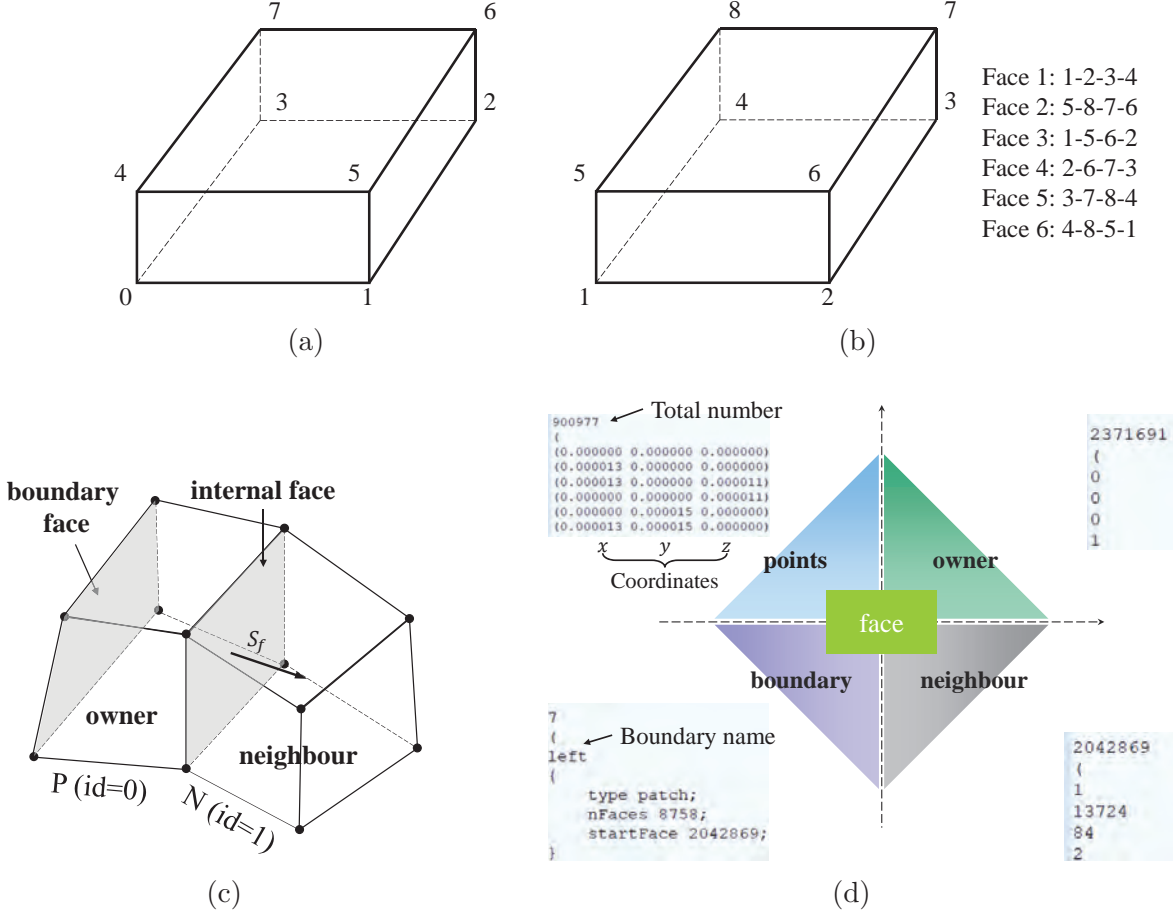


Figure 6.14 Representation and storage of hexahedral meshes: (a) VTK unstructured grid; (b) Abaqus input file (.inp); (c) components of `polyMesh` for *OpenFOAM*; (d) file structure of `polyMesh`.

of an internal face points is termed the neighbor of the face. The other element connected to the face is known as the face owner. Thus, each element is implicitly described through the connectivity of faces. Figure 6.14d illustrates the storage format of the node coordinates, owners, neighbors, and boundary patches.

6.11 Configurations for reference sample printing and permeability testing

Creating a reference sample involves using 3D printing technology to replicate the flow channels in the porous domain. The 3D printer must be able to distinguish the channels. Thus, an analysis was performed based on the volumetric image presented in Section 6.7. The channel size is determined by the largest sphere that can fit into the pixel location. The analysis was

conducted using the *BoneJ* plugin [263] provided by *ImageJ* [247].

The result is presented in Figure 6.15a. The warp and weft tows in the 3D orthogonal fabric are not vertically intertwined but rather arranged in an organized manner. Consequently, the mesopores also exhibit a high degree of regularity. The maximum diameter of the flow channel was 38 pixels (0.836 mm, with 1 pixel = 22 μm). In this context, the micropores within the fiber tows are disregarded due to their insignificant contribution to the flow and the challenges associated with imaging and replicating pores with a diameter below 10 μm .

The contribution of a mesopore to the overall flow capacity can be estimated using the Hagen-Poiseuille equation:

$$Q = \frac{\pi \cdot r^4 \cdot \Delta p}{8 \cdot \mu \cdot L} \quad (6.10)$$

where Q is the flow rate of the fluid (m^3/s) through a channel with radius of r and length of L (m). The pore size distribution and flow capacity are shown in Figure 6.15b. To have a significant contribution to the flow, the diameter of the flow channel should be larger than 0.2mm, namely, $d_{\min} = 0.2\text{mm}$.

The currently accessible 3D printer to the authors, the Ultimaker S3, is capable of printing objects with a resolution of 0.1 mm. However, this printing resolution cannot ensure accurately reproducing flow channels with a diameter of d_{\min} , as the printing resolution r_{res} should satisfy $r_{\text{res}} \ll d_{\min}$. Therefore, we adopted a "magnified twin" strategy proposed by Belot et al [264]. A magnified twin is created at a larger scale than its original size with a scaling factor $f_s > 1$. Belot et al. demonstrated that the permeability k_s of the magnified twin is related to the permeability k of the original sample as follows:

$$k = \frac{1}{f_s^2} k_s \quad (6.11)$$

Therefore, the model for printing can be enlarged, printed, and subsequently tested for permeability k_s . The permeability of the original sample can be determined using Equation 6.11. The magnified model should maintain the kinematic similarity with the original structure. This means that the geometry is scaled in a way that the flow behavior through the magnified twin mirrors the behavior of the original structure under similar conditions. This similarity is quantified with the Reynolds number Re_s :

$$Re_s = \frac{3\rho U \max(d_{i,s})}{2\mu\phi_p} = \frac{3\rho U \max(f_s d_i)}{2\mu\phi_p} \leq 1 \quad (6.12)$$

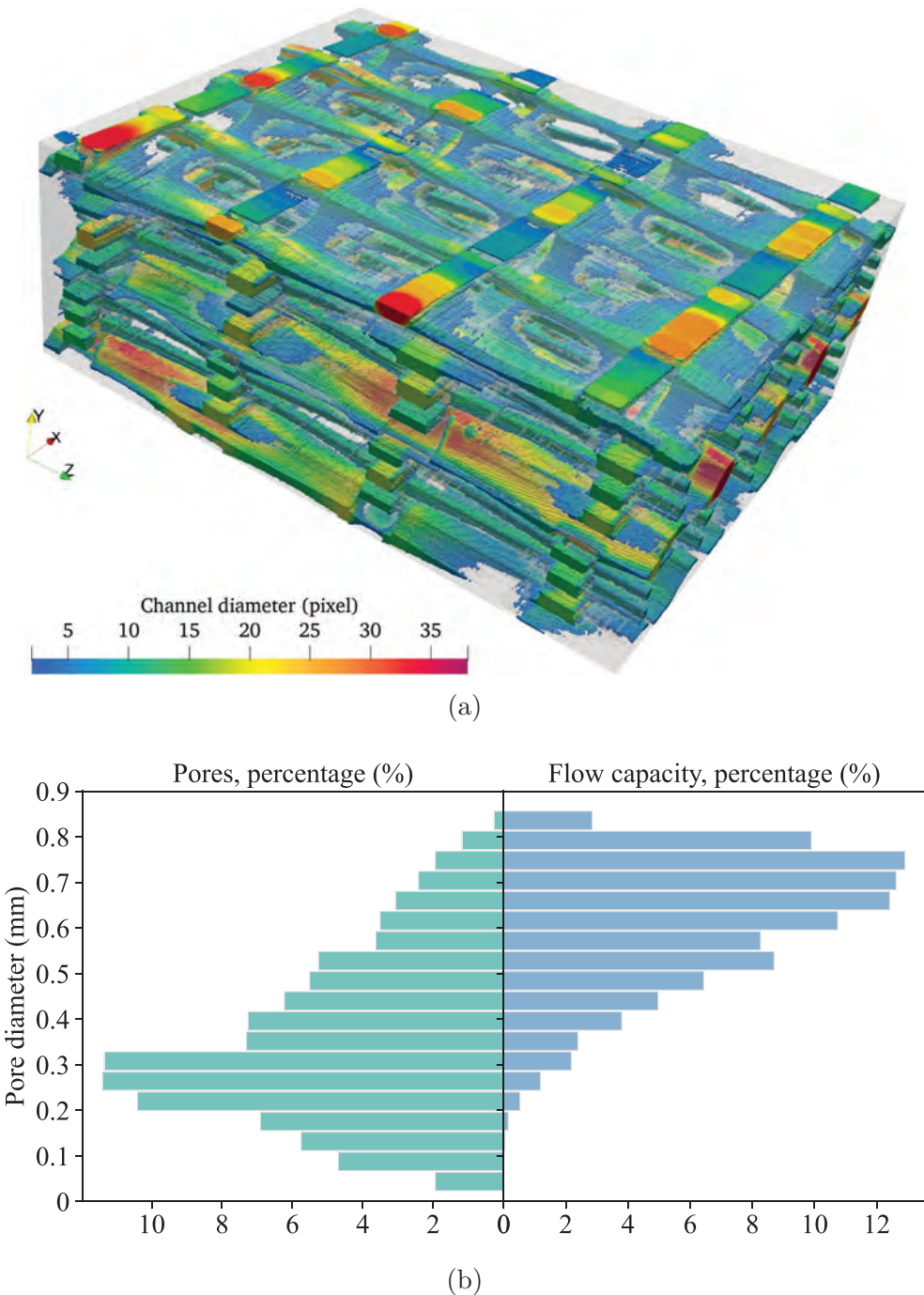


Figure 6.15 Flow channel size estimation: (a) pore size of mesopores estimated by fitting the maximum sphere that can be accommodated at the pixel location (1 pixel = 22 μm); (b) pore size distribution and flow capacity estimated with the Hagen-Poiseuille equation.

where U denotes the superficial velocity of the test fluid. $d_{i,s}$ and d_i represent the channel diameters of the magnified and the original samples. ϕ_p is the volume fraction of the meso-

pores (porosity). In the case study presented in Section 6.7, $\phi_p = 0.26$, test fluid dynamic viscosity $\mu = 0.1 \text{ Pa} \cdot \text{s}$ and density $\rho = 960 \text{ kg/m}^3$. We obtain:

$$f_s \leq \frac{2\mu\phi_p}{3\rho U \max(d_i)} = \frac{0.052}{2880 U \max(d_i)} \quad (6.13)$$

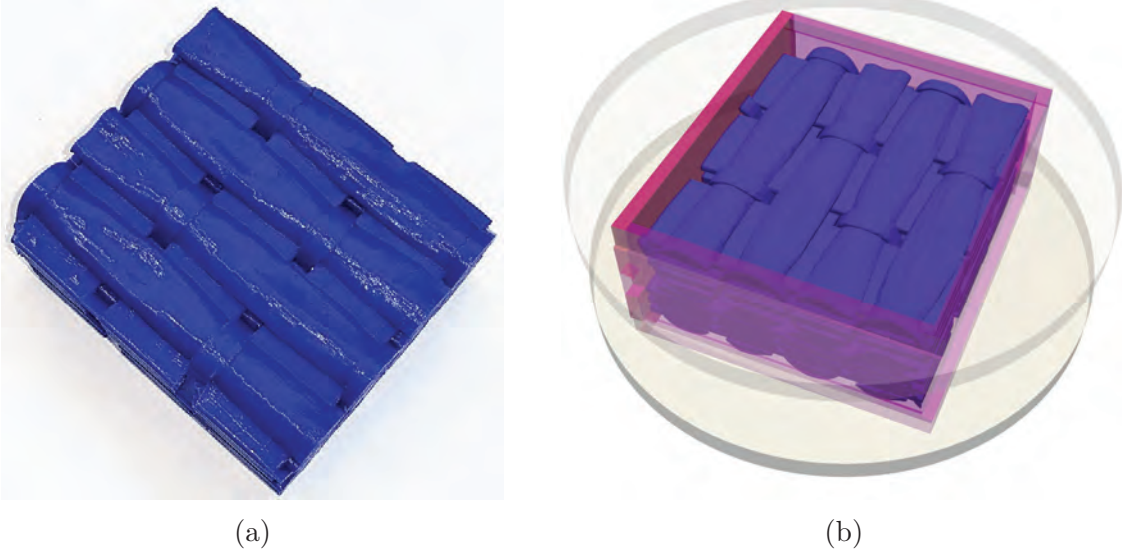


Figure 6.16 Reference sample for permeability validation: (a) . (b) the printed sample.

Furthermore, the size of the testing apparatus used for permeability testing also imposes a restriction on the scaling factor. The inner diameter of the testing apparatus used in current work is 96 mm. The magnified sample must fit within it. As a result, a scaling factor $f_s = 4.5$ was selected, as it meets all of the aforementioned constraints. The printing material was polylactic acid (PLA). Polyvinyl alcohol (PVA), a water-soluble material, was employed as the support material and subsequently removed once the PLA had solidified. A great accuracy and surface quality is achieved, as shown in Figure 6.16a. As the permeability test apparatus is designed for cylindrical samples, a fixture was designed to hold the sample in place (see Figure 6.16b). The fixture is tightened to ensure the sample remains stationary throughout the test. The sample is enclosed by impermeable plates on all sides (parts shown in dark red). Thus, the fluid can only pass through the sample in its thickness direction. The transverse permeability test device at Polytechnique Montréal and the test procedure are detailed in the work of Yang et al. [33].

CHAPTER 7 CONCLUSION

The process of impregnating dry textile preforms in the through-thickness direction has become more important to improve the fabrication efficiency of liquid composite molding techniques. This method has been incorporated into new variations of the LCM process, such as compression resin transfer molding (CRTM) and flexible injection molding (FI), which are commonly used in the manufacturing of high-performance composite components for the automotive and aerospace industries. Consequently, studying and understanding the behavior of the transverse resin flow is crucial to avoid manufacturing defects. The objective of this project was to develop techniques for accurately characterizing transverse flow in textile reinforcements, both experimentally and numerically.

This chapter presents a comprehensive synthesis of the study, beginning with a summary of the methodology used and the results obtained. Subsequently, it discusses the limitations of the present research and offers suggestions for future investigations.

7.1 Summary of works

Overall, this project makes two main contributions. First, it identifies some factors that affect the accuracy of the transverse permeability tests using the unidirectional method and suggests a correction algorithm to improve the reproducibility. Second, a Python package, *PolyTex*, was developed to automate the generation of high-fidelity digital material twin models and released as an open-source code. It allows engineers and researchers to create digital material twin models and perform virtual tests in various numerical environments with minimal effort. A synopsis of the conducted research and its corresponding outcomes in order to accomplish the two contributions is presented in the following.

The research began by examining the factors that influence the measurement accuracy of transverse permeability tests. This is a notable concern within the liquid composite molding community, as indicated by the latest international benchmark exercise. Alongside the factors associated with the testing apparatus, we identified for the first time that the permeability anisotropy and the thickness of the fibrous preform being tested also have an impact on the accuracy of the test results by the unidirectional method. Experiments were carried out to confirm and clarify this phenomenon. The findings indicated that although unidirectional test devices are widely used, they do not necessarily create a one-dimensional flow, as anticipated.

Numerical analyzes clearly demonstrated that in-plane flow was introduced due to the flow

distribution plates. These plates are essential to maintain the fiber content, but result in an underestimation of permeability. A performance indicator, the discharge coefficient, was proposed to quantify the performance of the test molds. Two molds with different geometries were examined with the indicator. The results show that the first mold underestimates the permeability of the tested fabrics by up to 51%, while the second mold underestimates it by up to 36%. A strong relationship was found between the indicator and the open-space ratio of the plates. Thanks to the newly proposed iterative correction algorithm, underestimations were eliminated, and the reproducibility between the two molds was improved.

While textile reinforcements possess a multiscale structure, the existing unidirectional test method fails to capture the flow occurring at the mesoscale and microscale levels. Hence, a parametric approach is suggested for modeling the geometry of textile reinforcements at the meso-level. These models are referred to as digital material twins because they accurately represent the geometric characteristics of their physical counterparts. It is primarily concerned with the representation of the tow surface, the trajectory, and the extraction of local geometric features. In contrast to the commonly used Laplacian filter, the proposed smoothing tool prevents volume shrinkage. This is crucial as the local fiber content depends on the volume of fiber tows. The cross sections orthogonal to the tow trajectory can be easily identified by intersecting implicit planes with the tow surface, thanks to the parametric representation. Validation shows that this method aligns with the mesh trimming approach but is more efficient.

Finally, we developed the *PolyTex* package to automate the generation of digital material twins. The package is capable of processing volumetric image data, extracting geometric features, and generating input files for various numerical environments. It is worth noting that the generated models are not restricted to numerical investigations of dual-scale flow but can also be utilized to predict the mechanical properties of textile composites. Therefore, the mechanisms behind the creation of manufacturing defects and the progression of damage in composite parts can be explored considering the spatial variability of the mesostructure. The virtual testing of transverse permeability was used as a case study to demonstrate the capacity of *PolyTex*. The results show an error of 14% compared to the experimental data.

7.2 Limitations

The following limitations are identified in the current work:

1. The performance evaluation and correction approach proposed in Chapter 4 was validated for the measurement of saturated transverse permeability only. The effect of

test devices on unsaturated permeability has not been investigated. Investigating this aspect is important considering that the resin impregnation process is unsaturated. Additionally, the two unidirectional test sets analyzed in this study have similar geometries. To further validate the proposed algorithm, it would be beneficial to compare unidirectional devices with different configurations (e.g., honeycomb or porous flow distribution plates) and cavity geometries.

2. The parametric kriging method (Chapter 5) can be computationally expensive for large datasets (> 150 points per cross section). The current implementation of *PolyTex* is not optimized for parallel computing. Therefore, the processing time increases significantly with increasing numbers of points in the data set.
3. Although a streamlined workflow and data persistence strategies are implemented in *PolyTex*, as presented in Chapter 6, the current version is not yet ready to manage projects with several different textiles. A more comprehensive database management system is required to facilitate the comparison of different models, which is interesting for studying the evolution of the internal geometry of textile reinforcement under various conditions.
4. *PolyTex* currently only supports the generation of voxel meshes. The stepwise boundary between the matrix and the reinforcement can cause artificial stress concentrations in the numerical investigation of damage progression.

7.3 Future research

In addition to addressing the limitations discussed in the previous sections, future work could also investigate the following research topics.

1. **Applying the performance indicator for the evaluation of test molds:** The suggested metric can be used to evaluate the performance of the test molds used by participants in future benchmark exercises. This will aid in identifying and understanding the performance difference between different testing devices, which can be beneficial in improving the reproducibility and reliability of the test results.
2. **Post-processing and visualization modules for *PolyTex*:** Future development plans include modules specifically for post-processing and visualizing the results generated by *PolyTex*. This enhancement would make it easier to interpret and use the analysis findings.

3. Use of MCMC methods for the generation of statistically equivalent models:

This refers to the generation of models that statistically mirror real physical structures through Markov chain Monte Carlo (MCMC) methods. The significance of this approach lies in its ability not only to describe existing structures but also to generate statistically equivalent models.

- 4. Homogenization module for performance prediction:** Incorporating a homogenization module would allow for simplified predictions of the properties of textile composites. This can be accomplished by integrating with existing open source software packages, like OpenLB for simulating fluid flow and OpenPNM for analyzing mesopore networks and predicting permeability. This approach avoids reinventing the wheel.
- 5. Digital twin model for various analyzes:** Although the current focus of the high-fidelity digital twin model is investigating permeability, the model also has the potential to study other aspects such as dual-scale resin flow, manufacturing defects, and mechanical properties. This could aid to gain a more comprehensive understanding of textile composites.

REFERENCES

- [1] S. Konstantopoulos, C. Hueber, I. Antoniadis, J. Summerscales, and R. Schledjewski, “Liquid composite molding reproducibility in real-world production of fiber reinforced polymeric composites: A review of challenges and solutions,” *Advanced Manufacturing: Polymer & Composites Science*, vol. 5, no. 3, pp. 85–99, 2019.
- [2] Q. Zhiwen, S. Qiang, Z. Mingming, R. Xiaomin, L. Caicai, W. Jihui, and X. Jianzhong, “Design and structural responses of a 38-meter sectional wind turbine blade under extreme static loads,” *Composite Structures*, vol. 290, p. 115487, 03 2022.
- [3] P. M. Bhat, *Simulation and validation of mold filling during compression resin transfer molding (CRTM) process*. University of Delaware, 2007.
- [4] B. Yang, T. Jin, and S. Wang, “Study on optimization of the pouring system in vacuum infusion molding process for composite yacht hull,” *Shipbuilding of China*, 2013.
- [5] Marsh and George, “Composites consolidate in commercial aviation,” *Reinforced Plastics*, pp. 302–305, 2016.
- [6] G. Marsh, “Aero engines lose weight thanks to composites,” *Reinforced Plastics*, vol. 56, no. 6, pp. 32–35, 2012. [Online]. Available: <https://www.sciencedirect.com/science/article/pii/S0034361712701467>
- [7] R. M. McDermott, J. S. Tate, and J. H. Koo, “Exploration of a new affordable thermal protection system utilizing 2.5d silica/polysiloxane composite,” *Journal of Composite Materials*, vol. 56, no. 5, pp. 685–698, 2022. [Online]. Available: <https://doi.org/10.1177/00219983211038622>
- [8] A. TPI, “Overview of the scrimp™ technology,” *Report No. Warren, RI: TPI Technology, Inc.* pp, 2001.
- [9] A. Hindersmann, “Confusion about infusion: An overview of infusion processes,” *Composites Part A: Applied Science and Manufacturing*, vol. 126, p. 105583, 2019.
- [10] P. Causse, E. Ruiz, and F. Trochu, “Experimental study of flexible injection to manufacture parts of strong curvature,” *Polymer composites*, vol. 32, no. 6, pp. 882–895, 2011.

- [11] X.-t. Pham and F. Trochu, "Simulation of compression resin transfer molding to manufacture thin composite shells," *Polymer Composites*, vol. 20, no. 3, pp. 436–459, 1999.
- [12] H. Darcy, "The public fountains of the city of dijon," *Victor Dalmont, Paris, France*, 1856.
- [13] A. Yong, A. Aktas, D. May, A. Endruweit, S. Advani, P. Hubert, S. Abaimov, D. Abliz, I. Akhatov, M. Ali *et al.*, "Out-of-plane permeability measurement for reinforcement textiles: A benchmark exercise," *Composites Part A Applied Science and Manufacturing*, vol. 148, no. 1, p. 106480, 2021.
- [14] F. Klunker, M. Danzi, and P. Ermanni, "Fiber deformation as a result of fluid injection: modeling and validation in the case of saturated permeability measurements in through thickness direction," *Journal of Composite Materials*, vol. 49, no. 9, pp. 1091–1105, 2015.
- [15] S. Scholz, J. W. Gillespie, and D. Heider, "Measurement of transverse permeability using gaseous and liquid flow," *Composites Part A Applied Science & Manufacturing*, vol. 38, no. 9, pp. 2034–2040, 2007.
- [16] Y. Nikishkov, L. Aioldi, and A. Makeev, "Measurement of voids in composites by x-ray computed tomography," *Composites Science and Technology*, vol. 89, pp. 89–97, 2013.
- [17] J. Vilà, F. Sket, F. Wilde, G. Requena, C. González, and J. LLorca, "An in situ investigation of microscopic infusion and void transport during vacuum-assisted infiltration by means of x-ray computed tomography," *Composites science and technology*, vol. 119, pp. 12–19, 2015.
- [18] X. Zeng, L. P. Brown, A. Endruweit, M. Matveev, and A. C. Long, "Geometrical modelling of 3d woven reinforcements for polymer composites: Prediction of fabric permeability and composite mechanical properties," *Composites Part A: Applied Science and Manufacturing*, vol. 56, pp. 150–160, 2014.
- [19] B. Wintiba, D. Vasiukov, S. Panier, S. V. Lomov, K. E. M. Kamel, and T. J. Massart, "Automated reconstruction and conformal discretization of 3d woven composite ct scans with local fiber volume fraction control," *Composite Structures*, vol. 248, p. 112438, 2020.
- [20] W. Wijaya, M. Ali, R. Umer, K. Khan, P. Kelly, and S. Bickerton, "An automatic methodology to ct-scans of 2d woven textile fabrics to structured finite element and

- voxel meshes,” *Composites Part A: Applied Science and Manufacturing*, vol. 125, p. 105561, 2019.
- [21] A. Rassineux, “Robust conformal adaptive meshing of complex textile composites unit cells,” *Composite Structures*, vol. 279, p. 114740, 2022.
 - [22] N. Saxena, R. Hofmann, F. O. Alpak, S. Berg, J. Dietderich, U. Agarwal, K. Tandon, S. Hunter, J. Freeman, and O. B. Wilson, “References and benchmarks for pore-scale flow simulated using micro-ct images of porous media and digital rocks,” *Advances in Water Resources*, vol. 109, pp. 211–235, 2017.
 - [23] M. Ali, R. Umer, K. Khan, and W. Cantwell, “In-plane virtual permeability characterization of 3d woven fabrics using a hybrid experimental and numerical approach,” *Composites Science and Technology*, vol. 173, pp. 99–109, 2019.
 - [24] W. Huang, P. Causse, H. Hu, and F. Trochu, “Numerical and experimental investigation of saturated transverse permeability of 2d woven glass fabrics based on material twins,” *Polymer Composites*, vol. 41, no. 4, pp. 1341–1355, 2020.
 - [25] X. Lei, W. Rui, Z. Shujie, and L. Yong, “Vibration characteristics of glass fabric/epoxy composites with different woven structures:,” *Journal of Composite Materials*, vol. 45, pp. 1069–1076, 2011.
 - [26] C. A. Chairman, S. Jayasathyakawin, S. P. Babu, and M. Ravichandran, “Mechanical properties of basalt fabric plain and twill weave reinforced epoxy composites,” *Materials Today: Proceedings*, 2020.
 - [27] I. D. Patiño, H. Power, C. Nieto-Londoño, and W. F. Flórez, “Stokes–brinkman formulation for prediction of void formation in dual-scale fibrous reinforcements: a bem/dr-bem simulation,” *Computational Mechanics*, vol. 59, pp. 555–577, 2017.
 - [28] F. Lebel, A. Fanaei, E. Ruiz, and F. Trochu, “Prediction of optimal flow front velocity to minimize void formation in dual scale fibrous reinforcements,” *International Journal of Material Forming*, vol. 7, pp. 93–116, 2014.
 - [29] E. Ruiz, V. Achim, S. Soukane, F. Trochu, and J. Bréard, “Optimization of injection flow rate to minimize micro/macro-voids formation in resin transfer molded composites,” *Composites science and technology*, vol. 66, no. 3-4, pp. 475–486, 2006.
 - [30] S. Facciotto, P. Simacek, S. G. Advani, and P. Middendorf, “Modeling of anisotropic dual scale flow in rtm using the finite elements method,” *Composites Part B: Engineering*, vol. 214, p. 108735, 2021.

- [31] B. Caglar, C. Tekin, F. Karasu, and V. Michaud, "Assessment of capillary phenomena in liquid composite molding," *Composites Part A: Applied Science and Manufacturing*, vol. 120, pp. 73–83, 2019.
- [32] X. Wu, J. Li, and R. Shenoi, "A new method to determine fiber transverse permeability," *Journal of composite materials*, vol. 41, no. 6, pp. 747–756, 2007.
- [33] B. Yang, Y. Sun, F. Trochu, C. Béguin, J. Wang, and P. Causse, "Performance evaluation of unidirectional molds used for measuring saturated transverse permeability of engineering textiles," *Composites Part A: Applied Science and Manufacturing*, vol. 169, p. 107524, 2023.
- [34] P. Ferland, D. Guittard, and F. Trochu, "Concurrent methods for permeability measurement in resin transfer molding," *Polymer composites*, vol. 17, no. 1, pp. 149–158, 1996.
- [35] R. Arbter, J. Beraud, C. Binetruy, L. Bizet, J. Bréard, S. Comas-Cardona, C. Demaria, A. Endruweit, P. Ermanni, F. Gommer *et al.*, "Experimental determination of the permeability of textiles: A benchmark exercise," *Composites Part A: Applied Science and Manufacturing*, vol. 42, no. 9, pp. 1157–1168, 2011.
- [36] N. Vernet, E. Ruiz, S. Advani, J. B. Alms, M. Aubert, M. Barburski, B. Barari, J. M. Beraud, D. C. Berg, N. Correia *et al.*, "Experimental determination of the permeability of engineering textiles: Benchmark ii," *Composites Part A: Applied Science and Manufacturing*, vol. 61, pp. 172–184, 2014.
- [37] J. Bréard, "Matériaux composites à matrice polymère: modélisation numérique de la phase de remplissage du procédé rtm et détermination expérimentale de la perméabilité d'un renfort fibreux," Ph.D. dissertation, Le Havre, 1997.
- [38] C. Demaria, E. Ruiz, and F. Trochu, "In-plane anisotropic permeability characterization of deformed woven fabrics by unidirectional injection. part i: Experimental results," *Polymer composites*, vol. 28, no. 6, pp. 797–811, 2007.
- [39] S. Sharma and D. A. Siginer, "Permeability measurement methods in porous media of fiber reinforced composites," *Applied Mechanics Reviews*, vol. 63, no. 2, p. 020802, 02 2010.
- [40] D. May, A. Aktas, S. Advani, D. Berg, A. Endruweit, E. Fauster, S. Lomov, A. Long, P. Mitschang, S. Abaimov *et al.*, "In-plane permeability characterization of engineering

- textiles based on radial flow experiments: A benchmark exercise,” *Composites Part A: Applied Science and Manufacturing*, vol. 121, pp. 100–114, 2019.
- [41] R. Pomeroy, S. Grove, J. Summerscales, Y. Wang, and A. Harper, “Measurement of permeability of continuous filament mat glass-fibre reinforcements by saturated radial airflow,” *Composites Part A: Applied Science and Manufacturing*, vol. 38, no. 5, pp. 1439–1443, 2007.
 - [42] R. S. Parnas and A. J. Salem, “A comparison of the unidirectional and radial in-plane flow of fluids through woven composite reinforcements,” *Polymer Composites*, vol. 14, no. 5, pp. 383–394, 1993.
 - [43] E. Heardman, C. Lekakou, and M. Bader, “Flow monitoring and permeability measurement under constant and transient flow conditions,” *Composites science and technology*, vol. 64, no. 9, pp. 1239–1249, 2004.
 - [44] Q. Liu, R. S. Parnas, and H. S. Giffard, “New set-up for in-plane permeability measurement,” *Composites Part A: Applied Science and Manufacturing*, vol. 38, no. 3, pp. 954–962, 2007.
 - [45] J. Weitzenböck, R. Shenoi, and P. Wilson, “Radial flow permeability measurement. part b: Application,” *Composites part A: applied science and manufacturing*, vol. 30, no. 6, pp. 797–813, 1999.
 - [46] ——, “Radial flow permeability measurement. part a: Theory,” *Composites Part A: Applied Science and Manufacturing*, vol. 30, no. 6, pp. 781–796, 1999.
 - [47] K. L. Adams, W. Russel, and L. Rebenfeld, “Radial penetration of a viscous liquid into a planar anisotropic porous medium,” *International Journal of Multiphase Flow*, vol. 14, no. 2, pp. 203–215, 1988.
 - [48] M.-k. Um and S.-k. Lee, “A study on the determination of in-plane permeability of fiber preforms,” *Polymer Composites*, vol. 20, no. 6, pp. 771–779, 1999.
 - [49] J. Bear, *Dynamics of fluids in porous media*. Courier Corporation, 2013.
 - [50] H. Tan and K. M. Pillai, “A method to estimate the accuracy of radial flow-based permeability measuring devices,” *Journal of composite materials*, vol. 43, no. 21, pp. 2307–2332, 2009.

- [51] B. Yang, J. Wang, Y. Feng, M. Zhan, and A. Ni, “Concurrent measurement of local and global in-plane permeability of reinforcement fabrics through real-time image processing,” *Polymers*, vol. 15, no. 15, p. 3233, 2023.
- [52] S. H. Ahn, W. I. Lee, and G. S. Springer, “Measurement of the three-dimensional permeability of fiber preforms using embedded fiber optic sensors,” *Journal of Composite Materials*, vol. 29, no. 6, pp. 714–733, 1995.
- [53] J. Weitzenböck, R. Shenoi, and P. Wilson, “Measurement of three-dimensional permeability,” *Composites Part A: Applied Science and Manufacturing*, vol. 29, no. 1-2, pp. 159–169, 1998.
- [54] W. O. Ballata, S. M. Walsh, and S. Advani, “Determination of the transverse permeability of a fiber preform,” *Journal of Reinforced Plastics & Composites*, vol. 18, no. 16, pp. 1450–1464, 1999.
- [55] P. B. Nedanov and S. G. Advani, “A method to determine 3d permeability of fibrous reinforcements,” *Journal of composite materials*, vol. 36, no. 2, pp. 241–254, 2002.
- [56] J. H. Jiang, Z. X. Wang, and N. L. Chen, “Measurement of transverse permeability of fabric preforms using ultrasound monitoring technique in lcm processes,” *Advanced Materials Research*, vol. 311, pp. 214–217, 2011.
- [57] J. Bréard, A. Saouab, and G. Bouquet, “Measurement of the spatial perméability of a three-dimensional reinforcement for composite materials à polymer matrix,” *The European Physical Journal-Applied Physics*, vol. 1, no. 2, pp. 269–278, 1998.
- [58] ——, “Dependence of the reinforcement anisotropy on a three dimensional resin flow observed by x-ray radioscopy,” *Journal of reinforced plastics and composites*, vol. 18, no. 9, pp. 814–826, 1999.
- [59] D. Becker, H. Grössing, S. Konstantopoulos, E. Fauster, P. Mitschang, and R. Schledjewski, “An evaluation of the reproducibility of ultrasonic sensor-based out-of-plane permeability measurements: a benchmarking study,” *Advanced Manufacturing: Polymer & Composites Science*, vol. 2, no. 1, pp. 34–45, 2016.
- [60] C.-H. Wu, T. James Wang, and L. James Lee, “Trans-plane fluid permeability measurement and its applications in liquid composite molding,” *Polymer Composites*, vol. 15, no. 4, pp. 289–298, 1994.

- [61] K. Okonkwo, P. Simacek, S. G. Advani, and R. S. Parnas, "Characterization of 3d fiber preform permeability tensor in radial flow using an inverse algorithm based on sensors and simulation," *Composites Part A Applied Science & Manufacturing*, vol. 42, no. 10, pp. 1283–1292, 2011.
- [62] L. Fang, J. Jiang, J. Wang, and C. Deng, "Effect of nesting on the out-of-plane permeability of unidirectional fabrics in resin transfer molding," *Applied Composite Materials*, vol. 22, pp. 231–249, 2015.
- [63] S. Comas-Cardona, C. Binetruy, and P. Krawczak, "Unidirectional compression of fibre reinforcements. part 2: A continuous permeability tensor measurement," *Composites Science and Technology*, vol. 67, pp. 638–645, 2007.
- [64] M. Buntain and S. Bickerton, "Compression flow permeability measurement: a continuous technique," *Composites Part A: Applied Science and Manufacturing*, vol. 34, no. 5, pp. 445–457, 2003.
- [65] X. Wu, J. Li, and R. Shenoi, "A new method to determine fiber transverse permeability," *Journal of composite materials*, vol. 41, no. 6, pp. 747–756, 2007.
- [66] F. V. Härter, J. A. Souza, L. A. Isoldi, E. D. d. Santos, and S. C. Amico, "Transverse permeability determination and influence in resin flow through an orthotropic medium in the rtm process," *Matéria (Rio de Janeiro)*, vol. 22, p. e11851, 2017.
- [67] X. Liu, D. Zhang, J. Sun, S. Yu, Y. Dai, Z. Zhang, J. Sun, G. Li, and K. Qian, "Refine reconstruction and verification of meso-scale modeling of three-dimensional five-directional braided composites from x-ray computed tomography data," *Composite Structures*, vol. 245, p. 112347, 2020.
- [68] B. K. Behera and P. Hari, *Woven textile structure: Theory and applications*. Elsevier, 2010.
- [69] N. Vernet and F. Trochu, "Analysis and modeling of 3d interlock fabric compaction behavior," *Composites Part A: Applied Science and Manufacturing*, vol. 80, pp. 182–193, 2016.
- [70] R. Bai, B. Chen, J. Colmars, and P. Boisse, "Physics-based evaluation of the drapability of textile composite reinforcements," *Composites Part B: Engineering*, vol. 242, p. 110089, 2022.

- [71] Z. Grofti, B. Croteau-Labouly, R. Boukhili, P. Causse, S. Belouettar, H. Perrin, and F. Trochu, “Simultaneous characterization of preform expansion and permeability in vacuum assisted resin infusion,” *Polymer Composites*, vol. 43, no. 6, pp. 3560–3573, 2022.
- [72] J. Hemmer, C. Burtin, S. Comas-Cardona, C. Binetruy, T. Savart, and A. Babeau, “Unloading during the infusion process: direct measurement of the dual-scale fibrous microstructure evolution with x-ray computed tomography,” *Composites Part A: Applied Science and Manufacturing*, vol. 115, pp. 147–156, 2018.
- [73] ISO 4410, “Test methods for the experimental characterization of in-plane permeability of fibrous reinforcements for liquid composite moulding,” pp. 1–32, 2023.
- [74] M. Mehdikhani, L. Gorbatikh, I. Verpoest, and S. V. Lomov, “Voids in fiber-reinforced polymer composites: A review on their formation, characteristics, and effects on mechanical performance,” *Journal of Composite Materials*, vol. 53, no. 12, pp. 1579–1669, 2019.
- [75] T. Lundstrom, B. Gebart, and C. Lundemo, “Void formation in rtm,” *Journal of reinforced plastics and composites*, vol. 12, no. 12, pp. 1339–1349, 1993.
- [76] B. Aaboud, A. Saouab, and Y. Nawab, “Simulation of air bubble’s creation, compression, and transport phenomena in resin transfer moulding,” *Journal of Composite Materials*, vol. 51, no. 29, pp. 4115–4127, 2017.
- [77] N. Patel and L. J. Lee, “Effects of fiber mat architecture on void formation and removal in liquid composite molding,” *Polymer Composites*, vol. 16, no. 5, pp. 386–399, 1995.
- [78] W. Huang, “Analysis of through-thickness injection in liquid composite molding based on digital material twins,” Ph.D. dissertation, Ecole Polytechnique, Montreal (Canada), 2020.
- [79] L. Labat, J. Bréard, S. Pillut-Lesavre, and G. Bouquet, “Void fraction prevision in lcm parts,” *The European Physical Journal-Applied Physics*, vol. 16, no. 2, pp. 157–164, 2001.
- [80] M. K. Kang, W. I. Lee, and H. T. Hahn, “Formation of microvoids during resin-transfer molding process,” *Composites Science and Technology*, vol. 60, no. 12-13, pp. 2427–2434, 2000.

- [81] R. Matuzaki, D. Seto, M. Naito, A. Todoroki, and Y. Mizutani, “Analytical prediction of void formation in geometrically anisotropic woven fabrics during resin transfer molding,” *Composites Science and Technology*, vol. 107, pp. 154–161, 2015.
- [82] B. Yang, T. Jin, F. Bi, Y. Wei, and J. Li, “Influence of fabric shear and flow direction on void formation during resin transfer molding,” *Composites Part A: Applied Science and Manufacturing*, vol. 68, pp. 10–18, 2015.
- [83] B. Yang, S. Wang, C. Ma, S. Wang, C. Zhao, and F. Bi, “Effect of horizontal shift between fabric layers on the meso-scale-void formation in liquid composite molding.” *Express Polymer Letters*, vol. 13, no. 6, 2019.
- [84] S. Gueroult, A. Lebel-Lavacry, C. H. Park, L. Bizet, A. Saouab, and J. Bréard, “Analytical modeling and in situ measurement of void formation in liquid composite molding processes,” *Advanced Composite Materials*, vol. 23, no. 1, pp. 31–42, 2014.
- [85] T. S. Lundström, V. Frishfelds, and A. Jakovics, “Bubble formation and motion in non-crimp fabrics with perturbed bundle geometry,” *Composites Part A: Applied Science and Manufacturing*, vol. 41, no. 1, pp. 83–92, 2010.
- [86] C. DeValve and R. Pitchumani, “Simulation of void formation in liquid composite molding processes,” *Composites Part A: Applied Science and Manufacturing*, vol. 51, pp. 22–32, 2013.
- [87] I. P. Arcila, H. Power, C. N. Londoño, and W. F. Escobar, “Boundary element method for the dynamic evolution of intra-tow voids in dual-scale fibrous reinforcements using a stokes–darcy formulation,” *Engineering Analysis with Boundary Elements*, vol. 87, pp. 133–152, 2018.
- [88] S. van Oosterom, A. Schreier, M. Battley, S. Bickerton, and T. Allen, “Influence of dissolved gasses in epoxy resin on resin infusion part quality,” *Composites Part A: Applied Science and Manufacturing*, vol. 132, p. 105818, 2020.
- [89] J. Juan, A. Silva, J. A. Tornero, J. Gámez, and N. Salán, “Void content minimization in vacuum infusion (vi) via effective degassing,” *Polymers*, vol. 13, no. 17, p. 2876, 2021.
- [90] F. LeBel, E. Ruiz, and F. Trochu, “Void content analysis and processing issues to minimize defects in liquid composite molding,” *Polymer Composites*, vol. 40, no. 1, pp. 109–120, 2019.

- [91] M. Shah and V. Chaudhary, “Flow modeling and simulation study of vacuum assisted resin transfer molding (vartm) process: A review,” in *IOP conference series: materials science and engineering*, vol. 872, no. 1. IOP Publishing, 2020, p. 012087.
- [92] M. Kozioł, “Simplified simulation of vari process using pam-rtm software,” *Composites Theory and Practice*, vol. 15, no. 4, pp. 218–227, 2015.
- [93] F. LeBel, A. E. Fanaei, E. Ruiz, and F. Trochu, “Experimental characterization by fluorescence of capillary flows in dual-scale engineering fabrics,” *Textile Research Journal*, vol. 83, no. 15, pp. 1634–1659, 2013.
- [94] D. Chen, K. Arakawa, and C. Xu, “Reduction of void content of vacuum-assisted resin transfer molded composites by infusion pressure control,” *Polymer Composites*, vol. 36, no. 9, pp. 1629–1637, 2015.
- [95] P. Carbone, F. Rubino, V. Paradiso, and F. Tucci, “Multi-scale modeling and online monitoring of resin flow through dual-scale textiles in liquid composite molding processes,” *The International Journal of Advanced Manufacturing Technology*, vol. 96, pp. 2215–2230, 2018.
- [96] Y. Oya, T. Matsumiya, A. Ito, R. Matsuzaki, and T. Okabe, “Gate optimization for resin transfer molding in dual-scale porous media: Numerical simulation and experiment measurement,” *Journal of Composite Materials*, vol. 54, no. 16, pp. 2131–2145, 2020.
- [97] J.-A. Almazán-Lázaro, E. López-Alba, and F.-A. Díaz-Garrido, “The mechanical effect of monitoring and controlling the impregnation in the resin infusion process,” *Polymer Composites*, vol. 43, no. 4, pp. 1916–1926, 2022.
- [98] S. V. Lomov, I. Verpoest, J. Cichosz, C. Hahn, D. S. Ivanov, and B. Verleye, “Meso-level textile composites simulations: Open data exchange and scripting,” *Journal of Composite Materials*, vol. 48, no. 5, pp. 621–637, 2014.
- [99] S. V. Lomov, “Modeling the geometry of textile composite reinforcements: Wisetex,” in *Composite Reinforcements for Optimum Performance (Second Edition)*, second edition ed., ser. Woodhead Publishing Series in Composites Science and Engineering, P. Boisse, Ed. Woodhead Publishing, 2021, pp. 199–236. [Online]. Available: <https://www.sciencedirect.com/science/article/pii/B9780128190050000071>

- [100] J. Gan, S. Bickerton, and M. Battley, “Quantifying variability within glass fibre reinforcements using an automated optical method,” *Composites Part A: Applied Science and Manufacturing*, vol. 43, no. 8, pp. 1169–1176, 2012.
- [101] F. Gommer, L. P. Brown, and R. Brooks, “Quantification of mesoscale variability and geometrical reconstruction of a textile,” *Journal of Composite Materials*, vol. 50, no. 23, pp. 3255–3266, 2016.
- [102] F. Desplentere, S. V. Lomov, D. Woerdeman, I. Verpoest, M. Wevers, P. Szucs, and A. Bogdanovich, “Geometrical characterization of 3-d warp-interlaced fabrics,” in *International SAMPE symposium and Exhibition*. SAMPE; 1999, 2003, pp. 1335–1347.
- [103] E. E. Swery, T. Allen, and P. Kelly, “Automated tool to determine geometric measurements of woven textiles using digital image analysis techniques,” *Textile Research Journal*, vol. 86, no. 6, pp. 618–635, 2016.
- [104] M. Karahan, S. V. Lomov, A. E. Bogdanovich, D. Mungalov, and I. Verpoest, “Internal geometry evaluation of non-crimp 3d orthogonal woven carbon fabric composite,” *Composites Part A: Applied Science and Manufacturing*, vol. 41, no. 9, pp. 1301–1311, 2010.
- [105] P. Vandeurzen, J. Ivens, and I. Verpoest, “Structure-performance analysis of two-dimensional woven fabric composites,” *Polymers and Polymer Composites*, vol. 4, no. 5, pp. 361–367, 1996.
- [106] P. He, W. Zhao, B. Yang, J. Wang, A. Ni, and S. Li, “Void content reduction of composites with sensor-aided injection strategy in liquid composite molding process,” *Materials Research Express*, vol. 8, no. 7, p. 075309, 2021.
- [107] K. Orhan *et al.*, “Micro-computed tomography (micro-ct) in medicine and engineering,” Springer, Tech. Rep., 2020.
- [108] D. R.-B. Aroush, E. Maire, C. Gauthier, S. Youssef, P. Cloetens, and H. Wagner, “A study of fracture of unidirectional composites using in situ high-resolution synchrotron x-ray microtomography,” *Composites science and technology*, vol. 66, no. 10, pp. 1348–1353, 2006.
- [109] A. Madra, N. El Hajj, and M. Benzeggagh, “X-ray microtomography applications for quantitative and qualitative analysis of porosity in woven glass fiber reinforced thermoplastic,” *Composites Science and technology*, vol. 95, pp. 50–58, 2014.

- [110] W. Huang, P. Causse, V. Brailovski, H. Hu, and F. Trochu, “Reconstruction of mesostructural material twin models of engineering textiles based on micro-ct aided geometric modeling,” *Composites Part A: Applied Science and Manufacturing*, vol. 124, p. 105481, 2019.
- [111] S. Hilal, *Characterization by microtomography of the mésostucture of fibrous reinforcements for the manufacture of composites*. Ecole Polytechnique, Montreal (Canada), 2018.
- [112] M. Ali, R. Umer, K. Khan, and W. Cantwell, “Application of x-ray computed tomography for the virtual permeability prediction of fiber reinforcements for liquid composite molding processes: A review,” *Composites Science and Technology*, vol. 184, p. 107828, 2019.
- [113] W. Huang, P. Causse, H. Hu, S. Belouettar, and F. Trochu, “Transverse compaction of 2d glass woven fabrics based on material twins—part i: Geometric analysis,” *Composite Structures*, vol. 237, p. 111929, 2020.
- [114] Y. Sinchuk, P. Kibleur, J. Aelterman, M. N. Boone, and W. Van Paepengem, “Variational and deep learning segmentation of very-low-contrast x-ray computed tomography images of carbon/epoxy woven composites,” *Materials*, vol. 13, no. 4, p. 936, 2020.
- [115] X.-W. Yu, H. Wang, and Z.-W. Wang, “Analysis of yarn fiber volume fraction in textile composites using scanning electron microscopy and x-ray micro-computed tomography,” *Journal of Reinforced Plastics and Composites*, vol. 38, no. 5, pp. 199–210, 2019.
- [116] H. Qian, “Micro ct experiment and the method of yarn segmentation in plain-weave composites of micro ct images,” Master’s thesis, National University of Defense Technology, 2015.
- [117] Z. Yousaf, P. Withers, and P. Potluri, “Compaction, nesting and image based permeability analysis of multi-layer dry preforms by computed tomography (ct),” *Composite Structures*, vol. 263, p. 113676, 2021.
- [118] A. Madra, F. Trochu, and P. Breitkopf, “Implicit kriging model of fibrous reinforcements in composites based on x-ray microtomography,” in *13e colloque national en calcul des structures*, 2017.

- [119] N. Naouar, E. Vidal-Salle, J. Schneider, E. Maire, and P. Boisse, “3d composite reinforcement meso fe analyses based on x-ray computed tomography,” *Composite Structures*, vol. 132, pp. 1094–1104, 2015.
- [120] N. Naouar, E. Vidal-Sallé, J. Schneider, E. Maire, and P. Boisse, “Meso-scale fe analyses of textile composite reinforcement deformation based on x-ray computed tomography,” *Composite structures*, vol. 116, pp. 165–176, 2014.
- [121] I. Straumit, S. V. Lomov, and M. Wevers, “Quantification of the internal structure and automatic generation of voxel models of textile composites from x-ray computed tomography data,” *Composites Part A: Applied Science and Manufacturing*, vol. 69, pp. 150–158, 2015.
- [122] A. Madra, P. Breitkopf, A. Rassineux, and F. Trochu, “Image-based model reconstruction and meshing of woven reinforcements in composites,” *International Journal for Numerical Methods in Engineering*, vol. 112, no. 9, pp. 1235–1252, 2017.
- [123] M. A. Ali, Q. Guan, R. Umer, W. J. Cantwell, and T. Zhang, “Efficient processing of μ ct images using deep learning tools for generating digital material twins of woven fabrics,” *Composites Science and Technology*, vol. 217, p. 109091, 2022.
- [124] K. Zheng, C. Wu, H. Chen, X. Zhang, Z. Wang, Z. Pan, B. Qiu, and Z. Wu, “Improved 3d image segmentation for x-ray tomographic data of biaxial warp-knitted composites,” *Journal of Reinforced Plastics and Composites*, p. 07316844231220716, 2023.
- [125] Y. Song, Z. Qu, H. Liao, and S. Ai, “Material twins generation of woven polymer composites based on resl-u-net convolutional neural networks,” *Composite Structures*, vol. 307, p. 116672, 2023.
- [126] M. Sherburn, “Geometric and mechanical modelling of textiles,” Ph.D. dissertation, University of Nottingham United Kingdom, 2007.
- [127] A. Long and L. Brown, “Modelling the geometry of textile reinforcements for composites: Texgen,” in *Composite reinforcements for optimum performance*. Elsevier, 2011, pp. 239–264.
- [128] I. Verpoest and S. V. Lomov, “Virtual textile composites software wisetex: Integration with micro-mechanical, permeability and structural analysis,” *Composites Science and Technology*, vol. 65, no. 15-16, pp. 2563–2574, 2005.

- [129] S. V. Lomov, D. S. Ivanov, I. Verpoest, M. Zako, T. Kurashiki, H. Nakai, and S. Hiro-sawa, “Meso-fe modelling of textile composites: Road map, data flow and algorithms,” *Composites science and technology*, vol. 67, no. 9, pp. 1870–1891, 2007.
- [130] A. Wendling, J. Daniel, G. Hivet, E. Vidal-Sallé, and P. Boisse, “Meshing preprocessor for the mesoscopic 3d finite element simulation of 2d and interlock fabric deformation,” *Applied Composite Materials*, vol. 22, pp. 869–886, 2015.
- [131] N. Isart, J. A. Mayugo, N. Blanco, L. Ripoll, A. Solà, and M. Soler, “Geometric model for 3d through-thickness orthogonal interlock composites,” *Composite Structures*, vol. 119, pp. 787–798, 2015.
- [132] B. Yang, S. Wang, and Q. Tang, “Geometry modeling and permeability prediction for textile preforms with nesting in laminates,” *Polymer Composites*, vol. 39, no. 12, pp. 4408–4415, 2018.
- [133] S. V. Lomov, “Wisetex software suit,” <https://www.mtm.kuleuven.be/english/research/scalint/cmg/software/downloads/wisetex-overview.pdf>, (Accessed on 01/21/2024).
- [134] P. Priyanka, H. Mali, and A. Dixit, “Geometrical modeling and performance analysis of textile composites using python scripted software platforms,” in *Advances in Simulation, Product Design and Development: Proceedings of AIMTDR 2018*. Springer, 2019, pp. 395–405.
- [135] T. Liao and S. Adanur, “A novel approach to three-dimensional modeling of interlaced fabric structures,” *Textile Research Journal*, vol. 68, no. 11, pp. 841–847, 1998.
- [136] Y. Wielhorski, A. Mendoza, M. Rubino, and S. Roux, “Numerical modeling of 3d woven composite reinforcements: A review,” *Composites Part A: Applied Science and Manufacturing*, vol. 154, p. 106729, 2022.
- [137] A. Vanaerschot, B. N. Cox, S. V. Lomov, and D. Vandepitte, “Stochastic multi-scale modelling of short-and long-range effects in textile composites based on experimental data,” in *Proceedings of the 16th European Conference on Composite Materials*, 2014, pp. 1–8.
- [138] J. Pazmino, V. Carvelli, and S. V. Lomov, “Micro-ct analysis of the internal deformed geometry of a non-crimp 3d orthogonal weave e-glass composite reinforcement,” *Composites Part B: Engineering*, vol. 65, pp. 147–157, 2014.

- [139] G. Zhou, X. Sun, and Y. Wang, "Multi-chain digital element analysis in textile mechanics," *Composites science and Technology*, vol. 64, no. 2, pp. 239–244, 2004.
- [140] S. Green, A. Long, B. El Said, and S. Hallett, "Numerical modelling of 3d woven preform deformations," *Composite Structures*, vol. 108, pp. 747–756, 2014.
- [141] Y. Wang and X. Sun, "Digital-element simulation of textile processes," *Composites science and technology*, vol. 61, no. 2, pp. 311–319, 2001.
- [142] D. Durville, "Simulation of the mechanical behaviour of woven fabrics at the scale of fibers," *International journal of material forming*, vol. 3, pp. 1241–1251, 2010.
- [143] Y. Mahadik and S. Hallett, "Finite element modelling of tow geometry in 3d woven fabrics," *Composites Part A: Applied Science and Manufacturing*, vol. 41, no. 9, pp. 1192–1200, 2010.
- [144] D. Durville, I. Baydoun, H. Moustacas, G. Périé, and Y. Wielhorski, "Determining the initial configuration and characterizing the mechanical properties of 3d angle-interlock fabrics using finite element simulation," *International Journal of Solids and Structures*, vol. 154, pp. 97–103, 2018.
- [145] L. Daelemans, J. Faes, S. Allaoui, G. Hivet, M. Dierick, L. Van Hoorebeke, and W. Van Paepegem, "Finite element simulation of the woven geometry and mechanical behaviour of a 3d woven dry fabric under tensile and shear loading using the digital element method," *Composites Science and Technology*, vol. 137, pp. 177–187, 2016.
- [146] A. Madra, J. Adrien, P. Breitkopf, E. Maire, and F. Trochu, "A clustering method for analysis of morphology of short natural fibers in composites based on x-ray microtomography," *Composites Part A: Applied Science and Manufacturing*, vol. 102, pp. 184–195, 2017.
- [147] A. Madra, P. Causse, F. Trochu, J. Adrien, E. Maire, and P. Breitkopf, "Stochastic characterization of textile reinforcements in composites based on x-ray microtomographic scans," *Composite Structures*, vol. 224, p. 111031, 2019.
- [148] W. Huang, P. Causse, H. Hu, S. Belouettar, and F. Trochu, "Transverse compaction of 2d glass woven fabrics based on material twins—part ii: Tow and fabric deformations," *Composite Structures*, vol. 237, p. 111963, 2020.
- [149] B. Wintiba, B. Sonon, K. E. M. Kamel, and T. J. Massart, "An automated procedure for the generation and conformal discretization of 3d woven composites rves," *Composite structures*, vol. 180, pp. 955–971, 2017.

- [150] A. Drach, B. Drach, and I. Tsukrov, “Processing of fiber architecture data for finite element modeling of 3d woven composites,” *Advances in Engineering Software*, vol. 72, pp. 18–27, 2014.
- [151] N. Isart, B. El Said, D. Ivanov, S. Hallett, J. Mayugo, and N. Blanco, “Internal geometric modelling of 3d woven composites: A comparison between different approaches,” *Composite Structures*, vol. 132, pp. 1219–1230, 2015.
- [152] P. Soltani, M. S. Johari, and M. Zarrebini, “Effect of 3d fiber orientation on permeability of realistic fibrous porous networks,” *Powder Technology*, vol. 254, pp. 44–56, 2014.
- [153] ——, “3d fiber orientation characterization of nonwoven fabrics using x-ray micro-computed tomography,” *World Journal of Textile Engineering and Technology*, vol. 1, no. 0, pp. 41–7, 2015.
- [154] M. Ali, R. Umer, K. Khan, S. Bickerton, and W. Cantwell, “Non-destructive evaluation of through-thickness permeability in 3d woven fabrics for composite fan blade applications,” *Aerospace Science and Technology*, vol. 82, pp. 520–533, 2018.
- [155] M. Cataldi, Y. Wielhorski, N. Moulin, A. Parret-Fréaud, M. F. Pucci, and P.-J. Liotier, “Accounting for mesoscale geometry and intra-yarn fiber volume fraction distribution on 3d angle-interlock fabric permeability,” *International Journal of Multiphase Flow*, p. 104721, 2024.
- [156] C. Li, A. Cantarel, and X. Gong, “Influence of structural parameters at microscale on the fiber reinforcement,” *Journal of Composite Materials*, vol. 53, no. 7, pp. 863–872, 2019.
- [157] C. Pengjun, Z. Wenbin, Y. Bin, N. Aiqing, and W. Jihui, “Meso-structure analysis and permeability prediction of satin fabric based on micro-ct,” *Acta Materiae Compositae Sinica*, vol. 40, no. 3, pp. 1751–1763, 2023.
- [158] M. Ali, R. Umer, and K. Khan, “A virtual permeability measurement framework for fiber reinforcements using micro ct generated digital twins,” *International Journal of Lightweight Materials and Manufacture*, vol. 3, no. 3, pp. 204–216, 2020.
- [159] M. Karaki, A. Hallal, R. Younes, F. Trochu, P. Lafon, A. Hayek, A. Kobeissy, and A. Fayad, “A comparative analytical, numerical and experimental analysis of the microscopic permeability of fiber bundles in composite materials,” *Int. J. Compos. Mater.*, vol. 7, no. 3, pp. 82–102, 2017.

- [160] C. Li, A. Cantarel, and X. Gong, “A study on resin infusion and effects of reinforcement structure at dual scales by a quasi-realistic numerical simulation method,” *Journal of Composite Materials*, vol. 54, no. 27, pp. 4157–4171, 2020.
- [161] E. Syerko, T. Schmidt, D. May, C. Binetruy, S. Advani, S. Lomov, L. Silva, S. Abaimov, N. Aissa, I. Akhatov *et al.*, “Benchmark exercise on image-based permeability determination of engineering textiles: Microscale predictions,” *Composites Part A: Applied Science and Manufacturing*, vol. 167, p. 107397, 2023.
- [162] M. A. Ali, R. Umer, and K. A. Khan, *Generation of Material Twin Using Micro CT Scanning*. Singapore: Springer Singapore, 2020, pp. 19–52. [Online]. Available: https://doi.org/10.1007/978-981-15-8021-5_2
- [163] Y. Zhao, G. Zhu, C. Zhang, S. Liu, D. Elsworth, and T. Zhang, “Pore-scale reconstruction and simulation of non-darcy flow in synthetic porous rocks,” *Journal of Geophysical Research: Solid Earth*, vol. 123, no. 4, pp. 2770–2786, 2018.
- [164] C. Soulaine, F. Gjetvaj, C. Garing, S. Roman, A. Russian, P. Gouze, and H. A. Tchelepi, “The impact of sub-resolution porosity of x-ray microtomography images on the permeability,” *Transport in porous media*, vol. 113, pp. 227–243, 2016.
- [165] A. Q. Raeini, B. Bijeljic, and M. J. Blunt, “Modelling capillary trapping using finite-volume simulation of two-phase flow directly on micro-ct images,” *Advances in Water Resources*, vol. 83, pp. 102–110, 2015.
- [166] A. Aziz, M. Ali, X. Zeng, R. Umer, P. Schubel, and W. Cantwell, “Transverse permeability of dry fiber preforms manufactured by automated fiber placement,” *Composites Science and Technology*, vol. 152, pp. 57–67, 2017.
- [167] A. Nabovati and A. Sousa, “Fluid flow simulation at open–porous medium interface using the lattice boltzmann method,” *International journal for numerical methods in fluids*, vol. 56, no. 8, pp. 1449–1456, 2008.
- [168] E. B. Belov, S. V. Lomov, I. Verpoest, T. Peters, D. Roose, R. Parnas, K. Hoes, and H. Sol, “Modelling of permeability of textile reinforcements: lattice boltzmann method,” *Composites Science and Technology*, vol. 64, no. 7-8, pp. 1069–1080, 2004.
- [169] S. Li, M. Dong, and P. Luo, “A crossflow model for an interacting capillary bundle: Development and application for waterflooding in tight oil reservoirs,” *Chemical Engineering Science*, vol. 164, pp. 133–147, 2017.

- [170] H. Teixidó, B. Caglar, and V. Michaud, “Effect of wettability and textile architecture on fluid displacement and pore formation during infiltration of carbon fibrous preforms,” *Composites Part A: Applied Science and Manufacturing*, vol. 174, p. 107733, 2023.
- [171] H. Dong and M. J. Blunt, “Pore-network extraction from micro-computerized-tomography images,” *Physical review E*, vol. 80, no. 3, p. 036307, 2009.
- [172] A. Endruweit, X. Zeng, M. Matveev, and A. C. Long, “Effect of yarn cross-sectional shape on resin flow through inter-yarn gaps in textile reinforcements,” *Composites Part A: Applied Science and Manufacturing*, vol. 104, pp. 139–150, 2018.
- [173] M. Karaki, A. Hallal, R. Younes, F. Trochu, and P. Lafon, “In-plane permeability prediction model for non-crimp and 3d orthogonal fabrics,” *The Journal of The Textile Institute*, vol. 109, no. 8, pp. 1110–1126, 2018.
- [174] J. Sirtautas, A. Pickett, and A. George, “Materials characterisation and analysis for flow simulation of liquid resin infusion,” *Applied Composite Materials*, vol. 22, pp. 323–341, 2015.
- [175] M. Shadhin, R. Jayaraman, and M. Rahman, “Effect of non-woven flax mat manufacturing parameters and consolidation pressure on properties of composites manufactured using vacuum-assisted resin transfer molding,” *Polymer Composites*, vol. 42, no. 11, pp. 5743–5754, 2021.
- [176] E. Fauster, C. Vierkötter, L. Appel, J. Lugo, W. Schijve, and D. Heider, “Experimental characterization of single ply out-of-plane permeability through gaseous flow,” *Polymer Composites*, vol. 39, no. 9, pp. 3247–3258, 2018.
- [177] E. E. Swery, T. Allen, S. Comas-Cardona, Q. Govignon, C. Hickey, J. Timms, L. Tournier, A. Walbran, P. Kelly, and S. Bickerton, “Efficient experimental characterisation of the permeability of fibrous textiles,” *Journal of composite materials*, vol. 50, no. 28, pp. 4023–4038, 2016.
- [178] P. Ouagne and J. Breard, “Continuous transverse permeability of fibrous media,” *Composites Part A: Applied Science and Manufacturing*, vol. 41, no. 1, pp. 22–28, 2010.
- [179] O. Rimmel, D. May, and P. Mitschang, “Impact of stitching on permeability and mechanical properties of preforms manufactured by dry fiber placement,” *Polymer Composites*, vol. 40, no. 4, pp. 1631–1642, 2019.

- [180] I. Crivelli Visconti, A. Langella, and M. Durante, “Analysis of transversal permeability for different types of glass fiber reinforcement,” *Applied composite materials*, vol. 10, pp. 119–127, 2003.
- [181] H. Alhussein, R. Umer, S. Rao, E. Swery, S. Bickerton, and W. Cantwell, “Characterization of 3d woven reinforcements for liquid composite molding processes,” *Journal of materials science*, vol. 51, pp. 3277–3288, 2016.
- [182] R. Graupner and K. Drechsler, “Quantitative transversal permeability testing-challenges and enhancements,” in *The 14th International Conference on Flow Processing in Composite Materials, Lulea*, 2018.
- [183] M. Li, S.-K. Wang, Y.-Z. Gu, Y.-X. Li, K. Potter, and Z.-G. Zhang, “Evaluation of through-thickness permeability and the capillary effect in vacuum assisted liquid molding process,” *Composites science and technology*, vol. 72, no. 8, pp. 873–878, 2012.
- [184] C.-H. Wu, T. James Wang, and L. James Lee, “Trans-plane fluid permeability measurement and its applications in liquid composite molding,” *Polymer Composites*, vol. 15, no. 4, pp. 289–298, 1994.
- [185] D. Merhi, V. Michaud, L. Kampfer, P. Vuillomenet, and J. A. E. Manson, “Transverse permeability of chopped fibre bundle beds,” *Composites Part A: Applied science and manufacturing*, vol. 38, no. 3, pp. 739–746, 2007.
- [186] J. Kratz and P. Hubert, “Anisotropic air permeability in out-of-autoclave prepgs: Effect on honeycomb panel evacuation prior to cure,” *Composites Part A: Applied Science and Manufacturing*, vol. 49, pp. 179–191, 2013.
- [187] D. Becker, J. Broser, and P. Mitschang, “An experimental study of the influence of process parameters on the textile reaction to transverse impregnation,” *Polymer Composites*, vol. 37, no. 9, pp. 2820–2831, 2016.
- [188] L. S. Bennethum, M. Murad, and J. Cushman, “Modified darcy’s law, terzaghi’s effective stress principle and fick’s law for swelling clay soils,” *Computers and Geotechnics*, vol. 20, no. 3-4, pp. 245–266, 1997.
- [189] M. Li, Y. Gu, Z. Zhang, and Z. Sun, “A simple method for the measurement of compaction and corresponding transverse permeability of composite prepgs,” *Polymer Composites*, vol. 28, no. 1, pp. 61–70, 2007.

- [190] R. S. Trindade, A. C. Ribeiro, J. A. Souza, and S. C. Amico, “Experimental investigation of transverse permeability applied to liquid molding,” *Polymer Composites*, vol. 40, no. 10, pp. 3938–3946, 2019.
- [191] P. Ouagne, T. Ouahbi, C. H. Park, J. Bréard, and A. Saouab, “Continuous measurement of fiber reinforcement permeability in the thickness direction: Experimental technique and validation,” *Composites Part B: Engineering*, vol. 45, no. 1, pp. 609–618, 2013.
- [192] P.-J. Liotier, Q. Govignon, E. Swery, S. Drapier, and S. Bickerton, “Characterisation of woven flax fibres reinforcements: Effect of the shear on the in-plane permeability,” *Journal of Composite Materials*, vol. 49, no. 27, pp. 3415–3430, 2015.
- [193] J. Studer, C. Dransfeld, J. J. Cano, A. Keller, M. Wink, K. Masania, and B. Fiedler, “Effect of fabric architecture, compaction and permeability on through thickness thermoplastic melt impregnation,” *Composites Part A: Applied Science and Manufacturing*, vol. 122, pp. 45–53, 2019.
- [194] D. Becker and P. Mitschang, “Measurement system for on-line compaction monitoring of textile reaction to out-of-plane impregnation,” *Advanced Composites Letters*, vol. 23, no. 2, p. 096369351402300202, 2014.
- [195] R. Graupner and K. Drechsler, “One step to comparable off-plane permeability results - an improved measuring method for transverse permeability and compaction behavior of textile fiber materials,” 2016. [Online]. Available: <https://publica.fraunhofer.de/handle/publica/400841>
- [196] P. Šimáček and S. G. Advani, “Desirable features in mold filling simulations for liquid composite molding processes,” *Polymer Composites*, vol. 25, no. 4, pp. 355–367, 2004.
- [197] F. Trochu, “A contouring program based on dual kriging interpolation,” *Engineering with computers*, vol. 9, pp. 160–177, 1993.
- [198] I. Rodrigues, S. C. Amico, J. A. Souza, and A. G. B. de Lima, “Numerical analysis of the resin transfer molding process via pam-rtm software,” in *Defect and Diffusion Forum*, vol. 365. Trans Tech Publ, 2015, pp. 88–93.
- [199] S. Konstantopoulos, H. Grössing, P. Hergan, M. Weninger, and R. Schledjewski, “Determination of the unsaturated through-thickness permeability of fibrous preforms based on flow front detection by ultrasound,” *Polymer Composites*, vol. 39, no. 2, pp. 360–367, 2018.

- [200] A. Fluent, “Fluent 14.0 user’s guide,” *Ansys Fluent Inc*, 2011.
- [201] J. Ward, “Turbulent flow in porous media,” *Journal of the hydraulics division*, vol. 90, no. 5, pp. 1–12, 1964.
- [202] F. Rubino and P. Carbone, “A semi-analytical model to predict infusion time and reinforcement thickness in vartm and scrim processes,” *Polymers*, vol. 11, no. 1, 2018.
- [203] L. Joubaud, V. Achim, and F. Trochu, “Numerical simulation of resin infusion and reinforcement consolidation under flexible cover,” *Polymer Composites*, vol. 26, no. 4, pp. 417–427, 2005.
- [204] S. Whitaker, *The method of volume averaging*. Springer Science & Business Media, 1998, vol. 13.
- [205] A. Aktas, G. Sims, C. Lira, and M. Stojkovic, “Survey of procedures in use for permeability measurements in liquid composite moulding processes.” <https://eprintspublications.npl.co.uk/7091/>, 2016, [Accessed 22-10-2023].
- [206] B. Yang, W. Huang, P. Causse, C. Béguin, J. Wang, and F. Trochu, “On the design of test molds based on unidirectional saturated flows to measure transverse permeability in liquid composite molding,” *Polymer Composites*, no. 4, p. 43, 2022.
- [207] M. A. Kabachi, L. Stettler, S. Arreguin, and P. Ermanni, “Concurrent characterization of through-thickness permeability and compaction of fiber reinforcements,” *Composites Part A: Applied Science and Manufacturing*, vol. 141, p. 106203, 2021.
- [208] B. Willenbacher, D. May, and P. Mitschang, “Metrological determination of inhomogeneous hydrodynamic compaction during unsaturated out-of-plane permeability measurement of technical textiles,” *Advanced Manufacturing: Polymer & Composites Science*, vol. 5, no. 2, pp. 51–54, 2019.
- [209] P. R. Barnett, Z. A. Cook, B. M. Hulett, N. H. Varma, and D. Penumadu, “Influence of processing parameters on permeability and infiltration of compression molded discontinuous carbon fiber organosheet composites,” *Composites, Part A. Applied science and manufacturing*, no. 152-, p. 152, 2022.
- [210] P. B. Nedanov and S. G. Advani, “A method to determine 3d permeability of fibrous reinforcements,” *Journal of Composite Materials*, vol. 36, no. 2, pp. 241–254, 2002.

- [211] M. Yun, H. Sas, P. Simacek, and S. G. Advani, "Characterization of 3d fabric permeability with skew terms," *Composites Part A Applied Science & Manufacturing*, vol. 97, pp. 51–59, 2017.
- [212] Karaki, M., Hallal, A., Younes, R., Trochu, F., Lafon, and P., "In-plane permeability prediction model for non-crimp and 3d orthogonal fabrics," *The Journal of the Textile Institute, Part 3. Technologies for a New Century*, vol. 109, no. 8, pp. 1110–1126, 2018.
- [213] B. Yang, S. Wang, and Y. Wang, "Effect of nesting in laminates on the through-thickness permeability of woven fabrics," *Applied Composite Materials*, 2018.
- [214] T. Roy, H. Tan, and K. M. Pillai, "A method to estimate the accuracy of 1-d flow based permeability measuring devices," *Journal of Composite Materials*, vol. 41, no. 17, pp. 2037–2055, 2007.
- [215] S. Patankar, "Numerical heat transfer and fluid flow: Crc press," 1980.
- [216] D. May, A. Aktas, S. Advani, D. Berg, A. Endruweit, E. Fauster, S. Lomov, A. Long, P. Mitschang, S. Abaimov, D. Abliz, I. Akhatov, M. Ali, T. Allen, S. Bickerton, M. Bodaghi, B. Caglar, H. Caglar, A. Chiminelli, N. Correia, B. Cosson, M. Danzi, J. Dittmann, P. Ermanni, G. Francucci, A. George, V. Grishaev, M. Hanciooglu, M. Kabachi, K. Kind, M. Deléglise-Lagardère, M. Laspalas, O. Lebedev, M. Lizaranzu, P.-J. Liotier, P. Middendorf, J. Morán, C.-H. Park, R. Pipes, M. Pucci, J. Raynal, E. Rodriguez, R. Schledjewski, R. Schubnel, N. Sharp, G. Sims, E. Sozer, P. Sousa, J. Thomas, R. Umer, W. Wijaya, B. Willenbacher, A. Yong, S. Zaremba, and G. Ziegmann, "In-plane permeability characterization of engineering textiles based on radial flow experiments: A benchmark exercise," *Composites Part A: Applied Science and Manufacturing*, vol. 121, pp. 100–114, 2019. [Online]. Available: <https://www.sciencedirect.com/science/article/pii/S1359835X1930079X>
- [217] P. C. Carman, "Fluid flow through granular beds," *Trans. Inst. Chem. Eng*, vol. 15, 1937.
- [218] W. Tao, P. Zhu, C. Xu, and Z. Liu, "Uncertainty quantification of mechanical properties for three-dimensional orthogonal woven composites. part i: Stochastic reinforcement geometry reconstruction," *Composite Structures*, vol. 235, p. 111763, 2020.
- [219] X. Zeng, A. Endruweit, L. P. Brown, and A. C. Long, "Numerical prediction of in-plane permeability for multilayer woven fabrics with manufacture-induced deformation," *Composites Part A: applied science and manufacturing*, vol. 77, pp. 266–274, 2015.

- [220] W. Huang, R. Xu, J. Yang, Q. Huang, and H. Hu, “Data-driven multiscale simulation of frp based on material twins,” *Composite Structures*, vol. 256, p. 113013, 2021.
- [221] T. Schmidt, F. Schimmer, A. Widera, D. May, N. Motsch, and C. Bauer, “A novel simulative-experimental approach to determine the permeability of technical textiles,” *Key Engineering Materials*, vol. 809, pp. 487–492, 2019.
- [222] A. Badran, D. Marshall, Z. Legault, R. Makovetsky, B. Provencher, N. Piché, and M. Marsh, “Automated segmentation of computed tomography images of fiber-reinforced composites by deep learning,” *Journal of Materials Science*, vol. 55, pp. 16 273–16 289, 2020.
- [223] A. Mendoza, R. Trullo, and Y. Wielhorski, “Descriptive modeling of textiles using fe simulations and deep learning,” *Composites Science and Technology*, vol. 213, p. 108897, 2021.
- [224] S. Garcea, Y. Wang, and P. Withers, “X-ray computed tomography of polymer composites,” *Composites Science and Technology*, vol. 156, pp. 305–319, 2018.
- [225] B. Wucher, S. Hallström, D. Dumas, T. Pardoen, C. Bailly, P. Martiny, and F. Lani, “Nonconformal mesh-based finite element strategy for 3d textile composites,” *Journal of Composite Materials*, vol. 51, no. 16, pp. 2315–2330, 2017.
- [226] Y. Jia, G. Yu, J. Du, X. Gao, Y. Song, and F. Wang, “Adopting traditional image algorithms and deep learning to build the finite model of a 2.5 d composite based on x-ray computed tomography,” *Composite Structures*, vol. 275, p. 114440, 2021.
- [227] M. Y. Matveev, L. P. Brown, and A. C. Long, “Efficient meshing technique for textile composites unit cells of arbitrary complexity,” *Composite Structures*, vol. 254, p. 112757, 2020.
- [228] S. Hilal, *Caractérisation par microtomographie de la mésostрукture des renforts fibreux pour la fabrication de composites*. Ecole Polytechnique, Montreal (Canada), 2018.
- [229] T. Ferreira and W. Rasband, *ImageJ User Guide: IJ 1.42 r*. National Institute of Health, 2012.
- [230] A. Vanaerschot, B. N. Cox, S. V. Lomov, and D. Vandepitte, “Stochastic framework for quantifying the geometrical variability of laminated textile composites using micro-computed tomography,” *Composites Part A: Applied Science and Manufacturing*, vol. 44, pp. 122–131, 2013.

- [231] D. W. Scott, *Multivariate density estimation: theory, practice, and visualization*. John Wiley & Sons, 2015.
- [232] F. Trochu, “A contouring program based on dual kriging interpolation,” *Engineering with computers*, vol. 9, pp. 160–177, 1993.
- [233] B. Yang, W. Huang, P. Causse, C. Béguin, J. Wang, and F. Trochu, “On the design of test molds based on unidirectional saturated flows to measure transverse permeability in liquid composite molding,” *Polymer Composites*, vol. 43, no. 4, pp. 2234–2251, 2022.
- [234] A. Limaiem and F. Trochu, “Geometric algorithms for the intersection of curves and surfaces,” *Computers & graphics*, vol. 19, no. 3, pp. 391–403, 1995.
- [235] B. Yang, “Polytex: A parametric geometry modeling package - documentation,” <https://polytex.readthedocs.io/>, (Accessed on 02/08/2024).
- [236] G. Täubin, “Curve and surface smoothing without shrinkage,” in *Proceedings of IEEE international conference on computer vision*. IEEE, 1995, pp. 852–857.
- [237] C. Sullivan and A. Kaszynski, “Pyvista: 3d plotting and mesh analysis through a streamlined interface for the visualization toolkit (vtk),” *Journal of Open Source Software*, vol. 4, no. 37, p. 1450, 2019.
- [238] F. Desplentere, S. V. Lomov, D. Woerdeman, I. Verpoest, M. Wevers, and A. Bogdanovich, “Micro-ct characterization of variability in 3d textile architecture,” *Composites Science and Technology*, vol. 65, no. 13, pp. 1920–1930, 2005.
- [239] Y. Liu, I. Straumit, D. Vasiukov, S. V. Lomov, and S. Panier, “Prediction of linear and non-linear behavior of 3d woven composite using mesoscopic voxel models reconstructed from x-ray micro-tomography,” *Composite structures*, vol. 179, pp. 568–579, 2017.
- [240] N. Naouar, D. Vasiukov, C. Park, S. Lomov, and P. Boisse, “Meso-fe modelling of textile composites and x-ray tomography,” *Journal of Materials Science*, vol. 55, pp. 16 969–16 989, 2020.
- [241] M. Ali, R. Umer, K. Khan, and W. Cantwell, “Xct-scan assisted flow path analysis and permeability prediction of a 3d woven fabric,” *Composites Part B: Engineering*, vol. 176, pp. 1–10, 2019.
- [242] M. Hill, S. Kamalakannan, A. Gururajan, H. Sari-Sarraf, and E. Hequet, “Dimensional change measurement and stain segmentation in printed fabrics,” *Textile Research Journal*, vol. 81, no. 16, pp. 1655–1672, 2011.

- [243] J. Schell, M. Renggli, G. H. van Lenthe, R. Müller, and P. Ermanni, “Micro-computed tomography determination of glass fibre reinforced polymer meso-structure,” *Composites Science and Technology*, vol. 66, no. 13, pp. 2016–2022, 2006.
- [244] N. Q. Nguyen, M. Mehdikhani, I. Straumit, L. Gorbatikh, L. Lessard, and S. V. Lomov, “Micro-ct measurement of fibre misalignment: Application to carbon/epoxy laminates manufactured in autoclave and by vacuum assisted resin transfer moulding,” *Composites Part A: Applied Science and Manufacturing*, vol. 104, pp. 14–23, 2018.
- [245] Y. Sinchuk, O. Shishkina, M. Gueguen, L. Signor, C. Nadot-Martin, H. Trumel, and W. Van Paepegem, “X-ray ct based multi-layer unit cell modeling of carbon fiber-reinforced textile composites: Segmentation, meshing and elastic property homogenization,” *Composite Structures*, vol. 298, p. 116003, 2022.
- [246] Y. Yu, W. Wu, W. Chen, Y. Shao, C. Zhu, X. Gu, and S. Hu, “3d geometric modeling of three-thread fleece fabric based on micro-ct,” *Textile Research Journal*, vol. 93, no. 9-10, pp. 1928–1937, 2023.
- [247] J. Schindelin, I. Arganda-Carreras, E. Frise, V. Kaynig, M. Longair, T. Pietzsch, S. Preibisch, C. Rueden, S. Saalfeld, B. Schmid *et al.*, “Fiji: an open-source platform for biological-image analysis,” *Nature methods*, vol. 9, no. 7, pp. 676–682, 2012.
- [248] S. Pieper, M. Halle, and R. Kikinis, “3d slicer,” in *2004 2nd IEEE international symposium on biomedical imaging: nano to macro (IEEE Cat No. 04EX821)*. IEEE, 2004, pp. 632–635.
- [249] B. C. Russell, A. Torralba, K. P. Murphy, and W. T. Freeman, “Labelme: a database and web-based tool for image annotation,” *International journal of computer vision*, vol. 77, pp. 157–173, 2008.
- [250] M. W. Tahir, S. Hallström, and M. Åkermo, “Effect of dual scale porosity on the overall permeability of fibrous structures,” *Composites science and technology*, vol. 103, pp. 56–62, 2014.
- [251] X. Xiao, A. Endruweit, X. Zeng, J. Hu, and A. Long, “Through-thickness permeability study of orthogonal and angle-interlock woven fabrics,” *Journal of materials science*, vol. 50, no. 3, pp. 1257–1266, 2015.
- [252] M. Imbert, S. Comas-Cardona, E. Abisset-Chavanne, and D. Prono, “Introduction of intra-tow release/storage mechanisms in reactive dual-scale flow numerical simulations,” *Journal of Composite Materials*, vol. 53, no. 1, pp. 125–140, 2019.

- [253] R. J. D'Mello, A. M. Waas, M. Maiaru, and R. Koon, “Integrated computational modeling for efficient material and process design for composite aerospace structures,” in *AIAA Scitech 2020 Forum*, 2020, p. 0655.
- [254] N. Schlömer, “meshio: Tools for mesh files,” <https://github.com/nschloe/meshio>, 2022, [Accessed 05-01-2024].
- [255] U. Ayachit, *The paraview guide: a parallel visualization application*. Kitware, Inc., 2015.
- [256] TexGen, “Extraction of Material Properties using Voxel Meshing and Abaqus - texgen.sourceforge.io,” https://texgen.sourceforge.io/index.php/Extraction_of_Material_Properties_using_Voxel_Meshing_and_Abaqus, [Accessed 02-01-2024].
- [257] Y. Bin, B. Cédric, C. Philippe, F. Yuwei, and W. Jihui, “Tomographic modeling and internal structure analysis of engineering textiles: a parametric approach,” *Composite Structures*, vol. (Submitted), 2024.
- [258] B. R. Gebart, “Permeability of unidirectional reinforcements for rtm,” *Journal of Composite Materials*, vol. 26, no. 8, pp. 1100–1133, 1992. [Online]. Available: <https://doi.org/10.1177/002199839202600802>
- [259] J. Drummond and M. Tahir, “Laminar viscous flow through regular arrays of parallel solid cylinders,” *International Journal of Multiphase Flow*, vol. 10, no. 5, pp. 515–540, 1984.
- [260] J. Lawrence, J. Bernal, and C. Witzgall, “A purely algebraic justification of the kabsch-umeyama algorithm,” *Journal of research of the National Institute of Standards and Technology*, vol. 124, p. 1, 2019.
- [261] J. A. Ochoa-Tapia and S. Whitaker, “Momentum transfer at the boundary between a porous medium and a homogeneous fluid—i. theoretical development,” *International Journal of Heat and Mass Transfer*, vol. 38, no. 14, pp. 2635–2646, 1995.
- [262] F. J. Carrillo, I. C. Bourg, and C. Soulaine, “Multiphase flow modeling in multiscale porous media: An open-source micro-continuum approach,” *Journal of Computational Physics: X*, vol. 8, p. 100073, 2020.
- [263] R. Domander, A. A. Felder, and M. Doube, “Bonej2-refactoring established research software,” *Wellcome Open Research*, vol. 6, 2021.

- [264] I. Belot, Y. Sun, D. Vidal, M. Votsmeier, P. Causse, F. Trochu, and F. Bertrand, “A 3d additive manufacturing approach for the validation of a numerical wall-scale model of catalytic particulate filters,” *Chemical Engineering Journal*, vol. 405, p. 126653, 2021.

APPENDIX A INSTALLATION OF POLYTEX PACKAGE

We release PolyTex as an open-source project that aims to facilitate the application of numerical simulations based on digital material twins to engineering problems. To install PolyTex using PyPI, run the following command:

```
1 $ pip install polytex
```

To install PolyTex from the source, begin by cloning the repository using Git:

```
2 $ git clone https://github.com/binyang424/polytex.git
```

For those who are not acquainted with Git, our tutorial Git for beginners can be consulted. Alternatively, the source code can be downloaded from GitHub as .zip file by visiting <https://github.com/binyang424/polytex>.

Once the repository is cloned, navigate to the root directory of the PolyTex repository where the ‘setup.py’ file is located, and execute the following command:

```
3 $ python setup.py install
```

To install PolyTex using the wheel file, navigate to the subdirectory `./dist/` of the downloaded repository, and run:

```
4 $ pip install polytex-<version>.whl
```

APPENDIX B SAMPLE SCRIPTS FOR THE USE OF POLYTEX PACKAGE

The scripts used to create the digital material twins of the fabric illustrated in Chapter 6 are shown here.

Tow

```

1 import polytex as pk
2 import numpy as np
3
4 filename = "towType_index"
5 resolution = 0.022 # mm/px
6
7 coordinates = ptx.read_imagej_roi("file/path/to/explicit/dataset.zip",
8                                     type="zip")
9
10 """ Utilization of the PolyTex Tow class """
11 tow = ptx.Tow(surf_points=coordinates, order="zyx", rho_fiber=2550,
12                 radius_fiber=8.5e-6, length_scale="mm", tex=275,
13                 name=filename, sort=True, resolution=resolution)
14
15 df_coord = tow.coordinates # parametric coordinates of the tow
16
17 ######
18 # Resampling
19 # -----
20 # Equidistant resampling of the tow control points in the radial direction
21 .
22 theta_res = 20 # number of control points in the radial direction
23 sample_position = np.linspace(0, 1, theta_res, endpoint=True)
24
25 # # Resampling according to distribution density
26 # cluster = tow.kde(bw=0.0013)
27 # sample_position = cluster["cluster centers"]
28
29 pts_krig, expr_krig = tow.resampling(krig_config=("lin", "lin"), skip=5,
30                                         sample_position=sample_position, smooth=0.00001)
31
32 mesh = tow.surf_mesh(plot=False, save_path=None, end_closed=True)
33 mesh.save(filename + '.vtk', binary=False)

```

```

34 #####
35 # Smoothing of tow surface and trajectory
36 # -----
37
38 tow.smoothing(smooth_factor=[0.0001, 0.0001], plot=True, save_path=None)
39
40 # Get the axial and radial lines of the tow (the lines connecting the
41 # parametrized control points in the axial and radial direction)
42 line_axi = tow.axial_lines(plot=True, save_path=None)
43 line_rad = tow.radial_lines(plot=True)
44
45 trajectory = tow.trajectory(smooth=0.00015, plot=True,
46                             save_path=None, orientation=True)
47
48 #####
49 # Get the normal cross-sections of the tow with different algorithms
50 # -----
51
52 # PyVista method (mesh trimming)
53 cross_section, plane, clipped = tow.normal_cross_section(algorithm=
54     "pyvista", plot=False, i_size=2, j_size=3, skip=2)
55
56 df_geom_pv = tow.geom_features.copy()      # geometrical features of the tow
57 area_pyvista = df_geom_pv.iloc[:, [0]]
58
59 # Kriging method
60 cross_section, plane, clipped = tow.normal_cross_section(
61     algorithm="kriging", plot=True, i_size=2, j_size=3, skip=4)
62
63 df_geom_krig = tow.geom_features      # geometrical features of the tow
64 area_kriging = df_geom_krig.iloc[:, [0]]
65
66 # save as ply file for data communication
67 vertices = tow.coordinates.iloc[:, -3:]
68 ptx.meshio_save("file/path/to/save/filename.ply", vertices=vertices.
    to_numpy())
69 tow.save("file/path/to/save/filename.tow")

```

Textile

```

1 import numpy as np
2 import polytex as ptx
3
4 # Create a textile object
5 textile = ptx.Textile(name="TG96N_Vf57")
6
7 path = ["./weft/", ".warp/", ".binder/"]
8
9 for tow_path in path:
10     files = ptx.filenames(tow_path, ".tow")
11     for file in files:
12         tow = ptx.Tow.from_file(tow_path + file)
13         textile.add_tow(tow)
14
15 # Bounding box for domain of meshing
16 bbox = np.array((0.6, 12, 1.07, 14.19, 0.2, 5.35))
17 # Voxel size in x, y, and z direction
18 voxel_sizes = np.array([[0.066, 0.066, 0.022]])
19
20 for voxel_size in voxel_sizes:
21     print("Voxel size: {}".format(voxel_size))
22
23     textile.meshing(bbox, voxel_size=voxel_size, show=False,
24                      labeling=True, surface_mesh=".stl", verbose=False)
25
26 """ Save voxel mesh """
27 textile.mesh.save("./file/path/to/save/filename.vtu", binary=True)
28
29 """ OpenFOAM mesh writing """
30 boundary_type = {"left": "wall", "right": "wall", "front": "wall",
31                  "back": "wall", "bottom": "patch", "top": "patch"}
32 textile.export_as_openfoam("./file/path/to/save/", scale=0.001,
33                           boundary_type=boundary_type, cell_data=["yarnIndex", "D"])
34 # OpenFOAM case preparation with provided template
35 textile.case_prepare()
36
37 """ABAQUS mesh writing """
38 textile.export_as_inp(fp='file/path/to/save/filename.inp', scale=1,
39 orientation=True)

```

APPENDIX C SCREENSHOTS OF POLYTEX VISUALIZATION TOOLS

Various visualization tools are provided to users thanks to a wrapper of *VTK - PyVista* [237]. These tools can be activated by switch on the parameter `plot` by `plot=True` in the functions where visualization is available. Some of the screenshots are shown here.

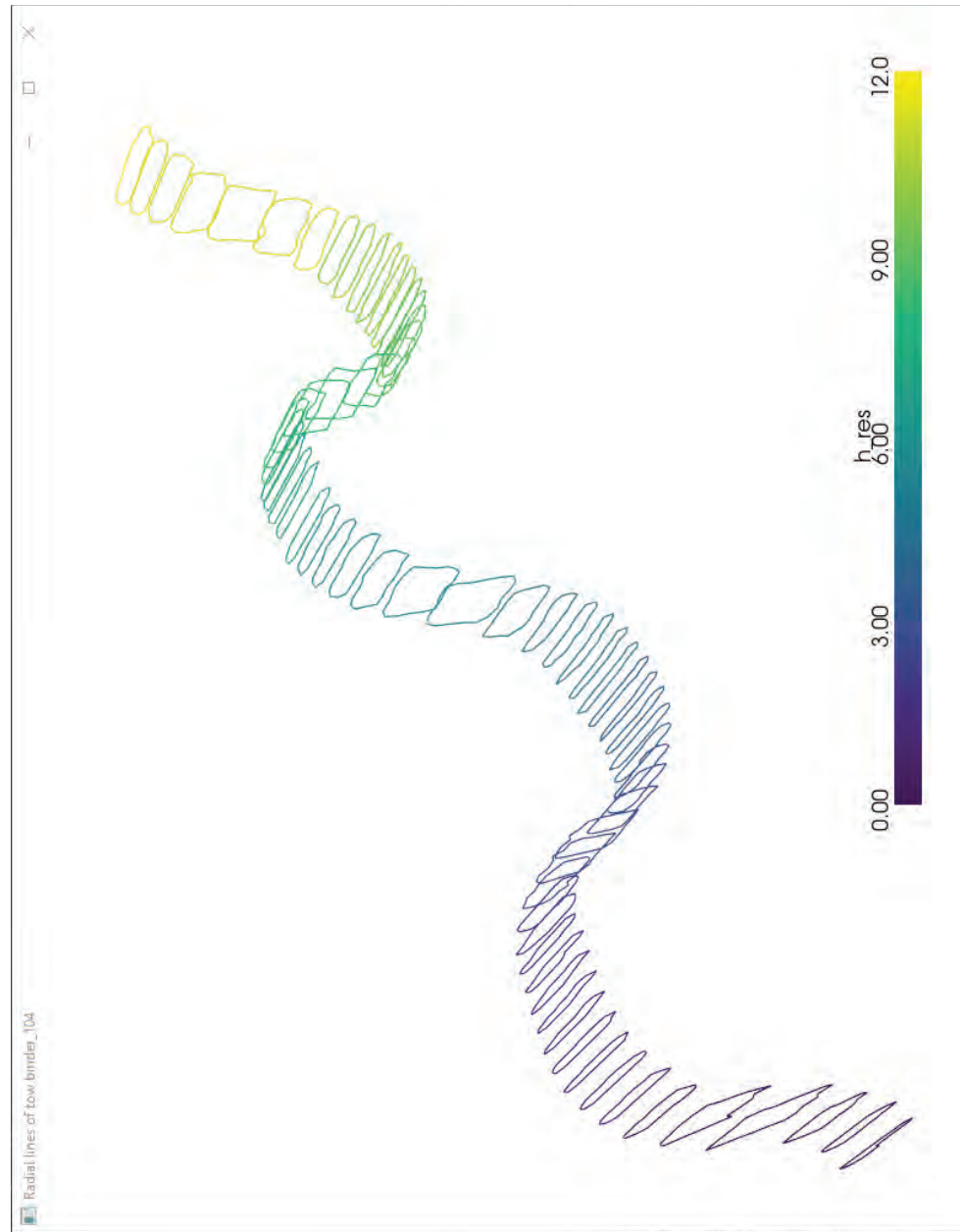


Figure C.1 Radial lines of a fiber tow

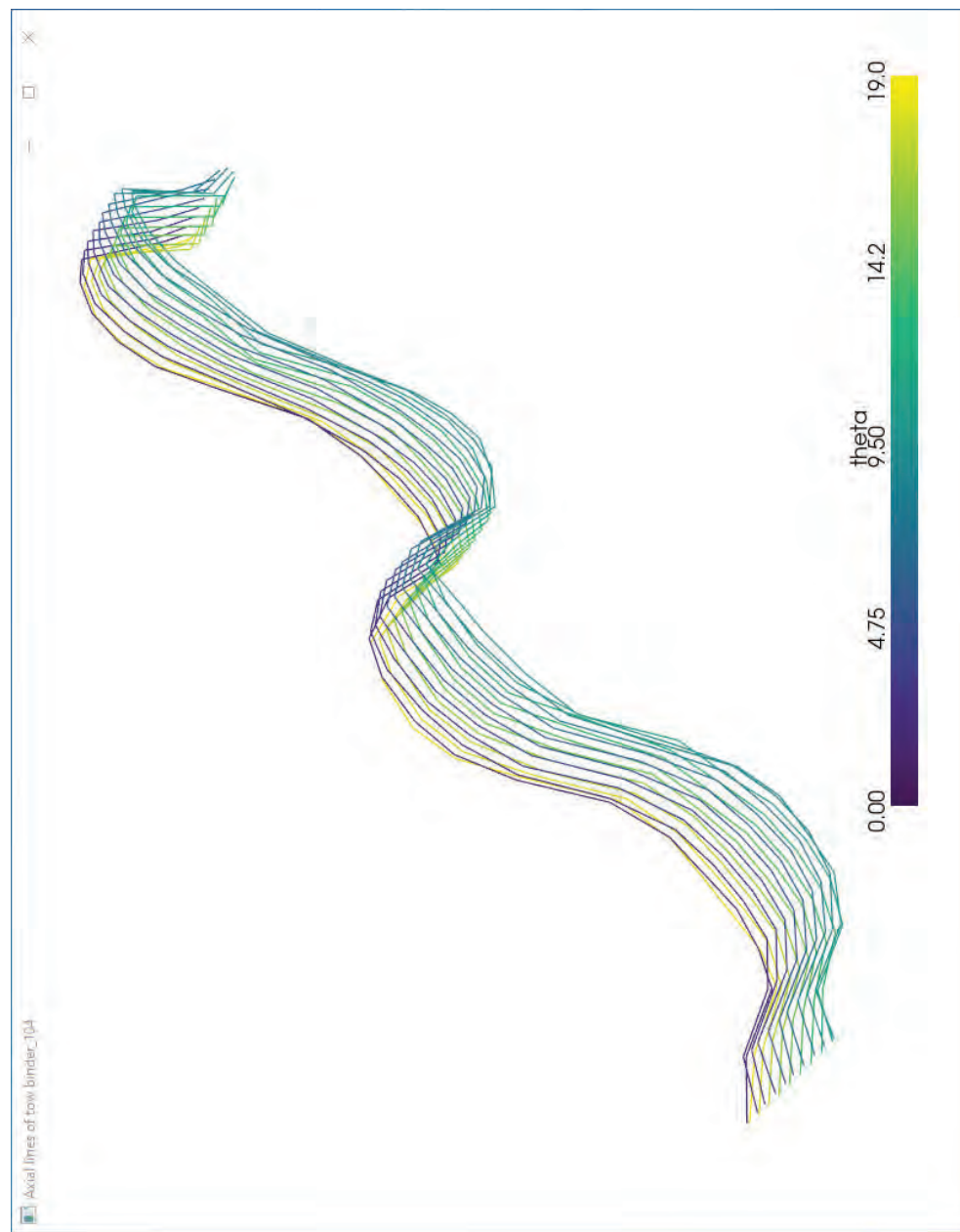


Figure C.2 Axial lines of a fiber tow

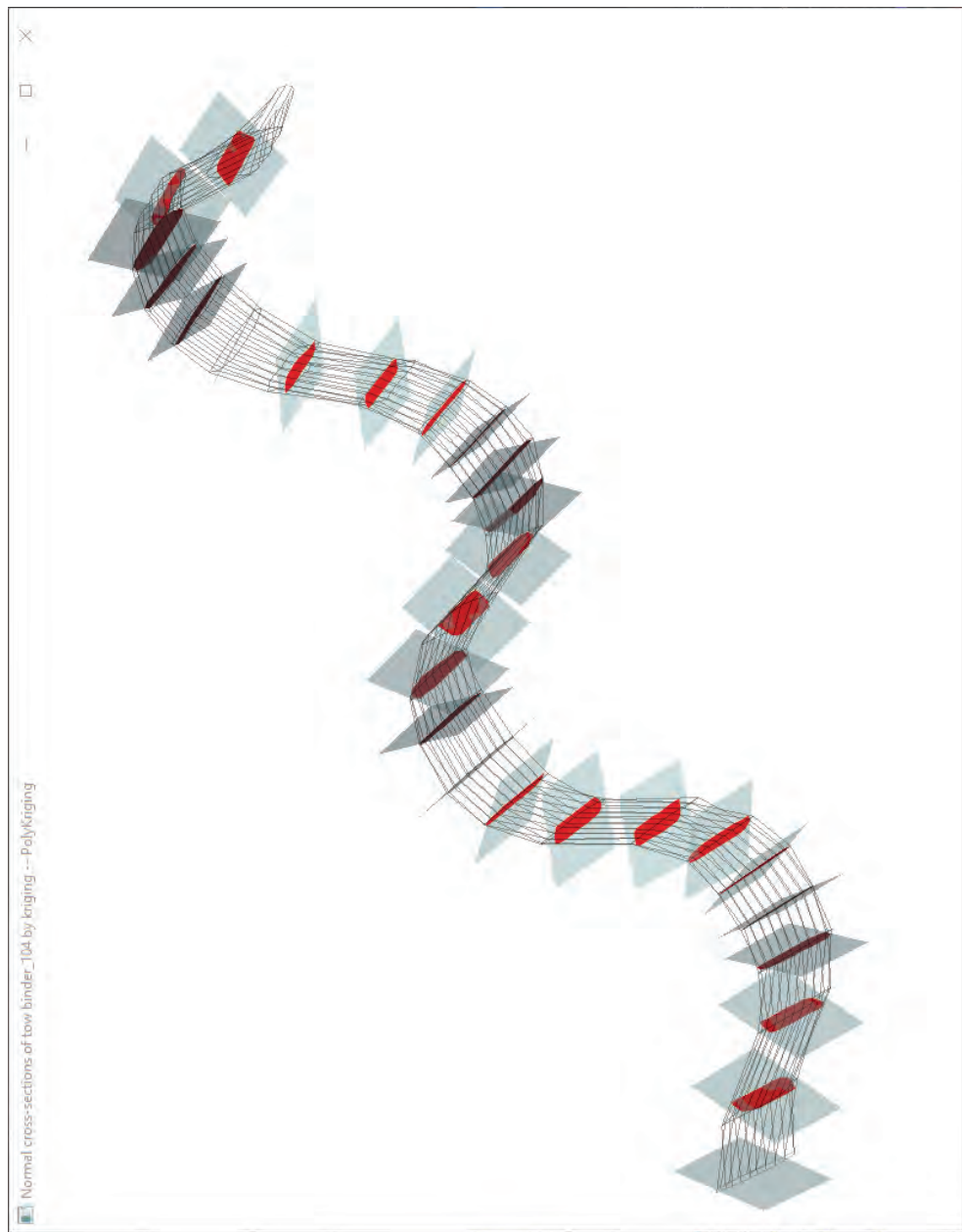


Figure C.3 Normal cross sections identified by proposed method based on parametric Kriging.

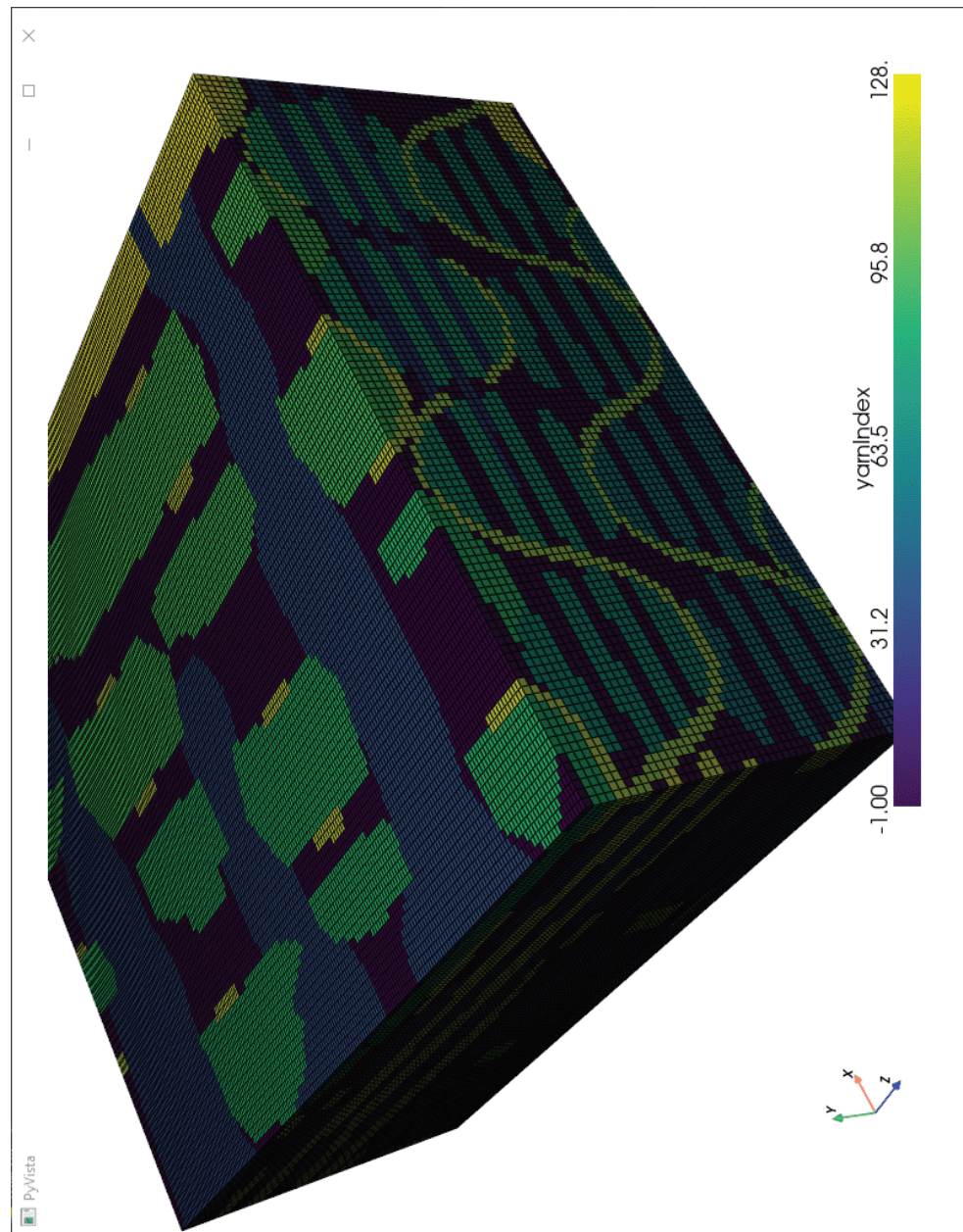


Figure C.4 Visualization of voxel mesh in PolyTex.

APPENDIX D CONFERENCE PRESENTATIONS, PAPERS, AND POSTERS

Presentations and/or papers

1. TROCHU François, YANG Bin, WANG Jihui, BÉGUIN Cédric, CAUSSE Philippe. Creation of Digital Material Twin (DMT) Geometric Models of High-performance Composites based on X-Ray Microtomography. 20th European Conference on Composite Materials (ECCM20). Lausanne, Switzerland, 2022. (**Conference paper**)
2. YANG Bin, WANG Jihui, CAUSSE Philippe, BÉGUIN Cédric, TROCHU François. On the Meso-structure Spatial Variability Characterizing and Geometric Modelling of Textile-Based Composite via Volume Imaging. 23rd International Conference on Composite Materials (ICCM-23). Belfast, UK, 2023. (**Conference presentation**)
3. YANG Bin, TROCHU François, BÉGUIN Cédric, WANG jihui, CAUSSE Philippe. Toward a Parametric Approach for Geometrical Modeling and Numerical Discretization of Textile Composites from Volumetric Image. 13th Canada-Japan Workshop on Composites (CJWC13). Quebec, Canada, 2023. (**Conference presentation and paper**)
4. FENG Yuwei, YANG Bin, WANG jihui, SUN Yixun, TROCHU François, CAUSSE Philippe. A Hybrid 1D/2D Numerical Framework for Flow Front Prediction in Perforated Foam Core Sandwich Composite Fabrication using VARTM. 13th Canada-Japan Workshop on Composites (CJWC13). Quebec, Canada, 2023. (**Conference paper**)

Poster

1. YANG Bin, TROCHU François, BÉGUIN Cédric, WANG Jihui, CAUSSE Philippe. Tomographic Modeling of Engineering Textiles for Numerical Simulation: A Parametric Approach. Research Center for High Performance Polymer and Composite (CREPEC) Annual Colloquium 2022.
2. YANG Bin, FENG Yuwei, BÉGUIN Cédric, CAUSSE Philippe, TROCHU François, WANG Jihui. Towards An Open Source Code for Image-based Numerical Simulations of Textile Reinforcements. Research Center for High Performance Polymer and Composite (CREPEC) Annual Colloquium 2023.